Effect of Non-Uniform Inlet Turbulence Distributions on High Pressure Turbine Heat Transfer

Ian Helms
Exeter College
University of Oxford

A thesis submitted for the degree of
Master of Science (Research)

Hilary 2011

Statement of Originality

The work presented in this thesis is, to the best of the candidate's knowledge and belief, original and the candidate's own work, except as acknowledged in the text. The material has not been submitted, either in whole or in part, for a degree at this or any other university.

Ian Helms

DISCLAIMER CLAUSE: The views expressed in this article are those of the author and do not reflect the official policy or position of the United States Air Force, Department of Defense, or the U.S. Government for Charles and Elizabeth Helms

Acknowledgements

I would like to first thank Lynn and Bart Holaday, you made the experience I have had the past two years possible. This program offers a fantastic opportunity for personal growth to an Academy graduate every year, and we can't thank you enough for this gift. Lynn recently passed away: in the short time I knew her I found her to be a warm, kind person and my goal has been to honor her memory by treating the Holaday's generosity with the respect it deserves. I am a lucky person.

I would also like to thank my family for their constant support, and my wonderful fiancée Alexandra for putting up with me throughout this process. They endured an astonishing amount of abuse in the form of arcane explanations of the minute details of my research, and made a fantastic effort at feigning interest and paying attention. Alex also had the arduous task of correcting my apparent failure to grasp the English language, a Herculean task for sure.

I would like to thank my supervisor Professor Li He, who maintained an unwavering high standard for my performance that pushed me to succeed at every step. He provided the crucial strategic vision and depth of knowledge whenever I foundered, for which I am deeply appreciative. I am a far better student and person because of his influence.

I would also like to thank Professor Martin Oldfield and Ashley Johnson for providing support in answering many questions I had regarding their work on the rotating bar experiments here at Oxford University.

To Devin, Richard, Adam, Francis, Chris, Rex, Brian, James, Imran and Rod: I want to thank for fielding what probably seemed like an endless barrage of questions testing every aspect of your technical knowledge from that obnoxious American Air Force officer...you guys provided a network of knowledge and directions that pulled me out of every rut I got into. Thanks to Adam, Brian, and Devin for feedback on some of the chapters in this thesis as well. I would like to thank my friend Andrew for providing feedback on some of the chapters, and answering a wide array of technical questions that always arise when constructing a long document. To Roni and Jason, thank you for responding to your friend's baffling assortment of unconnected engineering questions. Roni you also provided an invaluable editor's perspective, thank you.

Ian Helms
Oxford University, 2011

Abstract

The taxonomy of flow phenomena affecting turbine blade heat transfer has been widely researched and their specific effects established. However, the literature contains minimal consideration of circumferential length scales in the freestream turbulence intensity exiting the combustor despite experimental evidence for their existence in certain combustor geometries. The amplitude in these circumferential variations is demonstrated to vary up to 60% about the circumferential average. The distribution of the heat transfer coefficient on the surface of a turbine blade responds to variation in freestream turbulence intensity. Therefore it is necessary to study the effect of this circumferential variation in turbulence on turbine blade heat transfer.

This study utilized numerical methods to provide predictions of aerothermal conditions for eight high pressure turbine geometries and a NACA airfoil operating in transonic flow regimes. Included in the validation of the numerical solver were sensitivity studies of solver formulation and turbulence model selection. Comparative analysis using a NACA airfoil and high pressure turbine rotor blade for three solver formulations (density-based, pressure-based coupled, and pressure-based segregated) revealed that the pressure-based solvers retained improved computational efficiency and comparable aerothermal predictive performance relative to the density-based solver. However, the pressure-based solver required extensive native control at the start of the unsteady flow solutions in order to reach convergence, therefore rendering the density-based solver as the solver formulation of choice. In the parametric study of turbulence model sensitivity, the $k-\omega$ SST and Spalart-Allmaras models out-performed the others in predicting both surface pressure and heat transfer on two rotor blade profiles. In particular the $k-\omega$ SST model performed the best, predicting absolute levels of heat transfer to within 20% when the boundary-layer was fully turbulent. The two models also successfully captured the response of rotor heat transfer to variation in freestream turbulence intensity in steady flow. These turbulence models were then studied in simulations of two rotor profiles subjected to a passing upstream cylinder representing an upstream nozzle guide vane trailing edge. The two models were capable of resolving all of the unsteady flowfield features identified in previous experiments, as well as accurately predicting the time-averaged and unsteady rotor surface pressure conditions. The $k-\omega$ SST model outperformed the Spalart-Allmaras model in predicting both the time-averaged and unsteady heat transfer for the rotor subjected to a passing upstream bar. The accuracy of the $k-\omega$ SST model prediction of time-averaged rotor heat transfer was within 20% in fully turbulent regions of the rotor boundary-layer. Following final tuning, this high-performing turbulence model was used solely in the study of non-uniform inlet turbulence conditions.

The effectiveness of the code in predicting the aerodynamics and heat transfer in a range of validation studies provided justification for a numerical analysis of engine-representative turbulence intensity variation. This thesis employs circumferential freestream turbulence intensity variation in amplitudes ranging from 30% to 60%. Hot streaks were simulated at two ratios of maximum to minimum total temperature in the circumferential direction with values of 1.1 and 1.4. Combining the two distortions in phase allowed for the assessment of clocking on vane heat transfer. Combustor burner to vane count was simulated at 1:1 and 2:1. The predictions consistently showed the dependence of vane heat transfer coefficient distributions on turbulence distortion clocking to be on the order of 20%. This effect scaled on the amplitude of the circumferential turbulence variation. Simulations on a three-dimensional vane concurred with the two-dimensional results. These turbulence distortions propagated to the downstream rotor blade row, and altered rotor heat transfer unsteadiness. Overall, the engine-representative "turbulence streak" presents a new source of heat transfer that requires further experimental confirmation, creating another design variable to consider for turbine heat transfer engineers.

Nomenclature

Roman

a	speed of sound $[\frac{m}{s}]$
A	$k-\omega$ RANS model coefficient
$\vec{A}$	surface area $[m^2]$
c	chord length $[m]$
C_{ax}	axial chord $[m]$
C_p	specific heat capacity for constant pressure $[\frac{J}{kg \cdot K}]$
C_v	specific heat capacity for constant volume $[\frac{J}{kg \cdot K}]$
C_μ	empirical RANS turbulence model constant
D_H	hydraulic diameter $[m]$
e	internal energy $[J]$
E	energy $[J]$
$\bar{f}$	body forces $[N]$
h	convective heat transfer coefficient $[\frac{W}{m^2 \cdot K}]$
k	thermal conductivity $[\frac{W}{m \cdot K}]$, turbulent kinetic energy $[\frac{m^2}{s^2}]$
l	turbulence length scale $[m]$
M	Mach number
Nu	Nusselt number
P	pressure $[Pa]$, production of k $[\frac{kg}{m \cdot s^3}]$
$\dot{q}$	surface heat flux $[\frac{W}{m^2}]$
r	radial coordinate $[m]$, recovery factor
R	gas constant $[\frac{J}{kg \cdot K}]$, radius $[m]$, radius of curvature $[m]$
Re	Reynolds number
s	blade surface distance $[m]$
S	blade surface length $[m]$
St	Stanton number
t	time $[s]$
T	temperature $[K]$
T	period $[s]$
Tu	turbulence intensity $[\%]$
u	stream-wise velocity $[\frac{m}{s}]$
v	stream-normal velocity $[\frac{m}{s}]$
$\vec{v}$	velocity vector $[\frac{m}{s}]$
V	velocity magnitude $[\frac{m}{s}]$, volume $[m^3]$
w	bi-normal velocity $[\frac{m}{s}]$
x	axial distance $[m]$
y	circumferential distance $[m]$
Y	blade pitch $[m]$
y^+	non-dimensional measure of wall distance
z	span-wise distance $[m]$
Z	blade span $[m]$

Greek

α	inlet flow angle $[degrees]$, thermal diffusivity $[\frac{m^2}{s}]$
γ	ratio of specific heats
Γ	diffusion coefficient
ϵ	turbulence dissipation rate $[\frac{m^2}{s^3}]$
θ	angular coordinate $[radians]$
Λ	integral length scale of turbulence $[m]$
μ	dynamic viscosity $[\frac{kg}{m \cdot s}]$
$\tilde{\nu}$	Modified turbulent kinematic viscosity $[\frac{m^2}{s}]$
ρ	density $[\frac{kg}{m^3}]$
$\bar{\bar{\tau}}$	stress tensor $[Pa]$
ϕ	general transported scalar
ω	turbulence specific dissipation rate $[\frac{1}{s}]$

Subscripts/Superscripts

0	total conditions
2	initial wall temperature simulation
2	vane exit conditions, additional wall temperature simulation
3	rotor exit conditions
∞	freestream conditions
aw	adiabatic wall
f	film
i	inlet conditions
is	isentropic
ref	reference conditions
t	turbulent quantity
u	uniform inlet conditions
w	wall
$'$	fluctuating quantity

Abbreviations/Designators

2D	two-dimensional
3D	three-dimensional
ACE	Advanced Core Engine rotor blade profile
B22	Civil aircraft high pressure turbine rotor blade profile
B23	Civil aircraft high pressure turbine nozzle guide vane profile
CFD	computational fluid dynamics
C3X	Helicopter high pressure turbine nozzle guide vane profile
HGP	hot gas path
HPT	high pressure turbine
HTC	heat transfer coefficient
LE	leading edge
LPT	low pressure turbine
NACA	National Advisory Committee for Aeronautics
NGV	nozzle guide vane
ORF	Oxford Rotor Facility
PS	pressure surface
RANS	Reynolds-averaged Navier-Stokes
SA	Spalart-Allmaras
SS	suction surface
SST	shear stress transport
TE	trailing edge
TET	turbine entry temperature

Contents

1 Introduction **1**

1.1 Jet Engine Development and Operational Constraints 1

1.2 The High Pressure Turbine 2

1.3 Aims of the Thesis 5

1.4 Structure of the Thesis 6

2 Literature Review **7**

2.1 Overview 7

2.2 Heat Transfer Methods 7

2.2.1 Experimental Studies 8

2.2.2 Numerical Studies 10

2.3 Effects of Freestream Turbulence on Blade Heat Transfer 11

2.3.1 Experimental Studies 12

2.3.2 Numerical Studies 16

2.4 Effects of Unsteady Wakes on Blade Heat Transfer 17

2.4.1 Experimental Studies 18

2.4.2 Numerical Studies 20

2.5 Effects of Unsteady Shock Waves on Blade Heat Transfer 20

2.5.1 Experimental Studies 21

2.5.2 Numerical Studies 21

2.6 Combustor Representative Flowfields 22

2.6.1 Temperature Distortions 23

2.6.2 Combustor Exit Turbulence 25

2.7 Summary 27

3 Numerical Methods **29**

3.1 Overview 29

3.2 Numerical Tools 29

3.2.1 Governing Equations and the FLUENT Solver 29
3.2.2 Turbulence Modeling 31
3.2.3 Grid Generation 33
3.2.4 Boundary Conditions 35
3.2.5 Numerical Error and Compensation Strategies 36
3.3 Solutions Initialization and Convergence 37
3.4 Summary 39

4 Steady Flow Validation **40**
4.1 Overview 40
4.2 Analysis of FLUENT Solver Formulations in Transonic Flow 41
4.3 Steady Flow Validation for Two HPT Rotor Blade Profiles 48
4.3.1 Experimental and FLUENT Setup 48
4.3.2 Grid Dependency Studies 50
4.3.3 Predictions of Mid-Span Pressure and Heat Transfer Distributions 54
4.4 Summary 62

5 Unsteady Flow Validation **64**
5.1 Overview 64
5.2 Case Preparation and Dependency Studies 64
5.3 Predictions of Unsteady Rotor Blade Pressure Fields 68
5.4 Predictions of Unsteady Rotor Blade Heat Transfer 72
5.5 Summary 78

6 Non-Uniform Turbulence Effects on 2D Nozzle Guide Vane Heat Transfer **79**
6.1 Introduction and Overview 79
6.2 Turbulence Propagation Through a Turbine Blade Passage 80
6.3 2D Nozzle Blade Steady Flow Validation 87
6.4 Methods for Non-Uniform Inlet Boundary Conditions and Calculating Turbine Blade Heat Transfer Coefficient 89
6.4.1 Inlet Boundary Conditions 89
6.4.2 Calculating Heat Transfer Coefficient 92
6.5 Effects of Turbulence Distortion on B23 Heat Transfer 95
6.5.1 Single Passage 95
6.5.2 Two Vane Passages 99
6.6 Vane Exit Turbulence Intensity 102

6.7 Summary 103

7 Turbulence Distortion Effects on Downstream Rotor Blade Row 105

7.1 Overview 105
7.2 2D High Pressure Turbine Geometry and Dependency Studies 105
7.3 Case Preparation and Unsteady Heat Transfer Data Processing . . . 108
7.4 Effects of Inlet Turbulence Distortions on Rotor Heat Transfer 111
    7.4.1 Inlet Turbulence Distortion 111
    7.4.2 Inlet Temperature Distortion 115
    7.4.3 Inlet Combined Distortion 120
7.5 Summary 124

8 Turbulence Distortion Effects on a 3D Nozzle Guide Vane 126

8.1 Overview 126
8.2 3D NGV Geometry, Grid Generation, and Validation 126
8.3 3D Inlet Distortions and Heat Transfer Methods 130
8.4 Effects of Inlet Distortion on Nozzle Blade Heat Transfer 134
8.5 Summary 140

9 Conclusions 141

9.1 Summary and Conclusions 141
9.2 Recommendations for Future Work 145

A Computational Geometries and Grids, and Boundary Conditions 147

B Generation of Inlet Distortions 157

References 161

List of Figures

1.1 Cutaway of Pratt and Whitney 6000 Courtesy Cantwell (2005), Copyright United Technologies Corporation (Used with Permission) 3
1.2 Numerical Predictions of Turbine Passage Vortex Development Identified Via Modified Q Criterion, Courtesy Chang and Tavoularis (2009) 4

2.1 Heat transfer distribution to a turbine blade profile from Daniels and Schulz (1982), collected in Han et al. (2000) 12
2.2 Nozzle vane surface *St* response to variation in elevated levels of freestream turbulence, courtesy Ames et al. (2003b) 15
2.3 The rotating bar wake generator apparatus developed at Oxford University, courtesy Johnson, Rigby, and Oldfield (1989) 17
2.4 Simulated passing NGV trailing edge shock impacting rotor leading suction surface, courtesy Popp (1998) 22
2.5 Non-uniform temperature profile at the inlet to a high pressure turbine vane blade row, courtesy Povey and Qureshi (2008) 23
2.6 Instantaneous contours of entropy highlighting preferential heating effect on rotor pressure surface, courtesy He et al. (2007) 25
2.7 Combustor exit temperature and turbulence intensity normalized by circumferential mean, courtesy Heitor and Whitelaw (1986) 26

3.1 Arbitrary tetrahedral control volume, courtesy Cummings et al. (2004) 31
3.2 Grid for 2D nozzle vane highlighting prism layers and size functions, including magnifications of high curvature regions 34
3.3 Converted polyhedral computational grid for the 3D nozzle blade geometry 35
3.4 Example cell zones highlighting sliding grid method 35
3.5 Convergence history for 3D nozzle blade surface-averaged heat flux . 38
3.6 Converged unsteady flow monitor showing surface pressure on the suction surface of a civil aircraft rotor profile 38

4.1 NACA 0012 final grid and geometry 41
4.2 NACA 0012 grid dependency study of pressure coefficient (C_p) 42
4.3 NACA 0012 convergence history of the integral of pressure coefficient on upper surface 44
4.4 NACA 0012 solver sensitivity study comparing predictions to experimental data from Thibert et al. (1979) 44
4.5 ACE convergence history of the integral of blade surface heat flux . . 45
4.6 Sensitivity of ACE surface pressure to change in solver formulation . 46
4.7 Sensitivity of ACE surface Nu to change in solver formulation 46
4.8 Sensitivity of time-averaged ACE surface pressure to change in solver formulation 47
4.9 Converged steady flow density contours of ACE (left) and B22 (right) rotor profiles highlighting salient flowfield features 49
4.10 Grid dependency study for ACE blade surface isentropic Mach number 51
4.11 Effect of hade angle on ACE surface pressure prediction compared to experimental data from Johnson (1988) 52
4.12 Grid dependency study for ACE blade surface Nu 53
4.13 Grid dependency study for B22 blade surface isentropic Mach number 53
4.14 Grid dependency study for B22 blade surface Nu 54
4.15 Sensitivity study of ACE rotor surface pressure to RANS turbulence model 55
4.16 Comparison of turbulence models and experimental data from Johnson (1988) for ACE surface isentropic Mach number 56
4.17 Sensitivity study of B22 rotor surface pressure to RANS turbulence model 56
4.18 Sensitivity study of ACE rotor surface Nu to RANS turbulence model 57
4.19 Steady flow predictions of ACE surface Nu compared to experimental data from Johnson (1988) with 3% Tu in freestream 58
4.20 Sensitivity of B22 surface Nu to turbulence model–4.5% Tu 59
4.21 Sensitivity of B22 surface Nu to turbulence model–0.4% Tu 60
4.22 Experimental data from Doorly (1983) highlighting variation in blade surface Nu due to different levels of freestream turbulence 60
4.23 Predictions of variation in blade surface Nu due to different levels of freestream turbulence–$k - \omega$ SST model 61
4.24 Predictions of variation in blade surface Nu due to different levels of freestream turbulence–SA model 61

5.1 Velocity triangles at rotor inlet for the unsteady passing bar simulations 65
5.2 Grid dependency study for unsteady ACE rotor surface pressure . . . 66
5.3 Grid dependency study for time-averaged B22 surface heat flux . . . 66
5.4 Time-step dependency study for unsteady ACE rotor suction surface crown pressure monitor 67
5.5 Time-step dependency study for unsteady B22 rotor suction surface crown pressure monitor 67
5.6 Pressure (left) and entropy (right) contours showing taxonomy of unsteady rotating bar interactions with downstream ACE rotor profile . 68
5.7 Time-averaged ACE rotor surface pressure comparing FLUENT predictions and experimental data from Johnson (1988) 69
5.8 Comparison of time-resolved static pressure traces at three locations on ACE rotor surface showing FLUENT predictions and experimental data from Johnson (1988) 70
5.9 Effect of bar pitch on time-resolved experimental static pressure traces from Johnson (1988) 71
5.10 Velocity contours illustrating taxonomy of unsteady rotating bar interactions with downstream B22 rotor profile 72
5.11 Comparison of time-averaged B22 rotor surface heat flux (4.5%) Tu for FLUENT predictions and experimental data from Doorly (1983) . . . 73
5.12 Comparison of time-resolved heat flux traces at three locations on B22 suction surface showing FLUENT predictions and experimental data from Doorly (1983) 75
5.13 Effect of unsteady rotating bar on leading suction surface heat transfer at 4.5% Tu 76
5.14 Flow features of a cylinder subjected to transonic cross-flow conditions 76
5.15 B22 surface distributions of heat flux (upper) and pressure (lower) highlighting effect of passing bar on leading suction surface heat transfer 77

6.1 2D velocity contours for C3X nozzle vane highlighting exit measurement arc 81
6.2 C3X grid dependency study for vane surface isentropic Mach number distribution 82
6.3 Comparison of C3X vane surface Mach number for fine grid FLUENT prediction and experimental data from Ames (1994) 82

6.4 Initial and corrected exit turbulent kinetic energy compared to experimental data for grid-generated freestream turbulence 84
6.5 Corrected exit turbulent kinetic energy compared to experimental data for combustor-generated freestream Tu of 8% 86
6.6 Corrected exit turbulent kinetic energy compared to experimental data for combustor-generated freestream Tu of 12.1% 86
6.7 B23 grid dependency study for vane surface isentropic Mach number distribution, including experimental data from Nicholson (1981) . . . 87
6.8 B23 grid dependency study for vane surface heat flux distribution, including experimental data from Nicholson (1981) 88
6.9 Illustration of sinusoidal inlet distortion and various clocking positions for two distortion:NGV count ratios 90
6.10 Inlet total temperature and turbulence intensity profiles for 2D vane study at single clocking position 91
6.11 Summary map of inlet variations for the 2D nozzle blade 91
6.12 Range of calculated vane HTC distributions highlighting local linearity effect 92
6.13 Cross-passage propagation of pressure waves due to TE vortex shedding on the 2D vane 93
6.14 Comparison of single passage and two passage vane HTC distributions 94
6.15 Effect of non-uniform inlet turbulence distortion on 2D vane heat transfer at two clocking positions 96
6.16 Effect of non-uniform inlet turbulence distortion on 2D vane HTC at two offset clocking positions 96
6.17 Effect of non-uniform inlet temperature distortion on 2D vane heat transfer at two clocking positions 98
6.18 Effect of combined inlet turbulence and temperature distortion on 2D vane heat transfer at two clocking positions 98
6.19 Effect of non-uniform inlet turbulence distortion on two passage 2D vane HTC at two clocking positions 99
6.20 Effect of non-uniform inlet temperature distortion on two passage 2D vane HTC at two clocking positions 100
6.21 Effect of combined inlet turbulence and temperature distortion on 2D vane HTC at two offset clocking positions in two passage computational domain 101

6.22 Summary of clocking effects for various inlet distortion conditions on vane leading edge region HTC 102
6.23 2D vane exit turbulence intensity variation due to combined distortion clocking at combustor to vane ratio of 1:1 103

7.1 2D full stage grid dependency study of time-averaged surface heat flux 107
7.2 2D full stage grid dependency study of time-averaged surface heat flux 108
7.3 Summary map of inlet variations for the 2D HPT stage 109
7.4 Time-resolved HTC traces on rotor leading edge 110
7.5 Comparison of NGV exit turbulence intensity distributions with uniform flow and two clocking positions of inlet turbulence distortion . . 112
7.6 Time-averaged rotor surface heat flux for uniform flow and two clocking positions of inlet turbulence distortion 112
7.7 Time-averaged rotor surface HTC for uniform flow and two clocking positions of inlet turbulence distortion 113
7.8 Time-resolved rotor surface HTC for uniform flow and two clocking positions of inlet turbulence distortion over three vane passing periods 114
7.9 Close-up view of time-resolved rotor surface HTC at four locations– uniform and clocked turbulence distortions 114
7.10 Comparison of NGV exit turbulence intensity distributions with uniform flow and two clocking positions of inlet temperature distortion . 115
7.11 Temperature contours highlighting inlet temperature distortion clocking;(a) impinging on NGV leading edge;(b) impinging at NGV midpassage 116
7.12 Comparison of NGV exit turbulent kinetic energy distributions with uniform flow and two clocking positions of inlet temperature distortion 117
7.13 Time-averaged rotor surface heat flux for uniform flow and two clocking positions of inlet temperature distortion 118
7.14 Time-averaged rotor surface HTC for uniform flow and two clocking positions of inlet temperature distortion 118
7.15 Time-resolved rotor surface HTC for uniform flow and two clocking positions of inlet temperature distortion over three vane passing periods119
7.16 Close-up view of time-resolved rotor surface HTC at four locations– uniform and clocked temperature distortions 120

7.17 Comparison of NGV exit turbulence intensity distributions with uniform flow and two clocking positions of combined temperature and turbulence inlet distortion 121
7.18 Time-averaged rotor surface heat flux for uniform flow and two clocking positions of combined temperature and turbulence inlet distortion . . 122
7.19 Time-averaged rotor surface HTC for uniform flow and two clocking positions of combined temperature and turbulence inlet distortion . . 122
7.20 Time-resolved rotor surface HTC summary comparison of uniform flow, combined and temperature distortions, and two clocking positions . . 123
7.21 Time-averaged rotor surface HTC comparing temperature and combined distortions clocked to middle of NGV passage 124

8.1 3D nozzle vane geometry displaying three periodic repeats of the computational domain 127
8.2 Comparison of the 3D NGV surface Mach number and experimental data from Sheard (1989) at 10% span 128
8.3 Comparison of the 3D NGV surface Mach number and experimental data from Sheard (1989) at 50% span 129
8.4 Comparison of the 3D NGV surface Mach number and experimental data from Sheard (1989) at 90% span 129
8.5 Inlet radial temperature and turbulence distortion profile normalized to uniform inlet conditions 131
8.6 Inlet circumferential temperature and turbulence distortion profile normalized to uniform inlet conditions 131
8.7 Temperature contours at domain inlet illustrating hot streak clocked to middle of NGV passage 132
8.8 Turbulence intensity contours at domain inlet illustrating turbulence distortion clocked to middle of NGV passage 132
8.9 Summary of Inlet Profile Variations for the 3D nozzle blade 133
8.10 3D NGV surface heat flux augmentation, turbulence distortion on blade135
8.11 3D NGV surface heat transfer coefficient augmentation, turbulence distortion on blade 135
8.12 3D NGV surface heat transfer coefficient augmentation, turbulence distortion in middle of blade passage 136
8.13 3D NGV surface heat transfer coefficient augmentation, hot streak on blade 137

8.14 3D NGV surface heat transfer coefficient augmentation, hot streak in middle of blade passage . . . 137
8.15 3D NGV surface heat transfer coefficient augmentation, combined distortion on blade . . . 138
8.16 3D NGV surface heat transfer coefficient augmentation, combined distortion in middle of blade passage . . . 139
8.17 Summary of clocking effects for various inlet distortion conditions on vane leading edge region HTC—3D NGV domain . . . 139

A.1 NACA 0012 airfoil grid and geometry information . . . 148
A.2 Steady ACE rotor airfoil grid and geometry information . . . 149
A.3 Steady B22 rotor airfoil grid and geometry information . . . 150
A.4 Unsteady ACE rotor airfoil grid and geometry information . . . 151
A.5 Unsteady B22 rotor airfoil grid and geometry information . . . 152
A.6 C3X NGV airfoil grid and geometry information . . . 153
A.7 B23 NGV airfoil grid and geometry information . . . 154
A.8 2D HPT first stage grid and geometry information . . . 155
A.9 3D B23 NGV airfoil grid and geometry information . . . 156

B.1 Temperature contours at domain inlet illustrating hot streak clocked to middle of NGV passage . . . 160
B.2 Turbulence intensity contours at domain inlet illustrating turbulence distortion clocked to middle of NGV passage . . . 160

Chapter 1

Introduction

1.1 Jet Engine Development and Operational Constraints

Since the introduction of the De Havilland Comet in the 1950s, civil jet cargo and passenger aviation has exploded globally–along with the prevalence of the jet engine. In the year 2008, airports in the United Kingdom saw 315 billion passenger kilometres passing through their gates (Economic Regulations Group, 2010), and the UK Department of Transportation expects British air traffic to increase from 3.6% to 4.9% per annum in the foreseeable future. Jet engines do not operate on free energy. In 2008, US-flagged air cargo and passenger flights consumed 18.85 billion gallons of fuel, or 449 million barrels (Bureau of Transportation Statistics, 2010). The cost of jet fuel is highly volatile due to a number of factors, including intense world-wide demand and fluctuating economic externalities. The variable prices of oil extending back to 2007 and the global recession of 2008-2009 highlight the high level of uncertainty consumers of jet engine technology face, whether they are civilian or governmental organizations. In fact, the aforementioned volatility in oil prices was responsible for considerable losses totalling $4.3 billion in the US airline industry through the first three fiscal quarters of 2008 (Government Accountability Office, 2009).

Operators of jet aircraft must also deal with the realities of increasingly rigid regulatory frameworks dictating acceptable aircraft emissions. Although advances in jet engine technology have reduced noise emissions by up to thirty decibels from first generation civil jet aircraft (Guibet and Faure-Birchem, 1999), growing population density near airports and military bases demands continuing reduction in jet engine noise emissions. On a larger scale, growing recognition of the impact of human activity on the global climate has led all levels of government around the world to pay closer attention to emissions from a variety of sources. Scientists assert that the greenhouse gas effect from high-altitude emissions has a much larger climate impact than ground-based sources, and the expectation is that civilian aircraft will cause an increase in ozone levels by up to 13% by 2050 (Royal Commission on Environmental Pollution, 2002). The European Union has therefore begun implementing a “cap and trade” program to reduce emissions across the consortium (European Union, 2009), manufacturers of jet engines such as Rolls-Royce have voluntarily adopted goals to reduce noise and nitrous oxide pollutants from their engine emissions by 50% by 2010, and carbon dioxide emissions by ten percent (Royal Commission on Environmental Pollution, 2002).

All of these issues facing the end-user of jet engines in the aerospace community—whether it be increasing fuel efficiency to mitigate the financial impact of fuel price volatility, reducing noise emission impact on population centers and wildlife, or aiding the cause of reduction of greenhouse gases—demand a series of engineering solutions. In fact, a combination of improvements to airframe design and jet engines themselves has reduced per passenger fuel consumption by up to 70% in the past 60 years (Royal Commission on Environmental Pollution, 2002). Historically, the common trend in improving jet engine performance to solve the various demands of increased efficiency and reduced emissions has been an increase in the combustor operating temperature. The temperature of the combustor exit flow has long since passed the material limit for an uncooled blade; therefore understanding the flowfield within the combustor and turbine components of the jet engine, known collectively as the Hot Gas Path (Bunker, 2007), is critical to ensuring engine operability and durability.

1.2 The High Pressure Turbine

Examining a cutaway view of the Pratt and Whitney 6000 high-bypass turbofan engine clarifies the intensely hostile environment the components of the Hot Gas Path (HGP) endure (Figure 1.1). As air passes through the compressor and into the combustor, pressure rises to nearly 40 bar. Meanwhile, combustion of this high pressure air with the jet fuel results in temperatures that can exceed 2000 K in the combustor and just upstream of the initial turbine nozzle guide vane (NGV) blade row. As the combustor exit flow passes through the NGV passages, velocities will sometimes exceed the speed of sound. All these factors—high pressure, high temperatures, and

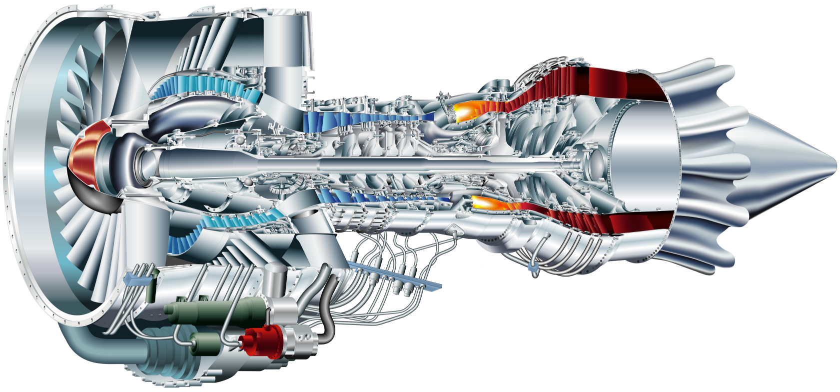

Figure 1.1: Cutaway of Pratt and Whitney 6000 Courtesy Cantwell (2005), Copyright United Technologies Corporation (Used with Permission)

transonic/supersonic flow regimes—in addition to the complex secondary flow structures that arise from rotating turbine blade rows and endwall effects render combating thermal loads in the turbine portion of the HGP a particularly challenging heat transfer engineering problem. In particular, this thesis focuses on the turbine component of the HGP.

Flow phenomena that increase the complexity of the turbine stage heat load can be found immediately at the combustor exit. For example, the air exiting the combustor retains high levels of freestream turbulence, which is shown to advance the onset of transition on a turbine blade surface. Accurate measurement of these combustor exit turbulence levels is important, as they are shown to affect even fully turbulent blade boundary layers. In addition to high turbulence, the air temperature has gradients in both the radial and circumferential directions that serve to re-arrange the driver temperature distribution on the NGV blade surface. Furthermore, boundary layer development on the endwalls of the engine upstream of the turbine splits upon reaching the vane leading edge, and spirals into the passage in the form of counter-rotating horseshoe vortices. These vortices contribute both to variations in vane heat transfer and downstream rotor heat transfer. Figure 1.2 highlights the development of various vortices in the first stage of a high pressure, transonic turbine, using modified Q criterion to identify vortices (Chang and Tavoularis, 2009). In addition to the vane leading edge, large-scale vortices develop off of the vane trailing edge, in the inter-blade row axial gap, and on multiple locations in the rotor blade passages, all of which can contribute to the heat transfer conditions on the blade surfaces. As

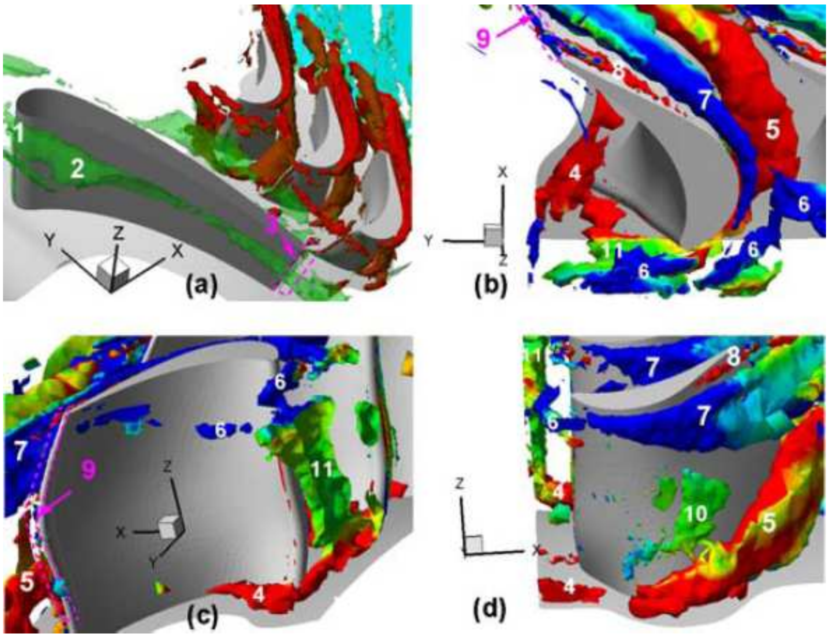

Figure 1.2: Numerical Predictions of Turbine Passage Vortex Development Identified Via Modified Q Criterion, Courtesy Chang and Tavoularis (2009)

mentioned previously, the acceleration of the flow through the vane throat frequently results in transonic or supersonic flow conditions. The result of these conditions is shock structures emanating from the trailing edge that impact both the adjacent vane suction surface and the downstream rotor blade row. At sufficient NGV exit Mach number, the upstream running shock can even reflect back onto the adjacent rotor blade row as well.

The first-stage rotor heat transfer environment inherits elements of the combustor exit fluid at lower temperatures in addition to the lossy fluid emanating from the vane row and the additional complexity of a rotating reference frame. Due to the velocity deficit in the vane wake, the reduction in the rotor relative inlet tangential velocity creates a "negative jet" (Hodson 1984, from Allan et al. (2008)) that pulls low-momentum boundary-layer fluid from the rotor pressure surface to the rotor suction surface. This negative jet has been shown to be dependent on combustor-turbine configurations, with the circumferential temperature distributions at the combustor exit overcoming the wake dynamics to induce preferential heating on the latter rotor pressure surface. The vane wake also acts as a periodic enhancement of the freestream turbulence at the vane passing frequency. This serves to induce earlier onset of boundary-layer transition on the rotor suction surface, as well as enact similar enhancement of turbulent boundary layer heat transfer as described above. Additional turbine stages experience similar three-dimensional flow gradients and unsteadiness, but at lower fluid temperatures, thus reducing the importance of heat transfer considerations in these downstream blade rows.

Categorizing and quantifying these flowfield effects is fundamentally important to effectively designing blade cooling techniques. There appears, however, to be a gap with respect to the topology of combustor exit turbulence. Obtaining detailed combustor exit turbulence at engine-representative aero-thermal conditions is a difficult task. However, circumferential variation in the combustor exit turbulence has been reported up to a level of 60% about the mean. There appears to be no report of the effect of this variation on turbine blade heat transfer in the available literature. Varying uniform freestream turbulence is a well-documented source of significant turbine blade heat transfer augmentation. Therefore it is important to characterize the effects of this engine-representative flow on the high pressure turbine heat transfer environment.

1.3 Aims of the Thesis

The purpose of this thesis is to show, via numerical predictions of turbine blade heat transfer, that circumferential length scales in the inlet turbulence field for a high pressure turbine can produce significant variation in the heat transfer environment not only on the initial vane blade row, but the downstream rotor blade row as well. The mechanism with which this variation in the convective heat transfer to the blade is derived is shown to be a variation in the convective heat transfer coefficient. The numerical tool will be shown to effectively predict not only the aerodynamics of steady and unsteady turbine blade rows in both two and three dimensions, but the propagation of turbulence through turbine blade rows and blade heat transfer as well. The consistency and amplitude of the effects of these engine representative non-uniform turbulence fields on high pressure turbine blade heat transfer throughout the numerical predictions will indicate an additional potential consideration for the designer of HPT blade cooling techniques. The range of computational studies will include a variety of geometries in transonic flow conditions. These geometries include an analytically derived 2D airfoil from the NACA 4-digit series of airfoils (the NACA

0012 to be precise), as well as a range of high pressure turbine blade profiles. Two NGV geometries will be employed, including a helicopter HPT NGV (the C3X) and the NGV currently employed in the Oxford Rotor Facility (the B23). The constant streamtube cut at mid-span and the full 3D geometry for the B23 will be evaluated in this thesis. Finally, two separate 2D HPT rotor blade profiles will be tested, a military aircraft rotor blade (ACE) and a civil aircraft rotor blade (the B22). The consistency of results across a range of geometries will provide greater confidence in the generality of the numerical predictions provided herein.

1.4 Structure of the Thesis

Following this introduction, **Chapter 2** surveys the current literature on turbine blade heat transfer studies concerning all of the aforementioned phenomena, and summarizes important findings.

Chapter 3 outlines the numerical methods adopted in this study.

Chapters 4 and 5 constitute the initial validation and verification studies conducted in this research.

Chapter 6 expands the focus of the thesis to investigate the effect of the circumferential length scales in turbine inlet turbulence on vane heat transfer.

Chapter 7 presents results for the effect of these turbulence variations on a downstream rotor blade row.

Chapter 8 further evaluates the inlet boundary profiles on a 3D nozzle blade geometry.

Chapter 9 offers conclusions and recommendations for future research.

Chapter 2

Literature Review

2.1 Overview

In reviewing the available literature on turbine blade heat transfer, the author sought two objectives. The first of these outcomes is to characterize the primary contributions from the turbine flowfield to turbine blade heat transfer. The process for identifying these contributions first requires a brief comparison of experimental and numerical methods used to solve the heat transfer problem (Section 2.2). This technique of comparing experimental and numerical studies is used throughout the chapter to establish expectations for the capabilities of numerical code to capture various elements of turbine flow and their influence on turbine heat transfer. Following the presentation of common heat transfer methods, the influence of freestream turbulence, unsteady passing wakes, and unsteady passing shocks on turbine heat transfer is distilled (Section 2.3 to 2.5). Summarizing the current state of research into combustor exit flow non-uniformity is the second objective of this literature review (Section 2.6). Until now, the focus has primarily been on temperature and total pressure non-uniformity. As it will be seen, the non-uniformity in turbulence intensity can be significant at the combustor exit, yet the effects of this non-uniformity on turbine blade heat transfer are rarely studied and poorly understood.

2.2 Heat Transfer Methods

Dunn (2001) notes that heat transfer results for turbine blades were originally developed as empirical correlations and were frequently reported in the form of the surface Stanton number St or Nusselt number Nu, where St is the ratio of the convective heat transfer to the heat capacity of the fluid, and Nu is the ratio of convective to conductive heat transfer. These non-dimensional values can be produced via a range of definitions, but they are generally presented as the following:

$$St = \frac{h}{\rho u_\infty C_p} \tag{2.1}$$

$$Nu = \frac{hL}{k_f} \tag{2.2}$$

The common element in these definitions of blade heat transfer is that all of them require a method for obtaining the convective heat transfer coefficient (HTC) h. The coefficient is the ratio of the blade surface heat flux to the difference in a reference temperature and the blade wall temperature as shown below in Equation 2.3.

$$h = \frac{q}{(T_{ref} - T_w)} \tag{2.3}$$

The exact process varies but, in general, experimental methods focus on obtaining the heat flux to the blade, whereas numerical solutions can calculate the HTC directly (Dunn, 2001). The following sections highlight the state of the art in heat transfer methods for both experimental and computational studies. The aim is to establish current trends in the methods, rather than conduct an exhaustive review of every technique available.

2.2.1 Experimental Studies

In order to construct the boundary conditions for the heat transfer problem, experimentalists must obtain measurements from the flowfield. The heat flux is typically measured in two ways. The first is to supply a flow of heated air to a blade surface at ambient temperature. The temperature of the fluid near the blade surface can then be measured by a device such as a thin film gauge. The actual setup for the gauge depends strongly on the test conditions. Blade material in a cascade rig typically consists of a machineable glass with very low thermal conductivity, such as in Nicholson (1981) or Doorly (1983), which allows for the use of a single-layer gauge. However the stress placed on the blades in a fully rotating rig requires a metal blade, in which multi-layer gauges are required, as in Dunn (2001).

Doorly and Oldfield (1987) described the theory of multi-layer thin film gauges. In this method a highly conductive metal is set in an insulated surface. This setup allows for a semi-infinite conduction assumption for the heat flux to the gauge. The governing equation for the heat transfer problem is then the one-dimensional conduction equation (shown in Equation 2.4).

$$\frac{\delta^2 T}{\delta^2 x} = \frac{1}{\alpha}\frac{\delta T}{\delta t} \tag{2.4}$$

The surface heat flux is then calculated from the relationship between the change in temperature and the change in resistance in the thin film gauge. This method is one of the most common in the literature. It has been used in a wide range of studies in many flow conditions, for example Arts and de Rouvroit (1992), Doorly (1983), Johnson (1988) and Ashworth (1987). The primary challenge and limitation of this method is the proper setup and careful calibration of the necessary devices, and the 1D conduction assumption (Dunn, 2001).

Alternatively, it is possible to directly supply the heat flux to the blade surface. Lowery and Vachon (1975) used strips of heater foil to provide the heat flux to a cylinder in cross flow. Completely wrapping the blade in a heater foil with constant flux is also a common method (Ames, 1997; Van Fossen and Bunker, 2001; Ames et al., 2003a). The primary limitation of this method of obtaining the heat flux is that it is necessary to account for the full energy balance to the blade. Radiative contributions to the heat flux are typically accounted for by a blackbody assumption for the blade surface (Ames et al., 2003b). Conductive heat loss is then ignored or accounted for via an additional numerical calculation, such as the finite element analysis used in Ames (1997).

Measurement or calculation of the reference and wall temperatures for the blade is accomplished in an array of methods. Blade surface temperature can be taken via a thermocouple embedded in the test geometry (Lowery and Vachon, 1975), or by using a thermally dependent coating on the blade surface such as liquid crystals (Giel et al., 2004; Ames et al., 2003a). The reference temperature has definitions in the literature that range from simply utilizing the freestream total temperature (Lowery and Vachon, 1975), to a more involved calculation of the local adiabatic wall temperature (Giel et al., 2004; Nasir et al., 2009) such as the following:

$$\frac{T_{aw}}{T'_{in}} = r + \frac{1-r}{1+0.5(\gamma-1)M_{is}^2} \tag{2.5}$$

Where r is the recovery factor, which accounts for irreversibilities in the boundary-layer (Holman, 1997). The thermal conductivity of the fluid is then derived from some combination of these temperature values and calculated using empirical relationships. The exact method varies between publications.

While the above methods are widely cited in the literature, it is also possible to employ a transient technique to determine the HTC directly. In this method a step change in the air temperature is imparted to steady flow, and the response in the wall temperature is measured continuously. These temperature measurements are obtained from variety of techniques, including thermocouples or liquid crystal thermography (Han et al., 2000). When thermocouples are employed, the time history of the temperature on the wall is supplied to the equation:

$$\frac{T_w(\text{steady state}) - T_w(t)}{T_w(\text{steady state}) - T_w(\text{initial})} = e^{-\alpha t} \tag{2.6}$$

Where the temperature history is then related to the HTC by:

$$\alpha = \frac{h_f}{\rho l C_p} \tag{2.7}$$

2.2.2 Numerical Studies

As in experimental studies, the definition of the boundary conditions for the heat transfer problem varies significantly. For example, an isothermal boundary condition can be enforced on the blade surface (Garg, 1998). The solver then computes the heat transfer coefficient directly, as the entire fluid domain is available for online processing. If the conduction of the heat into the blade itself is needed, it is possible to use a conjugate simulation of both the fluid and the solid domain, such as in He and Oldfield (2009). The ability to simultaneously store all the information required to solve the heat transfer problem is an advantage of numerical methods. The goal then is to accurately model the fluid physics in the domain. This requires proper meshing of the computational domain and appropriate models of the fluid material and turbulence. The overriding challenge in modeling the flow physics continues to be a suitable turbulence model.

Overall, numerical studies of turbine blade heat transfer have shown increasing fidelity over the years. However, the inability to directly resolve the full spectrum of turbulence has necessitated the use of limited turbulence models instead. There are a range of consequences that stem from the assumptions inherent to these models, but one of the most frequent sources of error in numerical solutions is inaccurate resolution of the boundary-layer transition point. For example, Maaroofi et al. (2007) generated a two-dimensional computational domain representing the VKI blade profile. Heat transfer was predicted utilizing the RANS equations, and a variety of turbulence models were used to provide closure. Transition was inaccurately resolved over nearly all the flow conditions considered, despite use of high y^+ resolution. The presence of increased turbulence (and expected earlier transition) did not seem to improve the predictive performance of any of the turbulence models presented.

In fact, the search for a broadly applicable turbulence model is ongoing. Comparative analyses amongst various models, show that the $k-\epsilon$ (Rahman et al., 2005), $k-\omega$ SST (Papa et al., 2007; Levchenya and Smirnov, 2010), and even algebraic models such as the Baldwin-Lomax model (Garg, 1998) all show good performance in predicting turbine heat transfer. In other studies (Kulisa and Dano, 2006; Liu, 2007), the heat transfer predictions with some of these same models tend to be poor; they fail not only to accurately capture the absolute value of the heat transfer distribution, but also do not resolve the qualitative trend over the surface. In some cases, the strongest contributions of the flowfield to turbine blade heat transfer are inviscid in nature, allowing for fairly simple models to provide accurate predictions. Haldeman et al. (2005) evaluated aerodynamic and heat-flux measurements and compared these with inviscid numerical predictions in a one and a half stage HPT at transonic operating conditions. They found that the inviscid code performed quite well in predicting the pressure field throughout the turbine.

Overall, the confidence of heat transfer prediction from the numerical tools seems to require strong validation against experimental results. In particular, heat transfer predictions tend to be more sensitive than aerodynamics to the accuracy in numerical solution methodology and choice of turbulence model adopted. Confidence in heat transfer predictions therefore require more attention and care in verification and validation before commencing large-scale simulations.

2.3 Effects of Freestream Turbulence on Blade Heat Transfer

Now that the common methods for determining turbine blade heat transfer have been established, it is instructive to frame the effects of the various flow disturbances on blade heat transfer. First consider a uniform, steady flow upstream of a turbine blade profile with little or no turbulence in the freestream, such as the rotor blade in Figure 2.1. As the air-flow over the blade is inherently viscous, boundary-layer growth occurs over the blade surface beginning at the leading edge. Depending on the geometry of the blade and the freestream velocity, the boundary-layer will transition from laminar

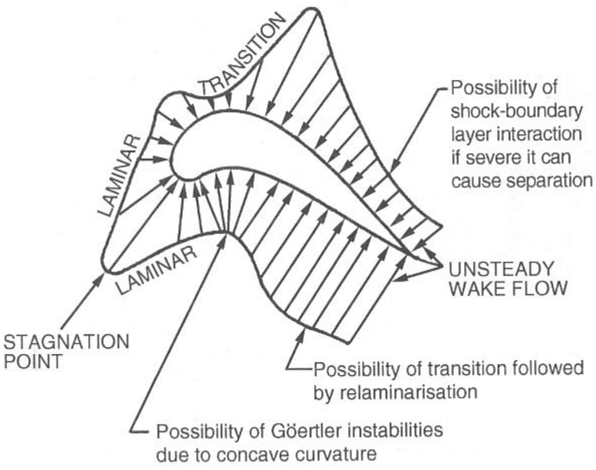

Figure 2.1: Heat transfer distribution to a turbine blade profile from Daniels and Schulz (1982), collected in Han et al. (2000)

to turbulent at some point on the blade surface per the critical Reynolds number. In some cases the boundary-layer will re-laminarise due to the favorable pressure gradient on the blade surface. The presence of a turbulent boundary-layer results in a significant increase in local heat flux on the blade surface. Figure 2.1 highlights these characteristics for a turbine blade at mid-span in laminar flow.

Studies of the effects of freestream turbulence on turbine blade heat transfer use a variety of methods to generate augmented levels of turbulence intensity, including grids and jets such as in Lowery and Vachon (1975) and Bons et al. (1996), respectively. Experimentally, turbulence is typically characterized by both its intensity and its length scale. The definitions for these quantities vary, but the generally accepted form relates the RMS velocity fluctuations of the turbulence to the magnitude of the flow velocity, and the length scale is the size of the bulk eddies in the turbulence field. When the turbulence is generated via upstream grids, the length scale can often be related to the size of the turbulence generating bars (ANSYS, 2006).

2.3.1 Experimental Studies

Variation in freestream turbulence intensity was first evaluated experimentally for its effects on the transitional nature of the boundary-layer, since the turbulent boundary-layer exhibits a dramatic increase in the heat transfer to the blade surface as compared to the laminar one. Talmor and Weber (1970) found that the freestream turbulence can also significantly affect the ability of a turbulent boundary-layer to re-laminarize under strong acceleration. Kearney et al. (1973) evaluated the Stanton number of a turbulent boundary-layer under strong acceleration. They found that the initial thermal condition of the boundary-layer significantly affects the entirety of the surface heat transfer characteristics throughout the boundary-layer. They also found that for an acceleration parameter up to $2.5 \cdot 10^{-}6$ the boundary-layer will not re-laminarize. McDuonald and Kreskovsky (1974) demonstrated that for a turbulent boundary layer an increase of 30% in heat transfer rates for a freestream turbulence level increase of 5% can be expected.

Lowery and Vachon (1975) studied the effects of freestream turbulence on cylinder heat transfer. The cylinders were tested in a range of Reynolds numbers from $1 \cdot 10^5$ to $3 \cdot 10^5$, and a range of freestream turbulence intensities from 0.4% to 14.2%. Turbulence scale was in the range of 1.5% to 9.5% of the cylinder diameter, and the absolute values of this integral length scale were from 0.113 to 0.426 inches. The turbulence was shown to effect a 61% increase in the cylinder heat transfer over theoretical Frossling ($\frac{Nu}{Re^{0.5}}$) number for zero inlet turbulence. A correlation was developed relating the Nu to the turbulence intensity and the square root of the Reynolds number. However, the belief is that the correlation only holds for subcritical flows. Sugawara et al. (1988) studied the effects of freestream turbulence on flat plate heat transfer. They found that increasing the freestream turbulence decreases the critical Reynolds number. The increasing turbulence in the freestream serves to increase the turbulence in the boundary-layer. The thickening of the turbulent layer and the thinning of the laminar sub-layer is thought to result in the increased heat transfer. They did not show a significant effect of increasing freestream turbulence on laminar heat transfer, but did witness increasing heat transfer in the turbulent boundary-layer. Freestream turbulence intensities in excess of 8% did not significantly affect flat plate Nu, and the maximum enhancement was on the order of 55% over the smallest freestream turbulence value. Arts and de Rouvroit (1992) demonstrated the influence of freestream turbulence on blade heat transfer in a range of Reynolds and Mach numbers. The greatest augmentation was seen in the earlier transition of the boundary-layer on the blade suction surface. The pressure surface boundary-layer remains laminar for most of the conditions tested, but the highest levels of freestream turbulence (6%) caused the boundary-layer to become fully turbulent once the exit Mach number exceeded unity.

It is interesting to note that Bons et al. (1996) studied the effect of high levels of freestream turbulence generated via jets, with intensities of 13.43% and 18.8%. They found that the freestream turbulence effect on the film cooling effectiveness is also dependent on the blowing ratio. In particular, high blowing ratios and high freestream turbulence actually increase effectiveness further downstream of the cooling holes. It also increases the lateral spread of the film cooling. The effects are sometimes pronounced, and variation depending on the combination of turbulence intensity and blowing ratio can be up to 200%. More recently, a strong correlation between the local velocity fluctuations and the heat transfer coefficient for a cylinder in the presence of elevated freestream turbulence has been demonstrated (Nix and Diller, 2009). This offers an avenue for linking the local conditions to the inlet conditions, and thereby establishing stronger correlations to estimate turbine blade leading edge heat transfer.

A modern strain of research into the effects of freestream turbulence focuses on combustor-representative turbulence. This turbulence is typically in excess of 10% in its intensity, and has larger length scales as compared to grid generated turbulence of a comparable intensity Ames and Plesniak (1997). This research stems largely from a finding that for a single combustor configuration the addition of the flame did not produce a significant variation in the exit turbulence field (Moss and Oldfield, 1991; Moss, 1992). As a result, many studies have been conducted utilizing representative combustor geometries upstream of turbine blades (Ames, 1994, 1997) to assess the effect on heat transfer. In Ames (1997) the experimental Reynolds numbers were at $5 \cdot 10^5$ and $8 \cdot 10^5$, and the exit Mach number was 0.27. The turbulence intensities tested in the experiment were a tunnel ambient level of 1%, grid and combustor turbulence at 8%, and a near combustor configuration with turbulence intensity of 12%. Integral length scales of the turbulence field ranged from 1 to 8.5 cm, and the energy-based length scales were in the range of 1 to 18.7 cm. The turbulence intensity and the length scale were shown to both affect on the heat transfer. Ames and Plesniak (1997) reported that the presence of the combustor turbulence contributed to a higher level of loss in the blade passage, which was attributed in part to increased turbulent mixing in the flow. The increase in freestream turbulence was shown to reduce the peak velocity deficit at the wake centerline, as well as to increase the wake half-width. Eddy diffusivity in the wake was found to be strongly affected by both the turbulence intensity and the turbulence length scale. Ames (1998) utilized blades with three film cooling configurations with the goal of evaluating varying levels of turbulence on film cooling performance. The highest levels of Stanton number augmentation within the

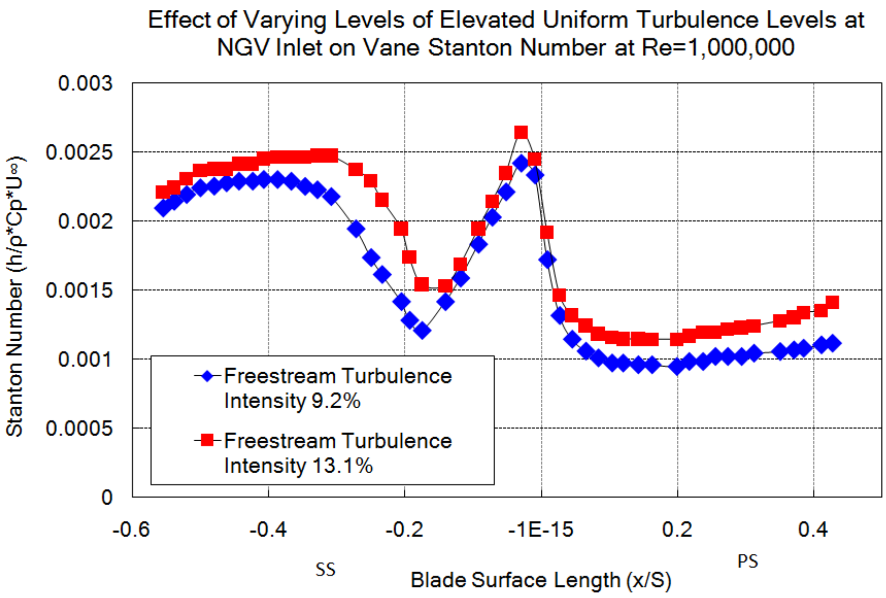

Figure 2.2: Nozzle vane surface *St* response to variation in elevated levels of freestream turbulence, courtesy Ames et al. (2003b)

results were found in the laminar regions as opposed to the turbulent regions of the blade boundary-layer when the freestream turbulence intensity was increased.

Van Fossen and Bunker (2001) generated high levels of combustor-representative freestream turbulence and found enhancement of the Frossling number to be approximately 180% of the laminar value, and 14% higher than a predicted value derived from a grid-generated turbulence correlation. Radomsky and Thole (2000) studied the effects of high levels of freestream turbulence on vane heat transfer. They found that a high freestream turbulence intensity of 19.5% and an integral length scale of around 0.25 vane pitch enhanced vane heat transfer by shifting the boundary-layer transition forward on the vane surface. The authors also witnessed lower shape parameters, which are indicative of turbulent boundary-layers. The pressure surface also exhibited fluctuations in velocity in the boundary-layer despite mean velocity profiles that are closer to laminar levels. This fluctuating behavior in the laminar boundary-layer has also been seen in LPT turbine blades with laminar boundary-layers subjected to elevated freestream turbulence (Choi et al., 2004). The augmentation of heat transfer is also evident at multiple levels of elevated freestream turbulence (Ames et al., 2003b). In fact, this variation at high levels of turbulence from 9% to 13% was shown to increase *St* on the order of 10% to 20% in both the laminar and transitional regions of a nozzle vane (Figure 2.2). Ames et al. (2004) evaluated the effect of turbulence generated from three combustor representative geometries on an aft-loaded vane's heat transfer distribution. They found significant augmentation of both the pressure surface and stagnation region heat transfer. The highest augmentation was found from the aero-derivative combustor geometry, which also produced the highest level of turbulence intensity.

The study of endwall heat transfer has also been conducted using these combustor simulators. Ames et al. (2003a) examined the effect of simulated combustor turbulence on vane endwall heat transfer. The experiment was conducted in a linear cascade in a range of Reynolds numbers from $5 \cdot 10^5$ to $2 \cdot 10^6$. The effect of the combustor turbulence on the endwall heat transfer was shown to decrease for increasing Reynolds numbers. However, the increased turbulence tended to reduce the effect of secondary flows on the qualitative behavior of the endwall heat transfer distribution due to increased turbulent mixing and influence of the secondary flow structures. This behavior was not seen in the wake regions and the leading edge horseshoe vortex. Lee et al. (2004) found that the combustor turbulence makes the endwall heat transfer more uniform. The leading edge and wake regions still retain high levels of heat transfer. Average heat transfer is enhanced by 27% over the low turbulence case.

2.3.2 Numerical Studies

Numerical studies are limited compared to experimental studies, and typically serve to complement the experimental results. Hori et al. (1997) utilized a two equation eddy viscosity model of the $k - \epsilon$ formulation to study the effect of freestream turbulence on a flat plate under a neutral pressure gradient for heat transfer. They found that the increase in turbulence intensity and integral length scale of turbulence in the freestream will increase the Nusselt number, but that these effects remain small if the integral length scale is relatively small. In turbine applications, the turbulence models have been shown to qualitatively detect the variation in heat transfer due to elevated freestream turbulence, but the absolute level of augmentation was not accurately captured (Nasir et al., 2009). Often, the quality of the prediction is again determined by the ability to accurately resolve the boundary-layer state (Ames et al., 2003b).

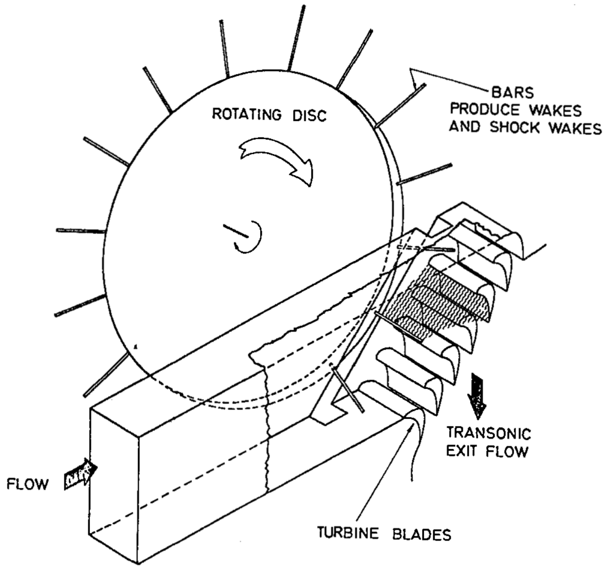

Figure 2.3: The rotating bar wake generator apparatus developed at Oxford University, courtesy Johnson, Rigby, and Oldfield (1989)

2.4 Effects of Unsteady Wakes on Blade Heat Transfer

The inherently unsteady nature of the flow in a turbine has been known for quite some time. Initial efforts to address this unsteadiness involved experimental apparati that were mechanically unable to isolate the wake turbulence from the freestream turbulence (Priddy and Bayley, 1985; Liu and Rodi, 1994). At Oxford University, a more effective device was implemented (Doorly, 1983) that spun a rotating bar wake generator in a transonic turbine cascade to allow for more accurate studies of the effect of these unsteady wakes on turbine blade heat transfer (Figure 2.3). The experimental setup effectively inverted the typical velocity triangle for the HPT first stage by using a cascade of stationary rotor blades, while the spinning upstream bar represented the nozzle vane trailing edge.

The initial use of this device in a simulated high pressure turbine environment has since been expanded to investigate unsteady wakes in both the compressor and the turbine. When used in conjunction with turbine geometries, heat transfer studies on cylinders and full turbine blade geometries have been investigated for a range of compressibility conditions. It is also noteworthy that the number of LPT wake generator studies is far more substantial than available studies in the high pressure stages. More recently, this form of wake generator has been tested to evaluate its effectiveness in clocking applications, with the stators implemented as full blades and the rotor represented by the bar (Konig and Stoffel, 2007).

2.4.1 Experimental Studies

Doorly (1983) operated the rotating bar apparatus with a simulated NGV exit Mach number of 0.96, and measured the heat flux to the rotor blade profiles using a thin film gauge. Obtaining accurate measurements of the heat flux in this transonic, unsteady operating environment was a considerable feat at the time. Freestream turbulent intensity ranged from 0.4% to 5% and dual bar passing frequencies showed a strong dependence from the time-averaged and time-resolved heat transfer on the freestream turbulence values. Steady flow for the varied turbulent conditions showed time-averaged heat transfer rates were enhanced by 600% at 50% surface length on the suction surface when the freestream value was increased from 0.4% to 5%. Wake passing led to enhanced heat flux over the low turbulent conditions as well, but decreased the heat transfer compared to the steady 5% turbulent value over the first 30% of the suction surface. Overall, the heat flux was tied directly to the boundary-layer state over the surface, as heat transfer levels for both the steady and bar-passing tests showed agreement once the boundary-layer had transitioned. Doorly also noted the unsteady transition of an otherwise laminar boundary-layer induced by the passing wake. This study also noted the dependence of the re-laminarization of the boundary-layer on the wake width. Overall the boundary-layer response to the unsteady wakes was inadequately captured by quasi-steady or steady approximations of the passing wake. Korakianitis et al. (2002) demonstrated quasi-steady boundary-layer approximations are sufficient to predict the unsteady heat transfer rate only when vane exit Mach conditions are subsonic, and when the boundary-layer reduced frequency is much smaller than the core flow reduced frequency.

Subsequently, Ashworth (1987) studied the influence of the wakes on a film-cooled version of the rotor profile utilized by Doorly, as well as the Advanced Core Engine (ACE) profile. The bar diameter for the ACE profile measured 1.6mm, and simulated exit flow from an NGV with a relative Mach number across a range of supersonic values, up to 1.4. Three separate flow incidences were tested as well, including 0°, $+5°$ and $-10°$. Heat transfer results were presented in time-resolved and time-mean form via the non-dimensionalized Nusselt number. The freestream turbulence, NGV exit Reynolds number, and flow incidence angle all influenced the onset of transition on the blade suction surface. The convected wake generated time-averaged Nusselt distributions over the blade surface equal to high levels of freestream turbulence with no passing bars. Furthermore, the wakes continued to influence the heat transfer on the blade surface with the addition of film cooling, but at a reduced level. The observation of reduced influence of bar wake on rotor heat transfer compared favorably with Doorly's work. Johnson (1988) and Johnson et al. (1989) utilized the ACE profile as well to evaluate the heat transfer environment. The flow incidence angle was the same as the Ashworth study ($-10°$) and the bar simulated an engine representative vane exit Mach of 1.13, and a low speed value of 0.73 to isolate the effects of the wake and the shocks. The presence of wakes generated enhanced Nusselt distributions over the rotor surface, and the high speed tests, including shocks, further enhanced the heat transfer distribution. Rigby (1990) utilized similar techniques and test conditions to evaluate film cooling effectiveness. Film cooling on the suction surface initially offsets the heat transfer enhancement from the wake, but degrades rapidly under passing wake conditions due to mixing of the freestream and coolant fluid.

Almost all other studies of unsteady wake effects have been conducted at much lower Mach and Reynolds numbers. Morehouse and Simoneau (1986) demonstrated the wakes did increase the turbulence over the clean flow run. Furthermore, increasing the freestream turbulence resulted in a uniform increase in both the clean flow and wake experiments. The authors also asserted that the wake ought to be classified separately from the freestream turbulence for the purpose of heat transfer analysis. There was an asymmetry in the heat transfer augmentation on the heated cylinder leading edge, which increased with both Strouhal number and wake size. Dullenkopf and Mayle (1994) evaluated the effect of free-stream turbulence and moving wakes on accelerating laminar boundary-layer's heat transfer. They noted that the turbulence in the turbine blade wake can be considered as a super-imposed increase in the freestream turbulence at the blade passing period. Averaging the influence of this wake to represent a steady increase in the overall freestream turbulence is inaccurate, as it does not properly account for the periodic boundary-layer transition that will occur in an unsteady turbine stage. The authors accounted for this intermittency effect in the blade nusselt number by including a weighted sum of the steady turbulent and laminar Nu for the blade surface. They noted that careful consideration of these unsteady conditions is important, as the transition can augment Nu distributions by up to 60%. They then proposed a new quasi-steady model for the effect of the passing wake on a laminar boundary-layer. The model was shown to match closely with experimental data.

Although much of the research focused on the aerodynamic impact of the incoming wakes, some studies on heat transfer in the LP blade rows have been conducted (Zhang and Han, 1995). Measurements in incompressible flow (7 to 21 m/s) of the mean turbulent intensity and the HTC indicated that for higher levels of freestream turbulence, the influence on the HTC due to negative jet effect was significantly smaller. Specifically, varying the freestream turbulent intensity while maintaining the bar frequency produced a range of HTC values that differed by as much as 15%, whereas variation of the bar frequency for a given turbulent intensity produced variation on the order of 0.3%. The submergence of the wake effect as freestream turbulence was increased has also been demonstrated elsewhere (Schobeiri et al., 2008), and this trend agrees with the results shown in the Oxford University work at engine representative conditions. Passing wakes with Strouhal number variation between 0.1 and 0.3 to a film-cooled LPT blade (Mehendale et al., 1994) demonstrated that the blowing ratio was the dominant factor controlling the HTC, but the effect was lessened with higher bar-passing frequency. Film cooling overall did reduce the heat transfer effect induced by the passing wake.

2.4.2 Numerical Studies

In general, the numerical studies of wake propagation are presented for aerodynamic considerations in LPT stages rather than heat transfer. The focus is on predicting transition of the boundary-layer. Although the ability of turbulence models to accomplish this task shows varying effectiveness, the heat transfer predictions in the fully turbulent and fully laminar portions of the blade have been shown to be fairly good (Wu and Durbin, 2000).

2.5 Effects of Unsteady Shock Waves on Blade Heat Transfer

Rotor blade heat transfer is further affected by the presence of passing NGV trailing edge shock structures. These shocks result from increasing Mach numbers at the nozzle vane exit plane, and are shown to reflect off of both the rotor and the latter nozzle vane surface (De la Loma et al., 2008). Doorly (1983) showed that the passing shock from a simulated upstream nozzle vane trailing edge can produce a separation bubble on the surface of a turbine blade, with low heat transfer rates inside the bubble, and a locally high rate of heat transfer where the bubble reattaches to the blade surface. This phenomenon has also been observed in other studies as well (Johnson, 1988; De la Loma et al., 2008). There is strong evidence of both mean (Johnson, 1988) and unsteady (Rigby, 1990) augmentation of the heat flux for a rotor surface subjected to these shocks.

2.5.1 Experimental Studies

Johnson (1988) and Johnson et al. (1989) showed the evolution of the shock reflections from the simulated vane trailing edge shock. The setup in this study utilized a bar passing at a supersonic relative Mach number, and as a result there was a pair of shocks passing upstream of the rotor cascade. The bow shock leading the bar and the trailing recompression shock were both fairly strong, therefore the applicability of the shock structure to engine conditions is limited. More recent numerical simulations, discussed further below, show that a downstream reflection of the pressure-surface nozzle vane trailing edge shock is possible, which would present a pair of shocks impacting the rotors (De la Loma et al., 2008). However, this shock is much weaker than the suction-surface trailing edge shock for the nozzle vane. Regardless of the accuracy of shock system geometry, the presence of the shocks in the Oxford studies was shown to cause unsteady fluctuations in the surface Nu up to 700%, and even cause negative heat transfer at the flow conditions used in the experiment Johnson et al. (1989). The Oxford studies (Johnson, 1988) also showed that the time mean increase of Nu on the rotor suction surface was significantly higher due to the passing shocks, although this has not been demonstrated elsewhere. Experiments utilizing the passing shock as an isolated unsteady phenomena (such as that shown in Figure 2.4) conclude that the mean effect on the blade heat transfer are actually limited, and rather the isentropic compression of the passing shock is what causes the increase in heat transfer (Popp, 1998).

2.5.2 Numerical Studies

Although the available body of experimental data for the Oxford University cascade tests is rich, the numerical data is quite limited due to constraints on available numerical codes at the time. The high speed conditions of the flow restricted the time-resolved evolution of the shock reflections in the rotor passages to low-frequency bar passing conditions, and the inviscid code employed on the coarse meshes in some of the studies only picked up first order effects at the bar passing frequency (Johnson,

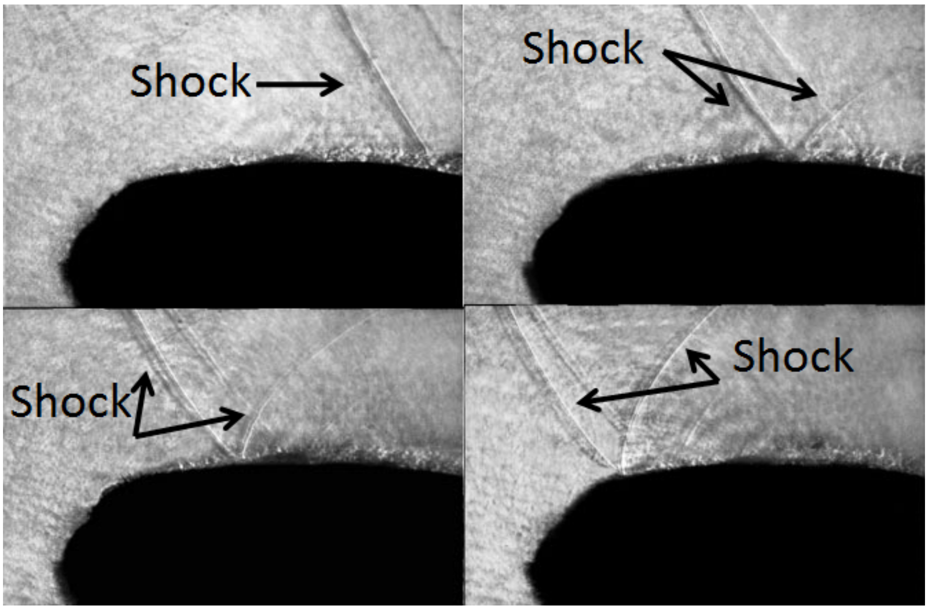

Figure 2.4: Simulated passing NGV trailing edge shock impacting rotor leading suction surface, courtesy Popp (1998)

1988). More recent numerical studies employing full turbine stage geometries have again focused on the influence of vane trailing edge shocks on turbine unsteadiness, and they show similar unsteady interaction behaviors to that of the Oxford rotating bar studies (De la Loma et al., 2008; Laumert et al., 2002). The propagation of these shocks in the blade passages is very similar to the Oxford studies, with the exception that the reflected NGV trailing edge shock is much weaker than the bow shock upstream of the rotating bar in the Oxford research.

2.6 Combustor Representative Flowfields

In recent years there is a clear trend towards higher fidelity simulations and experiments representing the non-uniform nature of the flow exiting the combustor. The focus of these studies is often on the radial gradients in the flow (Povey et al., 2007; Barringer et al., 2009a), including both the total temperature at the inlet and the total pressure. For example, the non-uniform radial distributions of the vane inlet total pressure have demonstrated significant effect on the secondary flow development in the vane (Barringer et al., 2009b,c), and in some cases the combination of temperature and total pressure distortions has shown a decrease in the temperature at the vane exit, as the cooler fluid is convected into the mid-span region due to the increased cross flow strength. However, circumferential variation can still be significant

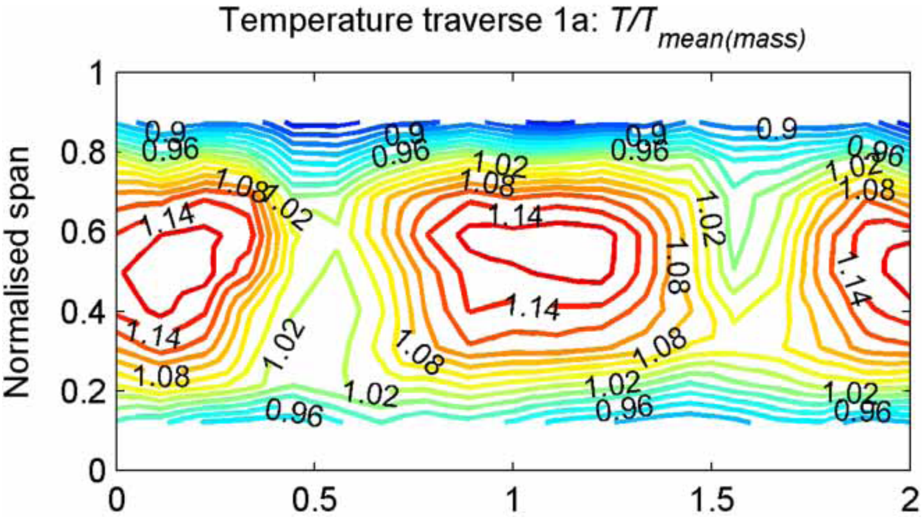

Figure 2.5: Non-uniform temperature profile at the inlet to a high pressure turbine vane blade row, courtesy Povey and Qureshi (2008)

depending on the combustor configuration. It is the effects of circumferential non-uniformity, specifically with respect to distributions of temperature and turbulence, that will be the focus of this section.

2.6.1 Temperature Distortions

Visual inspection of a cross-sectional slice downstream of the combustor reveals that, despite aggressive mixing of the flow following the flame regions, combustor geometries will lend themselves to non-uniform temperature distributions in the circumferential direction (Figure 2.5). The resulting hot and cold streaks will create significant variation in heat transfer across the nozzle vane surface as compared to a uniform inlet temperature. These hot streaks will affect the vane Nu via change in the driver temperature distribution on the blade surface, rather than a change in the HTC (Povey et al., 2007; Hurrion, 2002). This assertion would seem to be valid for the mid-span near the leading portion of the vane surface, but the presence of observed earlier onset in boundary-layer transition, and variation in the secondary flows challenges the assumption of a constant HTC on the blade surface (Barringer et al., 2009b; Hurrion, 2002). The greatest effect of the hot streaks was seen at the endwalls, which coincided with the greatest variation in temperature from the uniform values.

The increase in vane driver temperature is apparently mitigated somewhat by increasing levels of freestream turbulence and film cooling (Jenkins et al., 2004). It is thought that the mechanism that reduces the hot streak impact is enhanced by turbulent mixing in the flow, which dissipates the hot streak. The presence of both film cooling and the high levels of freestream turbulence served to substantially reduce the peak temperature in the hot streak (by about 75%). Clocking is not only important for the consideration of vane heat transfer, but the rotor blade row as well. Jenkins and Bogard (2005) reported that the hot streak clocking had significant effects on the attenuation of the hot streak as it passed through the rotor blade row. The experiment showed the qualitative behavior of the hot streak propagation appeared to be qualitatively independent of the freestream turbulence level. Overall the absolute magnitude of attenuation of the peak temperature was on the order of 2-3%. Jenkins and Bogard (2007) reported for a low subsonic vane with film cooling that attenuation of the hot streak as it passes to the rotor blade row could be achieved on the order of 55% when the hot streak was positioned on the blade with full coverage film cooling.

Numerous numerical studies on the effects of hot streaks at the turbine inlet have been conducted as well. Dorney and Sondak (2000) investigated the effect of tip clearance on hot streak migration in a high-subsonic single-stage turbine. They found the presence of tip clearance increases the distribution of the hot streak across the rotor surface, resulting in a higher mean rotor surface as compared to the rotor without tip clearance. Prasad and Hendricks (2000) utilized numerical methods to study the mechanisms that drive hot streak transport in turbine rotors. They found that the variation in flow density due to the hot streak, as well as the alteration of the rotor incidence angle, drives the variation in the rotor secondary flows.

He et al. (2004) studied the effects of hot streak counts on turbine blade heat load, in which hot streak counts of 8 and 32 were simulated. The authors contrasted the vane wake-induced “negative jet”, which convects high-entropy fluid from the rotor pressure surface to the suction surface, with the “positive jet” produced by the hot streak. The hot streak will create a preferential heating on the rotor pressure surface due to its additional tangential velocity relative to the surrounding flow. This process is demonstrated clearly in Figure 2.6, in which the 2D instantaneous contours of entropy are shown for the first stage of a transonic HPT. The hot streak is in red, clocked to the center of the vane passage, and the pooling of the hot fluid on the rotor pressure surface is evident. In effect the two jets then operate independently of each other and create cross-passage gradients in both directions. When they are in phase, the positive jet appears to be weakened by the presence of the wake, thereby lessening

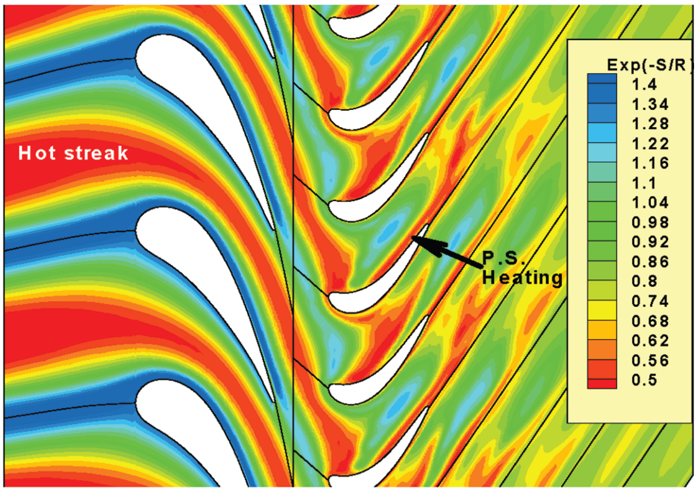

Figure 2.6: Instantaneous contours of entropy highlighting preferential heating effect on rotor pressure surface, courtesy He et al. (2007)

the effect of the positive jet on the rotor pressure surface. The circumferential length scale of the inlet hot streak also influenced the rotor blade heat load. More hot streaks increased the mean variation as compared to the uniform flow conditions, but had a smaller unsteady effect as compared to the fewer hot streaks. This is due to the longer residence time of the hot streak on the rotor blade surface for the lower hot streak count inlet condition. Hot streak influence on turbine blade heat transfer also extends beyond the first pair of blade rows to the downstream low pressure turbine. The increasing hot streak temperature ratio reduces the hot streak dissipation near the hub up to the middle span of the LPT rotor (Qingjun et al., 2008).

2.6.2 Combustor Exit Turbulence

While it is understood that the temperature distribution at the inlet to the NGV row is non-uniform, little or no attention is paid to the non-uniformity in the turbulence distribution upstream of the NGV. Turbulence is typically introduced as a range of uniform values, without any description of its distribution. The ambiguity is partially explained by the difficulty in obtaining turbulence measurements downstream of the combustor, simply due to the fact that the temperatures are so high near the combustor exit. The body of evidence regarding the presence of significant non-uniformity in the combustor exit flowfield is contradictory; experimental studies have demonstrated there is a range of results from “no difference” to “significant difference”. Moss and Oldfield (1991) utilized a can combustor geometry, and determined that the activation of a burner did not significantly affect the turbulence spectra, except

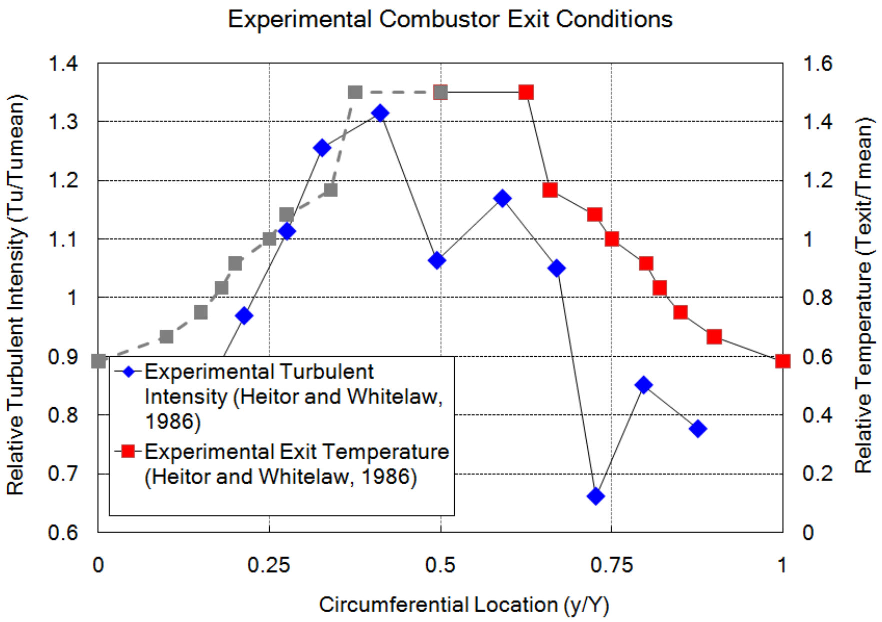

Figure 2.7: Combustor exit temperature and turbulence intensity normalized by circumferential mean, courtesy Heitor and Whitelaw (1986)

at low wavenumbers. Varying the combustion rate also did not affect the turbulence spectra. Heitor and Whitelaw (1986) evaluated the combustor exit conditions from a low-emissions tuboannular combustor with a swirl-stabilized flame. They measured the exit velocity and turbulence intensity 21mm downstream of the combustor exit, and found a circumferential variation in the turbulence intensity on the order of 60% about the mean (shown below in Figure 2.7). Temperatures at the exit plane also varied in the circumferential direction in a similar fashion to the turbulence variation.

In between these two extremes, a range of non-uniformity has been reported in the literature. Vakil and Thole (2005) measured aero-engine representative combustor exit flowfield conditions. They showed radial and circumferential variation in the turbulence field. Downstream of the last row of dilution holes the peak levels are near 16%, with the lowest levels near the hub endwall and away from the dilution holes. These measurements are some distance upstream of the turbine section, and therefore the extent of mixing these jets with the mainstream flow is not available. Turbine inlet turbulence intensity is represented as an averaged value of 20%. Sokolov et al. (1995) produced a numerical model of an annular gas turbine combustor. They showed experimentally that radial gradients of the turbulence field will exist and decrease as axial distance from the flame increases, without reporting the absolute levels of the variation at each axial station. Barringer et al. (2002) utilized a combustor representative geometry without flame. They found that the turbulence at the combustor exit varied in the circumferential direction at mid-span between 15 and 18% when the dilution jets were turned on. Therefore there exists the possibility that significant circumferential variation in the freestream turbulence is a combustor-representative condition for the turbine inlet.

2.7 Summary

In summary, this chapter reviewed the experimental and numerical methods currently available in the literature to solve the heat transfer problem. Numerical models developed are increasingly able to predict the trends and absolute levels of blade heat transfer, but significant variability in the effectiveness of the various numerical techniques exists. Careful attention to boundary-layer transition and the choice of turbulence model are a critical subset to the general requirement of appropriate model conditions that must be addressed in order to generate accurate predictions of turbine heat transfer.

There are many contributions in the complex flowfield of the turbine passages that affect turbine heat transfer. Freestream turbulence has been shown to both shift forward the onset of turbulent boundary-layer transition on the blade surface, and delay re-laminarization of the boundary-layer. It elevates turbulence in an already turbulent boundary-layer, and has been shown to create velocity fluctuations in a laminar boundary that are higher than expected. The effects on heat transfer vary with both the turbulence intensity and turbulence length scale in the freestream. The most dramatic changes in heat transfer levels occur when the freestream turbulence intensity increases up to 8%. However, additional augmentation is also evident in higher ranges of turbulence intensity as well. Unsteady flow structures, such as the turbine blade wakes and trailing edge shocks, produce both time-mean and unsteady augmentation of blade heat transfer. These effects are most prominent in a laminar boundary-layer. Unsteady wakes can enhance local heat flux by over 300%, and shock-induced augmentation of local heat transfer can reach 700%, as reported in the literature.

The trend towards increasing realism in both experimental and numerical representation of the combustor exit flowfield has evolved with increasingly sophisticated understanding of this region of the gas turbine. Temperature distortions exiting the combustor have been shown to redistribute the driver temperature on the nozzle blade surface, and affect rotor heat transfer by altering the dynamics of the flow entering the rotor passages. Finally, the existence of radial and circumferential gradients in the combustor exit turbulence field is certain, but the amplitude of the variations is debated. At the highest amplitudes of circumferential variation it seems likely that an effect on turbine blade HTC could occur. To the author's knowledge, no work has been conducted on the effect of these circumferential variations on turbine blade heat transfer, and it is this gap in the literature that this thesis will attempt to fill.

Chapter 3

Numerical Methods

3.1 Overview

This chapter will outline the methodology for the numerical studies in this thesis. In Section 3.2, the governing equations and the methods of their discretization in time and space are explored, as well as the turbulence models used in this study to close them. Grid generation strategies are discussed in this section as well, along with boundary conditions and mitigation of numerical error. In Section 3.3 a generalized conception of flow initialization for the domains is outlined, and the process of monitoring solutions to convergence is discussed. Section 3.4 summarizes the key points from the chapter.

3.2 Numerical Tools

In this section the numerical solver and selected methods of discretization will be described, and the strategy for computational mesh generation and boundary conditions will be discussed. The section concludes with techniques used to mitigate numerical error in this work.

3.2.1 Governing Equations and the FLUENT Solver

The governing equations for a viscous, compressible fluid are the three conservative laws of continuity, momentum, and energy. They are given in integral vector notation as:

$$\int_V \frac{\partial \rho}{\partial t}\, dV + \oint \rho\, \vec{v} \cdot d\vec{A} = 0 \tag{3.1}$$

$$\int_V \frac{\partial \rho \vec{v}}{\partial t}\, dV + \oint \nabla(\rho \vec{v}\vec{v} + P - \bar{\bar{\tau}}) \cdot d\vec{A} - \int_V \rho \vec{f}\, dV = 0 \tag{3.2}$$

$$\int_V \frac{\partial \rho E}{\partial t}\, dV + \oint \nabla[\vec{v}(\rho E + p - \bar{\bar{\tau}}) - \vec{q}] \cdot d\vec{A} = 0 \tag{3.3}$$

Whereas this formulation of the conservation of momentum in Equation 3.2 (after further decomposition along the three Cartesian axes) is referred to specifically as the Navier-Stokes equations, this nomenclature is also commonly applied to the entire system of the equations above. The system is actually incomplete, retaining multiple unknown variables—pressure, density, energy and the three components of the fluid velocity—for five equations. Stokes' assumption further links the stresses in the above equations to the velocity gradients, and assuming a calorically perfect, ideal gas extends the system to seven equations with seven unknowns:

$$e = C_v T \tag{3.4}$$

$$P = \rho R T \tag{3.5}$$

The commercial CFD package utilized in this thesis, ANSYS' FLUENT, employs a cell-centered finite-volume method to solve the governing equations on a computational domain that has been discretized into constituent control volumes. In the finite-volume method the transport of a given variable ϕ through a control volume V is described by the following equation:

$$\int_V \frac{\partial \rho\phi}{\partial t}\, dV + \oint \rho\phi\, \vec{v} \cdot d\vec{A} = \oint \Gamma_\phi\, \nabla\phi \cdot d\vec{A} + \int_V S_\phi\, dV \tag{3.6}$$

where the terms on the left hand side of the equation are the time rate of change of ϕ in the control volume and the convective flux through the volume, respectively. The terms on the right hand side describe the diffusion of ϕ and contributions from any volumetric source terms. Integrating the scalar transport equation over the control volume V (shown in Figure 3.1) results in vectors of ϕ that are then linearized. Additional discretization of the flux gradients and the time step are also required. In this thesis the method of Roe (ANSYS, 2006) is utilized for the inviscid fluxes, and second-order upwind schemes are employed for the remaining scalar quantities, such as turbulence. In order to supply the gradients for these second-order upwind schemes, the Green-Gauss Cell-Based Gradient scheme is employed. The implicit method of temporal discretization is used on the domains in both steady and unsteady flow. In the unsteady flow, a second-order scheme is employed for higher accuracy.

Once the solution has been initialized, the numerical code contains two primary formulations of the full solver for the Navier-Stokes equations. The two methods, pressure-based and density-based solvers, were originally intended for distinct flow

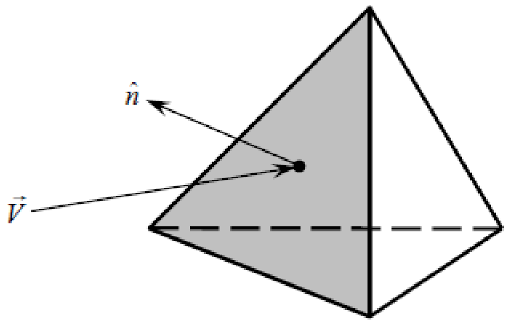

Figure 3.1: Arbitrary tetrahedral control volume, courtesy Cummings et al. (2004)

regimes (ANSYS, 2006). The density-based solver was derived for compressible flow, and the pressure-based solver was intended for low Mach numbers flow. Initially, the near-homogenous density fields of incompressible flow rendered the use of the density as the independent flow variable unfeasible. The documentation for the solver asserts that both of these solver formulations have since been expanded to accommodate wider ranges of flow conditions (ANSYS, 2006). In this thesis, the density-based solver and the coupled formulation of the pressure-based solver will first be compared to evaluate their relative performance in the transonic flow regime encountered frequently in the high pressure turbine stages of a jet engine.

3.2.2 Turbulence Modeling

The flows in high pressure turbines are inherently turbulent. The turbulence arises from several sources, including combustor-induced swirl and cooling flows, wakes and endwall flows, and finally the natural boundary-layer transition on the blades themselves. Accurate modeling of this phenomenon is therefore an important task for any numerical code. A turbulence field contains a wide spectrum of length scales for the fluctuating eddies within it. Resolving the entire spectrum for even the simplest flows is prohibitively expensive at Reynolds numbers typically seen in the high pressure turbine stage (Schiestel, 2008). Therefore simplifying assumptions regarding the nature of turbulence are necessary to utilize it in engineering applications. Considering the turbulence field from a statistical approach is well-established and necessary considering the lack of a complete understanding of all the boundary conditions for the turbulent flow problem (Pope, 2000; Monin and Yaglom, 1971). In a compressible flowfield, the statistical approach leads to a density-weighted, ensemble-averaged mean value for the flow and an additional fluctuating term, known as the Favre decomposition (Schiestel, 2008). Incorporating these elements into the Navier-Stokes equations results in the Favre-Reynolds Averaged Navier-Stokes equations. As a result of this process, additional terms are introduced into the momentum equation, called the Reynolds stress tensor. The presence of this term represents the closure problem for the ensemble-averaged Navier-Stokes equations, as the system is once again open.

In order to close the equations, a variety of methods have been developed. One of the most prevalent invokes the Boussinesq hypothesis, which asserts the fluctuating turbulent stresses are aligned with the local mean rate of strain tensor. The result is that the turbulent fluctuations can be modeled as a local effective or eddy viscosity. Furthermore, the Reynolds analogy relates the momentum transfer in the turbulent flow to heat transfer, thereby offering an avenue of closure for the open terms in the energy equation. Transport of this eddy viscosity is then accomplished either directly via a single-equation model such as the Spalart-Allmaras model (ANSYS, 2006), or computed from a combination of additional transported scalars such as the turbulent kinetic energy k and turbulent dissipation rate ϵ. These two-equation models arguably offer a higher level of relative generality than more simply eddy viscosity models (Schiestel, 2008). Understanding the implicit assumptions and their limitations is an important element when employing eddy viscosity models, in both the steady (RANS) and unsteady (URANS) cases. In the strictest interpretation of the hypothesis, the one-point models will hold for where the turbulence dynamics exhibit strong temporal and spatial locality (Hunt and Savill, 2005). Furthermore, the Boussinesq hypothesis assumes isotropy in the turbulence. The most recent models have been modified to accommodate time-history effects in the turbulence to some extent, for example the $k-\omega$ SST model incorporates a switch that activates transport of the principal Reynolds stresses in a boundary-layer (Menter, 1994). In unsteady periodic flows, which are found in several chapters in this thesis, the time scale of the turbulence in the domain also must be considered. If for example the rotating bar upstream of the rotor profiles passed at a frequency coincident with the time-scale of the grid-generated turbulence in the original experiment, the ensemble-averaging inherent in the URANS model no longer is valid (Davidson, 2004). Despite the limitations on these turbulence models, they have demonstrated accuracy when properly calibrated for the flow conditions in the computational domain. A calibration study is performed in Chapter 6 to address this issue prior to evaluation of the non-uniform inlet turbulence fields.

3.2.3 Grid Generation

The computational grids utilized throughout the study employed the software package GAMBIT, excepting the three-dimensional nozzle vane geometry in Chapter 8. In all the cases for the turbine blade geometries, a series of prism layers was attached to the wall geometries in order to provide accurate resolution of the boundary-layer. The first cell height was optimized to control y^+ values on the blade surface. Sizing functions were also employed to control the computational cost, and a balance between efficient use of computational resources and achieving a grid-independent solution was taken into consideration throughout the grid design process. Due to the wide range of computational domains employed in the thesis, a single summary of the relevant grid statistics would be impractical in this chapter. However, the overall grid generation strategies generally followed similar algorithms, and a sample case involving the grid generation strategy for the two-dimensional vane employed in Chapter 6 illustrates the process (the resultant grid is shown below in Figure 3.2):

- Based on expectations of the flow-field, generate an initial coarse grid for the domain. Key structural features of the grid include prism layers attached to the vane wall boundary, and size functions attached to the vane walls in expected high gradients of the flow.
- Refine initial estimates based on FLUENT results for the wall y^+ if necessary, as well as increase grid density to obtain grid dependence for solution based on determined metrics. Ensure grid quality metrics for cell skewness are controlled, and adjust to keep maximum skewness values around 0.5.

Initial attempts at creating grids demonstrated that triangular elements produced a grid with higher performance in various metrics of grid quality. Therefore these element types were employed in the freestream flow for all the domains. The combination of element topology (quadrilateral and triangular grid elements) throughout many of the domains also required careful attention at the interface between the prism layers assigned to the blade walls and the triangular elements to prevent rapid change in cell volume and skewness.

Additional case specific considerations also factored into the final grid design. For example, whereas the experimental validation simulations for the 2D nozzle blade

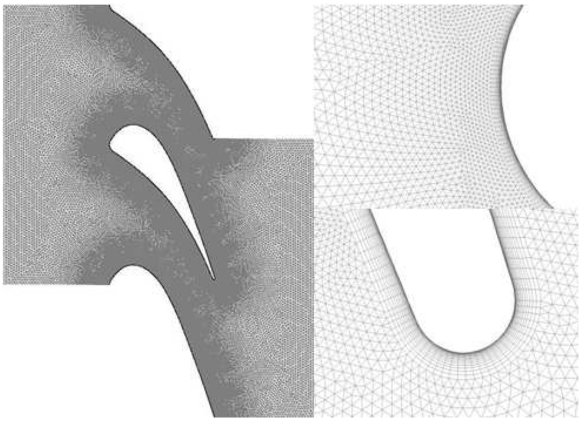

Figure 3.2: Grid for 2D nozzle vane highlighting prism layers and size functions, including magnifications of high curvature regions

demonstrated grid independence for a relatively low density grid, a final higher density grid was utilized for the simulations involving non-uniform inlet boundary condition profiles. The aim in this case was to both properly resolve the ideal profile interpolated into the domain, and to reduce the effects of numerical diffusion on the circumferential variation in turbulence upstream of the NGV.

As mentioned previously, the grid for the 3D NGV was generated using the ANSYS Meshing Program. The strategy employed similar prism layer and size function strategies to the two-dimensional grids in the rest of the thesis. The conflicting constraints of available computational memory for the grid generation software and ensuring a high enough grid density for the vane trailing edge and wall y^+ rendered the process of producing meshes with low skewness difficult. In order to accomplish the objective of generating a sufficiently high density grid, the initial tetrahedral freestream cells and hexahedral prism layers were converted to general polyhedral cells within the FLUENT solver package. FLUENT accomplishes this by generating new cell faces by connecting the original cell-centroids and face-centroids, then constructing new polyhedral cells from these new faces. The hexahedral boundary layer cells are left un-adjusted, except for the interface layer with the tetrahedral cells (ANSYS, 2006). The result is a high-quality grid from a skewness standpoint that retains a fine boundary-layer resolution near the blade wall. An example of the final grid is shown in Figure 3.3.

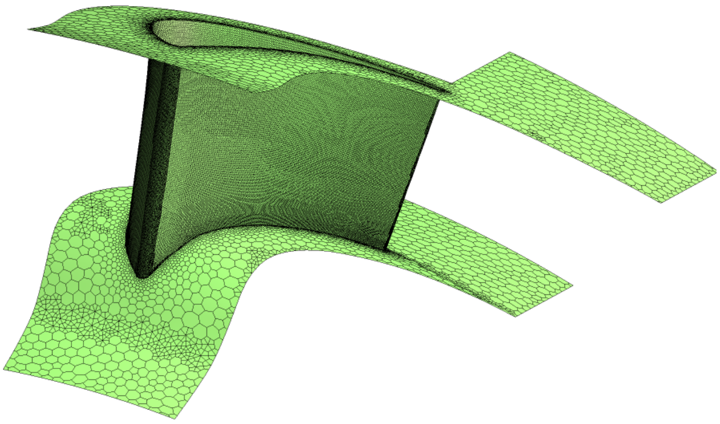

Figure 3.3: Converted polyhedral computational grid for the 3D nozzle blade geometry

3.2.4 Boundary Conditions

The aim for each of the validation studies was to establish the Mach and Reynolds numbers at experimental conditions, then where possible match dimensional flow parameters such as the total temperature or static pressure at the domain boundaries. In the unsteady flow simulations, a translational sliding grid was used to represent the passing bars or rotor blade rows (ANSYS, 2006). In this method, the computational grid is split into two or more cell zones with each cell zone wrapped to either the stationary or moving geometries. As a result, there is the need to properly interface between the two cell zones. Figure 3.4 shows an example of these zones detached to highlight the sharing of nodes along the common boundary.

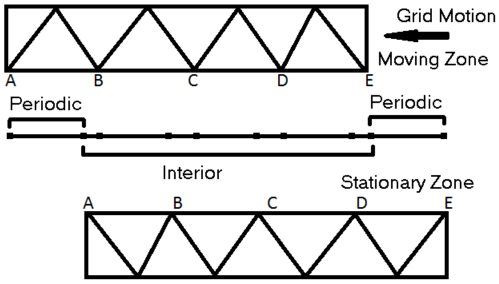

Figure 3.4: Example cell zones highlighting sliding grid method

The center nodes shared with both zones will exchange information as if no motion were occurring. The exception of course is that over the period of the sliding grid sometimes information will pass from more than one cell on one side of the interface into a single cell on the other side. The exposed faces are paired and treated as a periodic zone.

The remainder of the supplied boundary conditions can be described thusly:

- Enforce a pressure inlet and pressure outlet boundary types at the entrance and exit to the computational domain. Specify total pressure and temperature at the domain inlet, and static pressure at the domain exit. Specify inlet flow vectors and non-uniform inlet conditions when applicable.
- Enforce no-slip boundary conditions for the blade walls, and isothermal conditions for the calculation of heat transfer. In unsteady flows, set the wall motion to zero relative to the surrounding grid cells.
- In unsteady simulations of blade row/spinning bar interactions utilize velocity triangle to set tangential velocity for the sliding mesh zone containing the rotor blade row/bar. Set grid-interfaces between static and sliding mesh zones to be periodic repeats.
- Enforce periodic boundary conditions in the circumferential direction, the repeating boundaries were translational for all domains except the 3D nozzle blade. Rotational periodicity was enforced for this domain.

Individual variation occurred depending on individual study requirements. A complete summary of the boundary conditions and domain geometries can be referenced in Appendix A.

3.2.5 Numerical Error and Compensation Strategies

Numerical error can arise from several sources, including rounding error in the solver. In this case it is reduced by the employment of the double-precision formulation of the FLUENT solver. Truncation error in the solution arises in regions where the grid density is too low to resolve gradients in the flow, or the transition in the cell volume between adjacent grid elements is too large, and can manifest itself as numerical diffusion in the flow. Careful mesh design and obtaining grid-independent results of selected flow variables minimizes this problem. Finally, physical modelling errors are limited in this thesis via the use of high-order polynomials for specific heat capacity a constant pressure C_p and Sutherland's Law for the laminar viscosity of the air (ANSYS, 2006). Boundary conditions are carefully selected to match experimental results, and an extensive validation study of the available turbulence models is conducted in the next chapters to minimize the error introduced by turbulence modelling.

3.3 Solutions Initialization and Convergence

In the steady flow solutions for this thesis, full-multigrid initialization of the computational domain is utilized to accelerate convergence. In this technique, the full-approximation storage multigrid method constructs layers of coarse meshes based on the mesh supplied to the solver and solves the reduced governing equations for inviscid steady flow, known also as the Euler equations (ANSYS, 2006). In this thesis, five levels of coarse meshes of increasing refinement are employed, with an explicit first-order formulation of the solver providing an initial solution for the flow. For each level, the solution is swept from the current mesh down to the coarsest mesh. The solution is then interpolated into the finer mesh, and the process repeated until convergence is reached or the maximum number of cycles achieved. Utilizing this method reduced the number of iterations for a converged solution considerably. In fact, in the 3D computational domain, a converged solution with this technique could be achieved within a few hundred iterations. It is important to note that turbulence transport is obviously not accounted for with the inviscid solution calculated in this first stage. Therefore in order to minimize problems associated with turbulent solutions, careful selection of the turbulence quantities at the inlet is made for the transition to the full governing equations.

Convergence of the flow in the steady flow solutions is monitored through two metrics. The first is tracking the flow residuals for the continuity equation, the velocities, and the turbulent transport to ensure that they fall to approximately $1 \cdot 10^{-3}$ for the first two categories of residuals, and $1 \cdot 10^{-6}$ for the turbulence transport variables. In order to further confirm that the solution has achieved convergence, additional monitoring of a scalar in the flowfield at a critical point–for example the turbulent kinetic energy downstream of the turbine blade or the surface averaged heat flux to the blade surface. Figure 3.5 demonstrates the steady-flow convergence history for the 3D nozzle blade surface-averaged heat flux after approximately 400 iterations.

In the unsteady flow solutions, a dual-time-stepping procedure was employed, which required additional sub-iterations for each physical time step. The number of sub-iterations employed depended slightly on the solution. The aim was to have the flow residuals fall by approximately three orders of magnitude for each time step, and this typically occurred for 20 to 30 sub-iterations. Solution convergence was achieved when steady-state periodicity in the flow was observed in a selected monitoring point in the flow domain. A sample converged flow monitor is provided for the unsteady rotating bar simulation on the civil aircraft rotor profile in Chapter 5 in Figure 3.6.

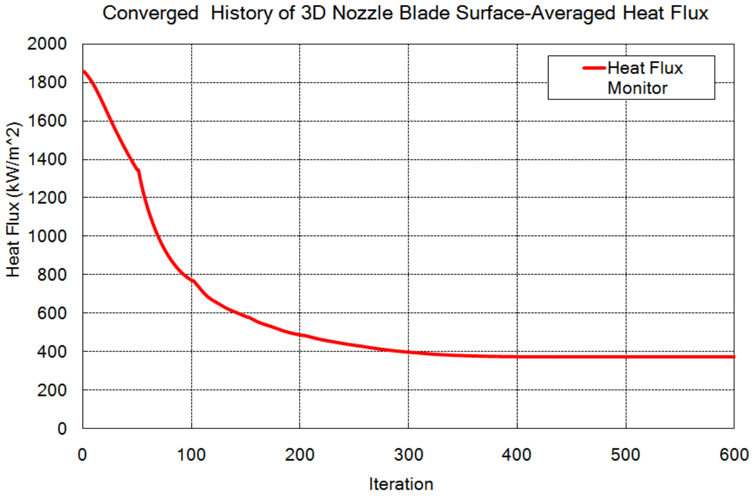

Figure 3.5: Convergence history for 3D nozzle blade surface-averaged heat flux

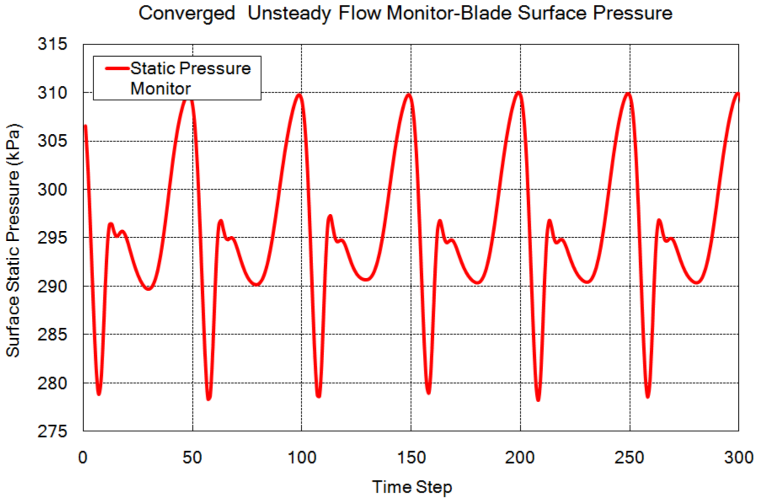

Figure 3.6: Converged unsteady flow monitor showing surface pressure on the suction surface of a civil aircraft rotor profile

3.4 Summary

The general methods for the study have been outlined. The commercial CFD package in this thesis is presented as a cell-centered-finite volume method, and the specific additional adjustments to the solver are presented. General grid generation strategies aim to increase grid density in regions of high flow gradients when possible, and to control y^+ near the blade walls to increase the accuracy of the eddy viscosity models employed in the thesis. A mixed topology of triangular and quadrilateral cells is the standard for the work, although constraints required the use of a polyhedral grid for the final three-dimensional geometry. Boundary conditions enforced on the resulting computational domains aim to represent non-dimensional conditions first, then match the dimensional flow variables when possible. Known sources of error in this methodology and mitigation strategies have also been presented. Finally, the general strategy for solution initialization and convergence were discussed. In the next few chapters, the results for the cases using the methods laid out in this chapter will be presented. A summary of these cases and the goal for each is presented in Table 3.1 for reference.

Table 3.1: Summary of Computational Domains Evaluated

Study	Goal
NACA 0012 airfoil in transonic flow	Compare FLUENT density and pressure-based solver performance
Military aircraft HPT rotor profile	Compare solver and turbulence model performance, Validate steady flow
Civil aircraft HPT rotor profile	Compare solver and turbulence model performance, Validate steady flow
Military aircraft HPT rotor profile	Compare solver and turbulence model performance, Validate unsteady flow
Civil aircraft HPT rotor profile	Compare turbulence model performance, Validate unsteady flow
HPT nozzle vane	Validate turbulence propagation through 2D vane passage
Oxford Rotor Facility nozzle vane	Effect of non-uniform turbulence on 2D nozzle vane
Oxford Rotor Facility first stage (2D)	Effect of non-uniform turbulence on 2D HPT stage geometry
Oxford Rotor Facility nozzle vane (3D)	Effect of non-uniform turbulence on 3D nozzle vane

Chapter 4

Steady Flow Validation

4.1 Overview

The aim of this chapter is to present a series of validation studies in steady flow conditions for the numerical solver. In order to develop a systematic approach, a parametric study of numerical solver formulation and turbulence models was conducted on four computational geometries, including the NACA 0012 airfoil and two HPT rotor profiles.

The first part of this chapter assesses ANSYS' assertion that the originally distinct capabilities of the two solver formulations packaged in FLUENT have since been broadly expanded to include a wider range of flow conditions. Two categories of test metrics are considered, including computational efficiency and accuracy of aerothermal predictions. The rate of convergence for the steady flow solutions is used as the metric for computational efficiency in each of the solutions. In the case of the NACA 0012 airfoil, the predictions are compared to experimental pressure coefficient distributions on the airfoil's upper surface. Additionally, the surface isentropic Mach number and Nusselt number distributions for an HPT rotor are compared between solver formulations and against experimental data.

Following this study of the solver formulation performance, an assessment of turbulence model performance is conducted on two rotor profiles. Steady flow validation studies compare blade surface pressure and heat transfer predictions to experimental results, and evaluate the ability of the turbulence models to predict aerothermal response to varying levels of freestream turbulence.

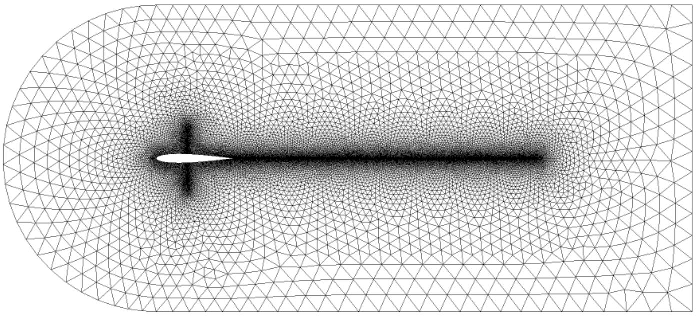

Figure 4.1: NACA 0012 final grid and geometry

4.2 Analysis of FLUENT Solver Formulations in Transonic Flow

As discussed previously in Chapter 3, FLUENT offers two distinct methods for solving the flowfield. The density-based solver was originally intended for high-speed compressible aerodynamic regimes, but has since been expanded to allow for solutions in low Mach number flows. Conversely, the pressure-based solver was originally designed for these incompressible flow conditions (ANSYS, 2006). In order to provide a first test of the pressure-based solver in transonic flow, experimental surface pressure coefficient data for a NACA 0012 airfoil will be compared to numerical predictions in FLUENT.

The NACA 0012 airfoil is an analytically derived geometry from the NACA 4-digit series of airfoils, and is described by the following equation:

$$y = \pm 0.6(0.2969\sqrt{x} - 0.126x - .3516x^2 + 0.2843x^3 - 0.1015x^4) \tag{4.1}$$

The airfoil axial chord was set to match the experimental Reynolds number of $4.09 \cdot 10^6$ (Thibert et al., 1979), and the above equation was uniformly discretized at 100 axial chord stations. A final axial coordinate was added on the abscissa a short distance downstream of the trailing edge to establish a closed curve for the airfoil. The domain extends two axial chord lengths radially in every direction from the leading edge of the airfoil, and six chord lengths downstream of the trailing edge. A sample of the computational domain is shown in Figure 4.1. In this particular simulation a pressure far-field boundary condition was enforced around the computational domain. This boundary accepts a freestream Mach number and static conditions (ANSYS, 2006), and these values were calculated from the reported experimental Reynolds number,

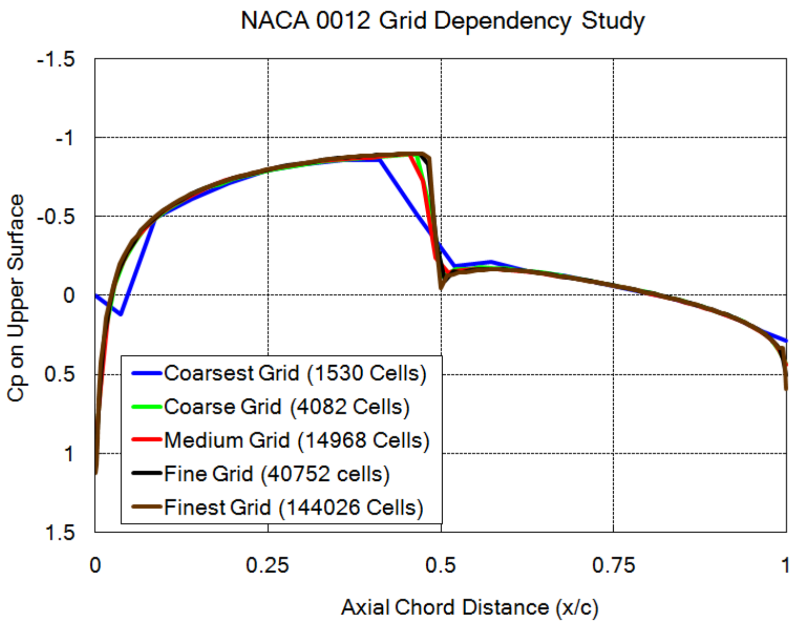

Figure 4.2: NACA 0012 grid dependency study of pressure coefficient (C_p)

Mach number and total conditions (Thibert et al., 1979). In the experiment, the freestream Mach number was approximately 0.8, and the pressure coefficient distribution on the upper surface clearly shows a standing normal shock wave on the airfoil surface ahead of mid-chord.

A grid dependency study was first conducted using the density-based solver. Figure 4.2 compares five grid densities' predictions of pressure coefficient on the NACA 0012 upper surface. Apart from the coarsest grid, there appears to be little sensitivity in the prediction aside from the location of the shock. The prediction of the shock location slides slightly further downstream for the higher grid densities, and reduced smearing of the shock is shown in the increasing grid density. The "fine" grid configuration was selected for the solver sensitivity study, as it demonstrated sharp resolution of the standing shock, and additional refinement produced no obvious variation in the upper surface pressure coefficient distribution. The sensitivity of the solution to variation in the solver was evaluated next. In addition to the density-based solver, solutions were calculated using both the coupled and segregated versions of the pressure-based solver. Second-order discretization schemes were used in all solvers, and the pressure interpolation scheme was set to PRESTO!. This method is recommended in particular for domains with strong curvature (ANSYS, 2006) and, as the aim was to compare the solvers in turbine geometries, this method was consistently used in each set of simulations. All other solver settings were left in their default configurations.

The first metric of comparison amongst the different solver configurations was computational efficiency. All tests were conducted on a computer equipped with a 2 GHz, dual-core Intel Core 2 Duo processor and 4 gigabytes of RAM for consistency. Figure 4.3 displays a convergence monitor of the integral of the pressure coefficient on the upper surface of the airfoil. All three solver formulations converge to near steady-state conditions within approximately 315 iterations (the pressure-based segregated solver), and the pressure-based coupled solver achieves this state the fastest by closing to within 1% of the final C_p value in about 12 iterations. The density-based solver is in between these two, taking about 189 iterations to settle to within 1% of the final value. The density-based solver closes to the $1 \cdot 10^{-3}$ accuracy limit of the C_p monitor occurs sooner (300 iterations) than the pressure-based solvers ($\sim$ 500 iterations). The efficiency of the solvers differ though: the pressure-based segregated solver clocks fastest at 0.3 seconds per iteration, followed by the pressure-based coupled solver at 0.7 seconds per iteration, and finally the density-based solver at 0.9 seconds per iteration. Therefore, the density-based solver took much longer than the other two solvers to settle within 1% of the final solution. In addition to convergence history, the accuracy of the converged solutions was evaluated. Figure 4.4 compares the pressure coefficient predictions with experimental data. Although all three solutions over-predict the axial chord distance for the shock position on the blade surface, they otherwise provide excellent predictions of the airfoil surface pressure. Interestingly, the pressure-based solvers outperform the density-based solver in predicting the location of the shock. There is little variation in the predictions of the two forms of the pressure-based solver. This similarity in performance for the two pressure-based solvers is also witnessed in the convergence history of the two pressure-based solver formulations nearer the steady-state portion of the monitor trace.

The study of solver sensitivity was then expanded to the HPT rotor profile for the Advanced Core Engine (ACE). The rotor exit Mach number in the experimental data used as the baseline for these numerical simulations was 1.2, resulting in a strong trailing edge shock that reflects downstream off the adjacent rotor blade suction surface. In the numerical predictions shown here, the discretization and pressure interpolation schemes were employed in a manner consistent with the NACA simulation. Each solution also incorporated the $k-\omega$ SST turbulence model. Convergence

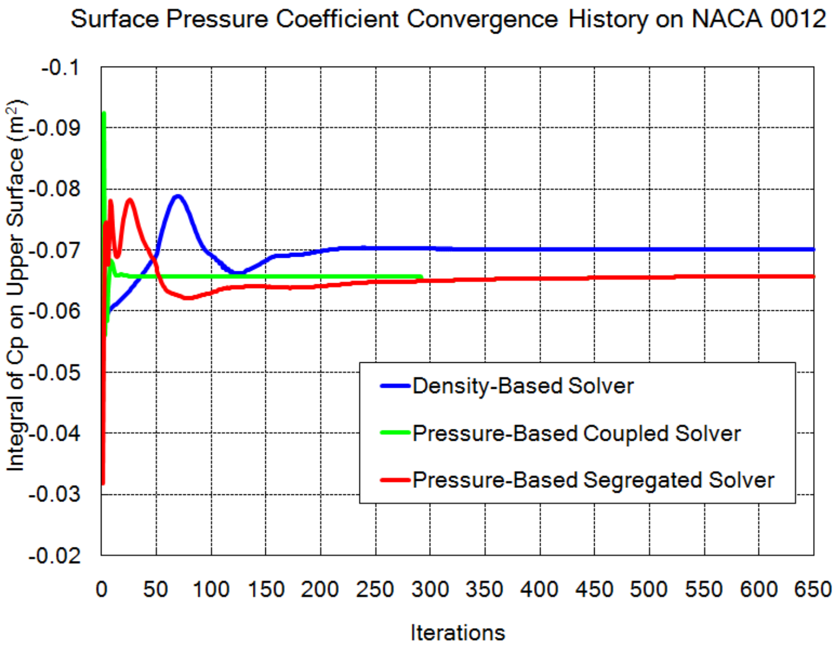

Figure 4.3: NACA 0012 convergence history of the integral of pressure coefficient on upper surface

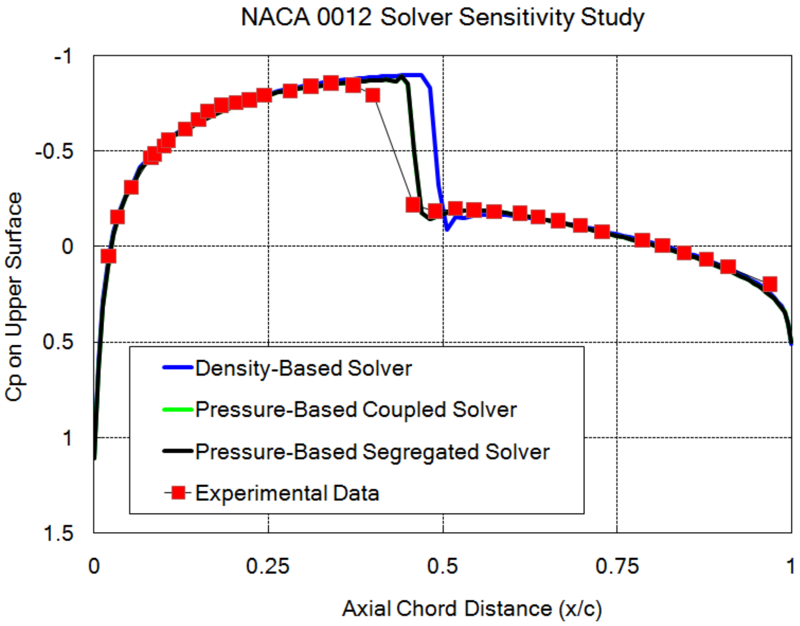

Figure 4.4: NACA 0012 solver sensitivity study comparing predictions to experimental data from Thibert et al. (1979)

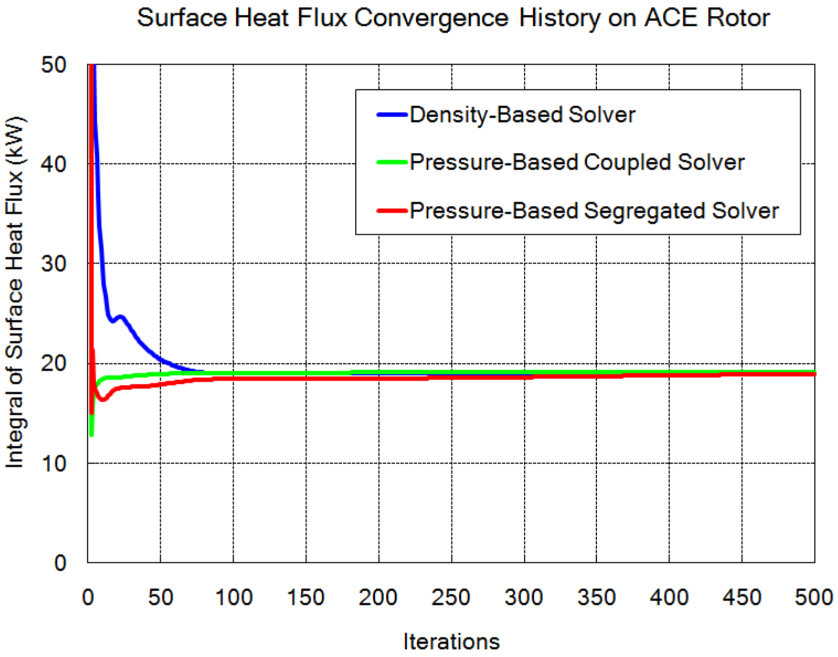

Figure 4.5: ACE convergence history of the integral of blade surface heat flux

history for the steady flow simulation of the rotor is presented in Figure 4.5. The qualitative trends witnessed in the convergence behavior for the NACA simulation hold in this case as well, with the pressure-based coupled solver showing the fastest convergence for a flow monitor using the surface integral of blade heat flux. Similarly, the density-based solver achieves steady-state convergence at the limit of the monitor accuracy before the two pressure-based solver formulations.

Sensitivity of the final solution to solver selection for the ACE rotor was minimal. All three solver formulations captured the salient shock structures in the rotor blade passage with little variation. The similarity of the blade surface isentropic Mach number distributions in Figure 4.6 highlights this behavior. The region of strongest interest is near the latter portion of the ACE suction surface, which is where the adjacent rotor trailing edge shock impacts. All three solvers predict the shock to impinge just downstream of 0.75 C_{ax} on the suction surface. The surface Nu distributions tell a similar story (Figure 4.7) to that of the surface isentropic Mach number. Figure 4.7 presents Nu based on freestream total conditions from the experimental definition in Johnson (1988). Again there appears to be little variation in the distribution of the data over the rotor surface between the three solver formulations.

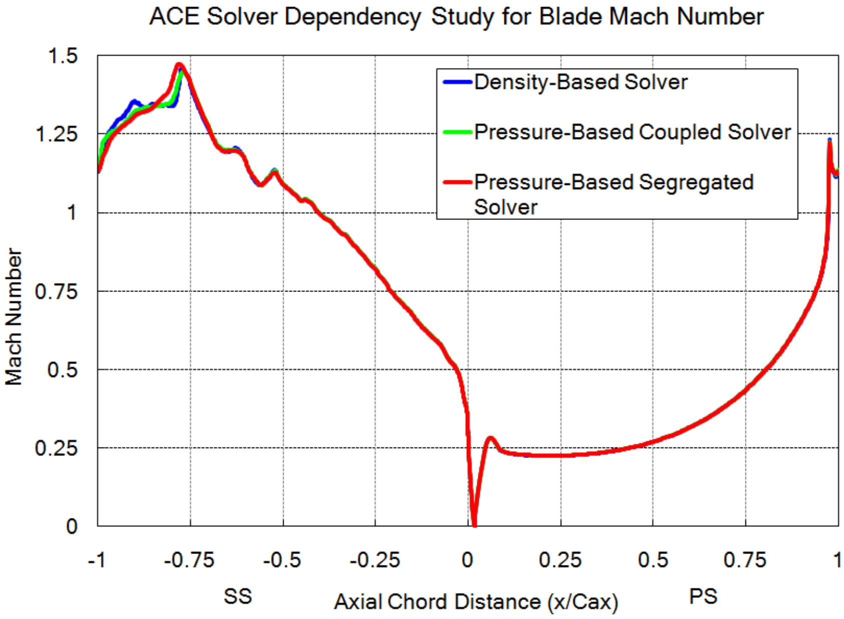

Figure 4.6: Sensitivity of ACE surface pressure to change in solver formulation

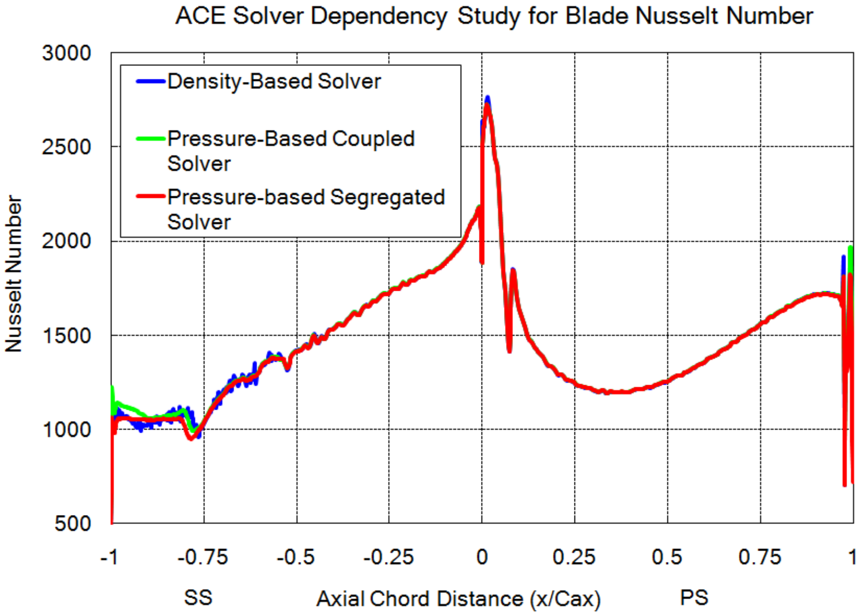

Figure 4.7: Sensitivity of ACE surface Nu to change in solver formulation

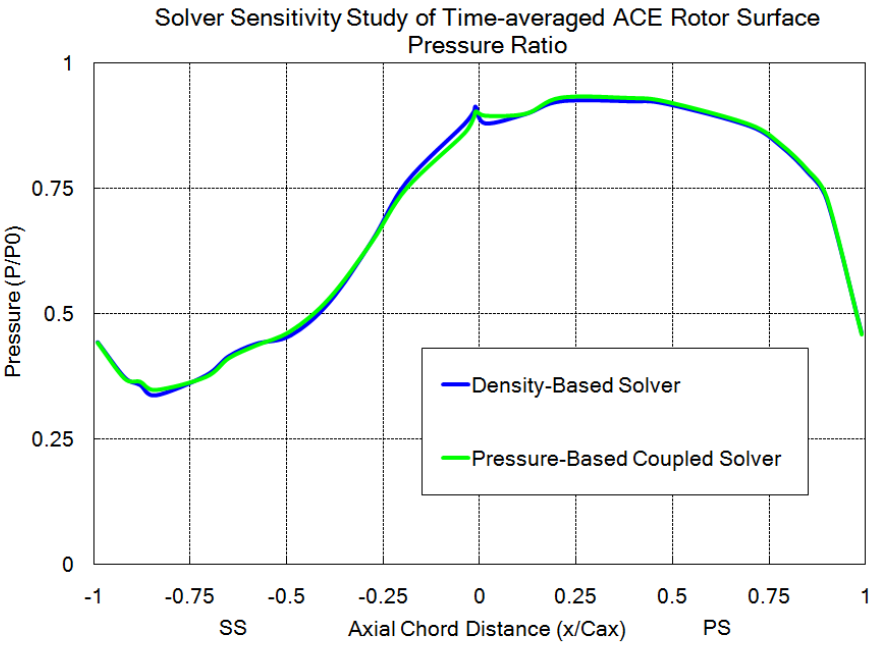

Figure 4.8: Sensitivity of time-averaged ACE surface pressure to change in solver formulation

Finally, the sensitivity of the solver performance was compared to an unsteady flow simulation of a 2D sliding bar wake generator upstream of the ACE rotor. The bar simulates the trailing edge of a transonic HPT nozzle guide vane. The aim was to provide a rigorous benchmark case for the pressure-based solver, as the case involved multiple shock waves propagating through the computational domain. The two pressure-based solvers immediately diverged at solution startup without significant control of both the under-relaxation factors. Ultimately, only the density-based solver and coupled formulation of pressure-based solver achieved convergence, but the significant native control of the startup phase of the solution makes a quantitative comparison of the convergence rate with the density-based solver infeasible. It is sufficient to say that whereas the density-based solver reached a steady-state time-periodic condition within 20 bar passing periods, the pressure-based solver took much longer. Once a converged solution was reached, the two solver formulations showed little variation in their predictions of the time-averaged surface pressure distribution (Figure 4.8). The significant additional required manipulation of the solver controls at the outset of the solution run render the pressure-based solvers ill-suited to predict unsteady transonic flow conditions for the ACE profile. As these flow conditions were frequently used in additional computational domains in this thesis, the density-based solver was selected as the sole solver formation in further studies.

4.3 Steady Flow Validation for Two HPT Rotor Blade Profiles

After establishing the density-based solver as the solver of choice for the remainder of the work, an additional element of code validation employed steady-flow solutions on two high pressure turbine rotor blade profiles. The aim was to identify a high-performing turbulence model for the turbulent flow conditions generated in the experiment.

4.3.1 Experimental and FLUENT Setup

The Advanced Core Engine HPT rotor blade, as described in Ashworth (1987) and Johnson (1988), is a military-aircraft turbine blade profile. In its design operating environment, the exit Mach number of the upstream NGV row approaches 1.2, thereby producing a system of strong NGV trailing edge shocks that impact along the frontal 50% of the rotor blade surface. As mentioned previously, the rotor blade row also exhibits high Mach number flow in the blade throat up to a Mach number of 1.2. The B22 is a transonic rotor profile utilized in civil aircraft applications. In the experiments used as the baseline for this numerical study, the rotor exit Mach number was transonic in the range of 0.93 to 0.96 (Doorly, 1983). Figure 4.9 provides a snapshot of 2D density contours for converged solutions of both the ACE and B22 profiles. In both cases, the rotor trailing edges retain shock structures that project both downstream and towards the adjacent blade suction surface. The B22 rotor in experimental conditions also showed an oscillating shock system due to vortex shedding in the blade wake (Nicholson, 1981) and a standing shock on the latter suction surface at these flow conditions.

In order to numerically model these experiments, two-dimensional computational domains derived from mid-span coordinates of the rotor blades were generated to match the experimental blade pitch and axial chord. Experimental non-dimensional parameters such as Reynolds and Mach numbers, as well as dimensional values including the inlet and exit pressures and air temperature, were implemented in the numerical solutions. Table 4.1 summarizes some of the experimental flow parameters, and a complete listing of the boundary conditions can be found in Appendix A.

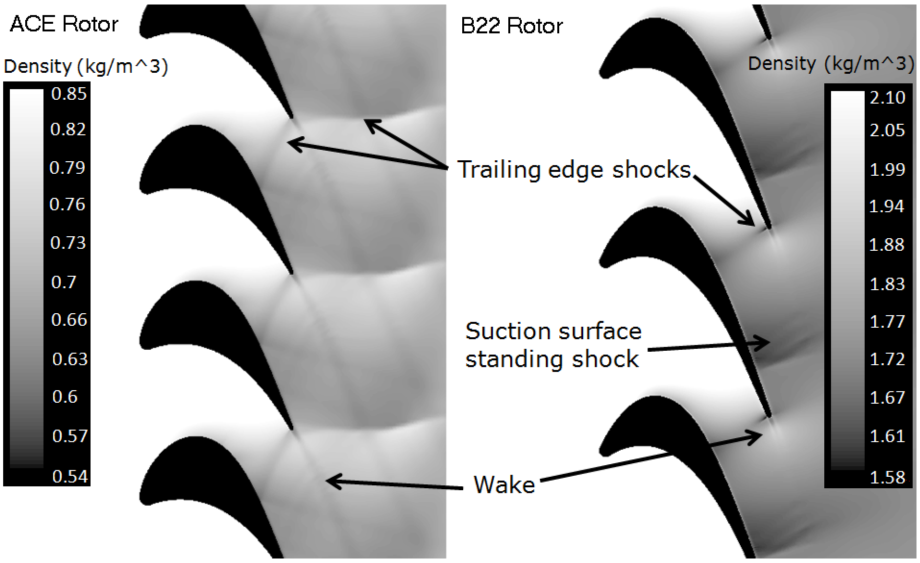

Figure 4.9: Converged steady flow density contours of ACE (left) and B22 (right) rotor profiles highlighting salient flowfield features

Table 4.1: Summary of Experimental Rotor Flow Conditions

Parameter	ACE	B22
Rotor Relative incidence angle	48°	42.75°
Rotor Relative inlet Mach number	0.38	0.315
Rotor exit Mach number	1.18	0.96
Rotor exit Reynolds number	$1 \cdot 10^6$	$2 \cdot 10^6$

Two points of comparison served to establish the performance of the solver in predicting the experimental results. In order to evaluate the accuracy of the predicted rotor passage aerodynamics, the blade surface isentropic Mach number was compared to experimental values. It is defined according to the following equation:

$$M_{is} = \sqrt{\left[\left(\frac{P_{0\infty}}{P}\right)^{\frac{\gamma-1}{\gamma}} - 1\right] \cdot \frac{2}{\gamma - 1}} \tag{4.2}$$

The second basis of comparison was blade surface heat transfer. The ACE experimental data (Johnson, 1988) presents the rotor heat transfer as the Nusselt number based on the freestream total conditions and the blade axial chord:

$$Nu = \frac{hC_{ax}}{k} = \frac{\dot{q}C_{ax}}{(T_0 - T_w)k} \tag{4.3}$$

The B22 experimental data from Doorly (1983) was originally presented as the raw heat flux to the blade surface $\dot{q}$. In order to maintain consistency, this data will instead be presented in this chapter as Nu using the definition in Equation 4.3. In both the experiments, the wall temperature T_w was 290K. The ACE experiment used an inlet total temperature of 460K for the heat transfer measurements, and the B22 heat transfer tests had an inlet total temperature of 432K. These gas–to–wall temperature ratios directly translated to the inlet total temperature boundary conditions in the numerical solutions presented in this chapter.

In both of the experiments, freestream turbulence was generated with turbulence grids. FLUENT offers the option of providing the turbulence intensity and turbulence length scale as inputs to the inlet boundary condition. Two general forms of eddy viscosity models are used in these validation studies; the one-equation Spalart-Allmaras model, which uses a modified turbulent viscosity, and a range of two-equation models that incorporate a turbulent kinetic energy and a turbulence dissipation rate. Each of these models use algebraic relationships to convert these velocity and length scale quantities of the experimental turbulence into model-specific transportable scalar quantities, such as the modified turbulence viscosity in the Spalart-Allmaras model ($\tilde{\nu}$), or turbulent kinetic energy (k) in the two-equation models. The turbulence intensity can be directly used in the solver input, and a generally applied rule for the turbulence length scale is to use the diameter of the turbulence grid bars (ANSYS, 2006). In the experiments, this length is 7.6mm for both rotor profiles. The B22 experiment also obtained heat transfer measurements using ambient tunnel turbulence levels. In this case an empirical correlation for the turbulence length scale is derived from the hydraulic diameter of the cascade:

$$\Lambda \approx 0.07 D_H \approx 0.07 \frac{2HW}{H+W} \tag{4.4}$$

The hydraulic diameter D_H in the above equation is the ratio of the wetted cross-sectional area of the wind tunnel walls upstream of the experimental blade cascade row to its perimeter (Ellenberger, 2010). Calculating this value resulted in a length scale estimate of 4.2mm, which is slightly smaller than the grid-generated length scale. The reported turbulence intensities from the experiments are 3% for the ACE profile, and two levels of 0.4% and 4.5% for the B22 profile.

4.3.2 Grid Dependency Studies

Establishing a grid independent solution was the first phase of the rotor passage steady flow validation studies. In each of the ACE rotor solutions, the Spalart-Allmaras (SA) turbulence model was used to provide a consistent basis of comparison between the

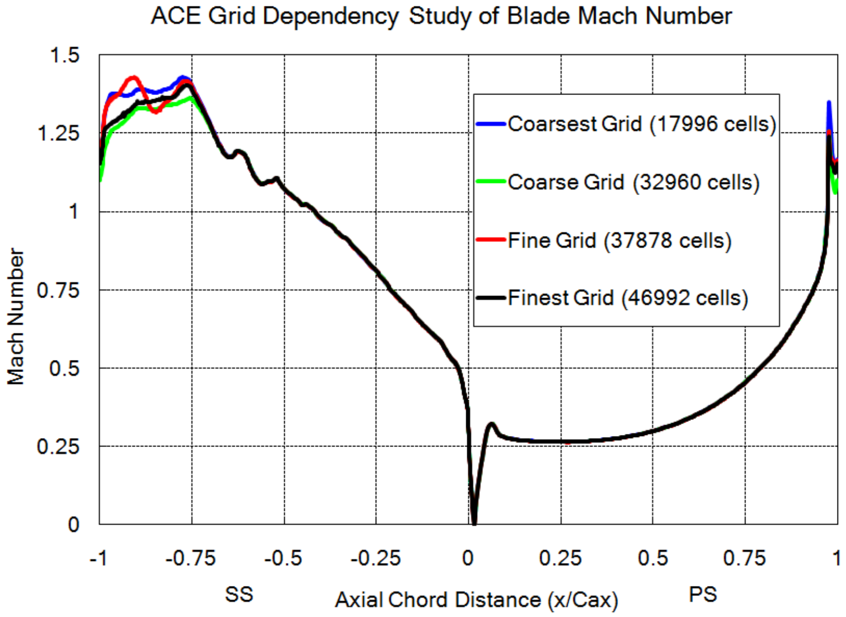

Figure 4.10: Grid dependency study for ACE blade surface isentropic Mach number

different computational grids. The ACE profile surface isentropic Mach number is presented in Figure 4.10 for a range of grid densities between $1.7 \cdot 10^4$ and $4.7 \cdot 10^4$ cells. Overall, the surface Mach number is largely insensitive to the change in grid density, and any variation is due to the different predictions of the oblique ACE trailing edge shock interaction with the adjacent suction surface boundary-layer.

Comparing the surface Mach number distribution showed that the leading portion of the suction surface was under-predicted. The source of this error has been documented previously (Johnson, 1988; Abhari, 1991), and is due to the increase of the wind tunnel width along the blade axial chord, also known as hade angle. In order to assess if this axial variation in stream-tube height in the experiment was the source of the error in the numerical simulation, an additional 3D computational domain was generated with 5 grid nodes in the span-wise direction and the area ratio at the inlet and exit planes for the rotor passage matched to experimental values based on the hade angle and blade span. A symmetry boundary condition was then enforced on the haded endwalls to complete a “quasi-3D” domain. The resulting Mach number distribution compares favorably to the experimental data (Figure 4.11).

It is important to note that the leading portion of the suction surface was transitional for the flow conditions presented, and none of the turbulence models evaluated

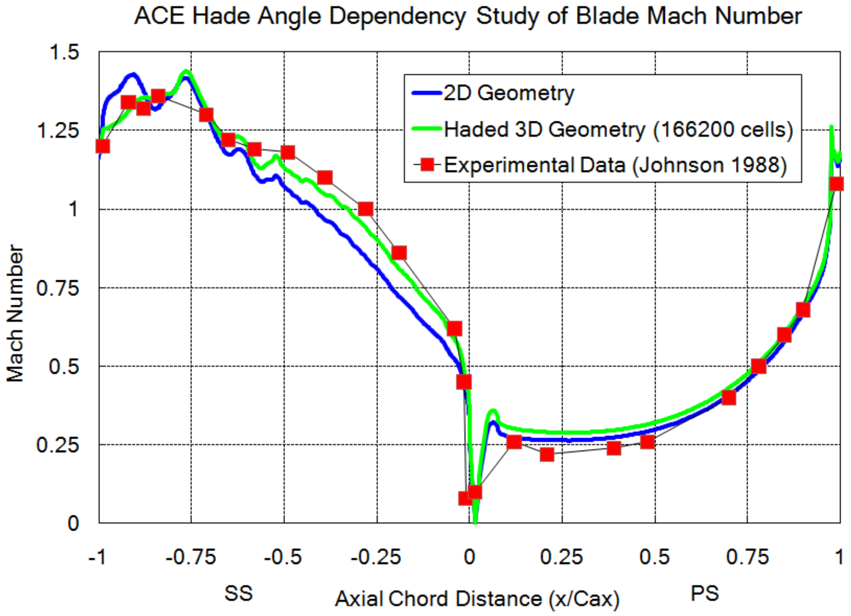

Figure 4.11: Effect of hade angle on ACE surface pressure prediction compared to experimental data from Johnson (1988)

in the study provided adequate resolution of this boundary-layer behavior. The result of this was a significant increase in the predicted Nu distribution on this portion of the blade surface as compared to experimental results. The improvement in blade surface pressure prediction on this portion of the suction surface due to the inclusion of the hade angle did not therefore result in significant improvement in prediction of Nu in this region. Thus the 2D computational domain was retained for the remainder of the validation studies. Further evaluation of grid dependency focused on the ACE heat transfer. The y^+ value at the blade wall in each grid was controlled to less than 2. Lessons learned from the grid dependency study of the B22 rotor indicated that this level of y^+ control should be sufficient for the purpose of heat transfer predictions. Figure 4.12 demonstrates a similar insensitivity in the blade Nu distributions to that seen previously in the blade surface Mach number over the range of grid densities tested.

The B22 grid dependency study was conducted using the $k - \omega$ SST turbulence model. The B22 rotor evaluated grid sizes from $5.4 \cdot 10^4$ cells to $1.3 \cdot 10^5$ cells. Refinement near the wall created a range of y^+ values from 25 to less than one. The rotor surface Mach number (Figure 4.13) is largely insensitive to the increasing grid density, except for the latter suction surface near the trailing edge.

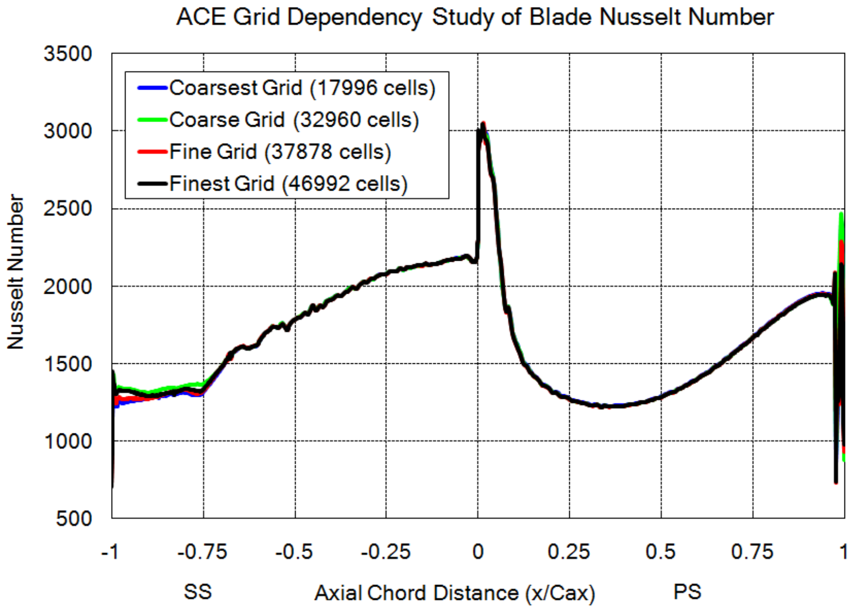

Figure 4.12: Grid dependency study for ACE blade surface Nu

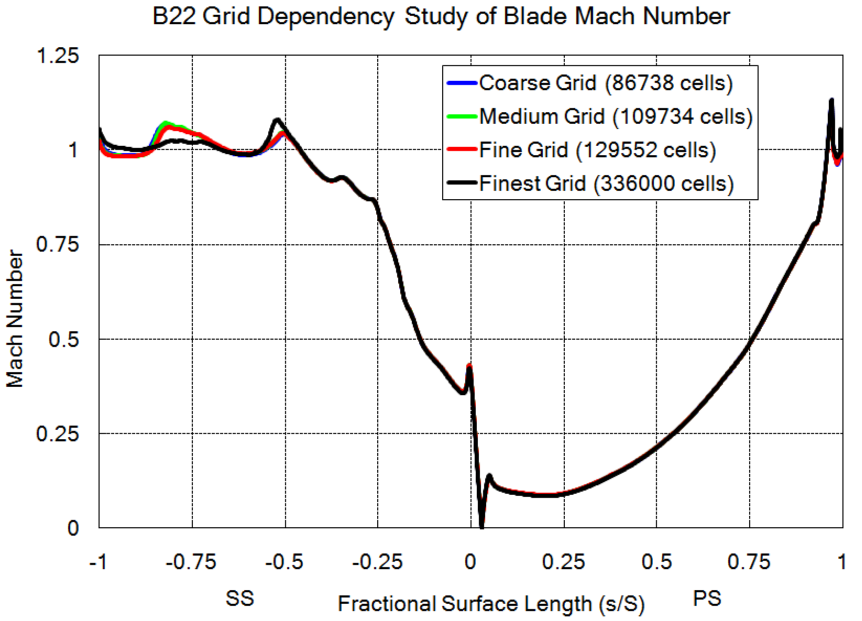

Figure 4.13: Grid dependency study for B22 blade surface isentropic Mach number

The B22 surface Nu distributions showed a strong dependence on the y^+ value. Controlling y^+ removed an oscillatory behavior in the blade heat transfer distribution and reduced the leading edge heat transfer. Figure 4.14 displays only the three highest levels of grid refinement for the B22 computational domain. It is evident that refining the grid such that y^+ is less than 1 on the rotor surface results in a grid independent solution for the blade heat transfer.

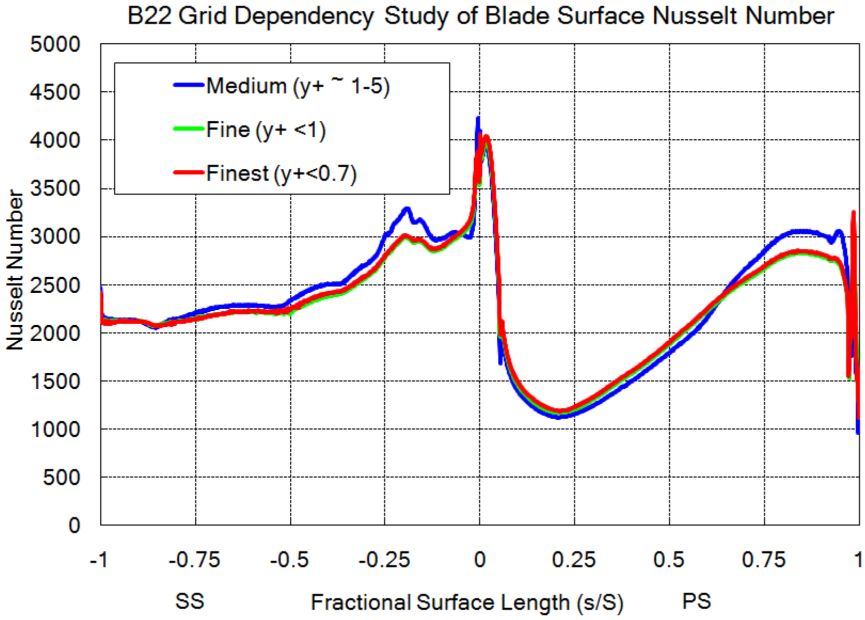

Figure 4.14: Grid dependency study for B22 blade surface Nu

4.3.3 Predictions of Mid-Span Pressure and Heat Transfer Distributions

Following the grid-dependency studies, the "fine" 2D grids for both the ACE and B22 rotors were selected to further compare the performance of selected turbulence models. The ACE computational domain employed a range of four eddy-viscosity turbulence models; the one-equation SA model, and three two-equation models (the standard $k-\epsilon$, the $k-\omega$, and the $k-\omega$ SST). Following these evaluations, the SA and $k-\omega$ SST models proved to be most accurate in their predictions of blade surface Mach number and Nu distributions, and were then further tested on the B22 rotor profile.

4.3.3.1 Blade Pressure Distributions

Figure 4.15 shows the blade surface Mach number predictions of the four turbulence models and experimental data from Johnson (1988). The SA and $k-\omega$ SST models on initial evaluation appear to match the experimental data on both the leading suction surface and the pressure surface better than the other two models. The $k-\omega$

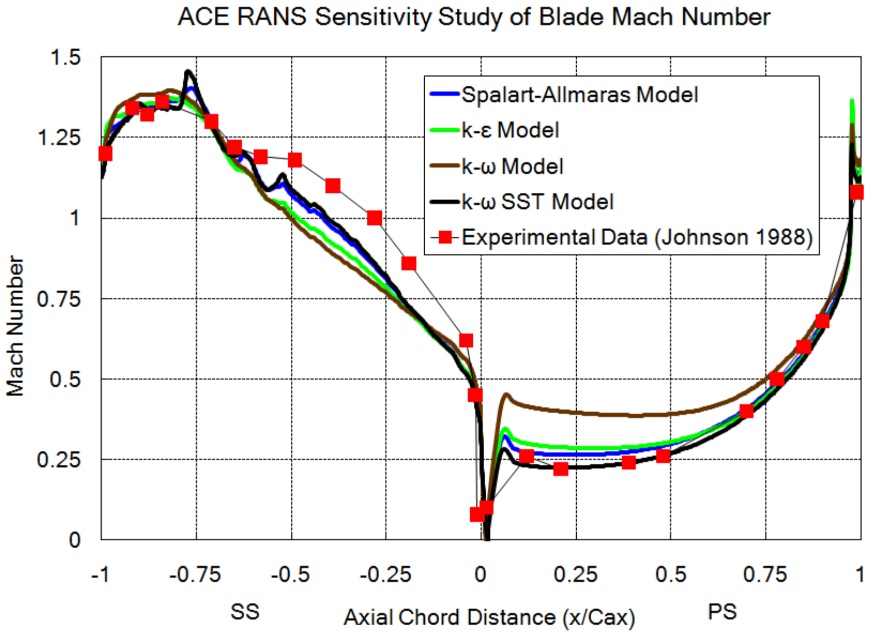

Figure 4.15: Sensitivity study of ACE rotor surface pressure to RANS turbulence model

model in particular seems to diverge from the other turbulence model predictions. In general it over-predicts the Mach number on the pressure surface, and under-predicts the Mach number on the suction surface. The SA and $k-\omega$ SST predictions are compared to the experimental data for the ACE rotor in Figure 4.16. The limitation of the hade angle exclusion is evident for both of these models, but the $k-\omega$ SST predicts the pressure surface Mach number distribution particularly well. Visual inspection of the pressure contours in the domain (not shown) reveal that the $k-\omega$ SST model also retains a sharper resolution of the ACE trailing edge shock. This is reflected in Figure 4.16 through the sharper Mach number peak on the latter suction surface.

These two turbulence models were then evaluated against the B22 surface Mach number distribution (Figure 4.17). The predictions for both models demonstrate slightly stronger acceleration on the blade pressure surface as compared to the experimental data. Overall the prediction is fairly close to experimental results. The SA model demonstrates this more strongly than the $k-\omega$ SST model. On the B22 suction surface, there is an under-prediction of the Mach number near the leading edge, and a slight over-prediction near the trailing edge. This variation is probably due to the slightly different profile sections used in the numerical simulation as compared to

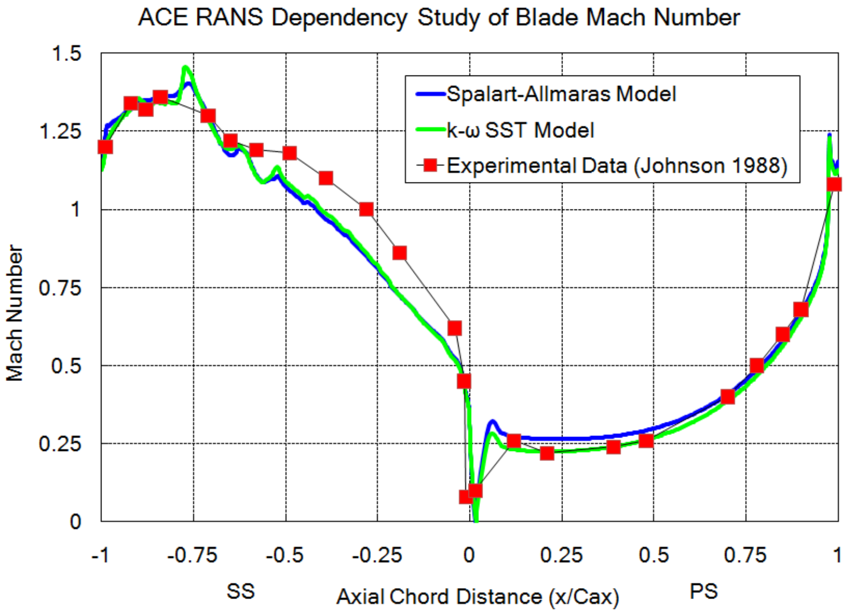

Figure 4.16: Comparison of turbulence models and experimental data from Johnson (1988) for ACE surface isentropic Mach number

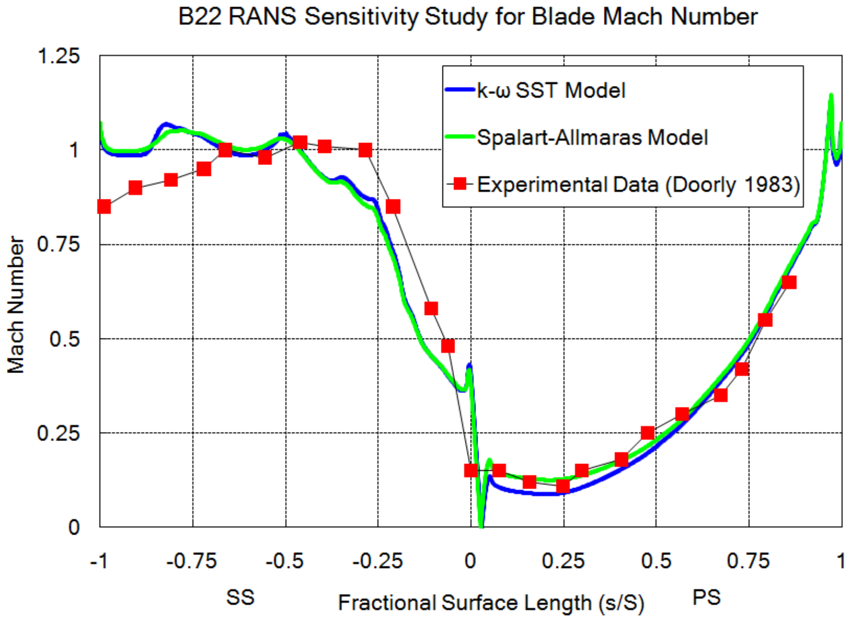

Figure 4.17: Sensitivity study of B22 rotor surface pressure to RANS turbulence model

the experiment. The rotor profile used here is the constant streamline at mid-span, whereas the experiment used a constant radius cut at mid-span (Nicholson, 1981).

4.3.3.2 Blade Heat Transfer Distribution

Heat transfer predictions for the ACE rotor profile showed a very high sensitivity to the selection of turbulence model. Figure 4.18 vividly demonstrates this behavior. The $k-\omega$ model Nu prediction in particular is significantly higher than the other models, although it does rapidly approach the other predictions further along the rotor suction surface. On the pressure surface the $k-\omega$ and $k-\epsilon$ models predict very high levels of Nu compared to the other two models.

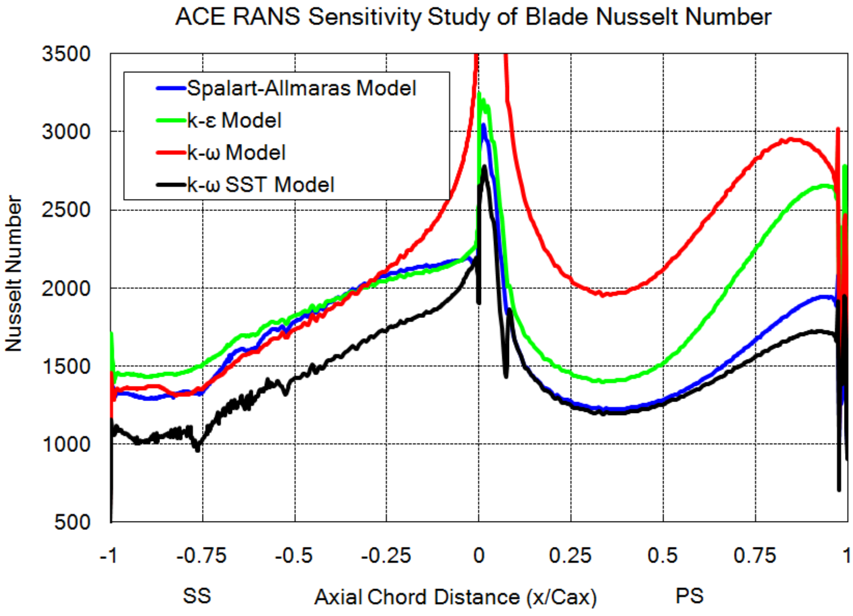

Figure 4.18: Sensitivity study of ACE rotor surface Nu to RANS turbulence model

Relative to experimental results, the SA and $k-\omega$ SST perform much better than the other two models. The Nu predictions for these two turbulence models are displayed in Figure 4.19 against the experimental data for the ACE rotor. The Nu prediction tends to be high over most of the blade surface, particularly along the suction surface. In the experiment, the freestream turbulence intensity was 3%, and therefore this portion of the blade surface exhibited a transitional boundary-layer up to 0.5 C_{ax}, which explains the over-prediction from both models. The $k-\omega$ SST model in general provides a more accurate prediction of the ACE Nu distribution. On the pressure surface where the boundary-layer is turbulent in the experiment, the

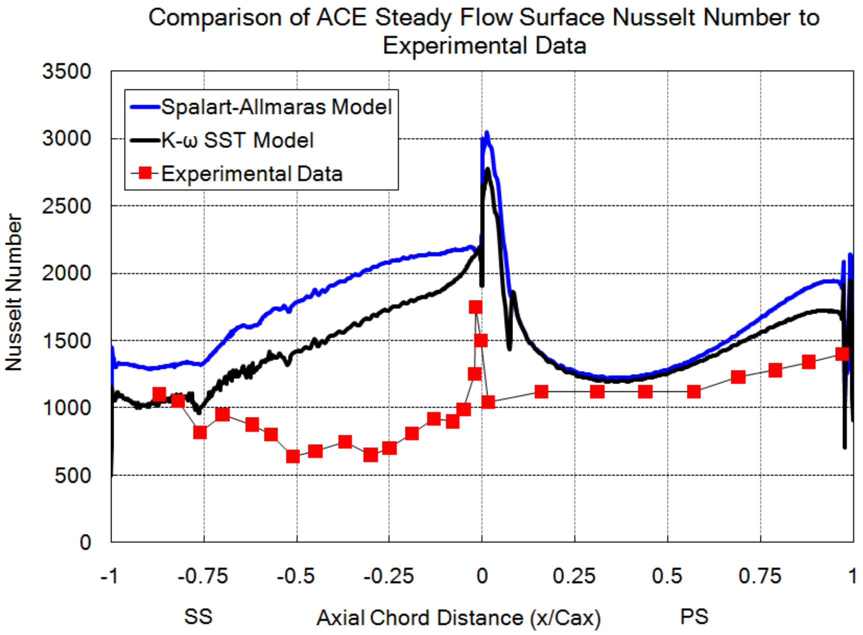

Figure 4.19: Steady flow predictions of ACE surface Nu compared to experimental data from Johnson (1988) with 3% Tu in freestream

prediction is accurate within 20%.

The SA and $k - \omega$ SST models were also tested on the B22 rotor profile at two freestream turbulence intensities of 0.4% and 4.5%. Figure 4.20 compares the Nu predictions for the SA and $k - \omega$ SST model against experimental data from Doorly (1983). The trend for both of the models is to over-predict the heat transfer on the rotor surface. On the rotor suction surface this is expected, as the boundary-layer is transitional through to 25% of the rotor suction surface. Unfortunately, experimental data is not available after 50% of the suction surface, but the $k - \omega$ SST model does close to the experimental data near that portion of the blade. The $k - \omega$ SST model outperforms the SA model once again, and is within 20% of the absolute heat transfer levels across almost all the B22 blade surface. Figure 4.21 presents the heat transfer predictions for the low freestream turbulence case. The suction surface prediction is poor as expected due to the laminar boundary-layer on this half of the blade. On the pressure surface both turbulence models perform fairly well in predicting the absolute levels of heat transfer as well as the trend along the pressure surface. This behavior is also expected as the boundary-layer on this portion of the blade is turbulent in the experimental data. Again, the $k - \omega$ SST model outperforms the SA model in predicting the pressure surface heat transfer over most of the blade.

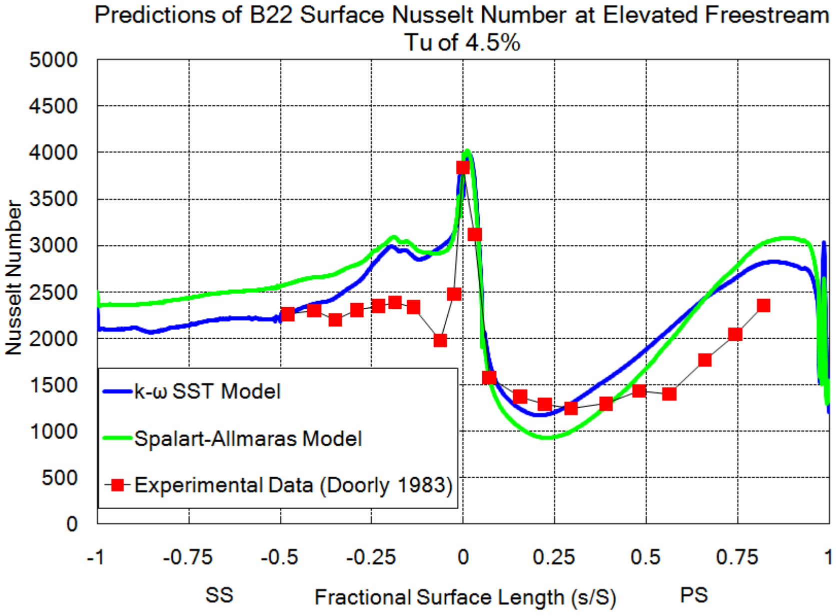

Figure 4.20: Sensitivity of B22 surface Nu to turbulence model–4.5% Tu

The uncertainties within the experimental data render strong statements assessing the accuracy of the turbulence model predictions difficult. For example, Figure 4.22 generally shows that for the lower freestream turbulence case, there is a reduction in heat transfer, even in the already turbulent portions of the blade boundary-layer. However, at the rotor leading edge, the reported Nu for the low turbulence intensity is much higher than the high freestream turbulence intensity result. This discrepancy and others in the experiment data are sometimes on the order of 15% to 20% (Doorly, 1983).

Nonetheless, the turbulence models also qualitatively predict the trend towards reduction in heat transfer with lower freestream turbulence intensity. This mimics both the experimental results and expectations of what should occur, despite the anomalous leading edge reading. Figures 4.23 and 4.24 demonstrate that predictions of B22 rotor heat transfer in both the $k-\omega$ SST and SA models respond to varying levels of freestream turbulence. Focusing on the B22 pressure surface, both turbulence models predict a variation in the Nu distribution on the order of 10% to 20%, which is in line with the 20% variation shown in the experimental results.

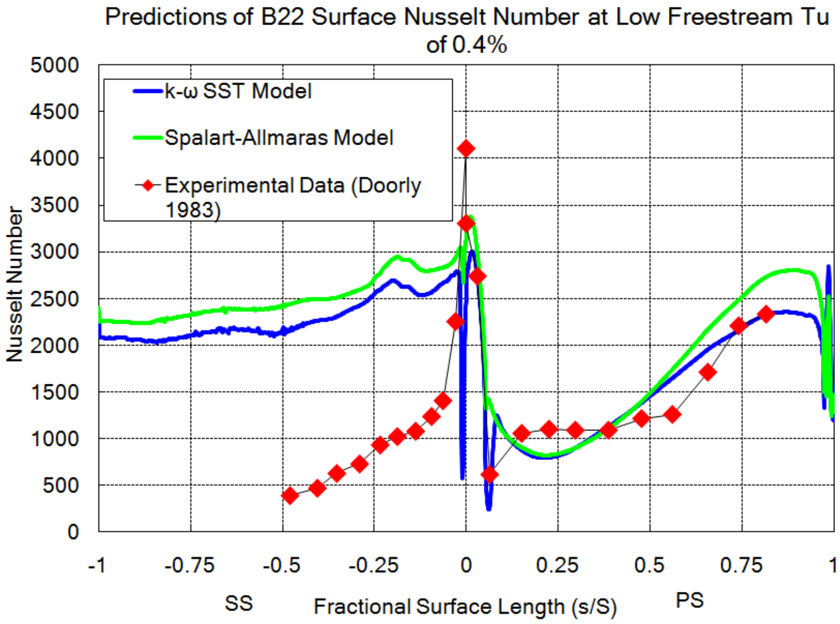

Figure 4.21: Sensitivity of B22 surface Nu to turbulence model–0.4% Tu

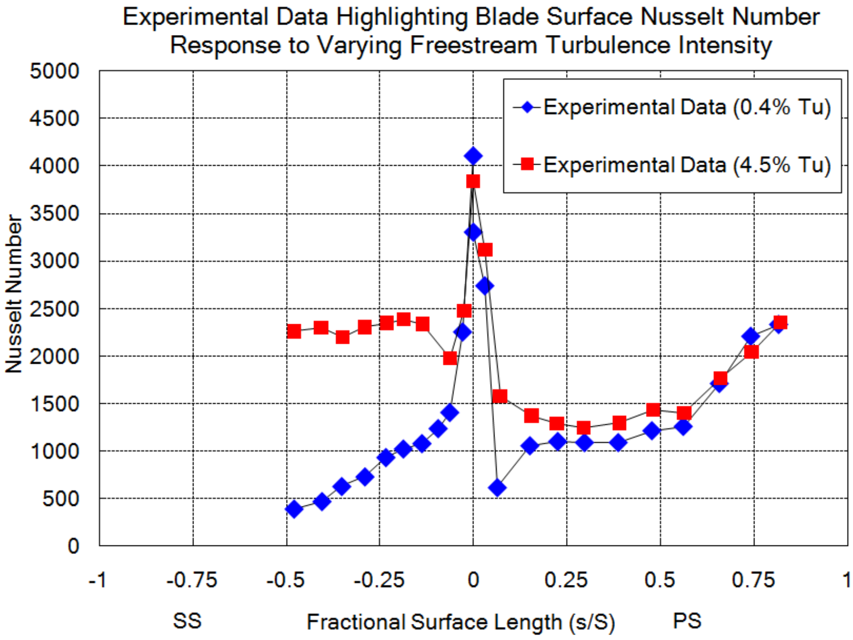

Figure 4.22: Experimental data from Doorly (1983) highlighting variation in blade surface Nu due to different levels of freestream turbulence

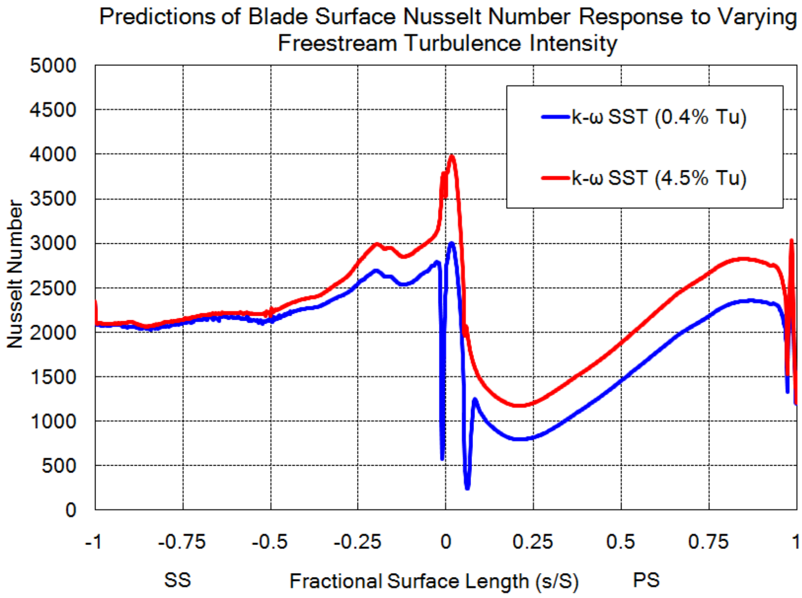

Figure 4.23: Predictions of variation in blade surface Nu due to different levels of freestream turbulence–$k-\omega$ SST model

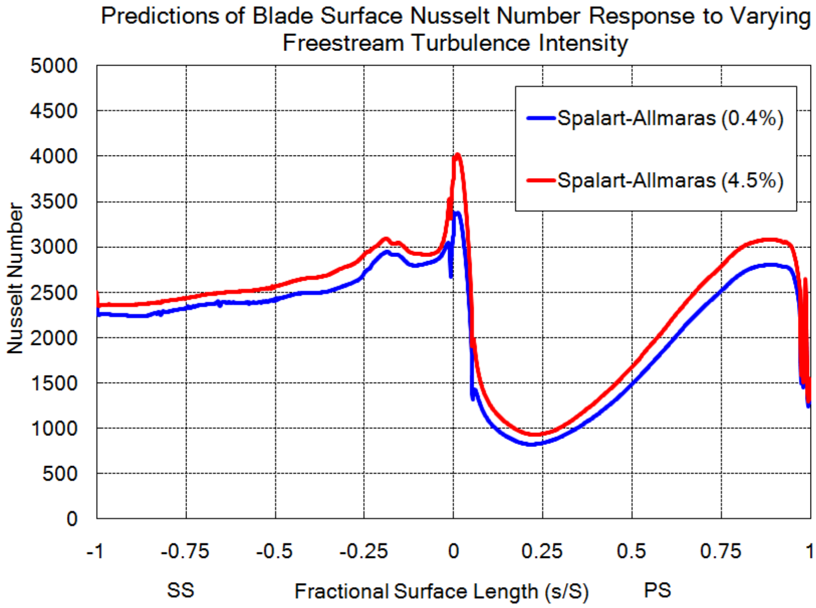

Figure 4.24: Predictions of variation in blade surface Nu due to different levels of freestream turbulence–SA model

4.4 Summary

In summary, this chapter presented validation studies for the FLUENT solver formulation and different turbulence models in a RANS solver using a variety of computational domains. Sensitivity of aerothermal predictions to solver formulation was assessed in steady and unsteady flow at transonic conditions for a simple airfoil and a high pressure turbine rotor profile. In the NACA 0012 airfoil study the density-based solver reached convergence sooner than the pressure-based solvers, but the pressure-based solvers more accurately predicted the location of the standing normal shock on the airfoil surface. Overall the three solver conditions tested showed an otherwise excellent prediction of the airfoil surface pressure. In the steady flow evaluation of the ACE rotor profile, the convergence trends seen in the NACA airfoil study were repeated. Additionally, there appeared to be little to no sensitivity in the predictions of blade surface pressure and Nu to solver selection. In the unsteady flow case for the ACE profile with a passing upstream cylinder, the pressure-based solvers required significant reduction of the under-relaxation factors to prevent solution divergence, and only the pressure-based coupled solver reached convergence. The relative difficulty in achieving solution stability in the unsteady flow case dictated the use of the density-based solver for the remainder of the work in the thesis.

The next phase of the validation study evaluated prediction of the aero-thermal conditions in two HPT rotor passages. Sensitivity and accuracy of various turbulence models in predicting the blade surface Mach number and blade surface Nu were presented. Initially, a quasi-3D grid was generated to accommodate the hade angle that was present in the experimental setup for the ACE rotor profile. Including the area ratio at the inlet and exit to the rotor passage resulted in accuracy within 5% of experimental results on the ACE suction surface. However, there was not an increase in the accuracy in predicted Nu when the hade angle was included. This is primarily due to the inability of the turbulence models to predict boundary-layer transition on the ACE suction surface. Therefore, the 2D computational domain was retained for further study. Overall, the two rotor profiles tested showed relative insensitivity in the pressure field to choice of turbulence model, whereas the predicted heat transfer significantly depended on turbulence model selection. Comparison of turbulence models demonstrated that the $k - \omega$ SST model performed the best in predicting the ACE surface Mach number and surface Nu. The heat transfer prediction was accurate to within approximately 20% in the turbulent regions of the blade surface, but the trend was to consistently over-predict the blade heat transfer. The SA model agreed with both the $k - \omega$ SST model and the experiment in predicting the trend of Nu behavior over the blade surface, but showed higher levels of heat transfer than the $k - \omega$ SST model. The standard $k - \epsilon$ model and $k - \omega$ model performed poorly in predicting both surface Mach number and surface Nu.

The two higher performing models were also evaluated against the B22 rotor. They both correctly predicted the trend of the Mach number distribution on the blade surface. The two models over-predict the Mach number on the latter portion of the rotor pressure surface, which limits the accuracy of the heat transfer prediction on that portion of the blade. The $k - \omega$ model outperforms the SA model in predicting the rotor heat transfer, and in the turbulent regions of the blade the accuracy is within about 20%. This level of accuracy is acceptable due to the reported variability in the experimental data. The trend of the experimental heat transfer distribution was to show an increase of about 20% in the blade heat transfer when the freestream turbulence increased from 0.4% to 4.5%. The two turbulence models' heat transfer predictions also demonstrated variation in the range of 10% to 30%.

Overall, the steady flow solutions using the SA and $k - \omega$ turbulence models appear to be reasonably accurate in predicting the rotor surface pressure. Heat transfer predictions are limited by the boundary-layer physics present in the experiment for both rotor blades. While recognizing the inherent deficiencies in predicting heat transfer in the laminar and transitional portions of the rotor surface, the predictions of turbulent heat transfer were within 20% of experimental values. Furthermore, the two models also correctly captured the qualitative trend in heat transfer variation due to different levels of freestream turbulence intensity. This established sufficient confidence in the predictive capabilities of the solver to evaluate these two rotor profiles in unsteady flow conditions in the next chapter.

Chapter 5

Unsteady Flow Validation

5.1 Overview

In Chapter 4, validation studies of surface pressure and heat transfer for the ACE and B22 rotor profiles in steady flow were conducted. In this chapter the same rotor profiles will be analyzed in unsteady flow simulations based on experimental work employing a rotating bar wake generator upstream of the rotor blades. A description of the computational domains and dependency studies for grid density and time-step are provided in Section 5.2. Then, the solver's ability to predict unsteady aerothermal conditions in transonic flow conditions is detailed in Sections 5.3 and 5.4. Section 5.5 summarizes the chapter.

5.2 Case Preparation and Dependency Studies

In these 2D unsteady simulations a circular bar is placed upstream of the rotor blade rows to represent the trailing edge of a nozzle guide vane (NGV). In the original experimental work, the diameters of these bars were adjusted so that velocity deficit in the wakes matched their representative NGV wakes (Doorly, 1983; Ashworth, 1987), and these bar diameters are used directly in the computational geometry. Additionally the numerical simulations presented in this case study use a sliding mesh to recreate the mid-span velocity triangles in the experiment. The inlet velocity triangles for the two rotor profiles are presented in Figure 5.1.

The bar to rotor blade count in each of the computational domains is 1:2. This directly matches the ratio for the B22 rotor, and is slightly off of the experimental ratio of 1:1.73 for the ACE rotor. All other geometry considerations for the rotor

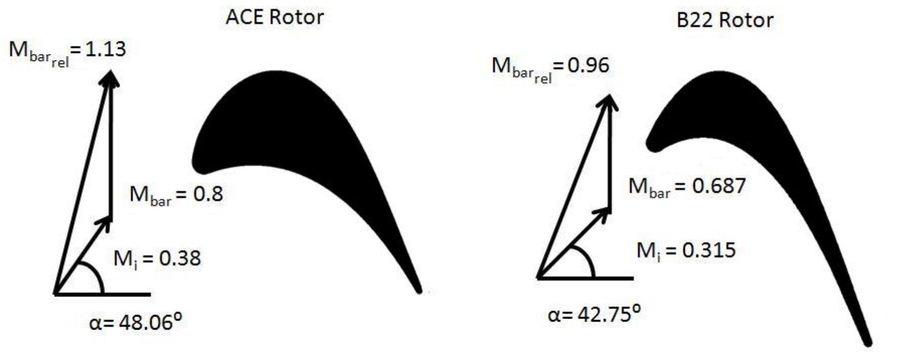

Figure 5.1: Velocity triangles at rotor inlet for the unsteady passing bar simulations

blades are identical to the steady flow domains in the previous chapter.

Grid and time-step dependency studies were first conducted for the two unsteady domains. Time-averaged quantities such as the surface heat transfer and unsteady quantities such as static pressure traces were evaluated on the rotor to assess whether the solution was grid independent. Variation of less than 1% for a subsequent level of refinement was set as the criteria for solution independence. Figure 5.2 shows an example of the grid dependency study for the ACE rotor. The converged unsteady static pressure time-history on the ACE suction surface is displayed over a single period. The solution shows independence for the grid with $3.5 \cdot 10^5$ cells. Figure 5.3 presents the time-averaged surface heat flux for the B22 rotor. Two grid densities of $1.9 \cdot 10^5$ and $5.3 \cdot 10^5$ cells were tested initially, and the solution showed no dependence despite the significant increase in grid density.

The grid independent solutions were then evaluated over a range of time-steps. Figures 5.4 (ACE rotor) and 5.5 (B22 rotor) show the time-resolved surface static pressure on the two rotor suction surface crowns. The ACE time-step dependency study shows that the solution achieves independence at a time-step of $T/80$. The B22 rotor solution is independent at a time-step of $T/50$.

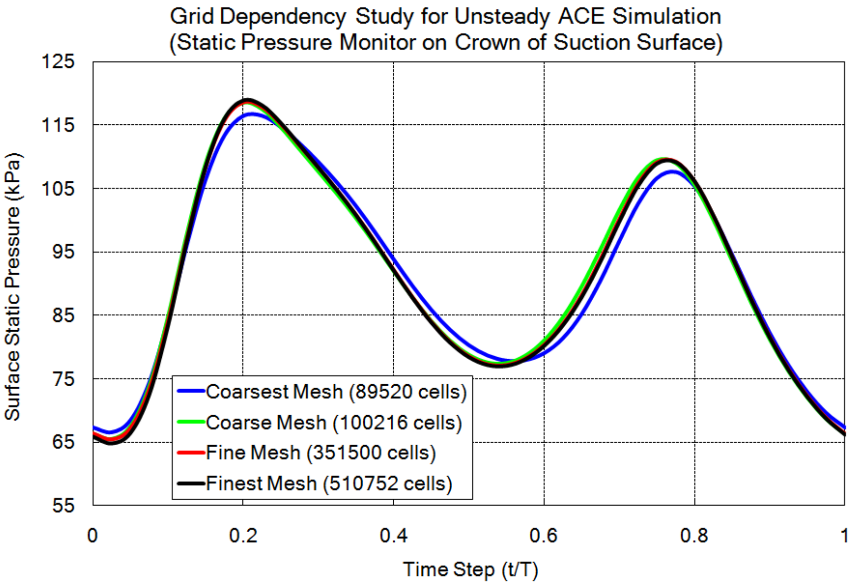

Figure 5.2: Grid dependency study for unsteady ACE rotor surface pressure

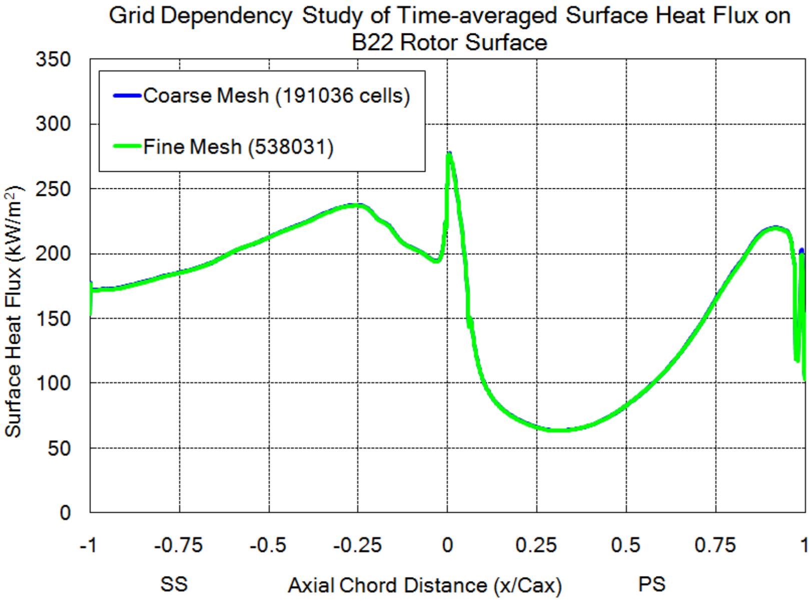

Figure 5.3: Grid dependency study for time-averaged B22 surface heat flux

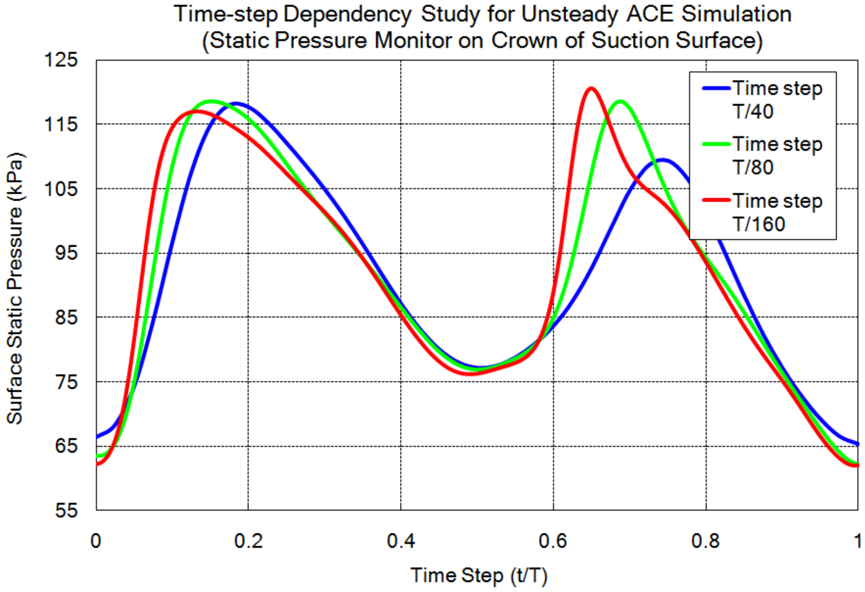

Figure 5.4: Time-step dependency study for unsteady ACE rotor suction surface crown pressure monitor

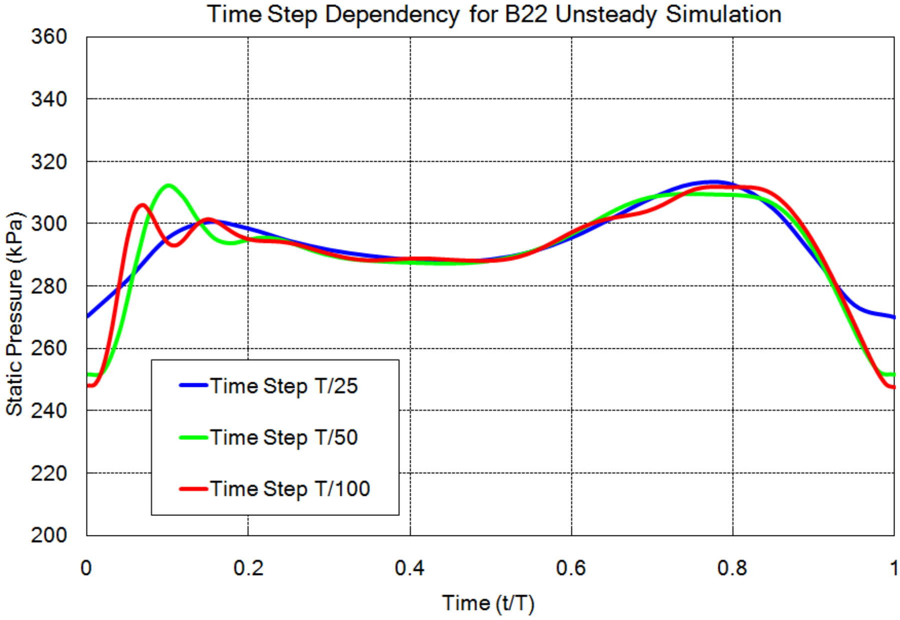

Figure 5.5: Time-step dependency study for unsteady B22 rotor suction surface crown pressure monitor

5.3 Predictions of Unsteady Rotor Blade Pressure Fields

Due to the unavailability of experimental high-frequency static pressure results for the B22 rotor, this section will focus on the ACE unsteady and time-averaged pressure results. Snapshots of the flowfield via contours of pressure (left) and entropy (right) are shown in Figure 5.6, and they highlight the complex nature of the unsteady interactions between the bar and the rotor blade row.

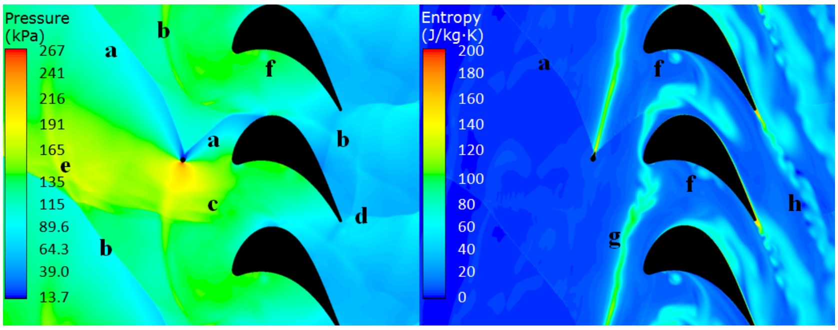

Figure 5.6: Pressure (left) and entropy (right) contours showing taxonomy of unsteady rotating bar interactions with downstream ACE rotor profile

The simulated NGV trailing edge generates a large number of interesting disturbances into the flow-field as illustrated in the figure. The moving bar has a system of shocks surrounding it, including the bow shock (c) and the recompression shocks on its trailing edge (a). Additionally, the bar trails a turbulent wake which impacts the downstream rotor blade row (g). The recompression and bow shocks impinge on the frontal ACE suction surface, and generate a series of high-frequency shock reflections in the rotor blade passage. The evolution of the primary reflection from the recompression shock (b) highlights this description. At first impact near the suction surface crown, the reflection can be seen extending even downstream of the rotor exit plane where the rotor trailing edge shocks are also present (d). As the bar continues downward, this primary reflection sweeps upstream, curling around the leading edge and propagating towards the inlet to the domain. It creates shock-shock interactions with the bow shock and the upstream recompression shock (e). As the recompression shock passes over the ACE rotor leading edge, the shock forms a vortex sheet which then rolls up into a boundary-layer separation bubble (Johnson, 1988). This bubble then propagates along the rotor pressure surface (f) and is further affected by the rotor wake (g). FLUENT also indicates that there is wake-wake interaction between

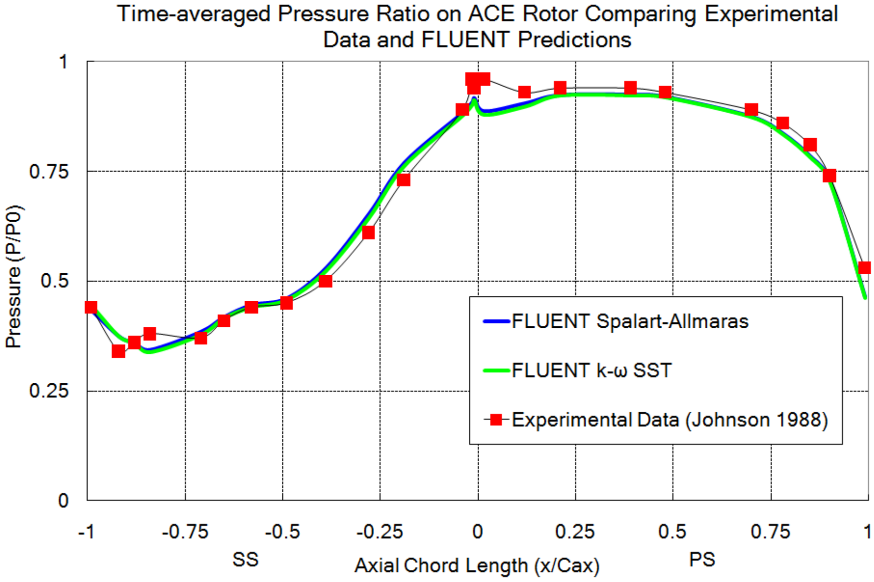

Figure 5.7: Time-averaged ACE rotor surface pressure comparing FLUENT predictions and experimental data from Johnson (1988)

the bar and the rotor (h). The progression of these interactions is very similar to descriptions of the low-frequency bar passing events described in Johnson (1988). In fact, the FLUENT simulation captures all the high-frequency shock reflections described in the experimental work.

The quantitative predictions of the unsteady pressure environment also appear to be accurate compared to experimental results. Figure 5.7 shows the time-averaged surface pressure distribution for the ACE rotor. There is little sensitivity of the predictions to choice of turbulence model. The predictions show strong agreement with the experimental data, and also capture the unloading of the leading suction surface compared to steady flow seen in the experimental results.

The two turbulence models also show consistent predictions of the unsteady pressure signals on the ACE rotor surface. Figure 5.8 shows the time-history of the surface pressure at three locations on the blade over four bar passing periods. The experimental data shown here is drawn from Johnson (1988), and digitized from the ensemble-averaged time traces. The leading edge data is shown in Figure 5.8a. There is some variation in the shape of the distribution, but the traces capture the salient signatures of the bar-passing events, such as the arrival of the recompression shock (near 1 T), and the passing bow shock (0.75 T). Furthermore the overall magnitude

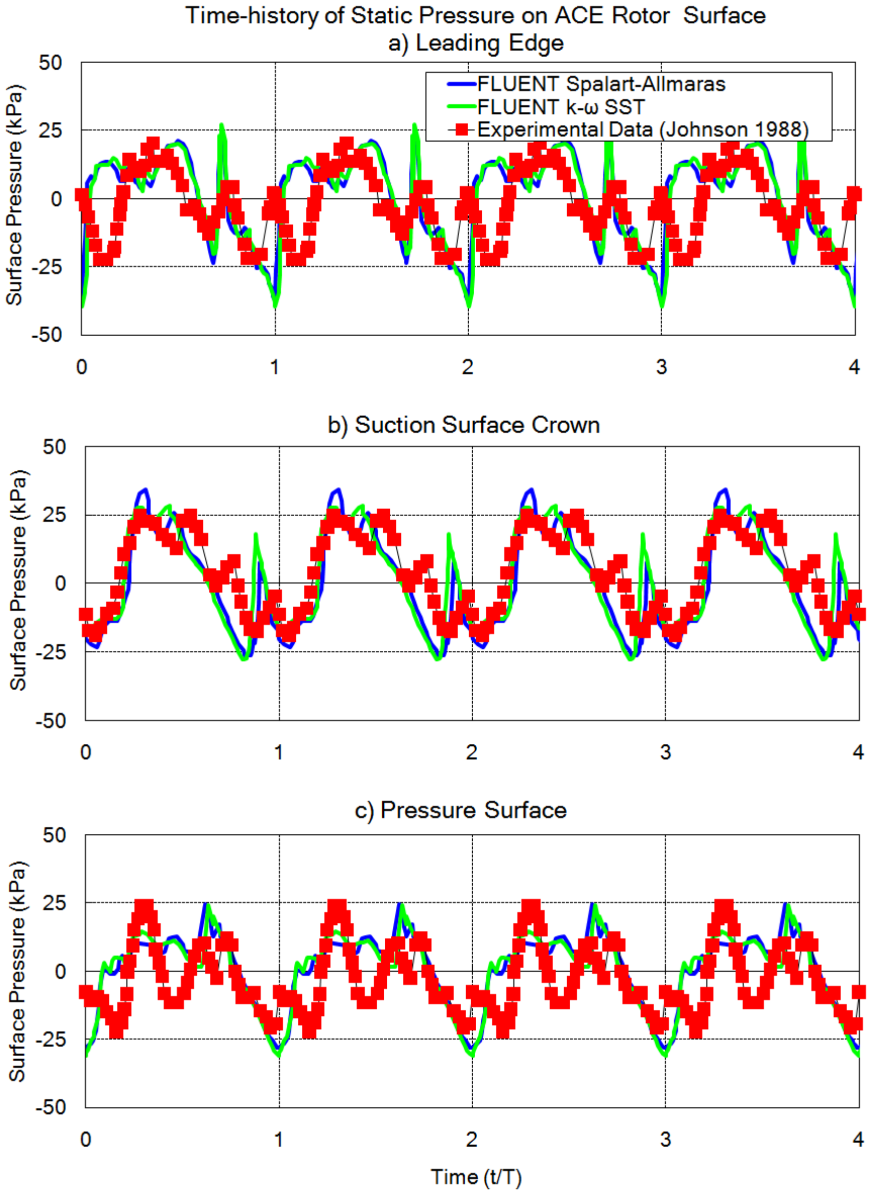

Figure 5.8: Comparison of time-resolved static pressure traces at three locations on ACE rotor surface showing FLUENT predictions and experimental data from Johnson (1988)

of unsteadiness in the FLUENT predictions agrees with the experimental data. The results on the suction surface crown (b) show strong agreement in both the level of unsteadiness and the shape of the distributions. The FLUENT solutions tend to over-predict the bow shock (near 0.9 T), but accurately capture the "double-peak" signature near 0.5 T. This behavior is due to the recompression shock impacting the rotor suction surface crown, followed closely by the upstream moving secondary reflection from this event. On the pressure surface (c), the overall unsteadiness is well-predicted, but both turbulence models tend to invert the relative strength of the bow shock and recompression shocks influence on the unsteady pressure trace.

Any variation between the FLUENT predictions and the experimental data is due to the different bar pitches employed in the experiment and the numerical solution. Figure 5.9 compares the experimental ensemble-averaged pressure trace on the rotor suction surface crown for the high-frequency bar passing tests shown in the previous figure and the phased low-frequency data for the same experimental flow conditions.

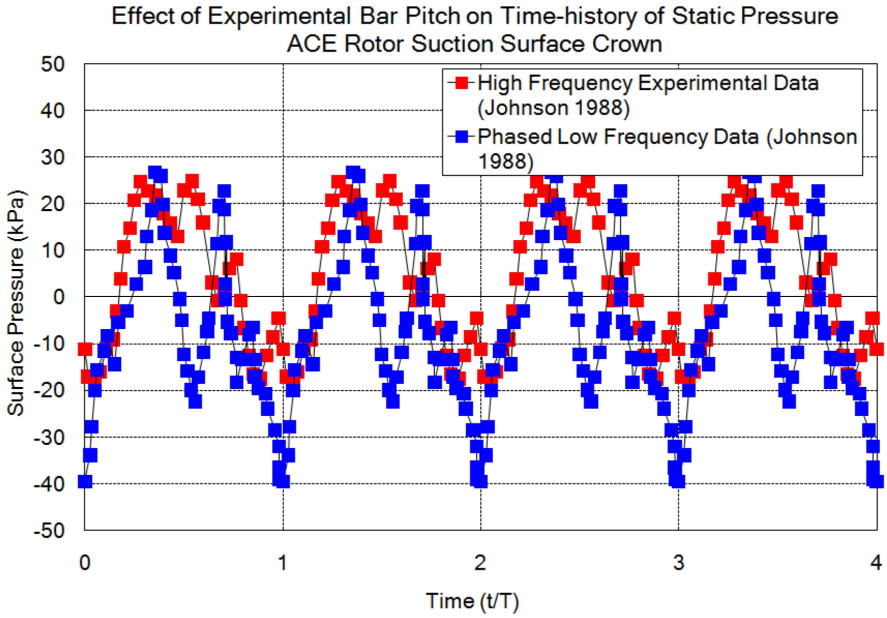

Figure 5.9: Effect of bar pitch on time-resolved experimental static pressure traces from Johnson (1988)

The increased unsteadiness and sharply different unsteady behavior between the two experimental sets indicate that there is non-linear coupling of the bar pitch and the resulting unsteady pressure field. Overall, the FLUENT solutions for both turbulence models appear to provide a reasonably accurate set of predictions for both the time-averaged and unsteady pressure field for the ACE rotor.

5.4 Predictions of Unsteady Rotor Blade Heat Transfer

In the unsteady flow conditions for the ACE rotor, the supersonic relative Mach number for the passing bar generates a pair of strong shocks, the bow shock and the recompression shock. While in certain cases the upstream NGV trailing edge could produce a weak shock reflection impinging on the rotor (De la Loma et al., 2008), the shock system generated by the bar is largely unrealistic in comparison to aero-engine conditions. The experimental heat transfer data from Doorly (1983) uses a passing bar with a transonic relative Mach number of 0.96, resulting in a single recompression shock (i.e. no bow shock) extending downstream to impact the rotor surface (Figure 5.10). This configuration of the unsteady flow, with just the single shock and bar wake influencing the unsteady rotor heat transfer environment, presents a more accurate representation of engine conditions. Therefore, this geometry will be used solely in the validation study of unsteady rotor heat transfer.

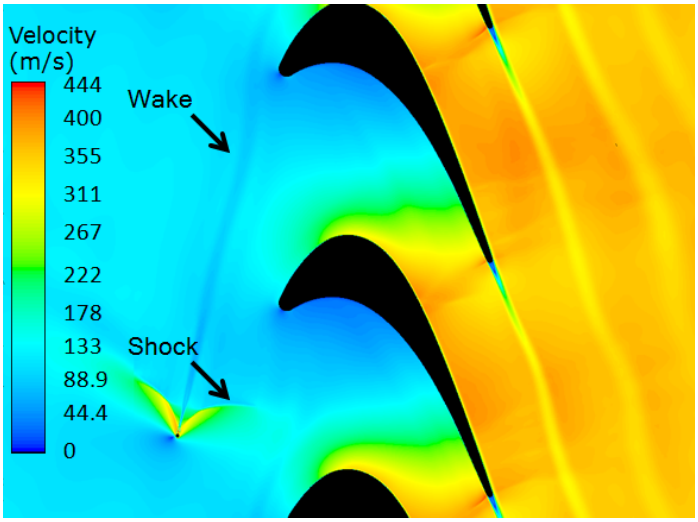

Figure 5.10: Velocity contours illustrating taxonomy of unsteady rotating bar interactions with downstream B22 rotor profile

The comparative validation of the Spalart-Allmaras and $k-\omega$ SST turbulence

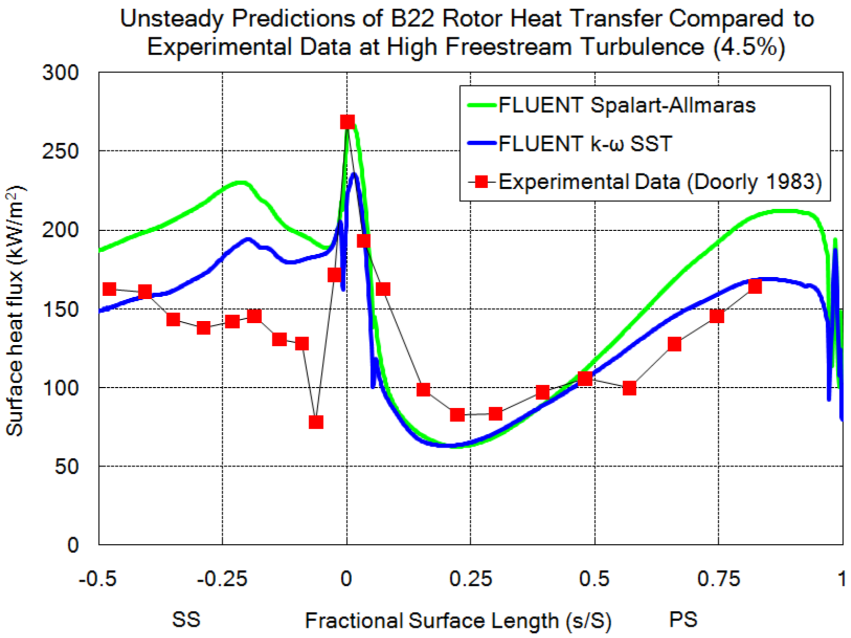

Figure 5.11: Comparison of time-averaged B22 rotor surface heat flux (4.5%) Tu for FLUENT predictions and experimental data from Doorly (1983)

models continued in the study of unsteady B22 heat transfer. The time-averaged rotor surface heat flux distributions subjected to bar-passing and freestream turbulence intensity of 4.5% for both the FLUENT predictions and the experimental data are shown in Figure 5.11. The quality of the predictions is consistent with previous validation studies in the last chapter. In the turbulent regions of the blade-boundary-layer, the prediction for the $k-\omega$ SST model is accurate to within 20% of experimental data. In the transitional and laminar portions of the blade on the leading suction surface the prediction is much worse. The Spalart-Allmaras model over-predicts the suction surface heat transfer, as well as the latter pressure surface heat transfer. The two models both tend to under-predict the heat transfer on the leading pressure surface, but capture the trend of the heat transfer distribution along the pressure surface length.

Unlike in the experimental pressure data for the ACE rotor, ensemble-averaged time-history traces of the surface heat flux were not available for the B22 rotor. Figure 5.12 therefore presents the unsteady FLUENT predictions compared to the raw heat flux signals from experimental data in order to compare the levels of unsteadiness along the rotor suction surface. Overall, the trend is for the Spalart-Allmaras model to significantly under-predict the levels of unsteadiness at each suction surface station. The $k-\omega$ SST model appears to match the levels of unsteadiness in the experimental traces on the leading edge and further down the suction surface (29% x/S). At 10% along the suction surface, where the boundary-layer in the experiment switches from laminar to turbulent due to the passing wake, it tends to under-predict the unsteadiness in the heat transfer signal. This behavior is expected, since the transition in boundary-layer state would not occur in the fully turbulent numerical solution presented here.

After evaluating predictions of surface pressure and heat transfer in both steady and unsteady flow conditions for two rotor profiles, it is possible to now make a judgment regarding the highest performing turbulence model. Out of the four turbulence models originally tested, the Spalart-Allmaras and $k-\omega$ SST turbulence models performed the best in predicting steady flow conditions for the ACE rotor. Subsequently the two models have shown little variation in their ability to predict steady and unsteady surface pressure conditions for the ACE and B22 rotor profiles. However, the consistently superior performance of the $k-\omega$ SST model in providing more accurate predictions of the rotor heat transfer in both steady and unsteady flow strongly supports its use as the sole turbulence model in the remainder of the work. The limitations in the accuracy of predictions from the $k-\omega$ SST model are similar to those limitations seen in the literature, namely lower accuracy in regions of laminar or transitional flow.

When there are sufficient levels of freestream turbulence intensity to trip the boundary-layer on the B22 rotor surface, the $k-\omega$ SST model shows the ability to not only capture the trends in B22 heat transfer, but explain the mechanisms driving change in rotor heat transfer. For example, experimental results showed that when the rotating bar was swept upstream of the rotor along with freestream turbulence intensity levels at 4.5%, the time-averaged heat flux on the leading 30% of the rotor suctions surface was decreased (Figure 5.13).

The cause of this decrease was poorly understood in the original experiment, but a closer examination of the flow around the passing bar illustrates a possible mechanism for this time-averaged reduction in heat transfer. In the bar relative reference frame, the flow approaching the cylinder accelerates as it passes over curved cylinder surfaces, generating a Prandtl-Meyer expansion fan (Figure 5.14). According to isentropic flow

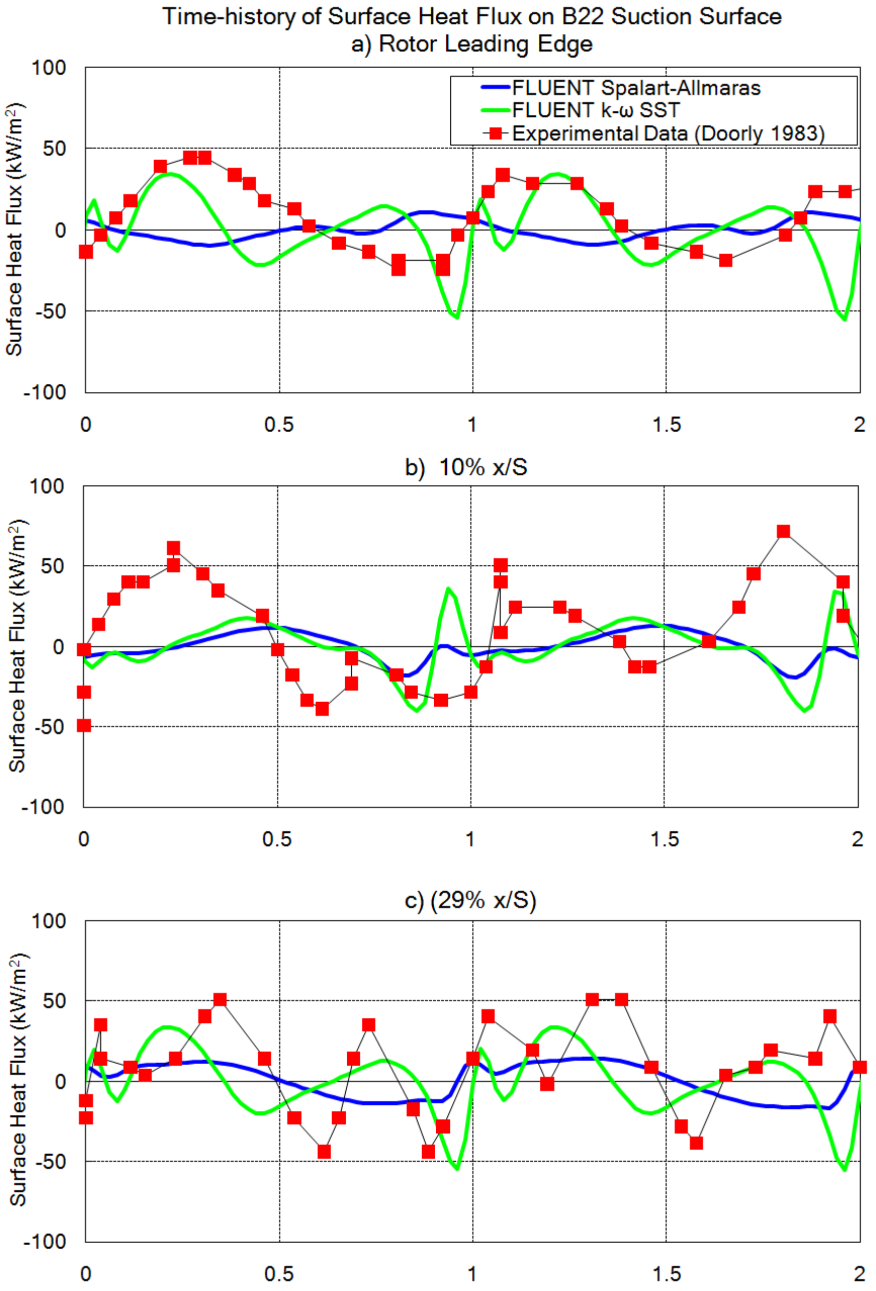

Figure 5.12: Comparison of time-resolved heat flux traces at three locations on B22 suction surface showing FLUENT predictions and experimental data from Doorly (1983)

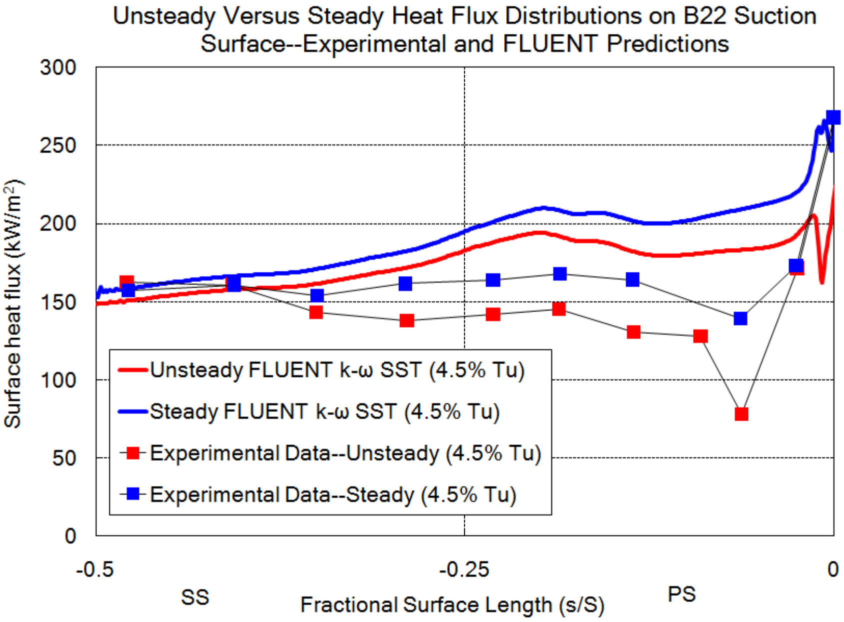

Figure 5.13: Effect of unsteady rotating bar on leading suction surface heat transfer at 4.5% Tu

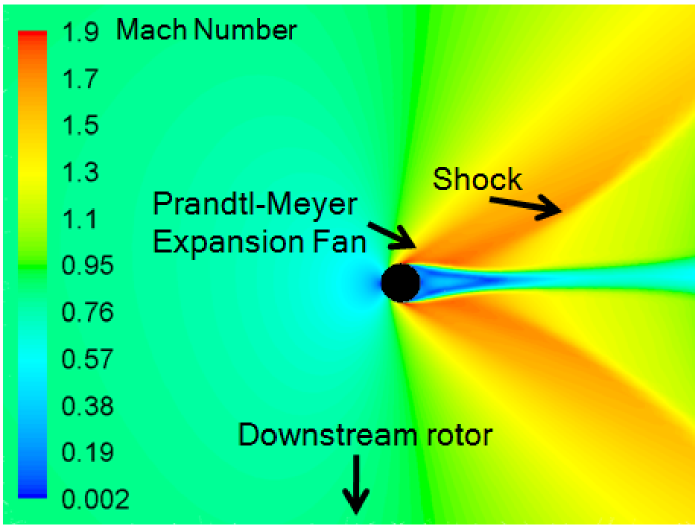

Figure 5.14: Flow features of a cylinder subjected to transonic cross-flow conditions

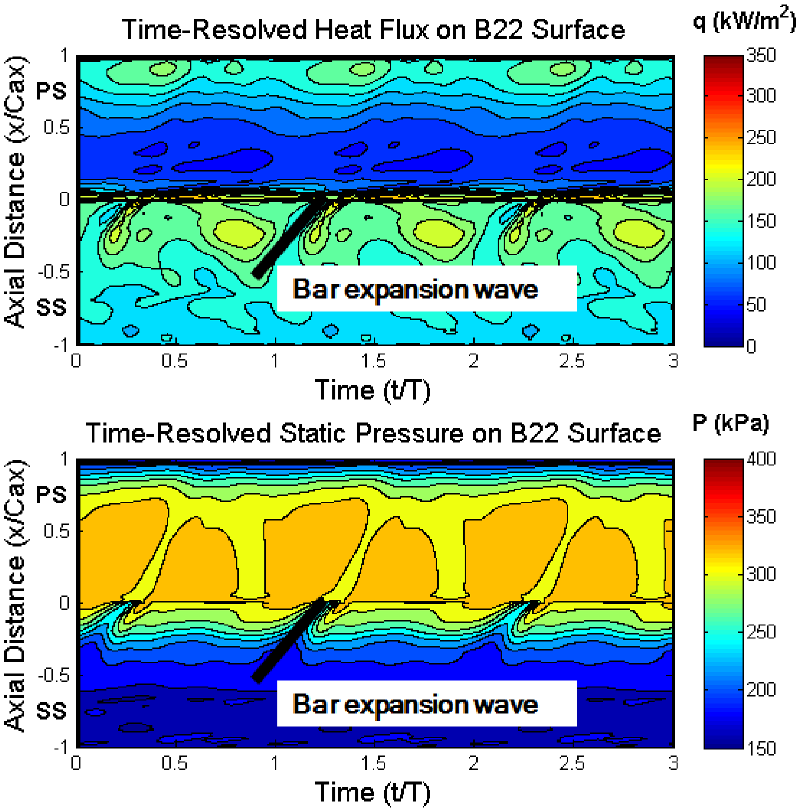

Figure 5.15: B22 surface distributions of heat flux (upper) and pressure (lower) highlighting effect of passing bar on leading suction surface heat transfer

relationships, this increasing Mach number results in a lower fluid temperature ahead of the bar recompression shock:

$$\frac{T_0}{T} = (1 + \frac{\gamma - 1}{2} M^2) \tag{5.1}$$

Given the transonic flow conditions for the passing bar, the expectation is that this expansion fan would show as a strong simultaneous reduction in both the heat flux and pressure signal on the rotor leading suction surface. Figure 5.15 shows the time-resolved surface heat flux (upper) and static pressure (lower) distributions on the B22 rotor leading suction surface over three bar passing periods. The suspected phasing of the passing expansion fan (shown as the blue trough in the pressure history) and the decrease in the surface heat flux does in fact exist.

5.5 Summary

In this chapter unsteady flow validation studies were conducted for two HPT rotor profiles subjected to passing bar wakes and shocks simulating an HPT first stage. The numerical solutions were able to capture all of the unsteady phenomena generated by the passing bar in the ACE simulation, including the shock-induced separation bubble on the pressure surface. During these studies, a comparative analysis of the performance of the Spalart-Allmaras and $k-\omega$ SST turbulence models was continued from the previous chapter. The turbulence models showed little sensitivity in their ability to predict both time-averaged and unsteady surface pressure. This result agreed with the trends in performance of the models in steady flow for the same rotor profile.

When these two models were used to predict unsteady B22 rotor heat transfer, the $k-\omega$ SST model demonstrated higher accuracy for both the time-averaged and unsteady heat transfer as compared to the Spalart-Allmaras model. This trend was also found in the steady flow validation chapter. The superior capabilities of the $k-\omega$ SST model in predicting both steady and unsteady heat transfer for the two rotor profiles led to the decision to use it exclusively in the remainder of the thesis. Using the $k-\omega$ SST model to evaluate unsteady B22 heat transfer identified the expansion wave attached to the high-speed passing bar as the mechanism behind the surprising reduction in time-averaged frontal suction surface heat transfer as compared to steady flow conditions.

Overall, these steady and unsteady validation studies have established a high level of confidence in the numerical solver's ability to predict the steady and unsteady pressure fields for HPT rotor blade passages. In regions of the boundary-layer where experiments have determined it to be in a fully turbulent state, the model is reasonably accurate in predicting the heat transfer to the rotor surface, with an upper limit in a range of flow conditions and geometries on the order of 20%. The model also is able to consistently capture trends in rotor heat transfer subjected to varying levels of freestream turbulence in steady flow, as well as variation between steady and unsteady flow. Therefore, the model is expected to be able to accurately respond to the non-uniform inlet flow conditions presented in the next chapter.

Chapter 6

Non-Uniform Turbulence Effects on 2D Nozzle Guide Vane Heat Transfer

6.1 Introduction and Overview

Following the validation studies of the ACE and B22 rotor profiles in the previous two chapters, it is instructive to pause and re-frame the fundamental question posed in this thesis: namely, can non-uniform circumferential distributions of turbulence intensity at the combustor exit influence turbine blade heat transfer? As noted in the literature review, the turbulence intensity at the combustor exit can potentially vary 60% about the circumferential average (Heitor and Whitelaw, 1986). Additionally, it has been shown that variation in uniform freestream turbulence can affect vane heat transfer (Ames et al., 2003b) even at elevated levels of freestream turbulence. In this chapter numerical simulations will attempt to bridge the gap between these two concepts by providing predictions of non-uniform turbulence intensity distributions' effects on a 2D nozzle guide vane geometry.

In the previous two chapters, the $k-\omega$ SST turbulence model has demonstrated consistently higher accuracy in predicting absolute levels of turbine blade heat transfer. Therefore, it will be the exclusive turbulence model of choice in the remainder of this thesis. The first portion of this chapter will provide a final validation study of this turbulence model to evaluate its effectiveness in predicting turbulence propagation through a nozzle vane passage similar in design to the heat transfer vane studied later in the chapter (Section 6.2). Section 6.3 describes the validation study for the heat transfer vane, and Section 6.4 presents the refined HTC calculation to account for the non-uniform inlet conditions and the development of the non-uniform inlet conditions themselves. Section 6.5 evaluates the effect of the non-uniform inlet distributions on the nozzle vane heat transfer, and Section 6.6 presents the effects of these distortions on the vane exit turbulence intensity distributions. Finally, the results are summarized in Section 6.7.

6.2 Turbulence Propagation Through a Turbine Blade Passage

As a prerequisite to the evaluation of inlet turbulence distortions effects on 2D NGV heat transfer, it was necessary to first validate the ability of the $k-\omega$ SST model to predict turbulence propagation through a turbine blade row. Complete sets of high fidelity, detailed turbulence measurements in turbine representative geometries were of limited availability in the literature. Ames (1994) provides a full range of detailed measurements for the NASA C3X vane geometry in a linear cascade. The C3X vane is a transonic, HPT vane with a similar flow exit angle to the heat transfer vane used later in the chapter; thus, the results could be reasonably translated between the two domains. The study tested four inlet turbulence conditions including the ambient tunnel conditions, a turbulence grid generating 8% turbulence intensity, and two combustor representative geometries producing large length scale and high turbulence intensity (8% and 12%) uniform turbulence fields upstream of the vane. Although the original C3X flow regime is transonic, the experimental vane exit Mach number in this case was 0.27. Therefore, there is large acceleration on the leading portion of the vane suction surface followed by rapid deceleration, which promotes the possibility of boundary-layer separation between 30% and 50% suction surface length. The Reynolds number based on exit conditions and vane axial chord was $8 \cdot 10^5$. Velocity magnitude, stream-wise and stream-normal velocity fluctuations were reported upstream and downstream of the vane. The experimental downstream measurements were made with an X-wire swept in an arc behind the measured vane trailing edge. The experimental exit turbulence was plotted in the stream-wise and stream-normal $(u-v)$ coordinate frame, using the vane flow exit angle as the stream-wise direction. This method was adopted for the presentation of the numerical results in this section. In order to convert the Cartesian coordinates from the arc to stream-wise and stream-normal coordinates, the author used the flow exit angle $\alpha = 72.38°$ as prescribed by the experimental methods, and performed a coordinate transform using

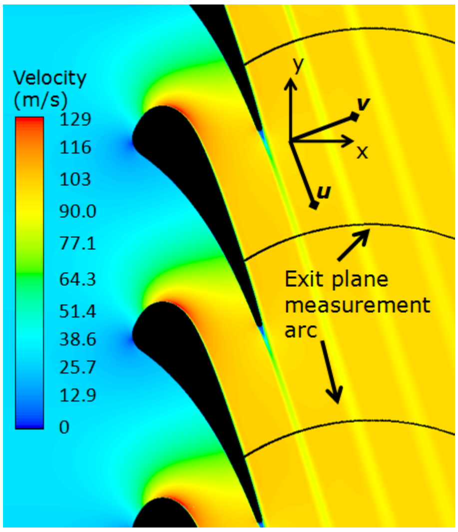

Figure 6.1: 2D velocity contours for C3X nozzle vane highlighting exit measurement arc

Equation 6.1:

$$A = \begin{bmatrix} cos(\alpha) & sin(\alpha) \\ -sin(\alpha) & cos(\alpha) \end{bmatrix} \tag{6.1}$$

The transformed coordinate system was then translated to set the origin at the intersection between the measurement arc and the adjacent vane suction surface. Figure 6.1 displays the C3X computational domain with several periodic repeats in the circumferential direction. The measurement arcs in the figure are centered behind the vane trailing edge, and the original and transformed axes are placed in the freestream exit flow to clarify this process.

The first stage in this turbulence validation study was to establish a grid independent solution. Figure 6.2 presents selected results of this grid dependency study. The figure shows that the "fine" grid of around $3 \cdot 10^5$ cells produced a grid-independent solution. Comparing this curve to the experimental data shows an excellent prediction of the vane surface Mach number distribution (Figure 6.3). Meanwhile, the turbulence field in the freestream demonstrated insensitivity to the level of grid refinement.

Initial solutions for the grid-generated inlet turbulence intensity poorly predicted both the turbulent kinetic energy and the specific dissipation rate at the exit to the C3X vane row, thereby necessitating a closer examination of the turbulence parameters at the inlet to the computational domain. As mentioned previously, the $k - \omega$

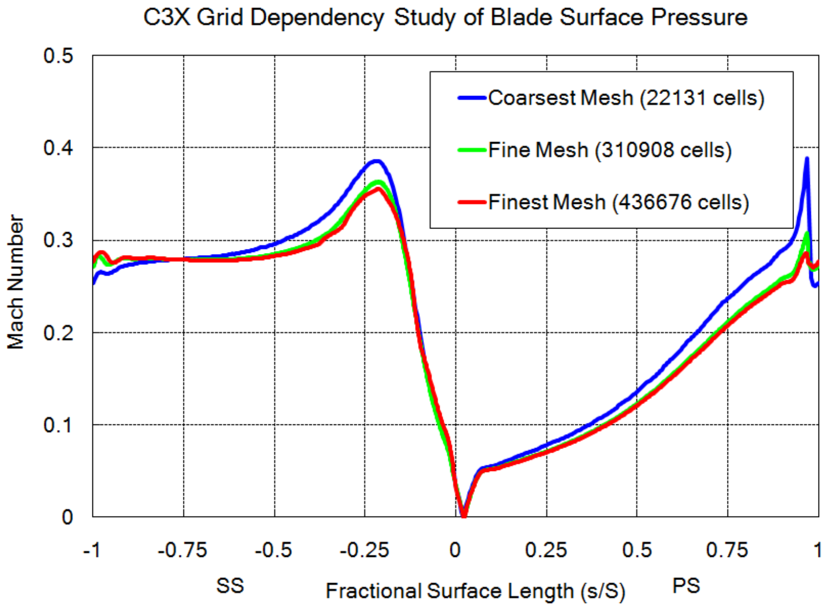

Figure 6.2: C3X grid dependency study for vane surface isentropic Mach number distribution

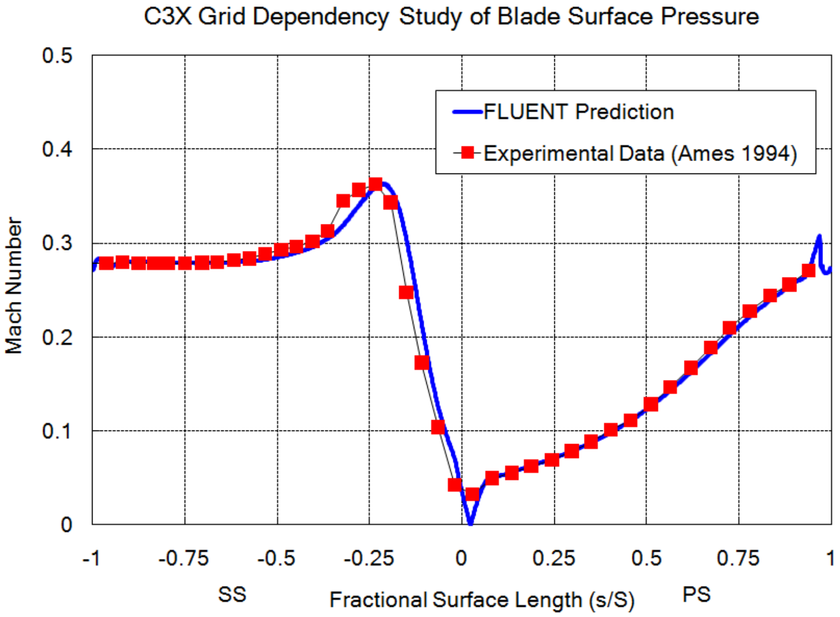

Figure 6.3: Comparison of C3X vane surface Mach number for fine grid FLUENT prediction and experimental data from Ames (1994)

SST model accepts inputs in the form of turbulence intensity and turbulence length scale. These two quantities are then converted to the turbulent kinetic energy k and specific dissipation rate ω via the following relationships (ANSYS, 2006):

$$k = 1.5(V \cdot Tu)^2 \tag{6.2}$$

$$\omega = \frac{\sqrt{k}}{C_\mu^{0.25} l} \tag{6.3}$$

where the turbulence length scale is again analogous to the integral length scale (i.e. $l \approx \Lambda$). It is also possible to input k and ω directly into the inlet boundary condition in FLUENT. In the experiment, the averaged velocity fluctuations and the turbulence dissipation rate are reported, making direct calculation of these two turbulence parameters possible. In order to tune the model, two corrections are made to the above equations, and consistently employed in the remainder of the thesis. The first correction deals with the relationship for the turbulent kinetic energy k. The above equation for k assumes that the fluctuating velocities in the turbulence field are equal (isotropic turbulence), which results in Equation 6.4:

$$1.5(V \cdot Tu)^2 = 1.5\overline{(u')^2} = 0.5[\overline{(u')^2} + \overline{(v')^2} + \overline{(w')^2}] \tag{6.4}$$

The computational domain in this study is 2D, therefore the bi-normal (w) velocity fluctuations do not contribute to the turbulent kinetic energy and can be dropped from the above equation. After calculating k from the experimental measurements, the next correction focused on the calculation of ω. Per the recommendations from the solver documentation, the bar diameter for the grid generated turbulence (12.82mm) was used to estimate Λ, and the calculated k from the experiment using the velocity fluctuations u' and v' was combined with Λ to determine ω from Equation 6.3. This value was then compared to the experimental results for the turbulence dissipation rate ϵ. The relationship of both ω and ϵ to the turbulent viscosity μ_t (shown in the below equations) made a direct comparison possible (ANSYS, 2006):

$$\omega = \rho \frac{k}{\mu_t} \tag{6.5}$$

$$\epsilon = \rho C_\mu \frac{k^2}{\mu_t} \tag{6.6}$$

Rearranging these equations results in the following for ω:

$$\omega = \frac{\epsilon}{C_\mu k} \tag{6.7}$$

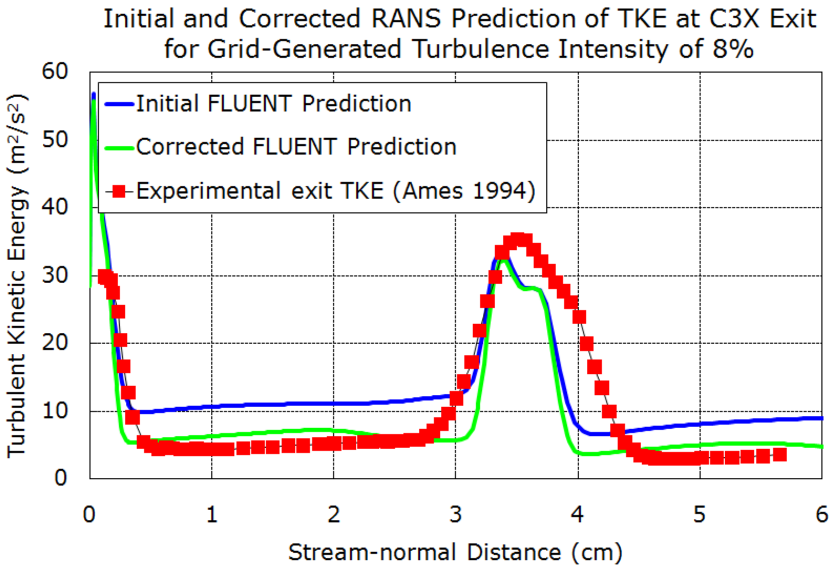

Figure 6.4: Initial and corrected exit turbulent kinetic energy compared to experimental data for grid-generated freestream turbulence

After comparing the results for ω based on the turbulence grid geometry and the actual experimental results, the geometry-based value of ω was much lower. The solution was to apply a linear coefficient to Equation 6.3 for the calculation of ω to correct the inlet conditions to match experimental measurements. This coefficient was equal to the ratio of the experimental and geometry derived values of the specific dissipation rate. Only the grid-generated turbulence inlet condition was used to develop this coefficient as the experimental combustor-generated turbulence data exhibits a high degree of anisotropy at the inlet, and it was expected this would add additional error to the tuned turbulence model rather than create a more robust correction. The final tuning of the model therefore consists of slight modifications to the definitions of k and ω at the inlet to the computational domain:

$$k = 0.5[\overline{(u')^2} + \overline{(v')^2}] \quad (6.8)$$

$$\omega = \frac{\sqrt{k}}{AC_\mu^{0.25} l} \quad (6.9)$$

$$A = .118$$

Figure 6.4 presents the original and corrected FLUENT predictions of turbulent kinetic energy along the measurement arc and compared to the experimental results. In the core flow, k is well predicted. The simulations were conducted using steady flow assumptions, therefore the wake width is under-predicted. Additionally, the turbulence in the wake is far more dependent on the local turbulence generation due to the separating boundary-layer at the trailing edge than freestream conditions, so it is of lesser concern in determining the effectiveness of turbulence model tuning. The corrected modelling was also expanded to the two combustor-generated turbulence conditions as well. Figure 6.5 compares the experimental results to the combustor configuration with generated turbulence intensity levels in the freestream of about 8%. This is a similar intensity to the grid-generated turbulence, but with a much larger length scale. The lower passage on the left hand side of the chart shows an over-prediction of the turbulent kinetic energy, but good accuracy in the upper passage. Figure 6.6 is the combustor configuration with turbulence intensity of 12.1%. The accuracy in the prediction trends similarly to that of the lower Tu combustor configuration, but overall over-predicts the core flow. The relative accuracy of the predictions in the core flow reflects the physics of the experimental flow as well. Namely, the accuracy of the FLUENT predictions was higher when the turbulence exhibited lower anisotropy in the vane exit plane. Lower anisotropy tended to occur experimentally further downstream of the C3X vanes, which explains why the upper passage flows tend to be more accurate for the all three inlet turbulence conditions. The grid-generated turbulence had the lowest degree of anisotropy in the exit turbulence, and the 12.1% Tu combustor turbulence exhibited the strongest anisotropy of the three configurations. Predictably, the grid-generated turbulence and 12.1% Tu combustor inlet turbulence conditions were the most accurate and least accurate predictions, respectively.

The reliability of the tuned FLUENT model in predicting the propagation of low-anisotropy turbulence through the C3X vane passage provides confidence for the evaluation of non-uniform turbulence distributions with the current numerical methodology. In the next section, a final validation study of the heat transfer vane will set the stage for the main focus of the research.

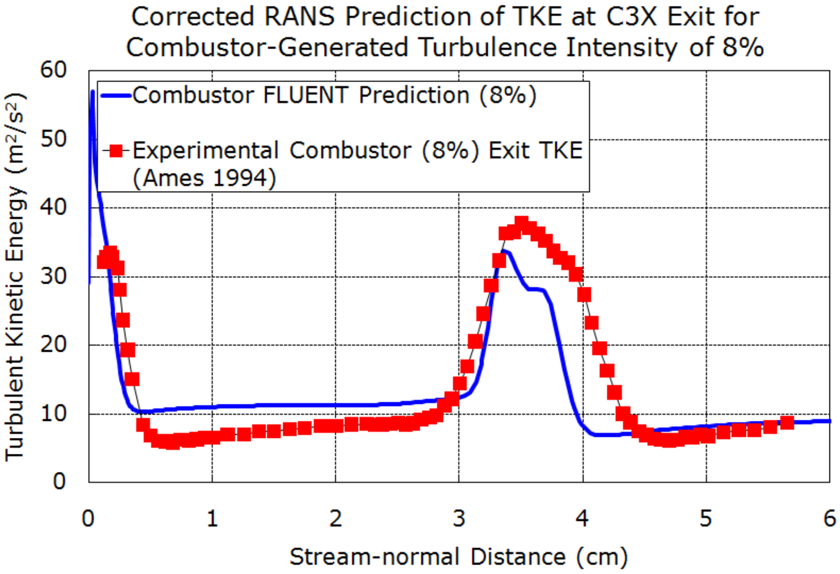

Figure 6.5: Corrected exit turbulent kinetic energy compared to experimental data for combustor-generated freestream Tu of 8%

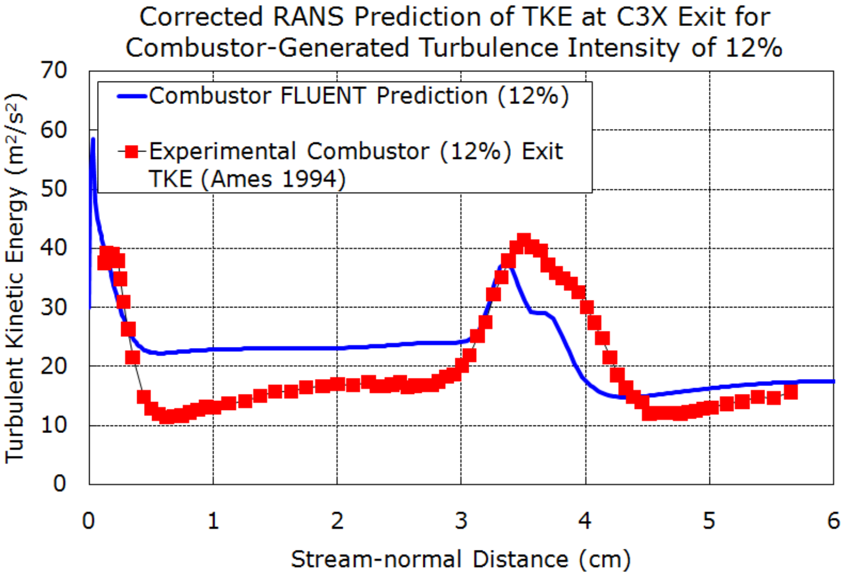

Figure 6.6: Corrected exit turbulent kinetic energy compared to experimental data for combustor-generated freestream Tu of 12.1%

6.3 2D Nozzle Blade Steady Flow Validation

The vane selected for the heat transfer tests is the B23 nozzle guide vane. The experimental data used for validation is from Nicholson (1981). The isentropic exit Mach number is 0.93, and the exit Reynolds number based on axial chord was $2.63 \cdot 10^6$. The gas to wall temperature ratio was 1.5 and the grid-generated freestream turbulence was 4.5%. Similar to the previous studies, a grid dependency study was conducted for both the vane surface isentropic Mach number and the surface heat transfer. Heat transfer will be presented as the raw heat flux to the vane surface as in the experimental results. This reporting convention will maintain consistency with the heat transfer results presented later in the chapter.

Once again a grid dependency study was conducted for the computational domain. Figure 6.7 shows the fairly strong independence of the pressure field to increasing grid density.

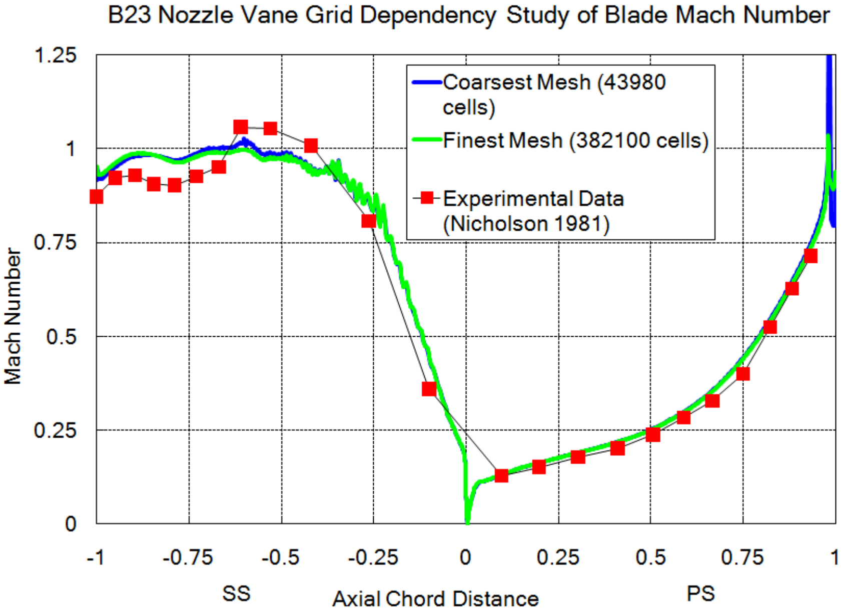

Figure 6.7: B23 grid dependency study for vane surface isentropic Mach number distribution, including experimental data from Nicholson (1981)

Although multiple grids were evaluated, only the coarsest and finest grids representing a cell count ratio of almost 5:1 are presented in the figure, and they show little variation in the surface Mach number distribution. Included in this chart are the experimental results for comparison. The pressure surface is well predicted, and

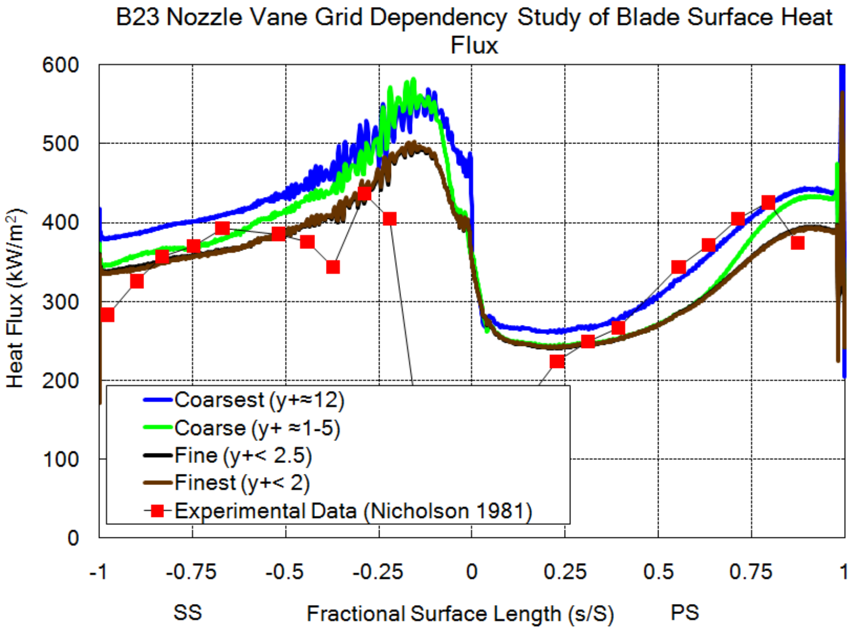

Figure 6.8: B23 grid dependency study for vane surface heat flux distribution, including experimental data from Nicholson (1981)

the suction surface up to approximately 0.5 C_{ax} also shows good agreement with experimental results. After this point, the data somewhat falls off. This behavior has been demonstrated previously (Sheard, 1989), and is thought to be due to the difference in profile definition. The geometry here is the constant streamline profile of the B23 vane at mid-span, whereas the profile in Nicholson's work is at a constant radius. The result is a less-strongly defined shock impacting near mid-chord on the suction surface. However, the overall prediction falls within 10% of the experimental results along the blade, even on the latter suction surface.

Figure 6.8 illustrates the grid dependency study for the vane heat transfer. At the wall y^+ decreased with increasing cell count to less than 2 for the highest density grid. There was gradual independence of the solution as the grid density increased, and at a resolution higher than the "fine" grid there was no change in the predicted surface heat transfer distribution. The figure also presents the experimental distribution of heat transfer on the vane surface (Nicholson, 1981). The prediction is accurate to within 15%, except near the leading edge. In the experiment the boundary-layer on the vane was laminar up to 0.2 to 0.25 C_{ax} on both the pressure and suction surfaces, this accounts for the large error in the prediction in this region of the vane, as the numerical solutions were fully turbulent.

6.4 Methods for Non-Uniform Inlet Boundary Conditions and Calculating Turbine Blade Heat Transfer Coefficient

6.4.1 Inlet Boundary Conditions

The baseline configuration for the HTC studies employed identical boundary conditions to the validation case in Nicholson (1981), with the exception of elevating the freestream turbulence intensity to 10% to align the turbulence levels to engine-realistic conditions. The added benefit for this increase in freestream turbulence was that in an experimental setup, such a high level of freestream turbulence would control the laminar and transitional regions of the vane boundary-layer. Since the $k - \omega$ SST model performed reasonably well in predicting turbulent boundary-layer heat transfer, this will increase confidence in the predictive capability of the solver. The turbulence length scale was not changed. An important element of this study involved analyzing the contribution of the non-uniform inlet turbulence profiles in the presence and absence of hot streaks. In the 2D computational domain in this chapter, these inlet temperature distortions were represented as sinusoidal curves along the inlet boundary that were circumferentially averaged to match the uniform flow condition. The pitch-wise location of these curves was then translated, or “clocked” at intervals of 25% of the blade pitch in order to determine the range of NGV heat transfer response to the position of the “peaks” and “troughs” of the inlet distortions. An idealized illustration of this concept for the two temperature distortion to NGV blade count ratios tested (1:1 and 1:2) is presented in Figure 6.9. The positions “0 y/Y” and “1 y/Y” represent the distortions placed directly upstream of the NGV leading edge, and the position “0.5 y/Y” is the middle of the NGV passage. In each of the clocking positions tested for temperature distortions, the ratio of the maximum to minimum total temperature at the inlet was 1.1. After establishing the inlet temperature profiles, the procedure for generating the turbulence at the inlet to the domain is as follows:

- Generate converged solutions for each inlet temperature distortion clocking position in order to provide the velocity field for the domain,
- Export the cell-centered velocity values at the inlet boundary and apply turbulence intensity distribution to the velocities to generate the inlet turbulence

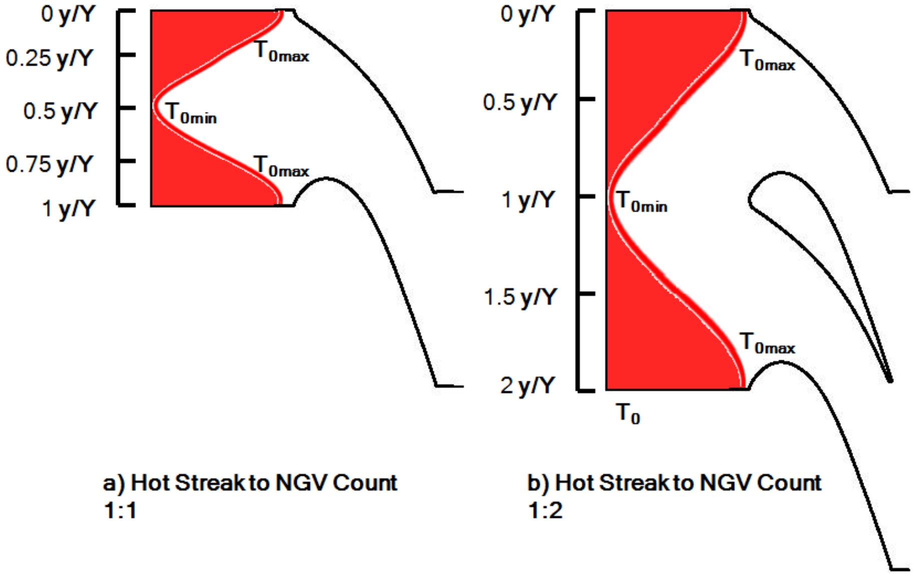

Figure 6.9: Illustration of sinusoidal inlet distortion and various clocking positions for two distortion:NGV count ratios

distribution based on these relationships:

$$\begin{aligned} k &= (V \cdot Tu)^2 \\ \omega &= \frac{\sqrt{k}}{AC_\mu^{0.25} l} \end{aligned}$$

- Re-run the solutions with finalized inlet turbulence conditions.

Two inlet turbulence distribution profile shapes were tested, uniform and sinusoidal. The non-uniform inlet turbulence profile varied between 7% and 13%. Two additional amplitudes of the turbulence profile were tested as well with the uniform inlet temperature only, with turbulence intensity ranges of 6.25% to 13.75% and 7.75% to 12.25%. In simulations with a temperature distortion at the inlet, the turbulence profile at the inlet was aligned in phase with the temperature profile. This positioning was chosen due to the relative positioning between the temperature and turbulence peaks seen experimentally in Heitor and Whitelaw (1986). The final inlet total temperature profile and baseline inlet turbulence profile for the clocking position upstream of the vane leading edge are available in Figure 6.10 to help illustrate the inlet conditions. A detailed description of the inlet profile development is available in Appendix B. A complete summary of the inlet flow configurations is available in Figure 6.11.

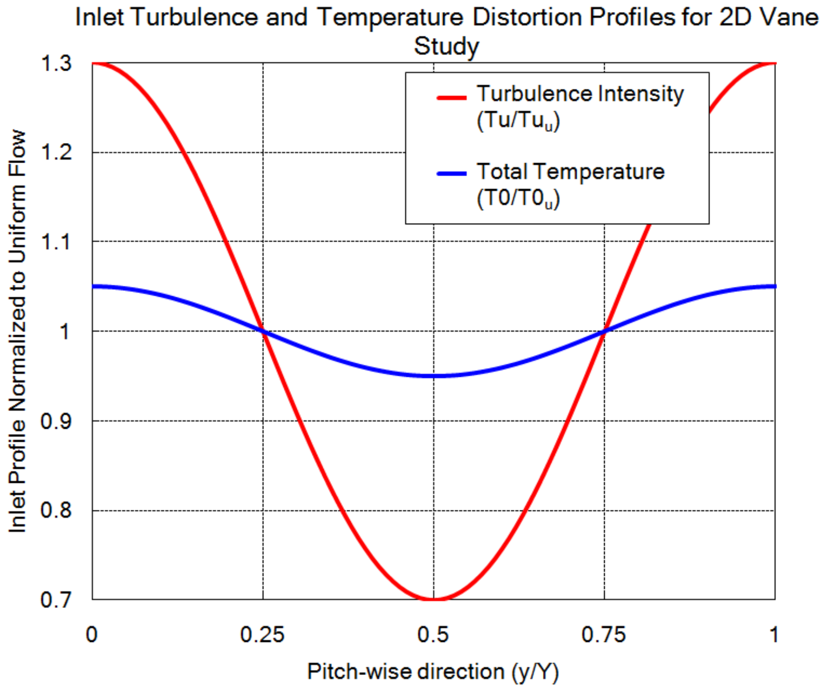

Figure 6.10: Inlet total temperature and turbulence intensity profiles for 2D vane study at single clocking position

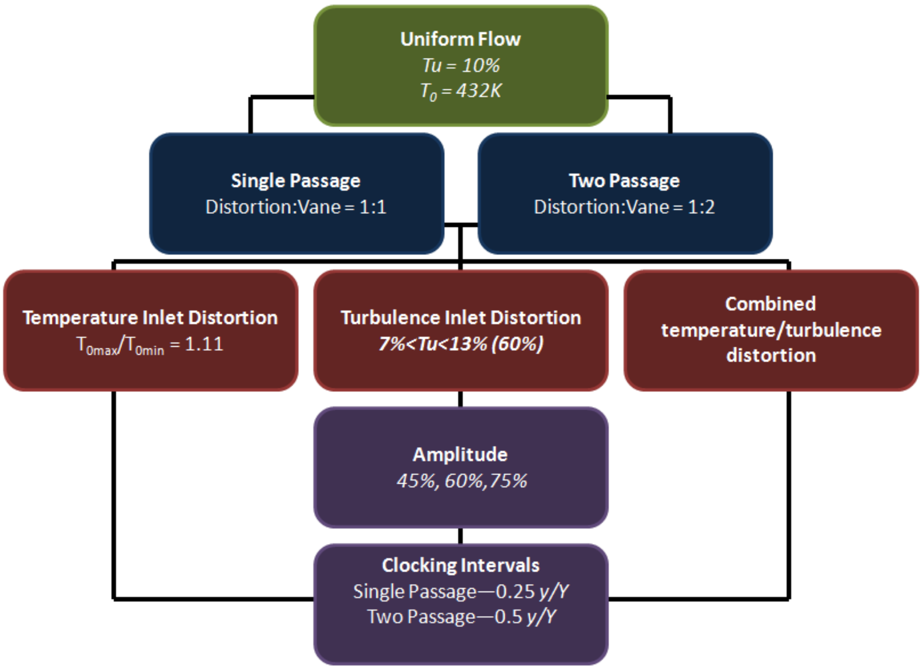

Figure 6.11: Summary map of inlet variations for the 2D nozzle blade

6.4.2 Calculating Heat Transfer Coefficient

Heat transfer results in this chapter are presented as surface heat flux, $\dot{q}$, adiabatic wall temperature T_{aw}, and convective HTC, h. The method for obtaining these values is to generate two converged solutions for the flowfield using two isothermal wall boundary conditions for the blade surfaces. The resulting pair of surface heat fluxes and known wall temperatures are then fed into a system of two convective heat transfer equations to solve for T_{aw} and h:

$$\dot{q}_1 = h(T_{aw} - T_{w1}) \tag{6.10}$$

$$\dot{q}_2 = h(T_{aw} - T_{w2}) \tag{6.11}$$

Initially a range of four wall temperatures were used to calculate multiple HTC distributions along the blade surface. The aim was to ensure that the HTC was in fact locally linear for the wall temperature pair tested. Figure 6.12 presents three HTC distributions over the surface of the B23 vane. The variation between the three curves is less than 1% over the entire surface, except for the region of the suction surface just past 0.5 C_{ax}. In this region of the blade, all three distributions display an oscillatory behavior.

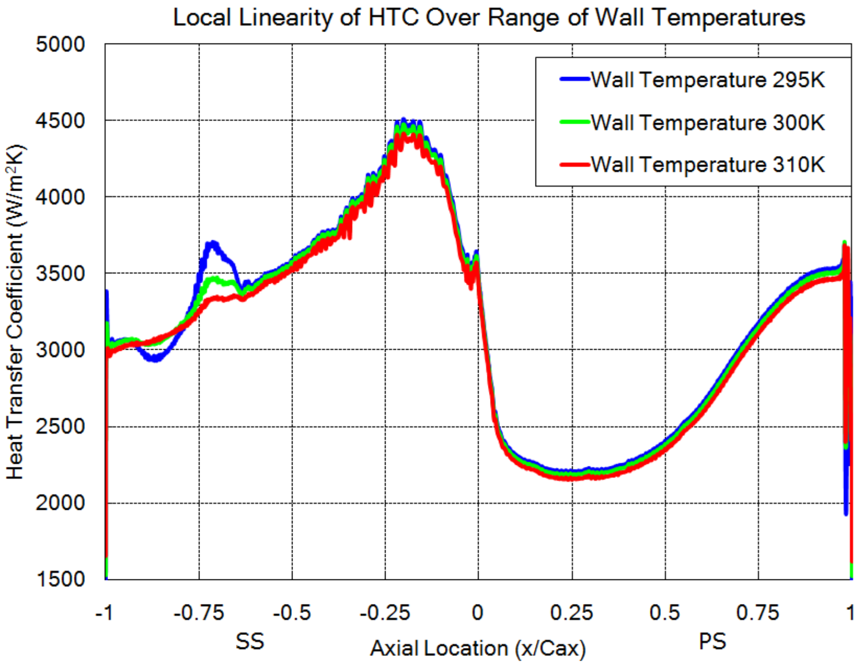

Figure 6.12: Range of calculated vane HTC distributions highlighting local linearity effect

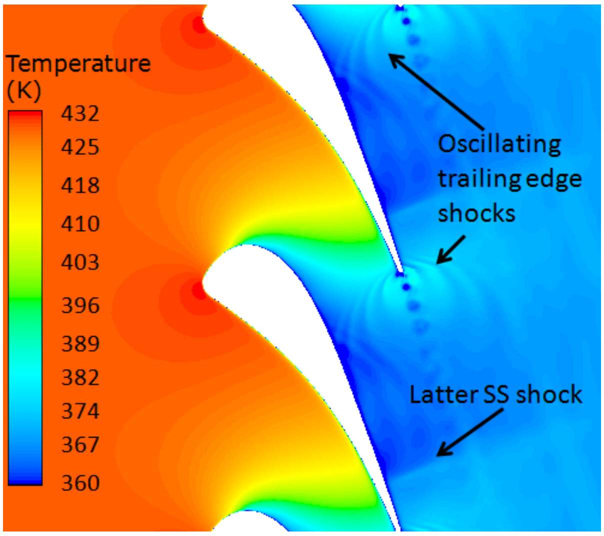

Figure 6.13: Cross-passage propagation of pressure waves due to TE vortex shedding on the 2D vane

The reason for this oscillation is the nature of the flowfield at the vane throat. At the transonic exit conditions for the NGV blade row, the trailing edge shock structure is highly sensitive to perturbations in the local velocity field. Nearby the location where the shock forms, the boundary-layer separates at the vane trailing edge and sheds vortices which form into the NGV wake (the von Karman vortex street). These eddies are in close enough proximity to the shock to cause it to form and disappear, and result in propagating pressure waves emanating from the NGV trailing edge (Figure 6.13). This complicates the calculation of the local adiabatic wall temperature and the heat transfer coefficient, as the unsteady surface heat flux subject to these propagating pressure waves can result in anomalous fluctuations on the order of 10% of the mean local heat flux on the latter suction surface of the adjacent NGV. Furthermore, the presence of inlet temperature distortions exacerbated this oscillatory behavior.

In order to eliminate the oscillations, second order time-accurate unsteady flow simulations with approximately 30 time steps per vortex shedding period for the steady flow condition were conducted. The data was then exported for 100 time steps after the solution reached a converged steady-state oscillation. A discrete FFT script was written in MATLAB to determine the exact vortex shedding period from the data. The reasoning behind this individual calculation of the vortex shedding period for each inlet condition was that the inlet temperature distortions were expected to slightly vary the vortex shedding frequency due to the change in vane exit Reynolds number. Averaging the surface heat flux at each wall-adjacent cell-centroid on the blade surface allowed for recalculation of the surface heat transfer coefficient. The resulting HTC distributions still showed oscillation in this region of the blade, indicating that at these flow conditions there is a slight coupling of the wall thermal boundary condition and the aerodynamic flowfield. This region of the latter suction surface in these flow conditions tends to remain within 1% of $M = 1$ and is again very sensitive to even slight changes in the flowfield; therefore, this coupling is not unexpected. The result however, is that the assumption of constant HTC will break down where the Mach number is very close to unity.

Fortunately, preliminary investigation of the HTC distributions from the non-uniform inlet conditions indicated that the primary variation on the vane surface was near the vane leading edge, and therefore the results in the remainder of this chapter will be truncated at 0.5 C_{ax} for the sake of clarity. A final check of the numerical methods was to ensure that the two passage and single passage computational domains did not demonstrate variation in the HTC results. Figure 6.14 confirms that all three vanes in the two computational domains are identical, which establishes confidence in making comparisons between them.

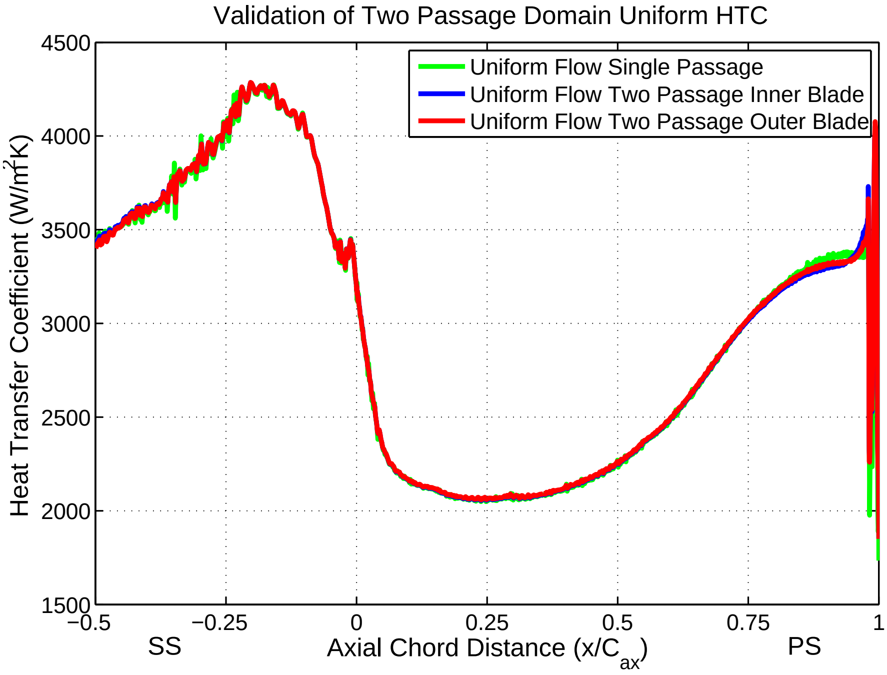

Figure 6.14: Comparison of single passage and two passage vane HTC distributions

6.5 Effects of Turbulence Distortion on B23 Heat Transfer

6.5.1 Single Passage

The first series of tests used only the non-uniform inlet turbulence intensity profile with turbulence intensity ranging from 7% to 13%. Four clocking positions were evaluated at intervals of 0.25 Y. Figure 6.15 provides the vane HTC, surface heat flux, and adiabatic wall temperature distributions. The two clocking positions align the turbulence “peak” such that it impinges directly on the vane leading edge and then directly into the middle of the passage. The peak augmentation relative to the uniform flow condition for the vane surface occurs on the pressure surface side of the leading edge at the stagnation point, and is predicted to be 17.3% when the peak is shifted from the vane leading edge to the middle of the passage. Along the pressure surface the variation in vane HTC is greater than 10% up to 0.25 C_{ax}, and above 5% until 0.5 C_{ax}. On the suction surface this 5% threshold is reached around 10% C_{ax}. In the lower left-hand plot, the surface heat flux also varies according to the trends seen in the vane HTC distributions. As is expected, the adiabatic wall temperature does not vary in the presence of the non-uniform inlet turbulence distortion.

Two additional clocking positions with the turbulence peak at 0.25 Y above and below the vane leading edge were also tested (Figure 6.16). In this configuration, the effect on the vane HTC is minimal, although the trend in augmentation over the blade surface is similar to the peak on blade/peak in passage configuration. Additionally, the relative augmentation trends behave as expected. When the peak is slightly below the leading edge, there is a slight augmentation of the vane HTC on the pressure surface (shown in the red curve). In either of the clocking positions just above or below the vane, the turbulence distortion appears to primarily propagate through the vane passage rather than influence the vane heat transfer environment.

As mentioned previously, two additional turbulence amplitudes were tested at the inlet to the computational domain as well. The shape of the HTC distribution for each turbulence amplitude was the same, with the peak augmentation occurring near the leading edge. The response of the vane HTC to changing amplitude also is in line with expectations, i.e. increasing augmentation is seen for increasing amplitude in turbulence distortion. Table 6.1 presents the summary of peak augmentation effects on vane leading edge HTC relative to the uniform inlet conditions. The important

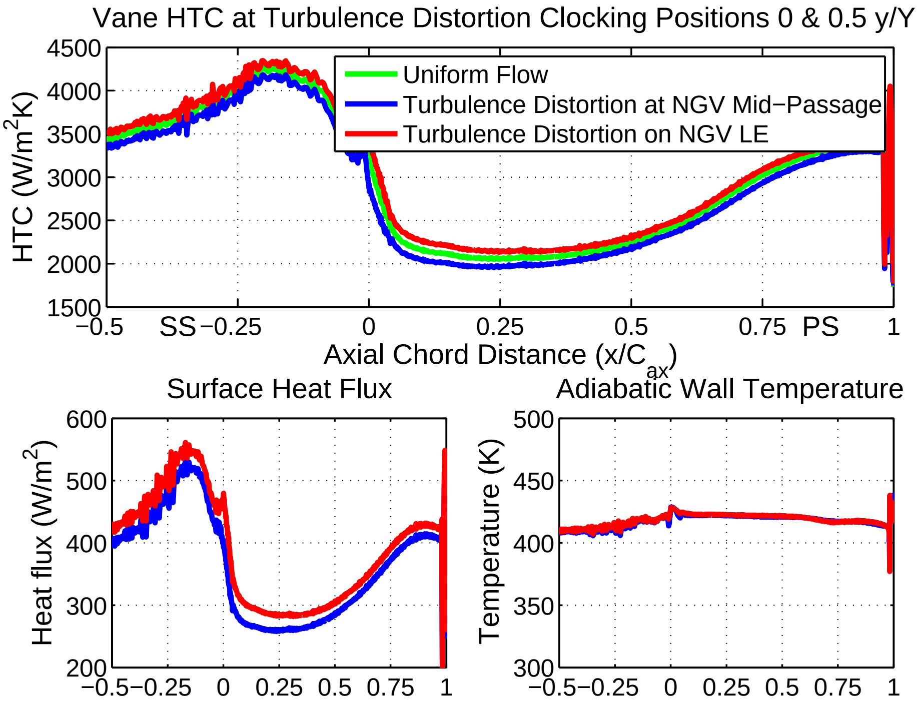

Figure 6.15: Effect of non-uniform inlet turbulence distortion on 2D vane heat transfer at two clocking positions

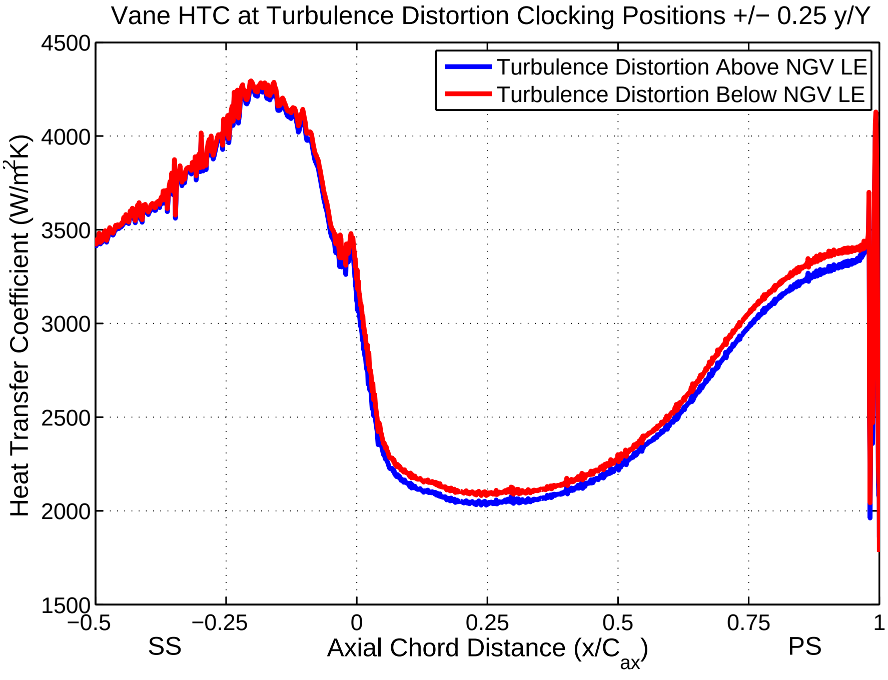

Figure 6.16: Effect of non-uniform inlet turbulence distortion on 2D vane HTC at two offset clocking positions

finding from these tests is that clocking the turbulence peak from the vane leading edge to the middle of the passage produces HTC variation in the range of 12.8% to 21.9% in the range of turbulence distortion amplitudes tested.

Table 6.1: Summary of effects of turbulence distortion amplitude at various clocking positions on 2D vane leading edge HTC augmentation

Amplitude	Peak on Blade	Peak in Passage	Peak below PS	Peak above SS
±22.5%	+6.0%	−6.8%	+1.6%	−1.4%
±30%	+7.8%	−9.5%	+2.2%	−1.8%
±37.5%	+9.5%	−12.4%	+2.8%	−2.5%

The next phase of the study established inlet temperature distortions upstream of the vane. The expectation was that clocking the hot streak would not affect the vane HTC, but rather the adiabatic wall temperature, e.g. Povey et al. (2007)). Figure 6.17 demonstrates that this is the case when the hot streak is clocked from upstream of the vane leading edge to the middle of the vane passage. The slight variation in the vane HTC near mid-axial chord on the suction surface for the hot streak impinging on blade curve is due to the shock-affected regions of the vane surface. The adiabatic wall temperature distributions in the plot on the lower right corner of the figure clearly demonstrates that T_{aw} is almost solely responsible for the variation in surface heat flux due to hot streak clocking.

The inlet temperature distortion was then paired with the baseline non-uniform turbulence profile with turbulence intensities from 7% to 13%. Figure 6.18 presents two clocking positions for this “combined” distortion impinging on the NGV leading edge and into the middle of the NGV passage. The HTC augmentation trend is similar to that of only the turbulence distortion at the inlet to the domain. Clocking between the two positions results in a variation of 20% in HTC on the vane leading edge. To understand the extent of the vane surface HTC distribution affected by the inlet distortions, it is worth noting the combined distortion shows HTC variation of at least 10% through about 0.35 C_{ax} on the pressure surface of the vane. Much like the turbulence distortion, the offset clocking with the combined peak above and below the blade results in lesser of just under 4% near the vane leading edge. Overall the combined distortion effects on the vane HTC and adiabatic wall temperature are

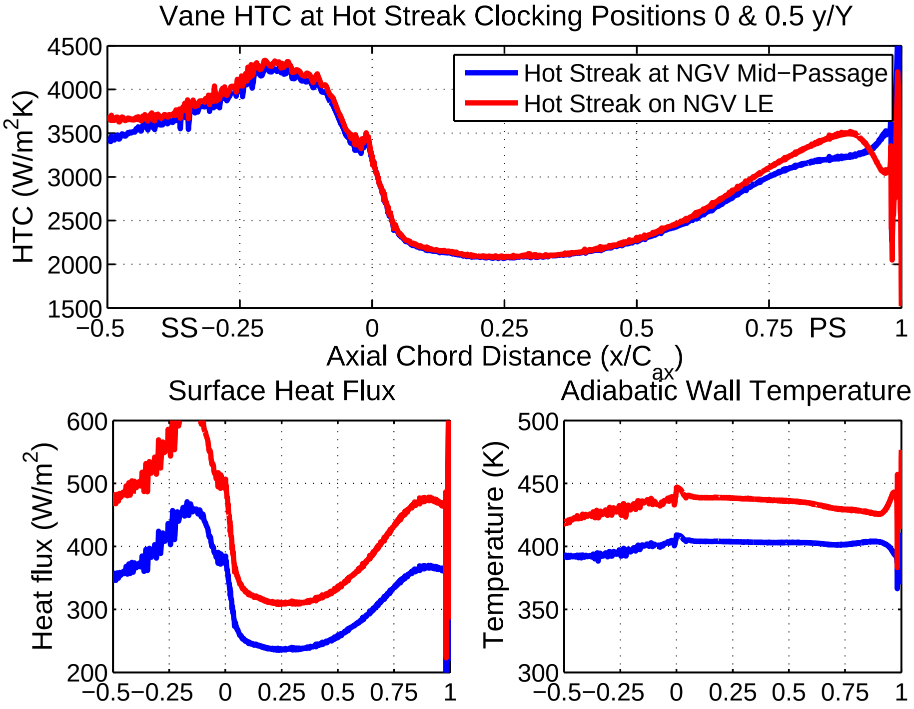

Figure 6.17: Effect of non-uniform inlet temperature distortion on 2D vane heat transfer at two clocking positions

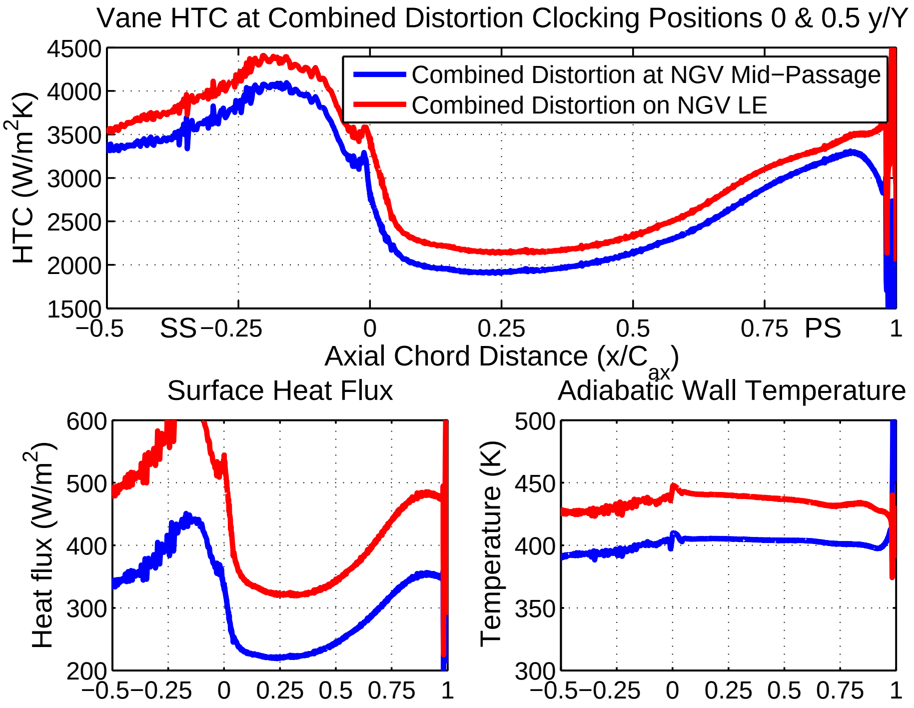

Figure 6.18: Effect of combined inlet turbulence and temperature distortion on 2D vane heat transfer at two clocking positions

primarily driven independently by the turbulence and temperature distortions respectively, resulting in the larger surface heat flux variation than either inlet distortion alone.

6.5.2 Two Vane Passages

A second computational domain was also evaluated, representing a combustor to vane ratio of 1:2. In this case two clocking positions were generated. The first position causes the "peak" and "trough" of the inlet variations to impinge directly onto the vane leading edges. The second clocking position shifts these maximum and minimum values directly into the middle of the vane passages. Overall the results were similar to that of the 1:1 combustor to vane ratio in terms of the vane HTC augmentation. Figure 6.19 presents the two vane HTC distributions for the first clocking position with only the baseline inlet turbulence distortion (varying from 7% to 13%). The peak variation in HTC augmentation is 18%, as compared to about 17.3% for the inlet distortion to NGV count of 1:1 (single passage domain).

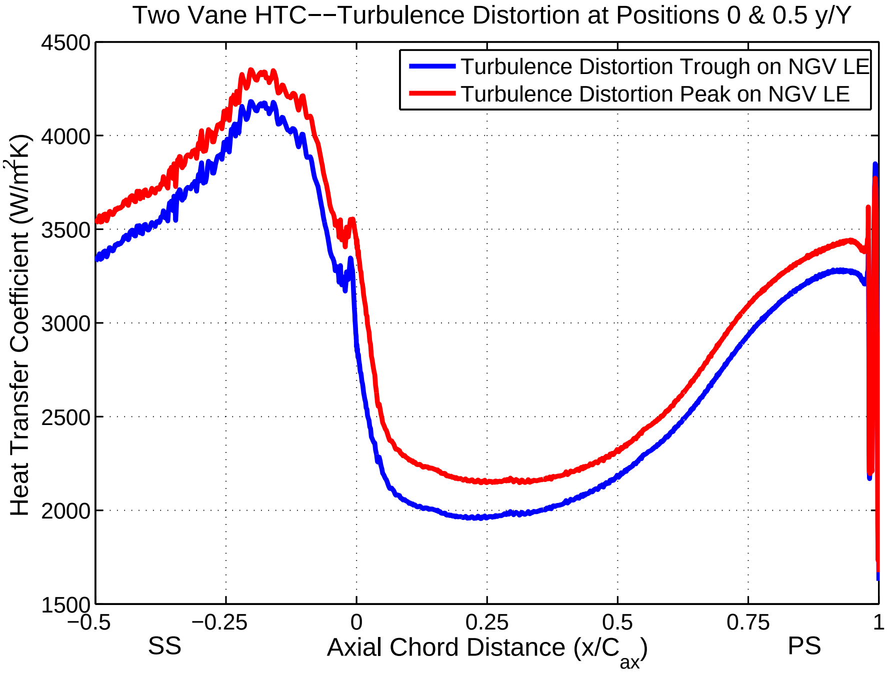

Figure 6.19: Effect of non-uniform inlet turbulence distortion on two passage 2D vane HTC at two clocking positions

Also similar to the single passage domain, the hot streak clocking for the two passage domain shows no influence on the vane HTC (Figure 6.20). Figure 6.21 displays the combined inlet distortions for the two passage domain. Again the effect on leading edge HTC due from vane to vane is significant, showing a variation of 18.5% from peak to trough for the combined inlet distortion. This is nearly identical to the inlet turbulence distortion alone. The turbulence and combined distortions were also clocked offset to the vanes by 0.5 Y to cause the distortions to propagate directly into the vane passages. The maximum variation in HTC from blade to blade was 3% in this clocking configuration.

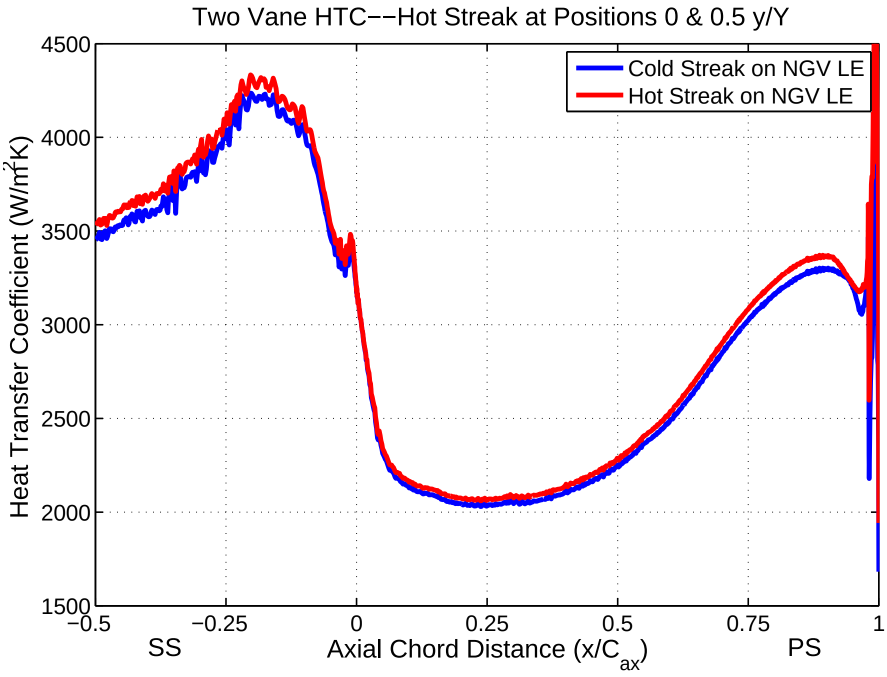

Figure 6.20: Effect of non-uniform inlet temperature distortion on two passage 2D vane HTC at two clocking positions

It is apparent that circumferential variation in inlet turbulence has a significant effect on 2D vane HTC distributions, particularly near the leading edge of the vane. It is interesting to note that the response of the vane HTC to the turbulence was independent of the presence of the inlet temperature distortion. Clocking the baseline inlet turbulence distortion from the leading edge to mid-passage produced the greatest variation in vane leading edge HTC of about 17%. In the two passage case, the clocking position with the peaks and troughs of the sinusoidal inlet distortion

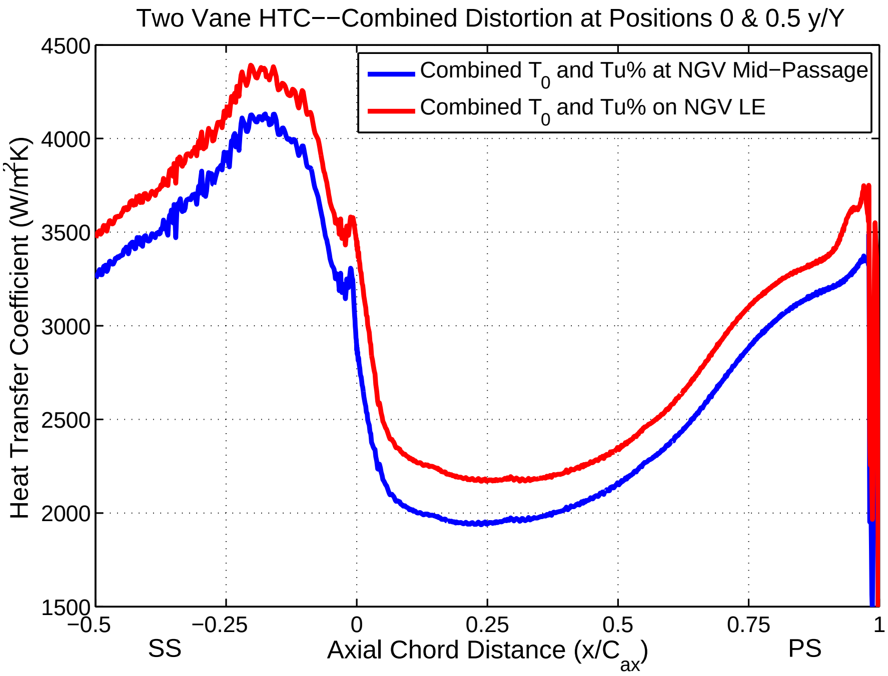

Figure 6.21: Effect of combined inlet turbulence and temperature distortion on 2D vane HTC at two offset clocking positions in two passage computational domain

impinging on the vane leading edges resulted in a variation of 18% in leading edge HTC from vane to vane.

Figure 6.22 summarizes the peak augmentation relative to uniform inlet conditions at the four clocking positions tested in this section. It is clear that the vane HTC responds similarly to the presence of the turbulence distortion, regardless of the presence of the inlet temperature distortion. Additionally, the expectation that vane HTC would remain unchanged due to clocking of the inlet temperature distortion is confirmed by inspecting the relatively flat shape of the hot streak data. Overall there appears to be a strong case for the influence of circumferential turbulence distributions on vane surface heat transfer. The next step is to evaluate whether these distortions could affect the downstream rotor blade row as well. In order to assess this possibility, an analysis of the exit turbulence intensity distributions subjected to the same inlet distortions will be performed in the next section.

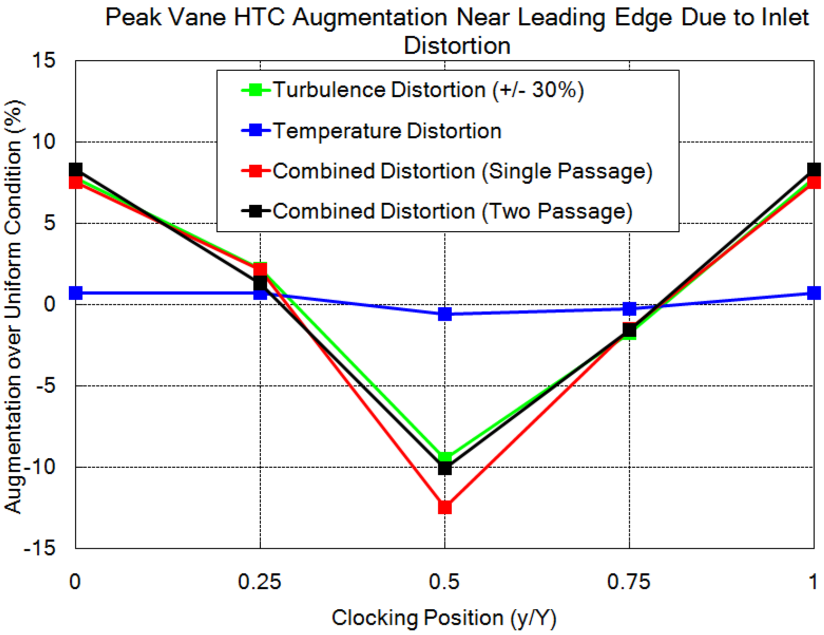

Figure 6.22: Summary of clocking effects for various inlet distortion conditions on vane leading edge region HTC

6.6 Vane Exit Turbulence Intensity

The original focus of the research predicted the effects of various flowfield phenomena on HPT rotor blade geometries. There was therefore significant interest in the influence of the non-uniform inlet boundary conditions on the vane exit turbulence intensity. The unsteady data processing procedure drew heavily from the unsteady heat transfer procedure described earlier in the chapter. The velocity magnitude V and turbulent kinetic energy k were exported at each time step for 100 time steps, and a discrete FFT performed on the time history-signals of these quantities to determine the period for each. This was particularly important for the two passage computational domain due to the slightly different vane trailing edge vortex shedding periods with inlet temperature distortions. Overall, the inlet distortions seemed to shift the distribution of the turbulence intensity at the vane exit rather than significantly affect the circumferential average. In both computational domains, the maximum absolute variation in the circumferentially averaged exit turbulence intensity was only 0.33%.

Figure 6.23 shows the response of the vane exit turbulence intensity to the clocking of the combined distortion impinging on the blade to impinging in the middle of the blade passage. There is a noticeable redistribution of the exit turbulence intensity

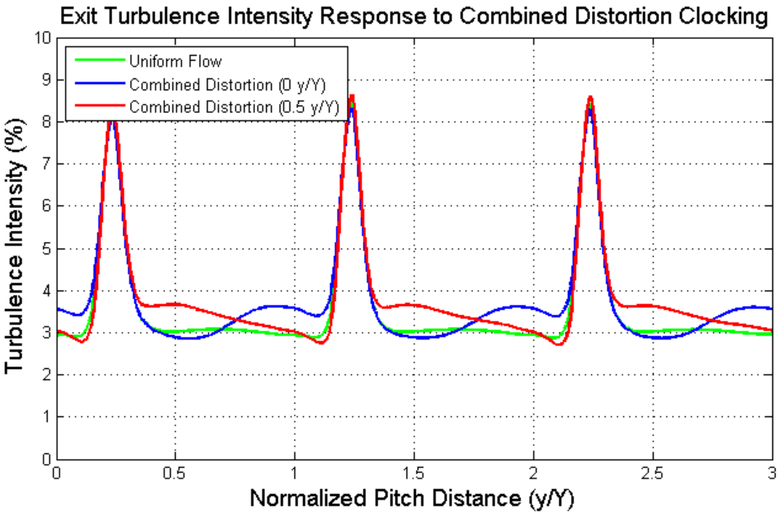

Figure 6.23: 2D vane exit turbulence intensity variation due to combined distortion clocking at combustor to vane ratio of 1:1

in the core flow, but the time-averaged variation at any point is no more than 1% Tu. The two passage domain exhibited similar behavior, with the exception that a single circumferential length scale exhibited the full range of variation seen in the single passage configurations. The expectation is then that these redistributions in exit turbulence intensity could affect the unsteady HTC on the rotor surface.

6.7 Summary

In summary, this chapter presented final validation and tuning of the $\kappa - \omega$ SST turbulence model, validation of a 2D HPT nozzle guide vane profile, and the effects of circumferentially varying non-uniform inlet temperature and turbulence distortions on NGV heat transfer. Final turbulence model tuning was performed on the C3X HPT nozzle vane in order to establish an adequately accurate prediction of turbulence propagation through an NGV passage. The tuned results showed reasonable agreement in the freestream with experimental results at the vane exit plane. This finding established confidence in the model to simulate the prediction of grid generated turbulence through the vane passage. Applying this correction also resulted in a largely accurate prediction of HPT heat transfer (within 15% of experiment).

Following these validation studies, circumferentially varying inlet temperature and turbulence distortions were introduced and analyzed on the numerical model. Heat transfer results in the form of surface heat flux, HTC and adiabatic wall temperature were then presented for a wide range of permutations of the baseline distortions, including amplitude of the turbulence profile, clocking, and circumferential length scale. The presence of the circumferentially-varying inlet turbulence distortion with turbulence intensities ranging from 7% to 13% influenced vane leading edge by up to 20% when clocked from upstream of the vane leading edge to the middle of the vane passage. Clocking the distortions just off the vane leading edge essentially eliminated the influence of the varying turbulence on vane heat transfer. The vane HTC response to turbulence distortion clocking occurred at similar levels independent of the presence of an inlet temperature distortion, and combustor to vane ratio. Clocking a hot streak alone upstream of the vane affected its surface heat transfer via augmentation of the adiabatic wall temperature (not HTC), which was in line with expectations. Based on the numerical evidence seen thus far the answer to the question of whether circumferential variation in inlet turbulence intensity can influence vane heat transfer is clearly, yes.

The final stage of analysis evaluated the effect of the various inlet distortions on the vane exit turbulence intensity. They were found to influence the exit turbulence intensity by redistributing the profile without significantly affecting the mean value at the exit. In the next chapter, these redistributions will be further evaluated to ascertain whether they have a significant influence on the unsteady rotor heat transfer environment.

Chapter 7

Turbulence Distortion Effects on Downstream Rotor Blade Row

7.1 Overview

In this chapter, a similar set of non-uniform inlet temperature and turbulence distortions to those tested in the previous chapter will be tested on a 2D HPT stage geometry representative of the Oxford Rotor Facility. The aim is to establish the effects of the non-uniform inlet turbulence distortions, if any, on HPT rotor heat transfer. Section 7.2 explains the simulated stage geometry and baseline flow configurations. It also presents studies of grid and time-step dependency for the domain. Section 7.3 outlines the scope of inlet distortions studied, and describes the method for processing the unsteady and time-mean heat transfer results for the rotor profiles. Section 7.4 discusses the influence of clocking for each distortion and compares the effect of distortion type at each clocking position. A summary of the chapter is found in Section 7.5.

7.2 2D High Pressure Turbine Geometry and Dependency Studies

The blade profiles that comprise the turbine stage in this study are the mid-span constant streamtube profiles of the B23 NGV and B22 rotor blades found in the Oxford Rotor Facility. The computational domain satisfies periodicity at its circumferential limits, and each period consists of three NGVs for every five rotor blades. A summary of the stage geometry is presented in Table 7.1 below.

Table 7.1: Summary of turbine stage geometry

Parameter	NGV Relative	Rotor Relative
Number of blades	3	5
Axial Chord	31.98 mm	24.21 mm
Pitch	44.51 mm	26.70 mm
Inlet flow angle	0°	$\sim 44.66°$
Exit flow angle	$\sim 71.55°$	$\sim -51.4°$
Axial Gap	$--$	8.2 mm

In the full 3D turbine stage, the rotor passage streamtube height increases in the axial direction due to the flared rotor casing. Employing a 2D computational domain eliminates this component of the turbine geometry. The resulting decreased pressure drop across the rotor blade row relative to the full turbine reduces the exit Mach number for the vane row. The decision was made to retain the current 2D configuration rather than use a 3D model of the turbine stage. Although this choice renders the vane exit Mach number to a high subsonic value of about 0.7, the absence of vane trailing edge shock structures should not significantly hinder the evaluation of the impact of the inlet turbulence distortions on rotor heat transfer. The primary aim of the study is to evaluate the rotor heat transfer response due to inlet distortion clocking, and this is possible with the vane exit flow limited to the high subsonic regime. As a result of the lower vane exit Mach number, the rotor speed was adjusted in order to maintain a similar velocity triangle for the rotor inlet, as a result the exit Mach number for the rotor is transonic. The flow conditions for the baseline (uniform flow) full stage configuration are presented in Table 7.2.

Table 7.2: Summary of turbine stage data for uniform inlet conditions

Parameter	Value
P_{0i}	804 kPa
P_3	282 kPa
T_{0i}	432 kPa
V_{rotor}	174 $\frac{m}{s}$
M_i	0.18
M_2	0.7
M_{2rotor}	0.32
M_{3rotor}	1.04

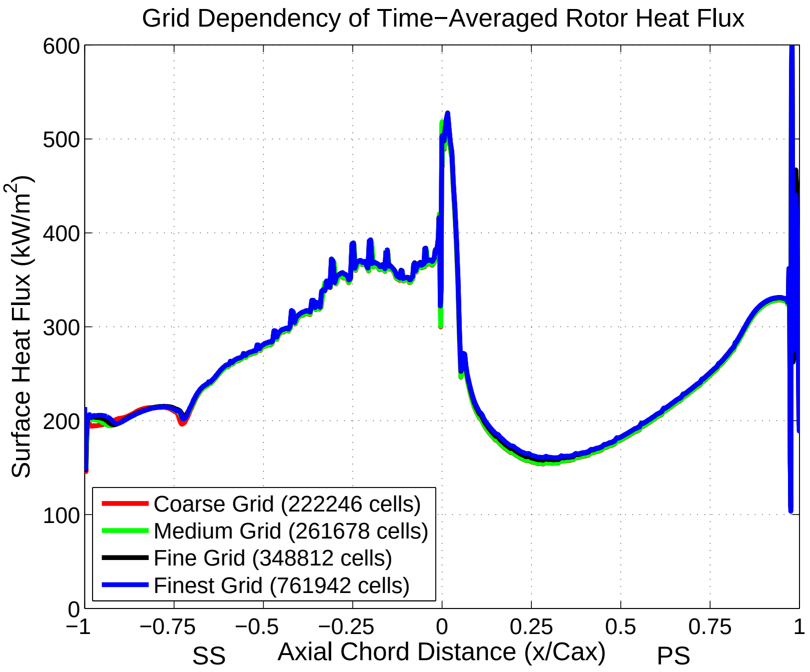

Figure 7.1: 2D full stage grid dependency study of time-averaged surface heat flux

Due to the significant variation between the flow conditions in the numerical model and available experimental data, direct validation against experimental data for the complete stage is not possible. However, these geometries have already been extensively validated in steady and unsteady flow conditions in the previous chapters. Additionally, the purpose of the numerical experiment is to establish trends in the heat transfer response to varying inlet conditions rather than matching specific absolute levels of rotor heat transfer. For these reasons, only dependency studies of the sensitivity of the solution to grid refinement and time-step size will be conducted.

In addition to the flow conditions described above, isothermal wall boundaries on the rotor surface of 290 K were enforced to provide a gas to wall temperature ratio of 1.5. Grids sizes in the range of $2.2 \cdot 10^5$ to $7.6 \cdot 10^5$ were generated for the computational domain. After reaching a converged solution, the time-averaged heat flux for the rotor surface over three vane passing periods (a single traverse of the circumferential length of the domain) was compared between the solutions. Figure 7.1 presents the mean surface heat flux against the rotor axial chord. The solution shows complete insensitivity to grid refinement past the grid with $3.5 \cdot 10^5$ cells.

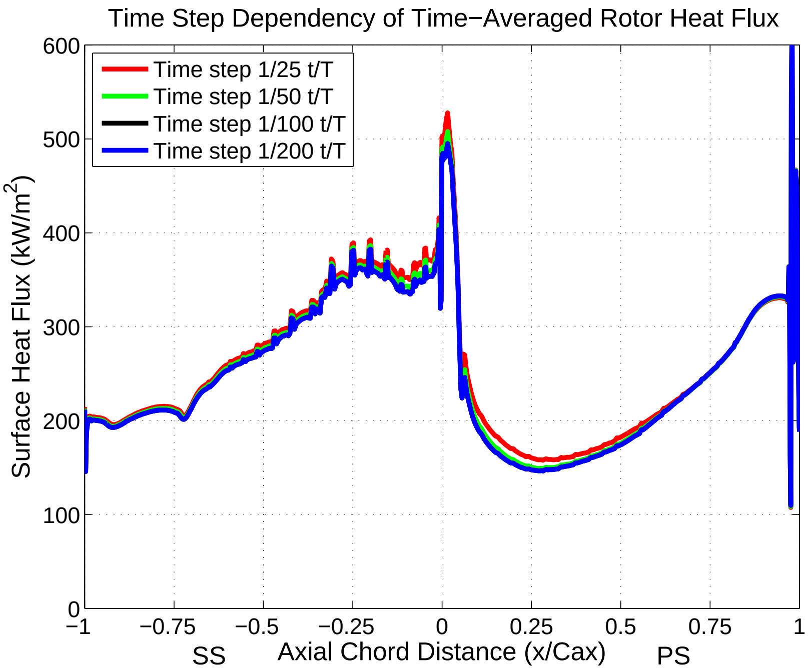

Figure 7.2: 2D full stage grid dependency study of time-averaged surface heat flux

Following the grid dependency study the solution was run over a range of time steps between $1 \cdot 10^{-5}$ and $1.25 \cdot 10^{-6}$. These time steps represented a ratio of time steps per vane passing period between 25:1 and 200:1. Figure 7.2 presents the time-averaged heat flux for each of the four time-step levels, and shows that independence of time-step variation is achieved for a the time interval of 50 steps per vane passing period

7.3 Case Preparation and Unsteady Heat Transfer Data Processing

The inlet turbulence and temperature distortions were similar to those used in the previous chapter with a slightly more limited scope. The baseline turbulence distortion with amplitudes ranging from 7% to 13% was again used for the current study. The temperature distortion used a larger amplitude than the configuration for the 2D vane study. It had a $\frac{T_{0max}}{T_{0min}}$ of 1.4. The reason for increasing the strength of the inlet temperature distortion was to ensure the preferential heating on the latter rotor pressure surface (He et al., 2004) would be captured by the solver. Based on the results

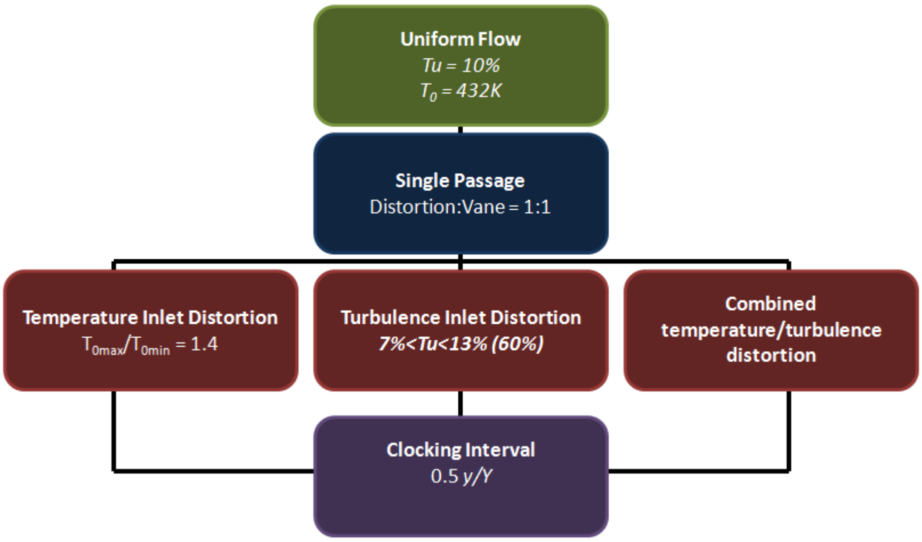

Figure 7.3: Summary map of inlet variations for the 2D HPT stage

thus far, it is apparent that clocking the inlet distortions from the vane leading edge to the center of the vane passage resulted in the greatest variation at the vane exit. Therefore only these two clocking positions were tested on the full stage. The same pattern of turbulence only distortions, temperature only distortions, and combined in phase distortions were used as in the 2D vane solutions. Figure 7.3 summarizes the parameter map for the case study.

The procedure for performing the heat transfer calculations began by running two solutions with isothermal wall temperatures of 290 K and 295 K on the rotor surfaces. These two solutions were maintained at identical time steps throughout the solution process. The surface heat flux was exported for each cell-centroid on a single rotor for a single vane passing period in the Tecplot data format at each time step. In order to manage the significant number of data files generated for the 14 solutions, a MATLAB script was written to import the heat flux data and concatenate a matrix containing this data for a full period at each cell-centroid on the rotor surface. The system of convective heat transfer equations was then solved for each cell at each time step:

$$\dot{q}_1 = h(T_{aw} - T_{w1}) \tag{7.1}$$

$$\dot{q}_2 = h(T_{aw} - T_{w2}) \tag{7.2}$$

In order to completely capture h and T_{aw}, the two variables must be evaluated for their time-averaged and unsteady components (i.e. $h = \overline{h} + \dot{h}$). In this manner, the

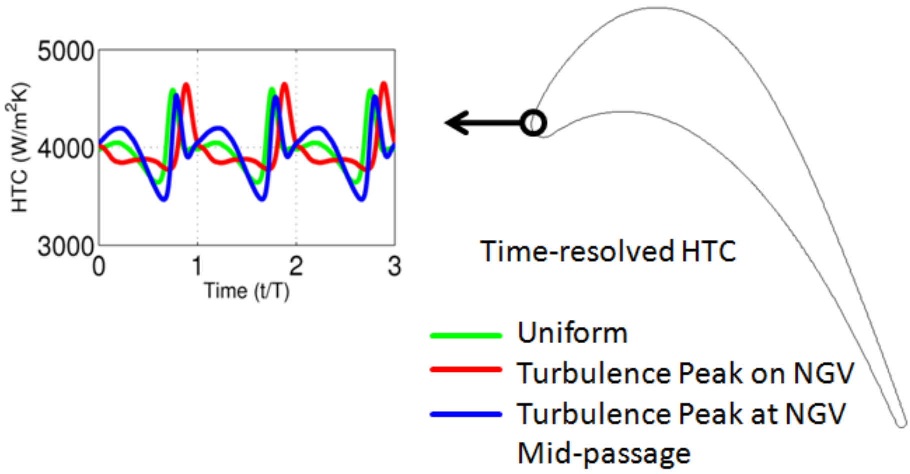

Figure 7.4: Time-resolved HTC traces on rotor leading edge

full convective heat transfer equation is represented by the following equation:

$$\bar{\dot{q}} = \bar{h}(\overline{T_{aw}} - T_w) + \overline{\dot{h}(\dot{T}_{aw} - T_w)} \tag{7.3}$$

This formulation of the heat transfer equation retains information from the unsteady component of the flow that would be lost in calculating $\bar{h}$ and $\overline{T_{aw}}$ based on the time-averaged heat flux for the two wall surfaces (Equation 7.4):

$$\bar{q} = \bar{h}(\overline{T_{aw}} - T_w) \tag{7.4}$$

Figure 7.4 highlights the need for the full decomposition of the steady and unsteady components for h. Even the uniform inlet flow condition will demonstrate strong local variation in the HTC due to the arriving wake (shown as the sharp peak in HTC on the green curve). Therefore, the flexibility of this procedure therefore allows for detailed analysis of both the time-mean and unsteady effects of the various inlet distortions configurations on the rotor surface heat transfer.

In addition to the rotor surface heat flux time histories, a variety of exit flow conditions were recorded approximately 10% of the vane axial chord downstream of the vane exit plane, including velocity, temperature, and turbulent kinetic energy. These quantities were each exported in the Tecplot format as well. The goal was to provide a broader snapshot in the vane relative reference frame of the flow conditions impacting the rotor blade row. These distributions would aid in explaining the rotor heat transfer results. A modified version of the MATLAB script written for the unsteady rotor heat flux data was used to create the time-averaged distributions of the vane exit flow.

7.4 Effects of Inlet Turbulence Distortions on Rotor Heat Transfer

The time-mean and unsteady heat transfer results for the full stage solutions with inlet distortions are presented in this section. The effect of clocking each distortion type is presented first for each distortion type separately. Subsequently the inlet temperature and combined distortions are compared directly to one another.

7.4.1 Inlet Turbulence Distortion

As mentioned in the previous chapter, enforcing the non-uniform turbulence distributions at the inlet to the domain rearranges the turbulence intensity distribution at the vane exit. Figure 7.5 displays the vane exit turbulence intensity distributions for the uniform flow and two clocking positions of the inlet turbulence distortion. The general trend in the core flow matches expectations. Clocking the distortion peak from the leading edge of the vane to the middle of the vane passage noticeably increases the turbulence intensity in the core flow. The peak variation in the core flow turbulence intensity is about 1% between clocking positions. Meanwhile clocking the distortion to the vane leading edge appears to slightly increase the vane wake width, which is expected as well.

Figure 7.6 presents the time-averaged rotor surface heat flux distribution for the two clocking positions of the turbulence distortion and the uniform flow. The variation between any of the curves is only around 1%. This result matches expectations, as there was essentially no variation in the circumferentially averaged turbulence intensity distribution at the vane exit due to clocking of the inlet turbulence distortion. Similarly, the time-averaged rotor surface HTC essentially shows no response to turbulence distortion clocking (Figure 7.7).

Evaluating the time-resolved HTC over the rotor surface shows a more significant influence of the turbulence distortion clocking. Figure 7.8 presents this data for the uniform flow (a) and two clocking positions (b and c). The time-space diagrams present the rotor blade unwrapped along its axial coordinates, with the pressure surface trailing edge at the top (1), and the suction surface trailing edge at the bottom (-1). The leading edge is in the center of the chart, and time advances to the right through three vane passing periods. The start time has been translated to match the impact of the wake on the rotor leading edge. Overall, clocking the

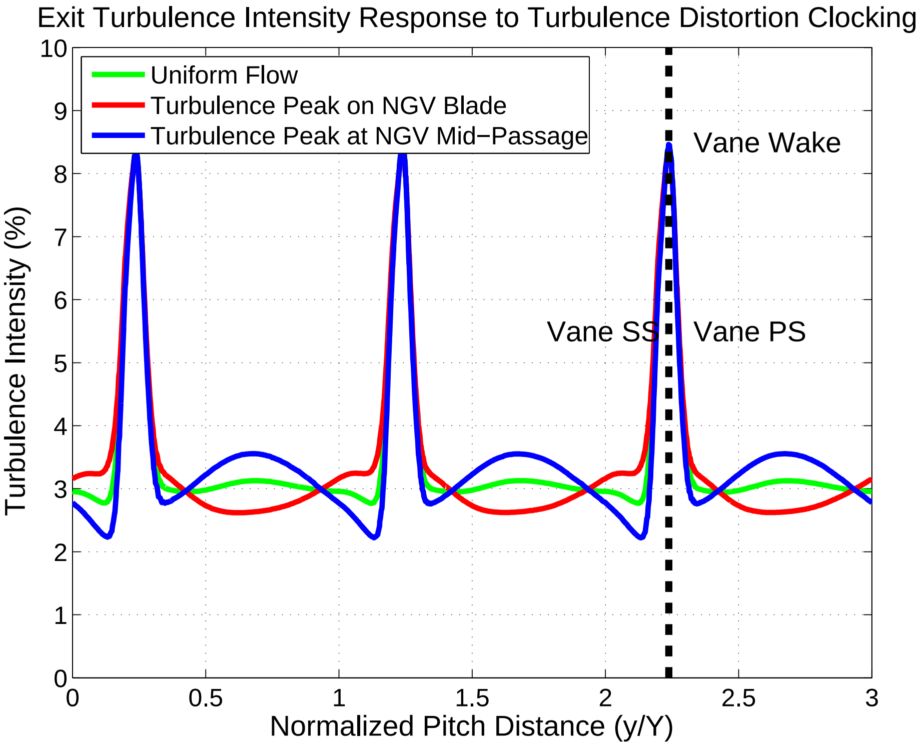

Figure 7.5: Comparison of NGV exit turbulence intensity distributions with uniform flow and two clocking positions of inlet turbulence distortion

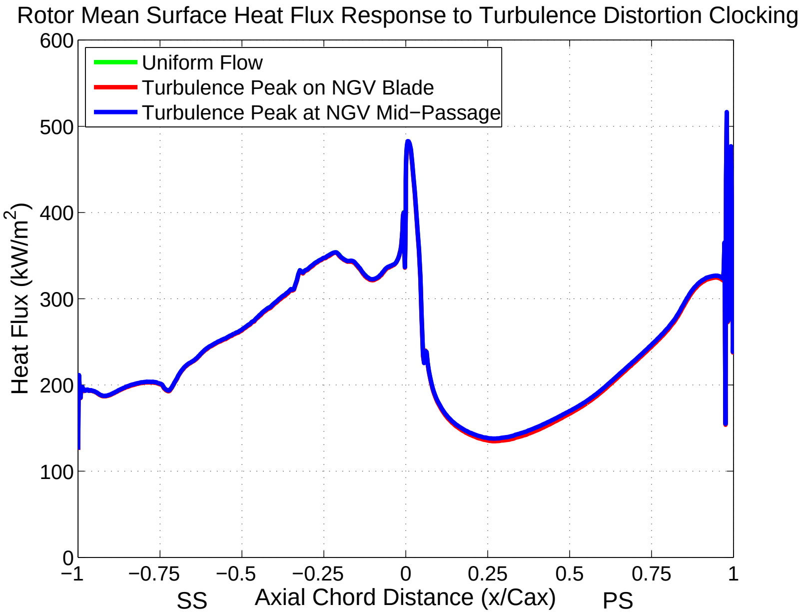

Figure 7.6: Time-averaged rotor surface heat flux for uniform flow and two clocking positions of inlet turbulence distortion

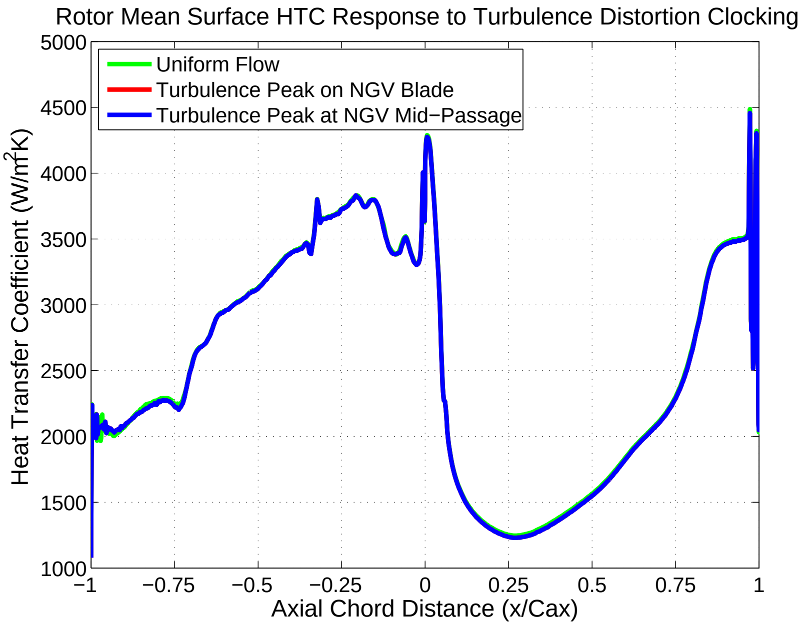

Figure 7.7: Time-averaged rotor surface HTC for uniform flow and two clocking positions of inlet turbulence distortion

turbulence distortions tends to affect the leading rotor suction and pressure surfaces, although there is noticeable variation near the pressure surface trailing edge. The trends in variation make sense as well. For example the patch of relatively low HTC on the pressure surface around 0.25 C_{ax} expands when the turbulence distortion is clocked to the vane leading edge (as shown in Figure 7.8b). The resulting lower value of turbulence intensity in the freestream then increases the patch size. Meanwhile, the increased turbulence intensity in the free-stream accounts when the turbulence distortion is clocked to the middle of the NGV passage results in the decreased size of the low patch of HTC on the frontal rotor pressure surface.

The magnitude of these variations is small. Figure 7.9 presents zoomed in time-history traces of the rotor surface HTC at 0.15 C_{ax} on the suction surface, the leading edge, and two locations pressure surface at 0.25 and 0.9 C_{ax}. Clocking the turbulence distortion to the middle of the vane passage tends to increase variation at all four stations, whereas clocking the distortion has a mixed effect on the unsteady variation around the blade surface. Clocking the turbulence distortion from the vane leading edge to the vane passage increases peak to peak variation in HTC on the rotor surface by up to 4%. Furthermore in some regions of the rotor clocking the inlet turbulence

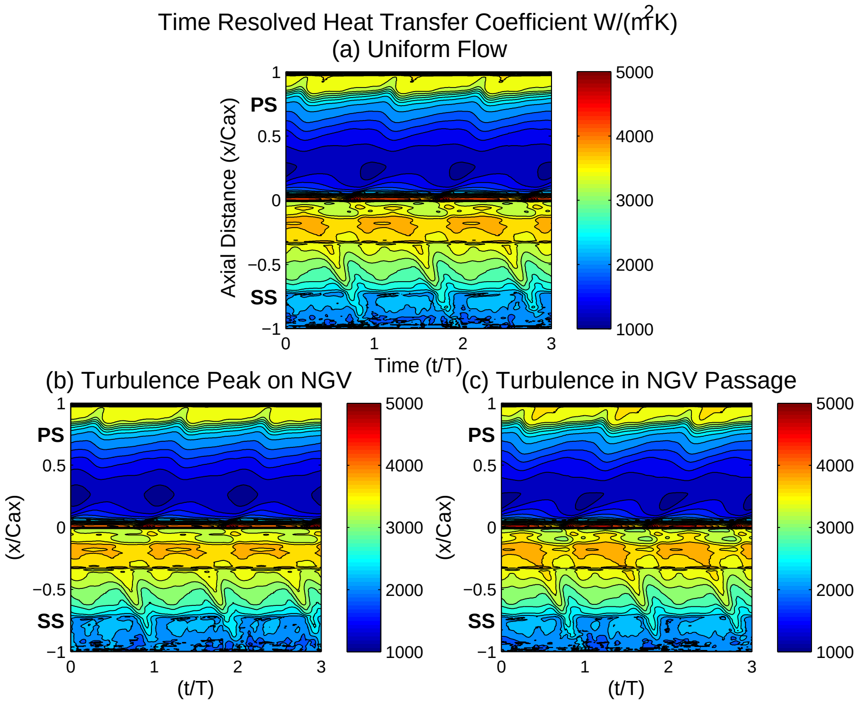

Figure 7.8: Time-resolved rotor surface HTC for uniform flow and two clocking positions of inlet turbulence distortion over three vane passing periods

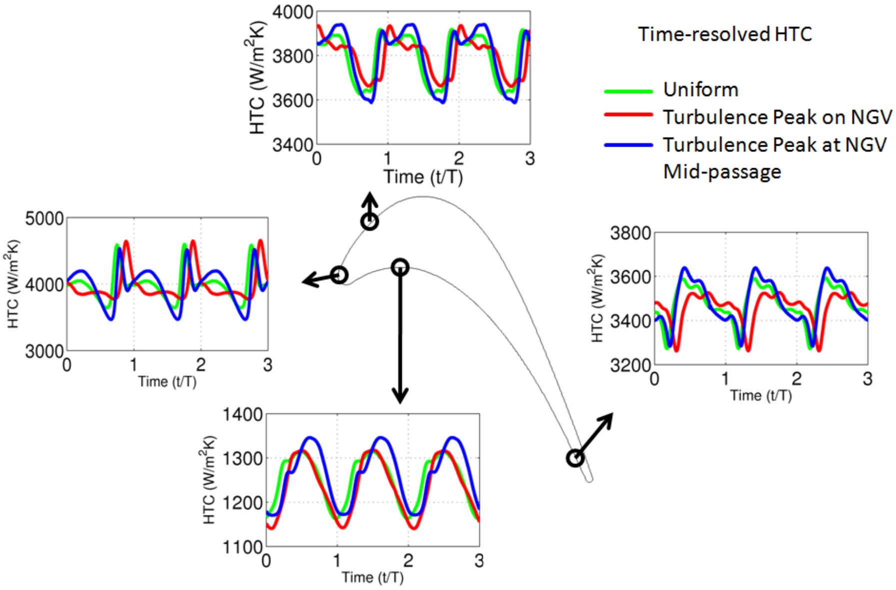

Figure 7.9: Close-up view of time-resolved rotor surface HTC at four locations–uniform and clocked turbulence distortions

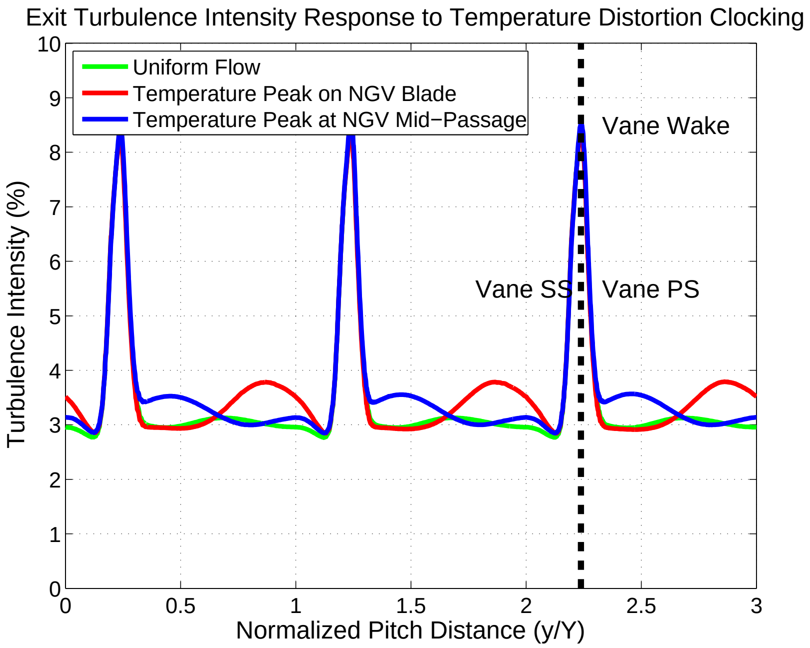

Figure 7.10: Comparison of NGV exit turbulence intensity distributions with uniform flow and two clocking positions of inlet temperature distortion

distortion results in the peak unsteady HTC increasing by about 2% to 3%.

7.4.2 Inlet Temperature Distortion

Following the evaluation of the turbulence distortion clocking on the rotor surface heat transfer, temperature distortions were enforced at the inlet to the computational domain. The exit turbulence intensity distributions for the uniform flow and two hot streak clocking positions are presented in Figure 7.10. The two clocking positions of the temperature distortion showed a slight increase in the freestream turbulence intensity at the vane exit. The location of the increased levels showed preference to either side of the vane passage depending on the clocking position. The reason for this variation can be explained by the contribution of the temperature gradient at the inlet to the velocity field through the vane passage. For a constant pressure ratio across the NGV row between the different inlet distortion clocking positions, the circumferential length scale of the hot streaks used in this study will generate an additional strong pitch-wise gradient in the velocity through the vane passage. As referenced in Radomsky and Thole (2000), the dominant term for TKE production is:

$$P(k) = -\overline{u'v'}\Big[(1+\frac{y}{R})\frac{\partial u}{\partial y} - \frac{u}{R} + \frac{\partial v}{\partial s}\Big] \tag{7.5}$$

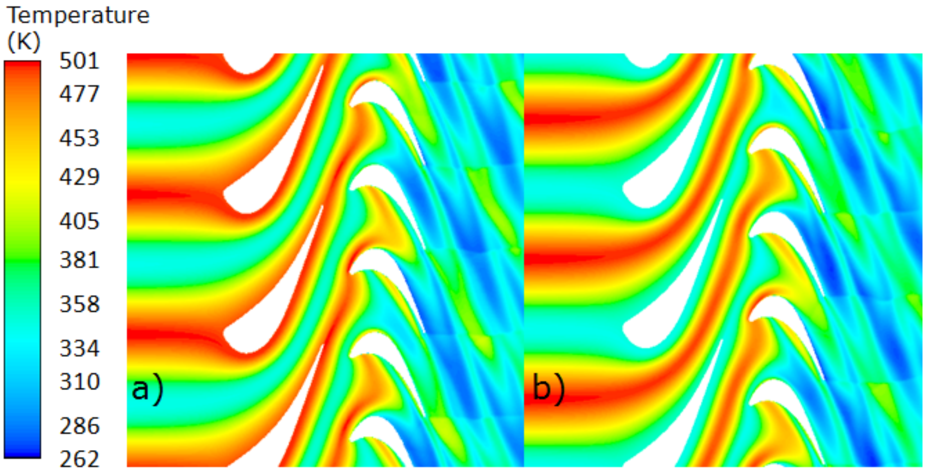

Figure 7.11: Temperature contours highlighting inlet temperature distortion clocking;(a) impinging on NGV leading edge;(b) impinging at NGV mid-passage

Where $\overline{u'v'}$ is the Reynolds stress tensor, and R the radius of curvature of the streamline. In the vane passage, R is fixed by the geometry of the blades. Near the suction surface where TKE production is expected to occur, it is evident according to the above equation that the local velocity has a direct effect on the production of TKE. Figure 7.11 shows that the hot streak impinging on the vane leading edge is wide enough to result in a higher velocity in the freestream below the suction surface. The opposite holds true for the temperature distortion clocked to the center of the vane passage. The expectation then is that the turbulence model would generate increased turbulent kinetic energy at the exit plane near the suction surface for the temperature distortion impacting the vane surface and lower TKE near the vane pressure surface.

Distributions of the turbulent kinetic energy at the exit for the uniform flow and two clocking positions of the temperature distortion confirm that this is the case (Figure 7.12). The local region where the greatest variation in TKE production occurs nearer the vane surface towards the leading edge and tends to propagate through the vane passages without diffusing completely through to the center of the vane exit flow. The misalignment of the TKE distributions with the temperature-affected velocity field at the vane exit then results in the net increase in turbulence intensity for both temperature clocking positions.

Heat transfer results for the temperature clocking are presented in the same manner as the inlet turbulence distortion study. The time-averaged surface heat flux is

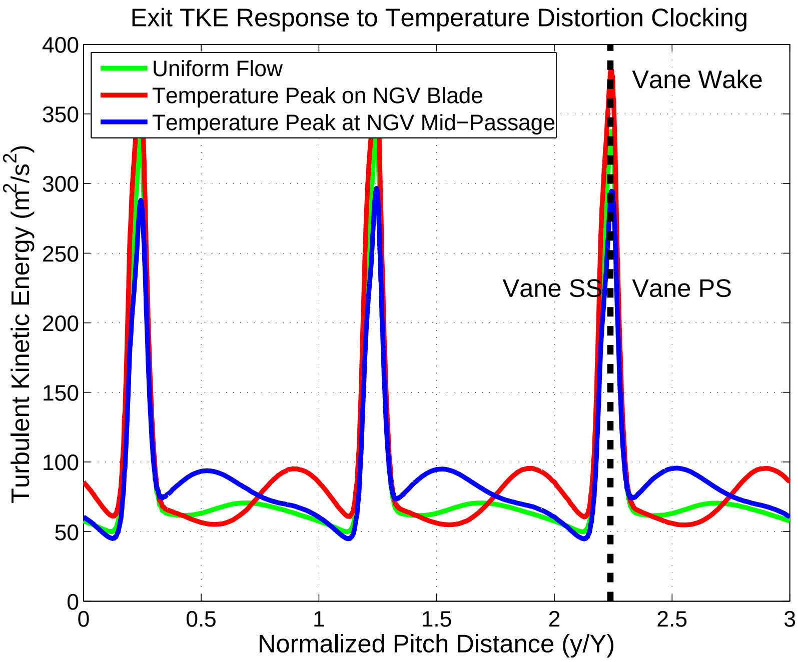

Figure 7.12: Comparison of NGV exit turbulent kinetic energy distributions with uniform flow and two clocking positions of inlet temperature distortion

shown in Figure 7.13. There is a small increase in the time-averaged suction surface heat flux for both clocking positions, but the significant variation is on the rotor pressure surface. This is due to the “positive jet” effect mentioned in previous chapters, where the additional tangential velocity in the hot streak results in preferential heating on the rotor pressure surface. Importantly the clocking of the hot streak from the center of the vane passage to the vane leading edge shows a sharp reduction in the rotor preferential heating, which matches previous studies conducted on this effect (He et al., 2004). The time-averaged HTC distribution on the rotor surface is presented in Figure 7.14. There is little to no variation in the three curves, either between clocking positions or relative to the uniform inlet conditions.

The time-resolved rotor surface HTC contours present a more complete picture of what occurs in the unsteady rotor heat transfer environment. The presence of the hot streaks strongly organizes the time-history of the rotor HTC. The rotor pressure surface in particular demonstrates wider regions of decreased heat transfer in the leading 50% of the axial chord, and again near the trailing edge. The suction surface is also affected. For example, the hot streaks serve to increase the peaks of HTC near the leading suction surface. The noisy regions on the latter rotor surface are due to

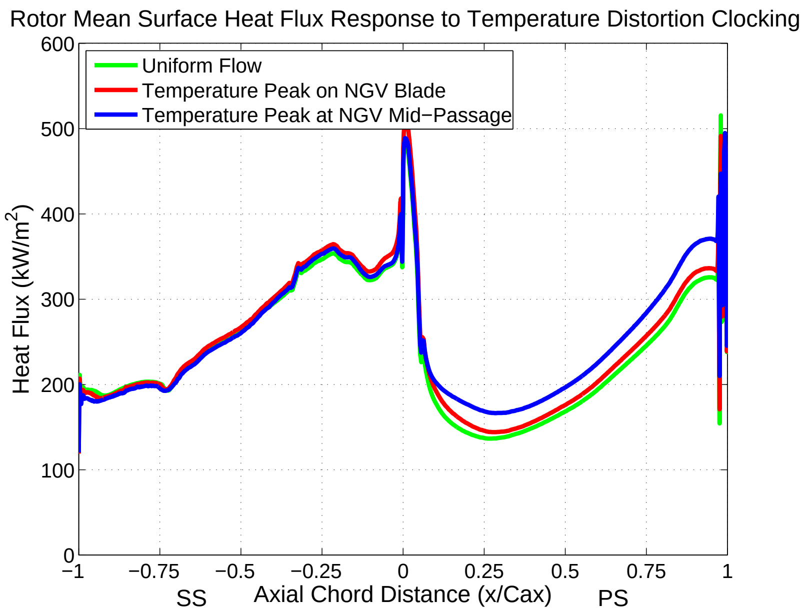

Figure 7.13: Time-averaged rotor surface heat flux for uniform flow and two clocking positions of inlet temperature distortion

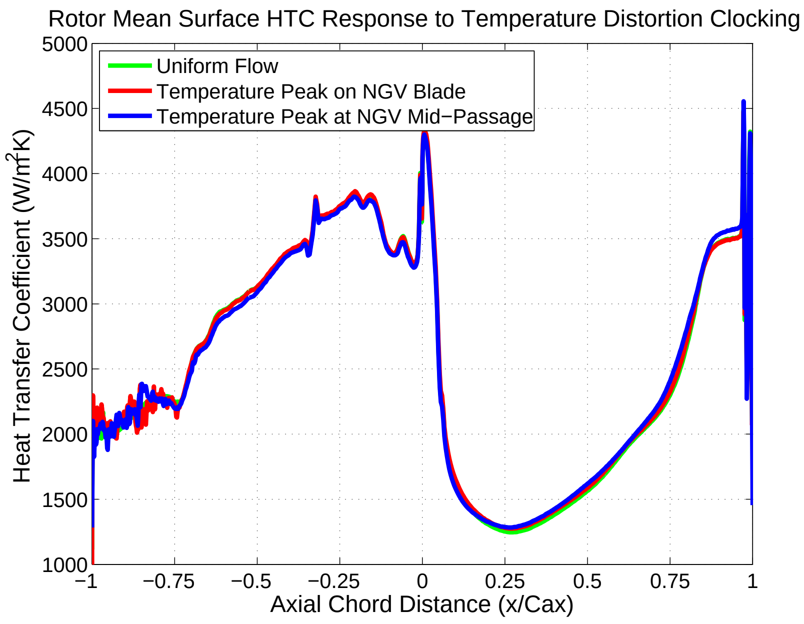

Figure 7.14: Time-averaged rotor surface HTC for uniform flow and two clocking positions of inlet temperature distortion

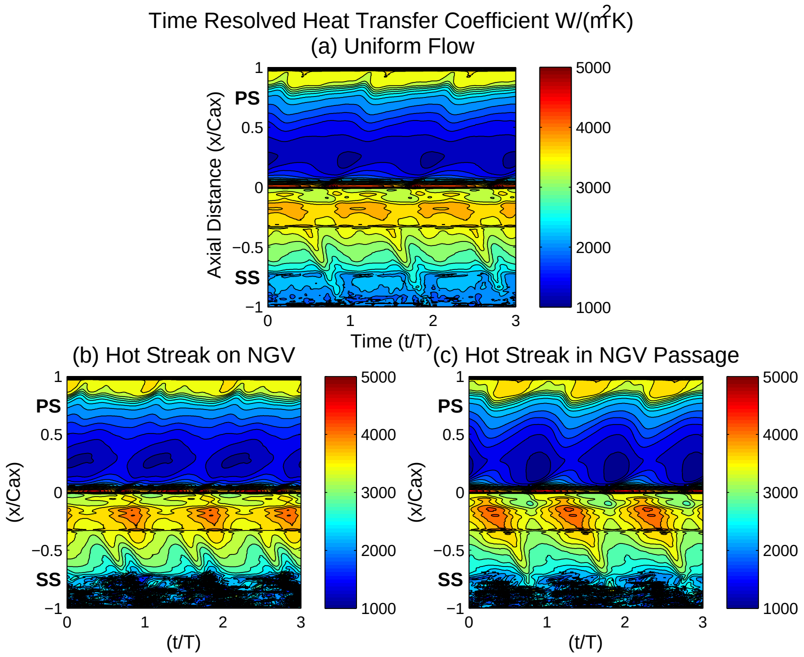

Figure 7.15: Time-resolved rotor surface HTC for uniform flow and two clocking positions of inlet temperature distortion over three vane passing periods

the influence of the hot streaks on the rotor trailing edge shock structures.

Closer examination of the time-resolved HTC traces at four points on the rotor surface expands on the understanding of the unsteady HTC environment for the rotor (Figure 7.16). In general, the trend of the hot streaks is to increase unsteadiness for the rotor HTC at each of the sampled axial chord stations. When the hot streak is clocked to the vane leading edge, this increase in unsteadiness is an additional 10% about the mean as compared to the uniform flow. In the vane passage clocking position this additional variation can be up to 18% over the uniform flow variation, as shown on the leading suction surface station.

At first glance, this significant additional unsteadiness in the rotor appears to be counter-intuitive since the vane HTC distributions in the previous chapter were unaffected by the inlet temperature distortion. However, a correlation for the augmentation of HTC due to freestream total temperature on a flat plate provides a guideline to account for the HTC variation due to the hot streaks impacting the downstream rotor blades (Fitt et al., 1986). Using the rotor relative inlet total temperatures of 475 K in the hot streak and 345 K in the cold streak in the following

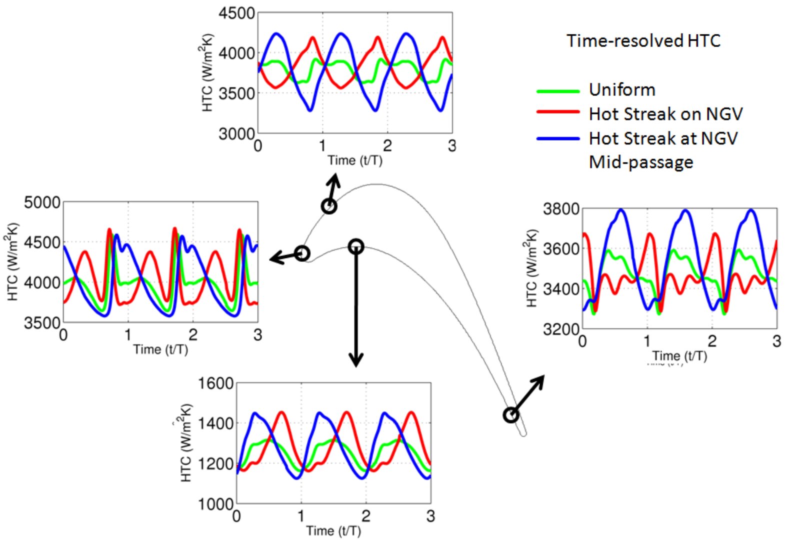

Figure 7.16: Close-up view of time-resolved rotor surface HTC at four locations–uniform and clocked temperature distortions

equation:

$$\frac{h_{hot}}{h_{cold}} = \left(\frac{T_{0hot}}{T_{0cold}}\right)^{0.25} = 1.083 \tag{7.6}$$

This change in HTC would seem to account for the additional unsteady augmentation when the hot streak is clocked to the vane leading edge. In the alternative clocking position, the source of the additional unsteadiness is most likely due to variation in the fluid dynamics through the rotor passage resulting from the offset wake and hot streaks.

7.4.3 Inlet Combined Distortion

Clocking the combined temperature and turbulence distortions comprised the final set of tests. The exit turbulence intensity distributions for these conditions are presented in Figure 7.17. The addition of the non-uniform turbulence distribution to the hot streak at the inlet results in greater variation in the core flow exiting the passage. When the distortion is clocked to the vane leading edge the absolute difference is about 1.5%, and nearly 2% for the clocking position in the core flow. Based on these distributions, the expectation is that combining the distortions would increase unsteadiness in the rotor HTC relative to the temperature only distortion.

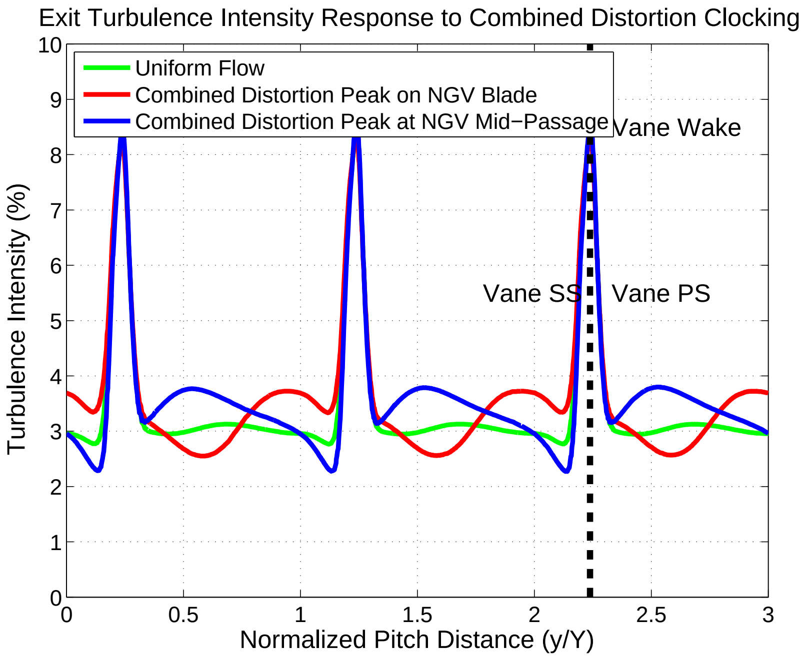

Figure 7.17: Comparison of NGV exit turbulence intensity distributions with uniform flow and two clocking positions of combined temperature and turbulence inlet distortion

The trends in time-averaged rotor surface heat flux for the combined distortions are very similar to the hot streak only results. For example preferential heating on the rotor pressure surface is significant when the distortion is clocked to the center of the vane passage (Figure 7.18). Additionally the lack of variation in the time-averaged surface HTC present in the previous clocking studies is reflected again for the combined distortions in Figure 7.19.

Comparing the time-resolved HTC amongst the temperature distortions and combined distortions over the rotor surface presents a more complete picture of their effects on the unsteady heat transfer environment (Figure 7.20). The combination of the temperature and turbulence distortions at the inlet to the domain serves to primarily affect the rotor pressure surface HTC. In particular, the patch of low HTC near the leading edge around 0.25 C_{ax} and again near the trailing edge beginning at about 0.8 C_{ax} show evidence of this behavior. In general the trend is to increase the unsteadiness between 2% and 5% when the turbulence distortion is present. The combined temperature and turbulence distortion also serves to generate additional time-averaged rotor HTC augmentation over the temperature distortion alone.

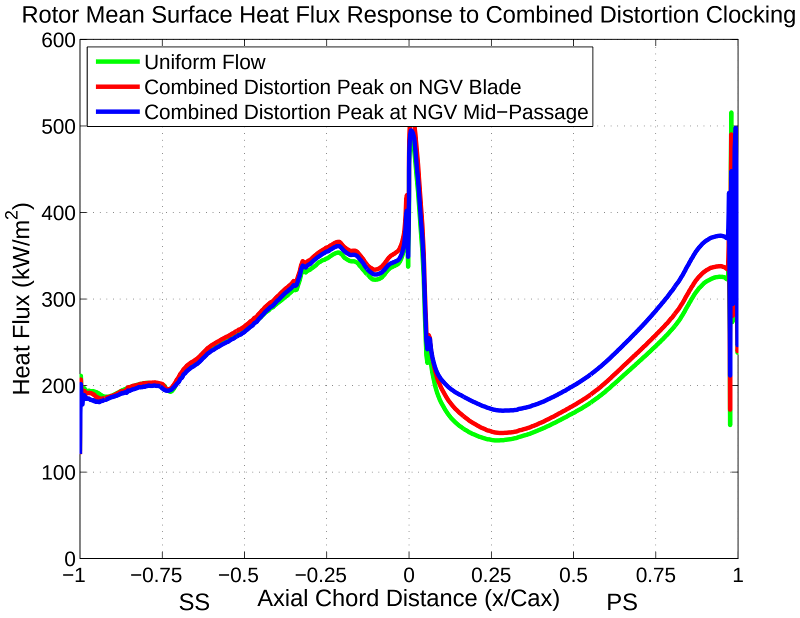

Figure 7.18: Time-averaged rotor surface heat flux for uniform flow and two clocking positions of combined temperature and turbulence inlet distortion

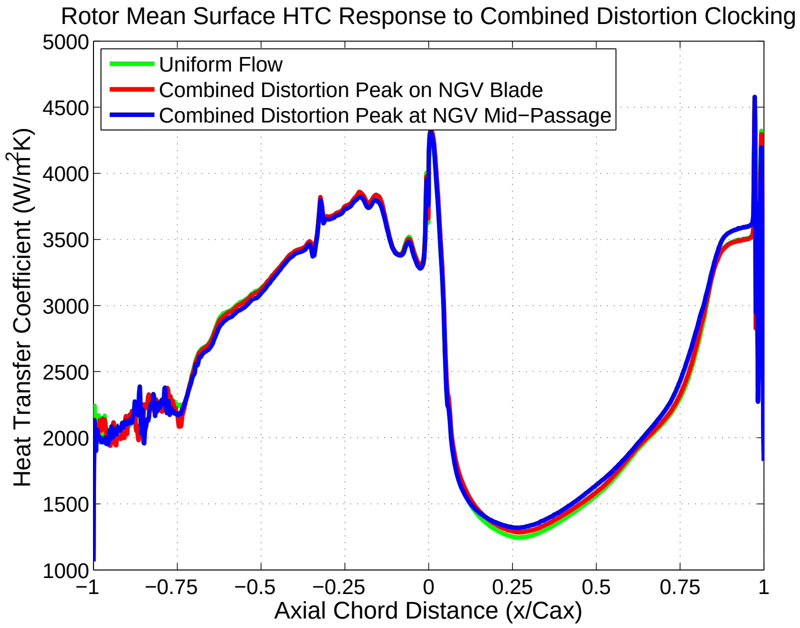

Figure 7.19: Time-averaged rotor surface HTC for uniform flow and two clocking positions of combined temperature and turbulence inlet distortion

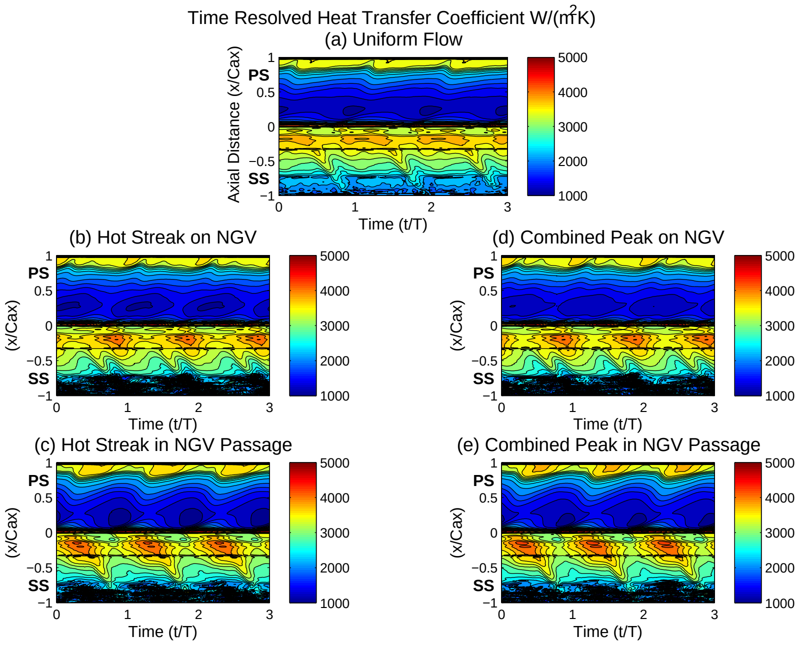

Figure 7.20: Time-resolved rotor surface HTC summary comparison of uniform flow, combined and temperature distortions, and two clocking positions

Figure 7.21 shows the time-averaged rotor HTC distributions for the temperature and combined distortions clocked to the middle of the NGV passage. At this clocking position the combined distortion increases the HTC on the rotor pressure surface by up to 3% on the rotor pressure surface. This trend is strongest near 0.25 C_{ax} and 0.8 C_{ax}. When the distortions are clocked to the NGV leading edge, the additional augmentation of the combined distortion as compared to the temperature distortion alone is limited to about 1%.

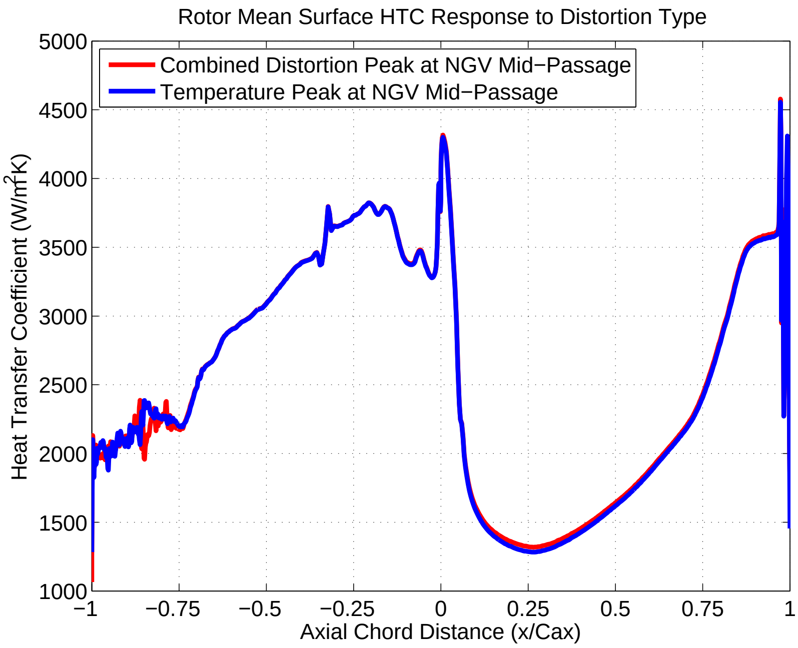

Figure 7.21: Time-averaged rotor surface HTC comparing temperature and combined distortions clocked to middle of NGV passage

7.5 Summary

In this chapter the effects of non-uniform inlet turbulence distortions on rotor surface HTC have been presented. The geometry employed in this study was a 2D mid-span cut of the HPT turbine stage used in the Oxford Rotor Facility. Following grid and time-step dependency studies, the time-history of the heat flux on the rotor surface was exported and processed to allow for more detailed analysis of the rotor heat transfer environment.

The inlet distortions used in this chapter were similar to those in Chapter 6, with a slightly stronger hot streak. The time-averaged effect of the turbulence distortions alone on the rotor surface HTC was minimal. However, when clocked together with the inlet temperature distortion in the middle of the NGV passage the turbulence peak augmented the time-averaged rotor pressure surface HTC by up to 3%. Meanwhile, the presence of the non-uniform conditions at the inlet served to increase the unsteadiness in rotor HTC as compared to the uniform flow condition. In the case of the turbulence distortion alone, this increase had a peak value of 4%. Enforcing the hot streaks at the inlet to the domain resulted in an increase in rotor HTC unsteadiness between 10% and 18%. Adding the turbulence distortion to the hot streak additionally augmented the unsteady components of HTC in a range of 2% to 5%. This result matches well with the effect of the turbulence distortion alone on rotor HTC unsteadiness. Overall the effect of circumferential turbulence distributions on rotor HTC can be characterized as increasing the levels of rotor HTC unsteadiness independent of the presence of a hot streak, and increasing the rotor pressure surface time-averaged HTC when coupled with the hot streak. The magnitude of this increase is small however when compared to the increase in time-averaged HTC due to presence of the hot streak alone.

Chapter 8

Turbulence Distortion Effects on a 3D Nozzle Guide Vane

8.1 Overview

In this chapter a final computational geometry, a 3D nozzle guide vane, will be subjected to a range of inlet distortions similar to those found in Chapter 6. The intent is to strengthen confidence in the predictions of circumferential turbulence variation on vane heat transfer by testing them on this more complex computational model. Section 8.2 explains the geometry and meshing procedure for the domain, and Section 8.3 describes the modified procedure for generating inlet distortions for the 3D computational domain. A validation study compared to experimental results is also presented in this section. In Section 8.4, the 3D inlet distortion configurations are described and their effects on vane heat transfer discussed. A summary of the chapter is presented in Section 8.5.

8.2 3D NGV Geometry, Grid Generation, and Validation

The exact geometry used in this chapter is a single passage of the B23 NGV used in the Oxford Rotor Facility (Figure 8.1), reflecting a circumferential period of $\frac{1}{36}$ the full annulus. The computational domain extends approximately 0.33 C_{ax} upstream of the vane leading edge, and a full axial chord length downstream of the vane trailing edge. Rotational periodicity is enforced on the circumferential boundaries to the domain, and the remaining boundary conditions were established in a similar manner to that used in previous chapters. The computational grid was generated via ANSYS Meshing Program. The change in software compared to earlier chapters was due to

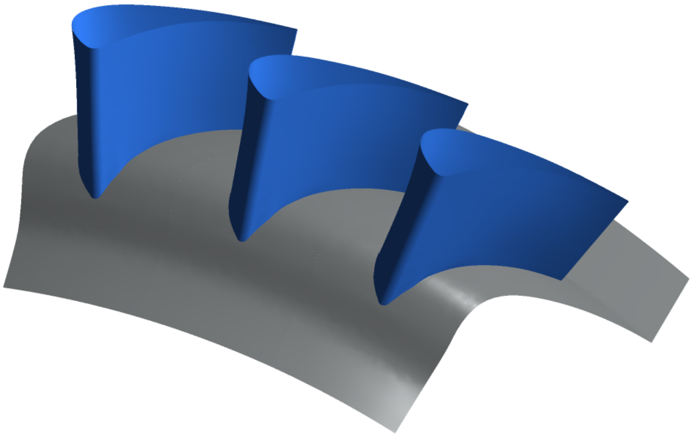

Figure 8.1: 3D nozzle vane geometry displaying three periodic repeats of the computational domain

problems with available memory when using GAMBIT. These limitations arose from the conflicting requirements of maintaining appropriate levels of y^+ control and still using sufficient grid refinement upstream of the NGV to prevent excessive numerical diffusion of the inlet distortions before they reached the vane leading edge. The final grid controlled y^+ values to between 10-15 on the vane surface. However, the grid also displayed high levels of skewness near the vane trailing edge and leading edge near the hub. Therefore the grid was converted to a polyhedral domain using the procedure described in Chapter 3 to eliminate the skewed cells. The final polyhedral grid contained $9.65 \cdot 10^5$ cells.

Experimental data from Sheard (1989) offered a basis for validation in the form of the surface isentropic Mach number. The isentropic vane exit Mach number at mid-span was 0.95 in the experiment, and the Reynolds number based on axial chord and isentropic exit conditions was $1.86 \cdot 10^6$. A radial equilibrium condition was enforced at the exit to the domain in order to match the radial pressure gradient for the experimental flow conditions. Comparisons between the FLUENT prediction and the experimental data at three span-wise locations were made. In Figure 8.2, the hub surface Mach number at 10% span is presented. The prediction is excellent along the vane surface except near the suction surface trailing edge. The reason for this is the relatively coarse grid used in the middle of the vane passage due to previously mentioned memory limitations.

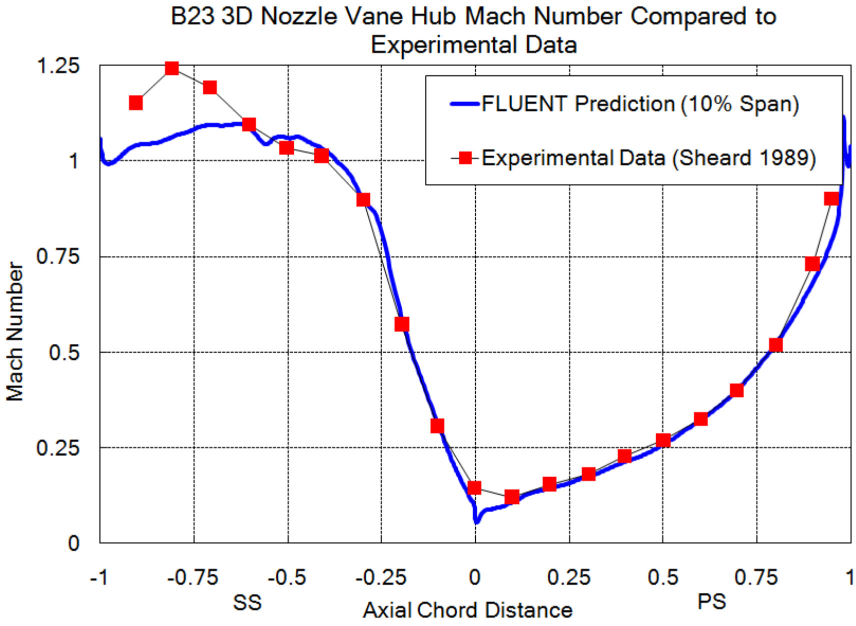

Figure 8.2: Comparison of the 3D NGV surface Mach number and experimental data from Sheard (1989) at 10% span

Figure 8.3 compares the prediction and experimental data for the vane mid-span. Again the only significant deviation from the experimental data in the prediction is in the region of the trailing edge shock. Finally, the 90% span data is presented in Figure 8.4. The surface Mach number is slightly over-predicted near mid-chord, but overall the prediction closely matches the experimental results. In the absence of experimental heat transfer data for this geometry, the high degree of accuracy in the vane surface Mach number prediction and the reasonable control in the y^+ on the vane establishes confidence that the model will provide an accurate reflection of the trends in vane heat transfer response.

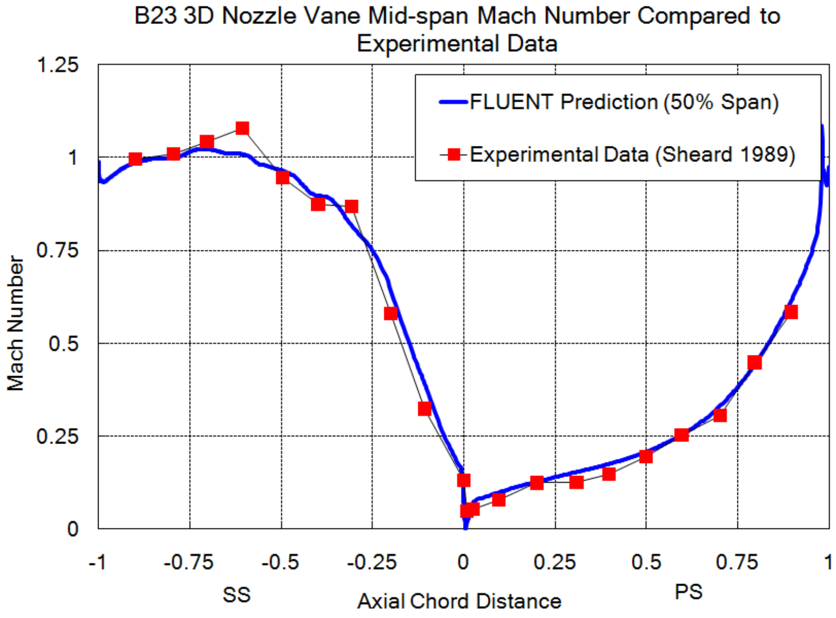

Figure 8.3: Comparison of the 3D NGV surface Mach number and experimental data from Sheard (1989) at 50% span

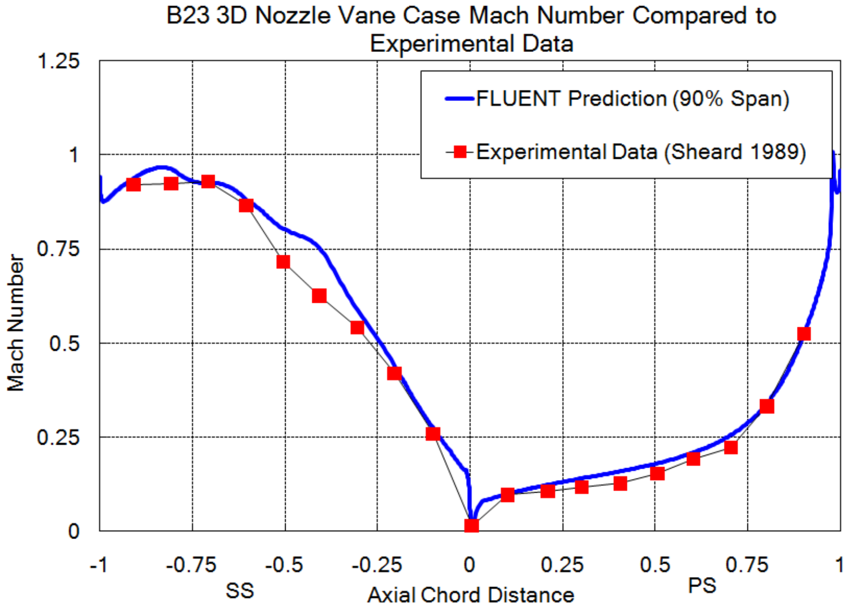

Figure 8.4: Comparison of the 3D NGV surface Mach number and experimental data from Sheard (1989) at 90% span

8.3 3D Inlet Distortions and Heat Transfer Methods

In the heat transfer tests, the baseline uniform inlet case used the same exit Mach number as the Sheard (1989) experiment, but with a gas to wall temperature ratio of 1.5. The vane wall boundary used an isothermal wall temperature of 290K to give an identical gas to wall temperature ratio as the 2D vane study. The uniform inlet turbulence condition was set at 10%. The inlet temperature distortion was similar to those described in Povey et al. (2007). Povey and Qureshi (2008) note the difficulty in ascribing a single metric to characterize the inlet temperature distortion. The hot streak in this study employs a sinusoidal radial temperature profile varying from 0.95 T_{0u} near the hub and case to 1.05 T_{0u} at mid-height on the inlet boundary. An additional sinusoidal circumferential variation is applied to the radial profile, resulting in a peak temperature in the center of the inlet boundary of 1.1 T_{0u}. The overall $\frac{T_{0max}}{T_{0min}}$ for the inlet temperature distortion is 1.16. The inlet turbulence distortion uses a flat radial profile rather than making assumptions about the radial distribution of the turbulence at the inlet to the turbine. Essentially, the focus is on comparing circumferential variation in turbulence primarily at the mid-span, rather than attempting to create a radial profile that accounts for various combustor geometry configurations to the turbulence field (e.g. dilution hole cooling). At mid-span the turbulence variation in the circumferential direction matches that of the 2D vane study and the 2D first stage study. Furthermore, amplitude of the circumferential variation in both the temperature and turbulence profiles tapers smoothly to zero at the endwalls. Figures 8.5 and 8.6 display the idealized radial and circumferential cuts for total temperature and turbulence intensity on the inlet boundary.

Generating the inlet conditions required a similar procedure as in the previous chapters. Two clocking positions for the inlet distortions were introduced to the 3D domain—impinging on the vane leading edge, and directly into the vane passage. After obtaining the inlet velocity fields, the inlet turbulent kinetic energy and specific dissipation rate were derived from the inlet turbulence intensity profile and interpolated onto the inlet domain. In this 3D domain the 2D correction for turbulent kinetic energy was removed. The final inlet total temperature and turbulence intensity distortions impinging on the vane leading edge are displayed in Figures 8.7 and 8.8. Full derivations of the inlet distortions are available in Appendix B.

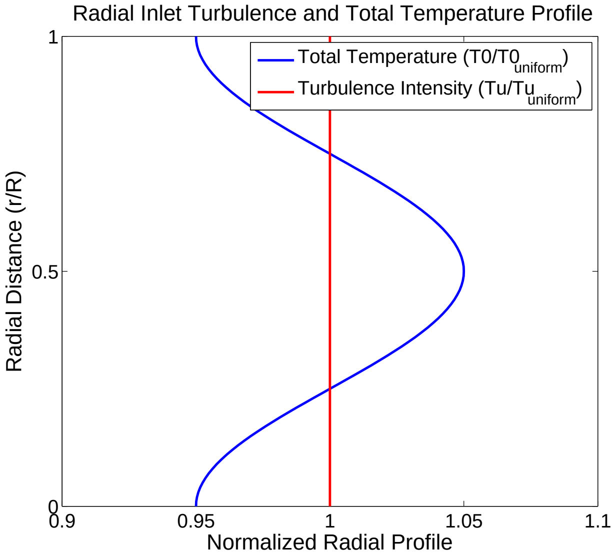

Figure 8.5: Inlet radial temperature and turbulence distortion profile normalized to uniform inlet conditions

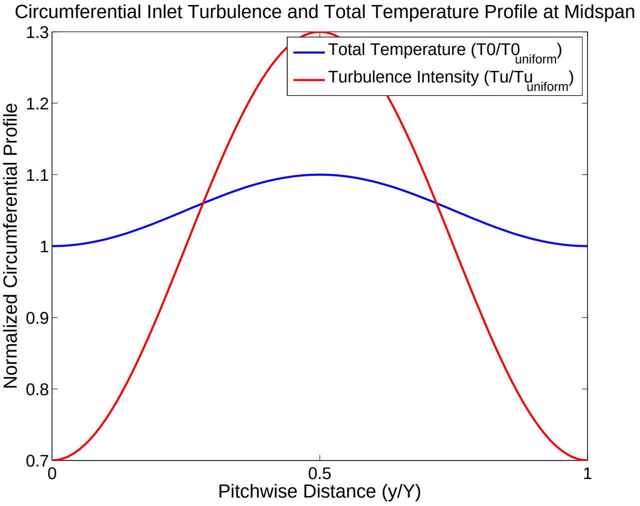

Figure 8.6: Inlet circumferential temperature and turbulence distortion profile normalized to uniform inlet conditions

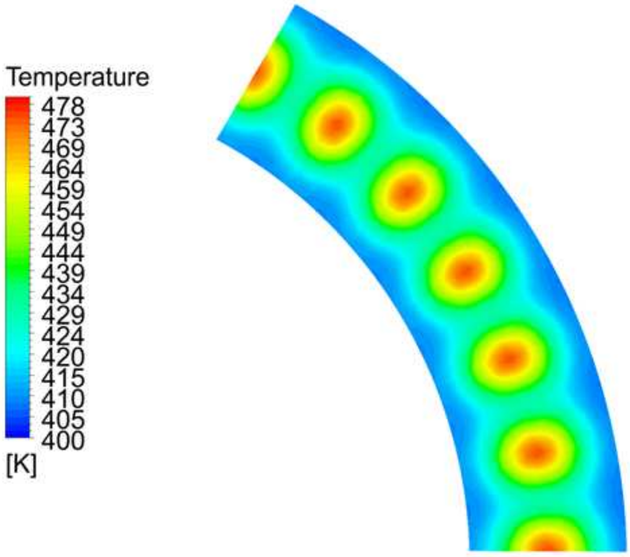

Figure 8.7: Temperature contours at domain inlet illustrating hot streak clocked to middle of NGV passage

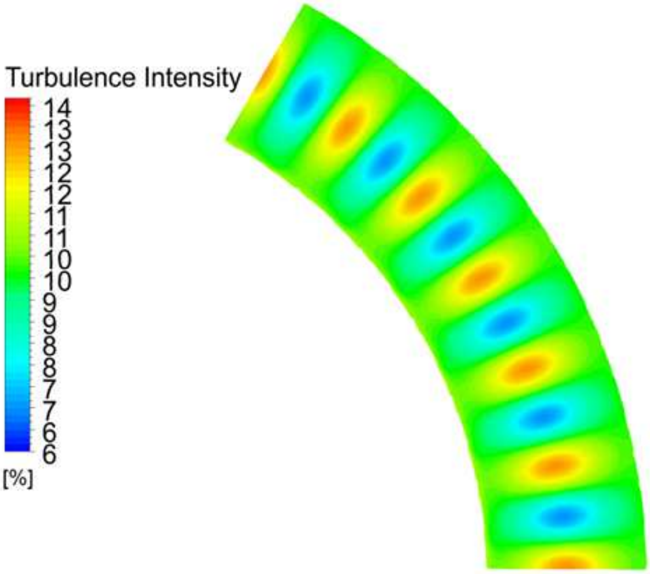

Figure 8.8: Turbulence intensity contours at domain inlet illustrating turbulence distortion clocked to middle of NGV passage

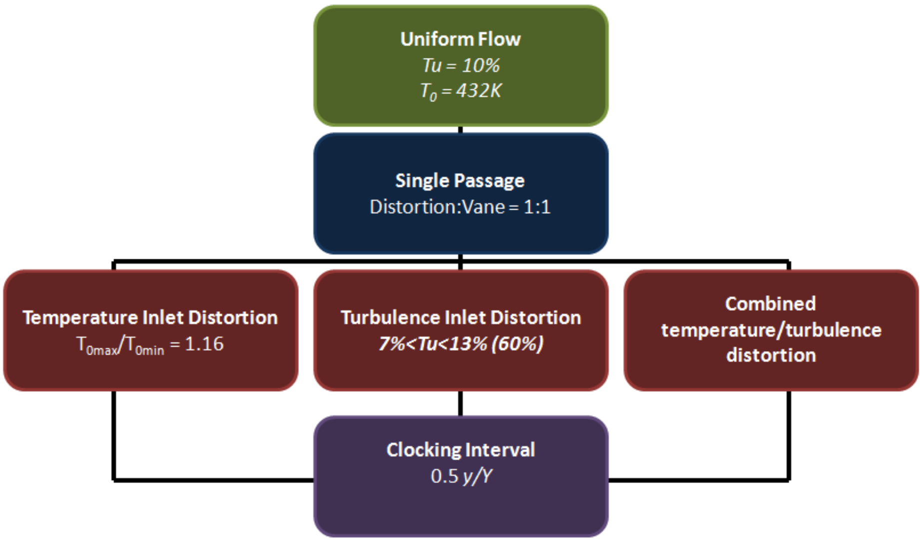

Figure 8.9: Summary of Inlet Profile Variations for the 3D nozzle blade

The final operating map for the various inlet conditions in this case study is displayed in Figure 8.9. The parameters evaluated in this 3D study were restricted in a similar fashion to the 2D first stage study. Only a single amplitude for both the temperature and turbulence is used in this study, and one simulated combustor to vane ratio of 1:1 is employed, and the three types of inlet profiles (turbulence only, temperature only, and combined distortion) were evaluated at two clocking positions (impinging on the NGV leading edge and impinging in the middle of the NGV passage). The reason for the narrower range of clocking positions is that clocking the inlet distortions on the vane leading edge and in the passage had previously demonstrated the highest degree of variation in the vane HTC distribution.

The procedure for determining the 3D vane adiabatic wall temperature and HTC were similar to the 2D vane study. Two isothermal wall boundaries of 290K and 295K were used to generate the requisite surface heat flux distributions. The blade geometry is a complete profile in the center of the domain, rather than the split geometry used in the single passage 2D vane study. In order to isolate the vane suction and pressure surfaces, the face normal vector for each vane-adjacent grid cell was exported and analyzed against the Cartesian coordinate frame. Cells with positive y-values were designated as suction surface elements and vice versa. In order to simplify comparisons, all heat transfer data was converted to augmentation levels according to the following equation:

$$\Phi_{augment} = \frac{\Phi}{\Phi_u} \tag{8.1}$$

where Φ can represent the surface heat flux $\dot{q}$ or heat transfer coefficient h. The heat transfer data was then interpolated onto a 2D grid generated in MATLAB to present the full vane surface along the span-wise and axial chord directions. Similar difficulties relating to aerothermodynamic coupling in shock affected regions of the suction surface were encountered in the 3D study as in the 2D vane study. Therefore the data was truncated to 0.5 C_{ax} on the suction surface. Additionally, some anomalous data in the HTC contours can be seen near the pressure surface trailing edge, this behavior is similarly due to the presence of trailing edge shocks and should be ignored.

8.4 Effects of Inlet Distortion on Nozzle Blade Heat Transfer

Clocking the turbulence distortion upstream of the vane leading edge produced similar results to the 2D vane heat transfer study. Figure 8.10 displays contours of surface heat flux augmentation over the vane surface. The peak augmentation occurs on the pressure side of the leading edge at a peak level between 7% and 8%. The augmentation quickly trails off radially away from mid-span, which is expected as the turbulence peak drops smoothly towards the uniform levels near the endwalls. The pressure surface shows a wider influence of the turbulence distortions effect than the suction surface. This trend was also seen in the 2D vane study. The source of this preferential augmentation on the pressure surface is the slight difference between the stagnation point and the geometric center of the domain inlet.

Figure 8.11 shows that the surface heat flux augmentation is accounted for solely by the variation in HTC on the vane surface. The distribution of the HTC augmentation is very similar to that of the surface heat flux augmentation, and so is the magnitude of the augmentation near the leading edge. The leading edge variation is between 7% and 9%. Meanwhile, sampling of the adiabatic wall temperature data over the vane surface showed that the variation from the uniform flow was less than 1%. Clocking the turbulence distortion to the middle of the vane passage produces inverse augmentation from the previous inlet distortion configuration. Figure 8.12 displays the HTC augmentation on the vane surface for this inlet condition. The

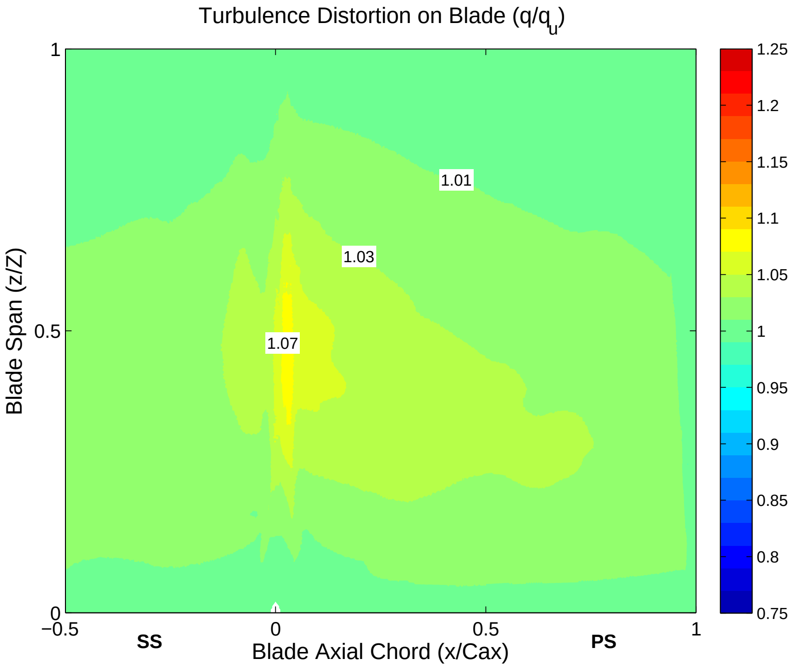

Figure 8.10: 3D NGV surface heat flux augmentation, turbulence distortion on blade

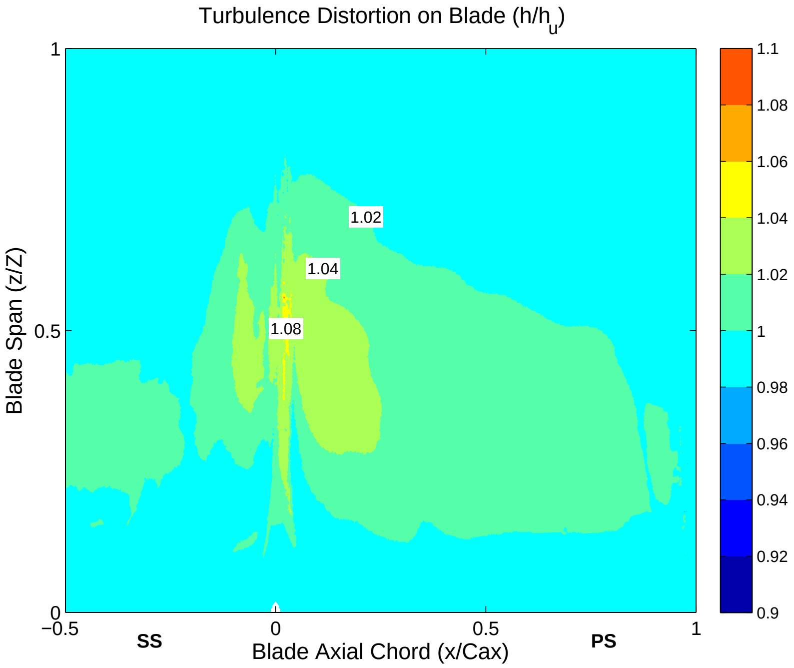

Figure 8.11: 3D NGV surface heat transfer coefficient augmentation, turbulence distortion on blade

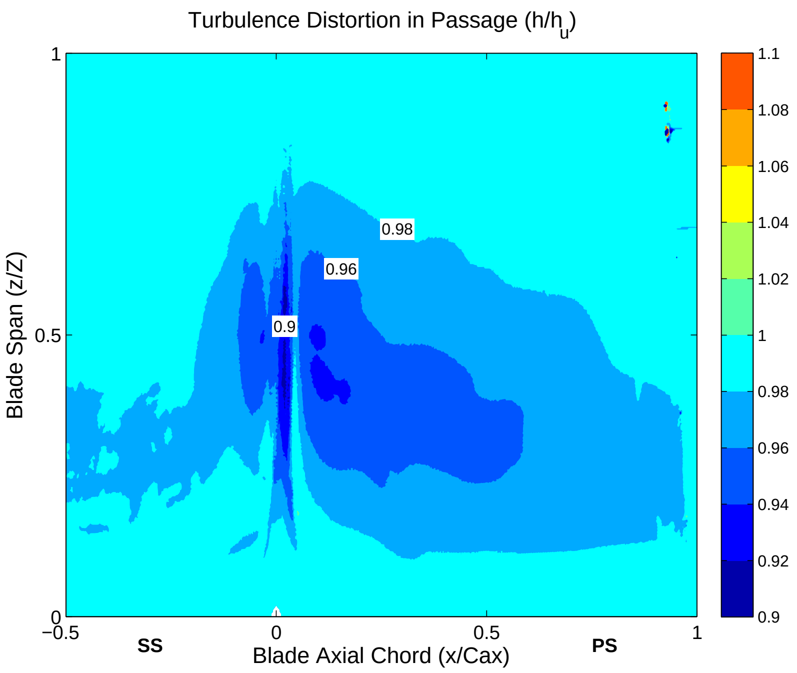

Figure 8.12: 3D NGV surface heat transfer coefficient augmentation, turbulence distortion in middle of blade passage

average HTC reduction near the vane leading edge is about 8%, but as much as 10%.

Clocking the hot streak upstream of the vane leading edge largely has no effect on the vane HTC distribution (Figure 8.13 and Figure 8.14). What variation does occur near the leading edge can be explained by the small variation that would occur due to the change in upstream total temperature (Fitt et al., 1986) as described in the previous chapter. The correlation predicts that for the ratio of peak temperature in the inlet distortion to the uniform inlet total temperature, a variation in HTC up to 3% could be expected. This is approximately the variation seen when clocking the inlet temperature distortion onto the vane leading edge. Overall the relative insensitivity to hot streak clocking agrees with both the 2D vane study and previously mentioned experimental results (Povey et al., 2007). Ultimately the primary contribution from the hot streak to any surface heat flux augmentation is derived from variation in the adiabatic wall temperature.

Contrasting the HTC distribution on the vane surface in Figure 8.13 with the combined turbulence and temperature distribution impinging on the vane leading edge (Figure 8.15) shows a striking variation in the leading edge region surface heat

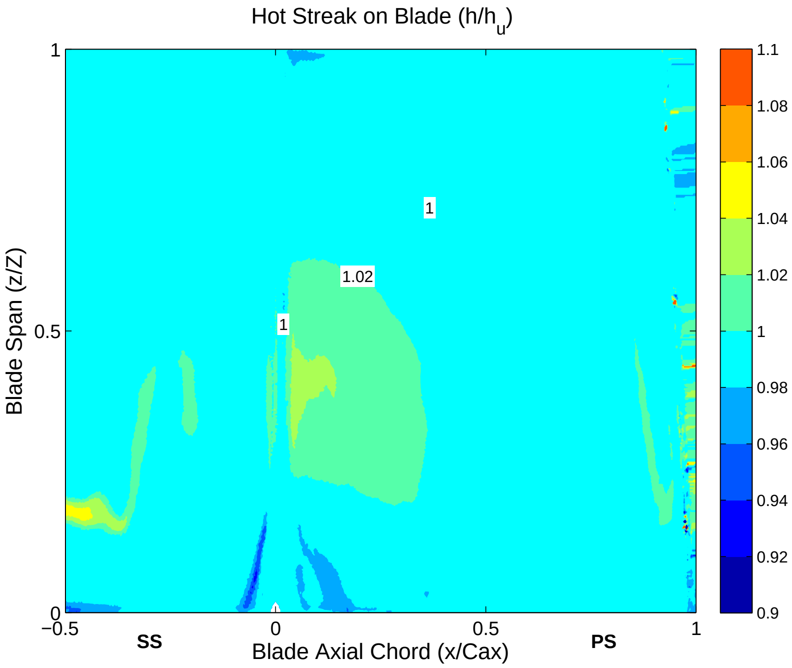

Figure 8.13: 3D NGV surface heat transfer coefficient augmentation, hot streak on blade

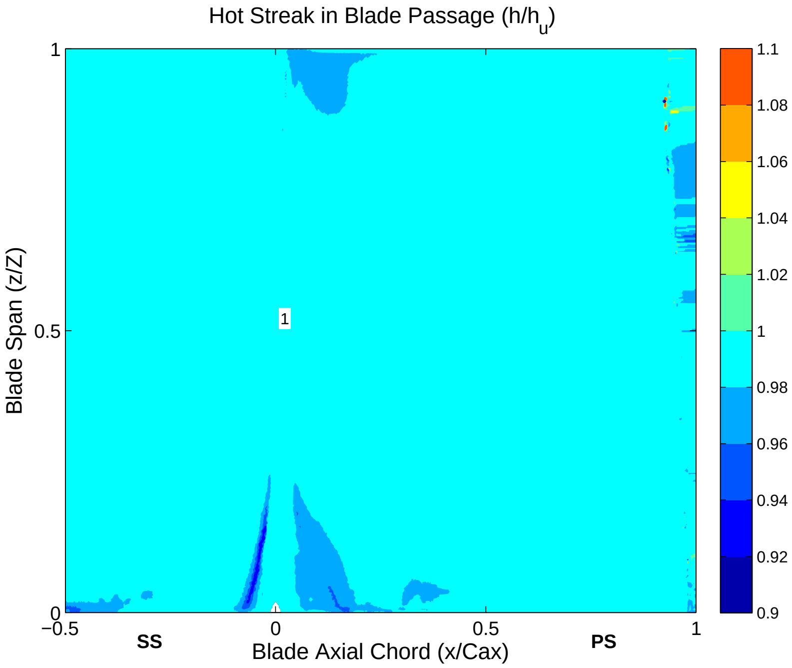

Figure 8.14: 3D NGV surface heat transfer coefficient augmentation, hot streak in middle of blade passage

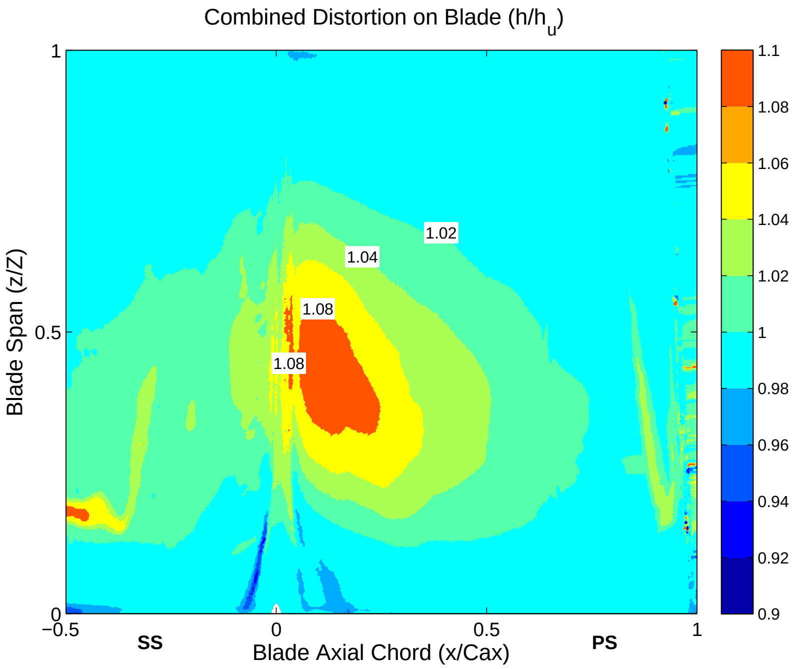

Figure 8.15: 3D NGV surface heat transfer coefficient augmentation, combined distortion on blade

transfer coefficient distribution. There is significant augmentation of the vane HTC leading edge, especially on the pressure surface. This augmentation is in the range of 8% to 9%, and extends to about 0.25 C_{ax} on the pressure surface. The high region of HTC augmentation covers approximately 25% of the vane span as well. On the pressure surface the HTC augmentation near mid-span remains above 5% until about 0.4 C_{ax}.

Clocking the combined distortion to the middle of the vane passage also results in a significant variation in the vane HTC distribution as compared to the configuration with only the inlet hot streak. The average augmentation near the leading edge at mid-span is between 8% and 9%, and peaks at almost 10%. The reduction in vane HTC near mid-span is greater than 5% up to about 0.25 C_{ax}. The radial extent of this distortion is roughly 30% of vane span near the leading edge, although this coverage rapidly diminishes further away from the vane leading edge.

Figure 8.17 summarizes the peak HTC augmentation over uniform conditions due to clocking of the various inlet distortions. Although there is some HTC augmentation seen in clocking the hot streak, it is much smaller compared to both the turbulence

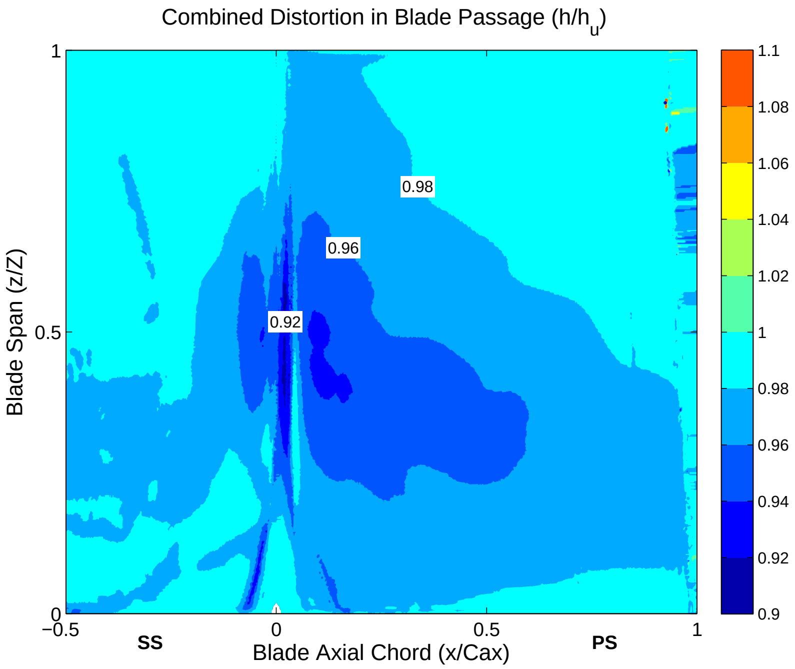

Figure 8.16: 3D NGV surface heat transfer coefficient augmentation, combined distortion in middle of blade passage

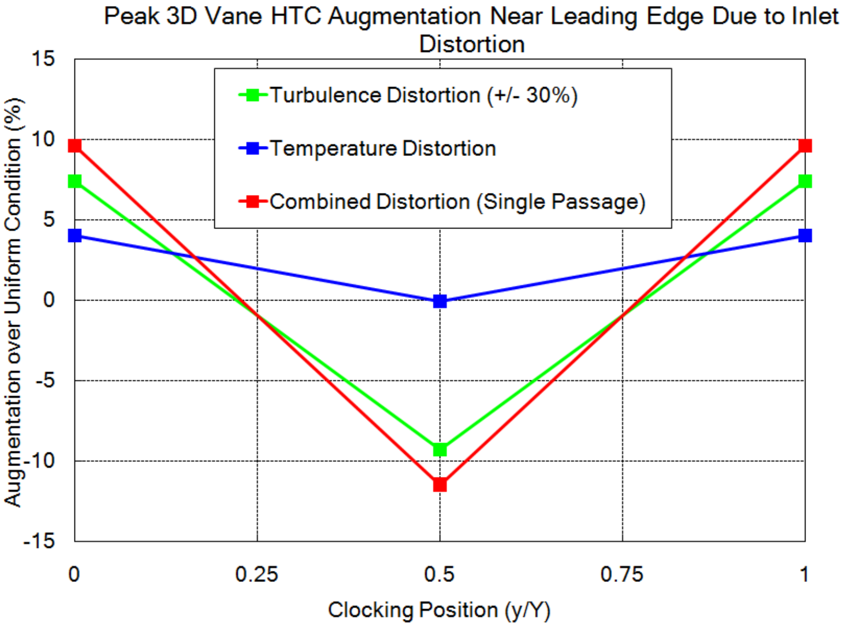

Figure 8.17: Summary of clocking effects for various inlet distortion conditions on vane leading edge region HTC—3D NGV domain

distortion and the combined distortions. Overall, clocking the turbulence distortion with and without the presence of the hot streak results in leading edge region augmentation of the 3D vane HTC could be expected to create variation in the range of 16% to 20%.

8.5 Summary

In summary, this chapter presented the effects of non-uniform inlet conditions on a 3D nozzle guide vane. Validation studies indicated that the numerical model performs well in predicting experimental results for surface pressure at a range of span locations. The expectation was that although the near-wall grid in this domain was coarser than previous studies, it would be sufficient to capture the trends in vane HTC as it responds to varying inlet conditions. The inlet distortions employed in the previous two chapters were expanded to suit the 3D computational domain in this chapter, and the hot streak at the inlet is based on a previously used experimental hot streak. The heat transfer methodology employed in Chapter 6 was re-used in this chapter.

The presence of turbulence distortions upstream of the vane resulted in augmentation between 14% and 17% depending on clocking position. Applying the hot streak only at the inlet to the domain resulted in no significant variation in the vane surface HTC distribution. Meanwhile, clocking the combined distortion at the inlet to the domain produced variation in the range up to 20%. There appears to be a synergistic effect of the combined distortion on the vane HTC distribution. There was additional peak augmentation around 2%, and the extent of the higher levels of augmentation was significantly larger as compared to the turbulence distortions alone. However, in general the 3D domain results appear to largely concur with the 2D vane heat transfer study.

Chapter 9

Conclusions

9.1 Summary and Conclusions

The goal of this thesis has been to investigate the influence of non-uniform inlet turbulence distributions on HPT heat transfer. This objective has been accomplished using an extensively validated numerical tool on case studies of 2D and 3D NGV geometries in steady flow, and on a 2D HPT first stage in unsteady flow subjected to a variety of non-uniform inlet flow conditions. The important findings contained in this thesis and their implications are summarized below.

Solver Formulation Case Study The first string of research conducted in this thesis aimed to evaluate the performance of the pressure-based solver outside of its originally intended low Mach number regime. Two forms of the pressure-based solver were used (coupled and segregated) and their performance was compared to the density-based solver. Aerothermal experimental data from a NACA 0012 airfoil and the ACE HPT rotor profile served as the validation source for the numerical results. The pressure-based solvers were both significantly faster than the density-solver. For example in the NACA 0012 airfoil study, the density-based solver took approximately 0.9 seconds per iteration, whereas the pressure-based segregated solver took 0.7 seconds per iteration and the pressure-based coupled solver used only 0.3 seconds per iteration. The sensitivity of the surface pressure and heat transfer predictions were minimal between the three solver formulations, but the pressure-based solvers slightly out-performed the density-based solver in predicting the location of the standing normal shock wave on the NACA airfoil surface. In the unsteady simulation, the pressure-based solver required significant modification of various under-relaxation factors in order to reach a converged solution. In fact only the pressure-based coupled solver actually converged. In comparison the density-based solver smoothly drove to convergence in only 20 periods of the passing upstream bar. In this case the density-based solver proved to be the optimal choice of solver formulation. However, it seems that in steady flow conditions, the pressure-based solver is as capable, and in some ways superior to the density-based solver in the transonic Mach number regime.

Turbulence Model Case Study The primary goal of this vein of research was to identify a high-performing turbulence model for the transonic turbine blade geometries used throughout the work. The motivation for this study stemmed from the lack of relative generality for turbulence model performance seen in the literature. Two additional sub-objectives were embedded in this study. The first was to validate the ability of the solver to accurately predict the aerothermal conditions for the rotor and NGV profiles tested in order to establish confidence in the later studies of non-uniform inlet conditions. The second was to perform additional tuning, if necessary, on the final turbulence model to further establish confidence in its predictive capabilities. The ACE rotor blade was the first geometry tested, and the accuracy of the surface pressure prediction on the pressure surface was very good for the $k-\omega$ SST and SA turbulence models. The blade surface Mach number under-prediction on the suction surface was due to the use of a 2D computational domain, and additional simulations including the experimental hade angle of 10° confirmed that the turbulence models were performing correctly. In the experiment the freestream turbulence intensity was 3%, leading to a transitional boundary-layer on the frontal ACE suction surface. Therefore the predictions for all four turbulence models were very poor on the ACE suction surface. The $k-\omega$ SST model performed the best in predicting the turbulent boundary-layer heat transfer. Its predictions were within 20% on these areas of the rotor surface. This level of accuracy in predicting the absolute values of steady rotor heat transfer was also demonstrated on the B22 rotor. The scope of the turbulence model study was narrowed for the B22 rotor, and only the SA model was tested in addition to the $k-\omega$ SST model. The trends in insensitivity of surface pressure prediction between the two turbulence models was repeated for the B22 rotor, as well as the slightly improved heat transfer prediction for the $k-\omega$ SST model as compared to the SA model. The two models responded accurately to the variation in freestream turbulence intensity from 0.4% to 4.5% by predicting the turbulent boundary-layer heat transfer augmentation of 10% to 30% seen in the experimental results. Ultimately the heat transfer results from the unsteady flow simulations confirmed that the $k-\omega$ SST model was the consistently superior turbulence model for predicting rotor heat transfer, and was selected for final tuning. Correcting the basic FLUENT relationships for the inlet turbulence boundary conditions led to satisfactory results for the prediction of turbulence propagation through the C3X vane passage. The tuned $k - \omega$ SST model also demonstrated an increased ability to predict NGV heat transfer to within 15% of experimental values when the NGV boundary-layer was turbulent. The high degree of sensitivity in predicted heat transfer results to turbulence model formulation witnessed in the steady flow validation indicates that such sensitivity studies should be a prerequisite for any numerical study of turbine heat transfer using RANS turbulence models.

Unsteady Rotating Bar Wake Generator Case Study There were two motivations for this particular study. The first was to determine the ability of the numerical solver to predict the complex unsteady environment resulting from simulated blade row interactions in transonic flow. The unsteady ACE simulation in particular generated multiple shock reflections propagating through the rotor blade rows in both upstream and downstream directions. The second goal was to identify any flow interactions embedded the unsteady environment that were previously hidden due to the limitations in experimental measurements and available numerical tools when the experimental work was originally conducted at Oxford University. In the unsteady ACE simulation, the two turbulence models were both very successful in predicting both the time-averaged and unsteady pressure fluctuations in the flowfield. Furthermore, qualitative analysis of flowfield showed that the models captured all of the salient unsteady interactions between the passing bar and the rotor blade row, including the shock-induced separation bubble on the rotor pressure surface. The performance of the two turbulence models in predicting unsteady heat transfer for the B22 rotor showed the same trends as their performance in predicting steady B22 heat transfer. As mentioned previously this led to the use of the $k - \omega$ SST model solely in the remainder of the work. In the experimental results for the unsteady B22 heat transfer, the time-averaged heat transfer on the suction surface was lower than the steady flow. This observation seems counter-intuitive as the expectation is that the wake would increase the heat transfer by tripping the otherwise laminar boundary-layer in this region of the blade. The fully turbulent solution provided by the $k - \omega$ SST model also demonstrated this reduction in time-averaged heat transfer, and the cause was found to be the expansion wave associated with the passing upstream bar. Overall the study established a high level of confidence in the ability of the solver to predict unsteady inviscid interactions associated with shock waves and potential interactions between the rotating bar and rotor blades. Additionally, the accuracy of heat transfer predictions from the $k - \omega$ SST turbulence model were consistent with steady flow results. This consistency, as well as the model's ability to pick up the relative trend between steady and unsteady time-averaged heat transfer on the rotor suction surface, established confidence that the model would provide reasonable predictions of absolute levels of heat transfer and be able to accurately respond to variation in inlet conditions upstream of a given turbine blade geometry. This last point is particularly important when considering the effectiveness of the model in predicting the effects of non-uniform conditions at the domain inlet.

Effects of Non-Uniform Inlet Turbulence Distortions on 2D NGV Heat Transfer The goal of this case study was to introduce and analyze the effects of turbulence, temperature, and combined temperature and turbulence distortions at the inlet to a 2D NGV blade row. Heat transfer results were generated via two solutions of the flow with slightly different wall temperatures on the NGV surface and a system of convective heat transfer equations. This study evaluated a range of inlet distortion configurations. The parameters that were varied included turbulence distortion amplitude, various clocking intervals for all types of distortion, and simulated distortion to NGV blade counts of 1:1 and 1:2. The baseline configuration of the turbulence distortion produced a peak variation in NGV HTC near the leading edge greater than 17% when the peak of the distortion was shifted from upstream of the NGV leading edge to the middle of the NGV passage. Clocking the hot streak alone from the NGV leading edge to the middle of the NGV passage resulted in little to no variation in the NGV HTC distribution. This result matches previous experimental results. Meanwhile, the introduction of the combined temperature and turbulence distortion at the inlet to the domain results in similar augmentation of the NGV HTC distribution as did the turbulence distortion alone. Changing the circumferential length scale of the inlet distortions to the distortion to NGV count of 1:2 showed no significant variation from the results of the smaller circumferential wavelength. The effect of the inlet distortions on the NGV exit conditions was to produce redistribution in the NGV exit turbulence intensity, which provided the foundation for further study on a downstream rotor blade row. Overall, the effect of the inlet turbulence distortions and inlet hot streaks is to independently augment the vane heat transfer. The turbulence distortion results in a change in the NGV HTC distribution, while the hot streak affects the NGV T_{aw} distribution.

Effects of Non-Uniform Inlet Turbulence Distortions on 2D HPT First Stage Heat Transfer The goal of this study was to evaluate the effects of the inlet turbulence distortions on a downstream rotor blade row. Overall, the time-averaged effect of the turbulence distortion alone on rotor heat transfer was minimal. When combined with the inlet hot streak there was some time-averaged increase in the rotor pressure surface HTC distribution as compared to the hot streak alone. The maximum value of this additional time-averaged augmentation was only about 3% however. Rotor HTC unsteadiness was slightly increased by about 4% when turbulence distortion was clocked from the NGV leading edge to the middle of the NGV passage. This increase in unsteadiness was much less than that due to the hot streak alone, which increased unsteadiness by 10% to 18%. The combination of the two distortions appeared to have a summative effect on rotor HTC unsteadiness. The implications of these findings are that the rotor HTC distribution can also be affected by the inlet hot streak, and that the primary contribution of the inlet turbulence distortion to the rotor HTC environment is a small increase in the unsteady HTC component, rather than the time-averaged HTC.

Effects of Non-Uniform Inlet Turbulence Distortions on 3D NGV Heat Transfer The goal of this final study was to evaluate the effects of the inlet distortions previously studied on a 3D NGV geometry. The results largely concurred with those found in the study of 2D NGV heat transfer. The combined inlet distortion produced variation in the NGV HTC distribution by about 20%. The clear and consistent message these results support is that the distribution of the inlet turbulence intensity field is as important for the heat transfer design as the mean turbulence intensity level at the inlet to the high pressure turbine.

9.2 Recommendations for Future Work

To the author's knowledge this thesis represents the first characterization of the effects of circumferential variation in inlet turbulence intensity on HPT first stage heat transfer. The clear influence on NGV HTC due to circumferentially-varying inlet turbulence intensity profiles shown in the results indicates that these engine-representative flow conditions need to be incorporated into future experimental research to further evaluate the effect of inlet turbulence distortions on turbine heat transfer. There are several questions that remain unanswered. For example, the solver is limited to fully turbulent solutions, and therefore the influence of these distortions on a possible laminar or transitional boundary-layer near the NGV leading edge have not been evaluated. Furthermore the effects, if any, of these circumferential inlet turbulence distortions on NGV endwall heat transfer are poorly understood due to the limited computational resources available for this study. As a result, NGV endwall heat transfer represents an additional avenue of future research for both computational and experimental studies. All studies conducted in this thesis assumed that the turbine blades were uncooled. Therefore the interaction between the inlet turbulence distortions and any blade cooling technologies is a gap in the literature that could be exploited in future research. Ultimately, the significant variation in NGV HTC demonstrated indicates a potentially wide avenue of future study for the turbine heat transfer engineer.

Appendix A

Computational Geometries and Grids, and Boundary Conditions

The purpose of this appendix is to provide a quick reference for the geometry details and boundary conditions used in the various computational domains found in this thesis. This data is presented at the end of the thesis so as not to break the continuity of the previous chapters. The parallel objective is to provide a single reference point for a wide variety of flow conditions that would otherwise need to be found in multiple theses. This appendix provides a snapshot of the computational domain, including tables of important geometry measurements in the domain. Any pertinent notations follow the table.

NACA 0012 Airfoil

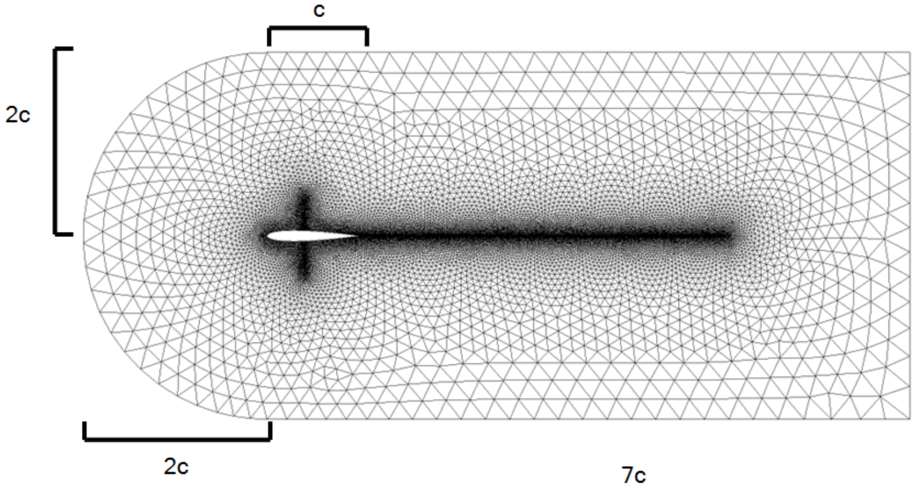

Figure A.1: NACA 0012 airfoil grid and geometry information

Table A.1: Reference data for NACA 0012 airfoil

Parameter	Value
c	210 mm
P_∞	85.267 kPa
M_∞	0.8
T_∞	242 K

Notes: This study utilized a pressure farfield boundary condition at the limits of the domain, therefore the boundary conditions are in a different format as compared to the other cases. Experimental conditions used for this study are found in Thibert et al. (1979).

Steady ACE Rotor

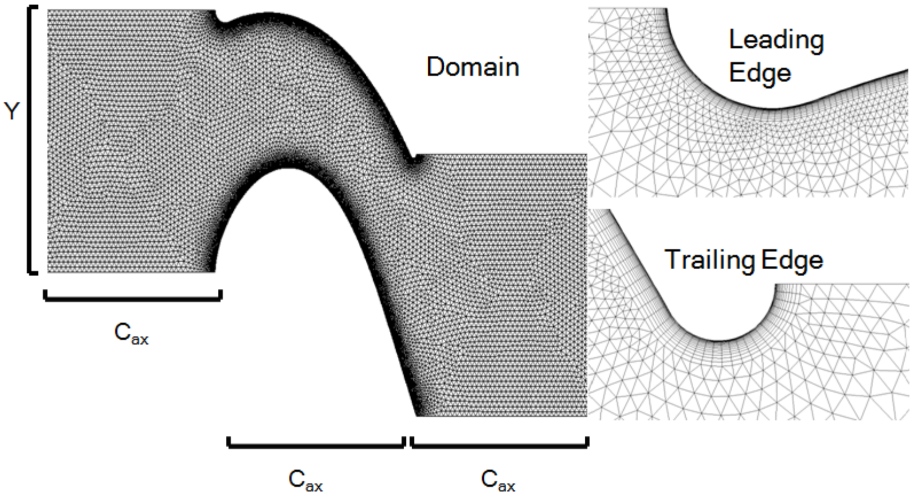

Figure A.2: Steady ACE rotor airfoil grid and geometry information

Table A.2: Reference data for ACE rotor blade

Parameter	Value
C_{ax}	34.002 mm
Y	34.3 mm
P_{0p}	164 kPa
T_{0p}	300 K
P_{3p}	70 kPa
P_{0q}	290 kPa
T_{0q}	460 K
P_{3q}	123 kPa
Tu	3%
Λ	7.6 mm
M_i	0.38
Rotor Incidence Angle	48°

Notes: The experimental results used two separate gas to wall temperature ratios (and hence Reynolds numbers) for the measurements of pressure (subscript p) and heat transfer (subscript q). Turbulence measurements were the same for both flow conditions. Experimental data for this study is drawn from Johnson (1988).

Steady B22 Rotor

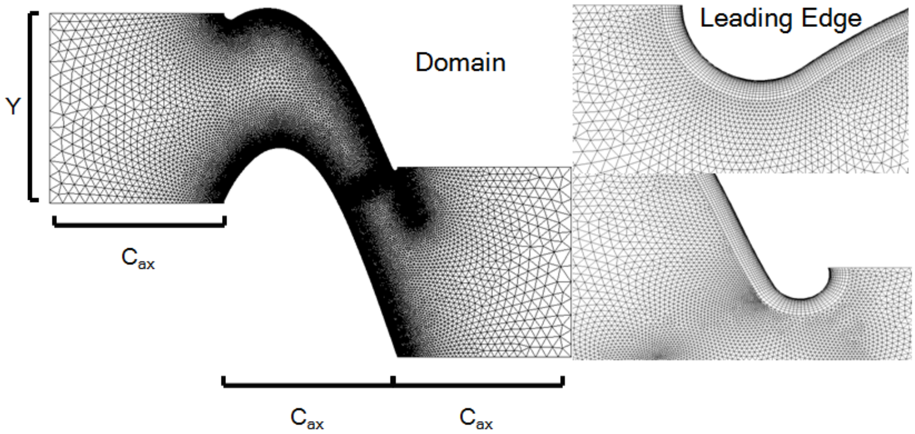

Figure A.3: Steady B22 rotor airfoil grid and geometry information

Table A.3: Reference data for B22 rotor blade

Parameter	Value
C_{ax}	51.9 mm
Y	56.7 mm
P_0	331 kPa
T_0	432 K
P_3	183.1 kPa
Tu_{hi}	4.5%
Λ_{hi}	7.6 mm
Tu_{low}	0.4%
Λ_{low}	4.2 mm
M_i	0.315
Rotor Incidence Angle	42.75°

Notes: Two experimental freestream turbulence conditions were tested for this rotor blade. The experimental data used to generate the boundary conditions is from Doorly (1983).

Unsteady ACE Rotor

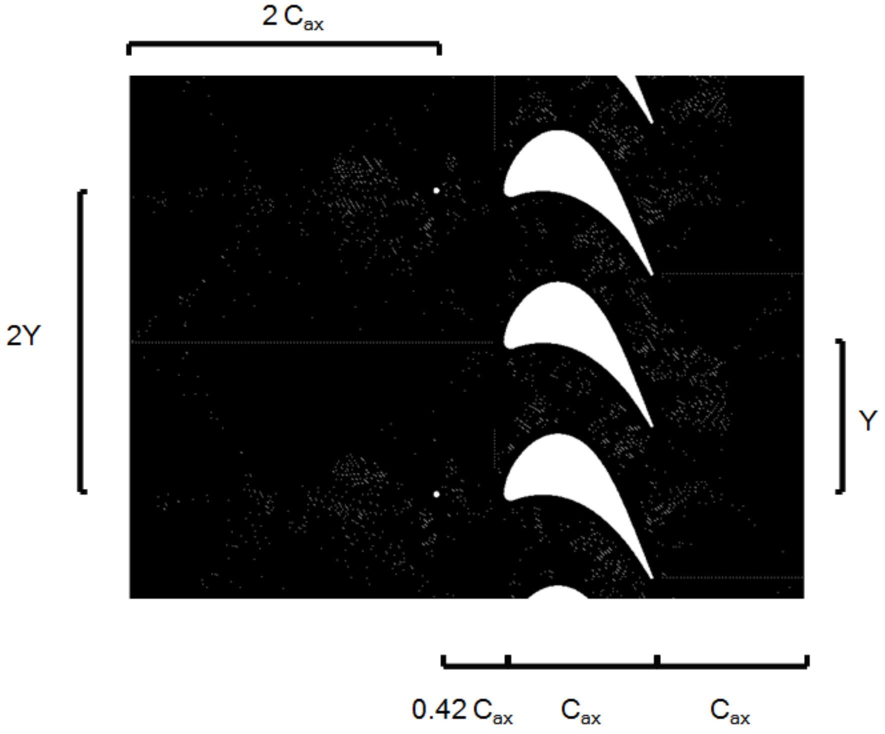

Figure A.4: Unsteady ACE rotor airfoil grid and geometry information

Table A.4: Reference data for unsteady ACE rotor blade

Parameter	Value
M_{bar}	1.18
d	1.6 mm

Notes: The above figure illustrates multiple periods of the computational domain. All other geometry and flow conditions are identical to the steady flow values.

Unsteady B22 Rotor

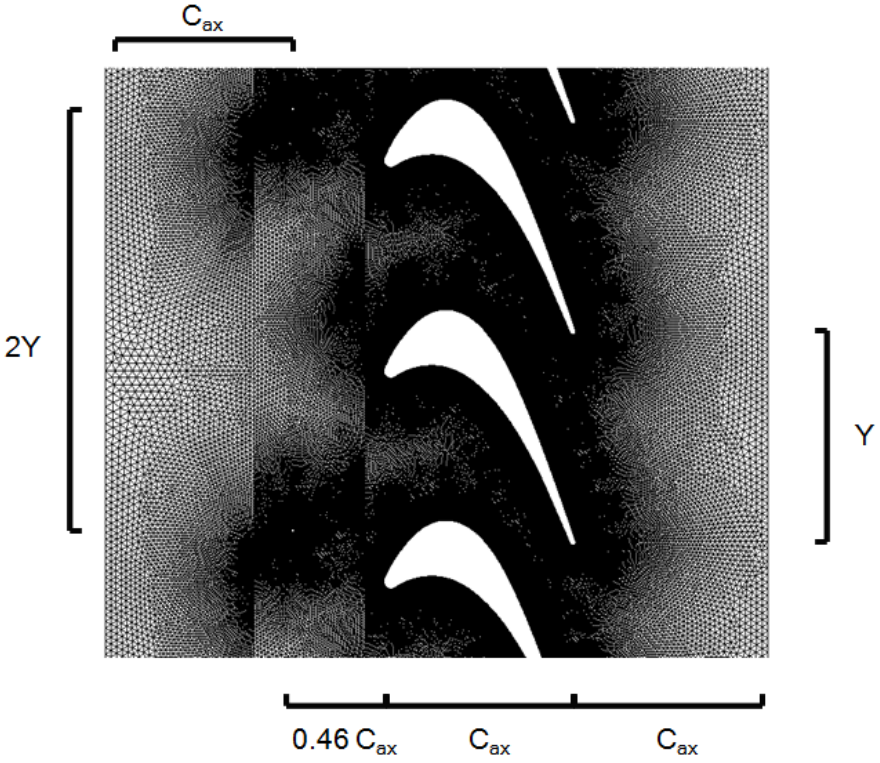

Figure A.5: Unsteady B22 rotor airfoil grid and geometry information

Table A.5: Reference data for unsteady B22 rotor blade

Parameter	Value
M_{bar}	0.96
d	0.9 mm

Notes: The above figure illustrates multiple periods of the computational domain. All other geometry and flow conditions are identical to the steady flow values.

C3X NGV

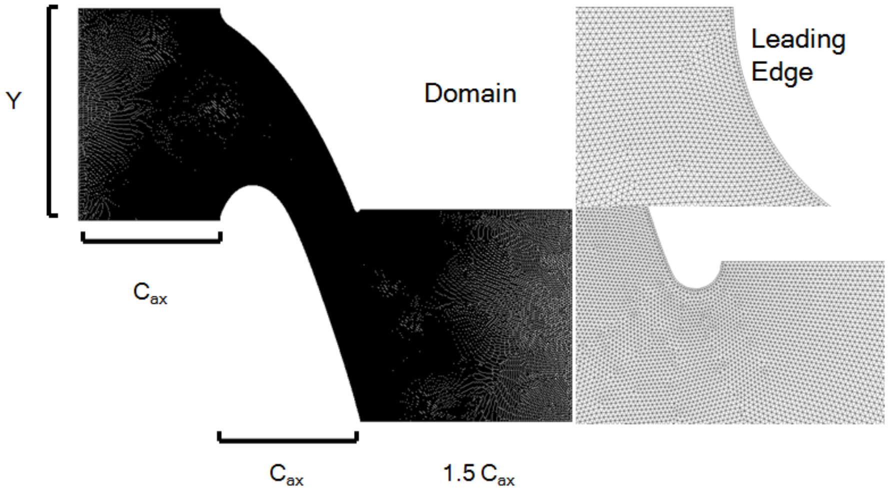

Figure A.6: C3X NGV airfoil grid and geometry information

Table A.6: Reference data for C3X NGV

Parameter	Value
C_{ax}	7.816 cm
Y	11.773 cm
P_0	95.1 kPa
T_0	301 K
P_2	90.4 kPa
Tu_{grid}	7.8%
Λ_{grid}	1.28 cm
$k_{corrected}$	$5.77\ \frac{m^2}{s^2}$
$\omega_{corrected}$	$2780\ s^{-1}$

Notes: The turbulence values presented here are the raw experimental measurements and the corrected values for the turbulent kinetic energy k and specific dissipation rate ω for reference. The two sets of values are both derived from the grid generated turbulence conditions in Ames (1994).

B23 NGV

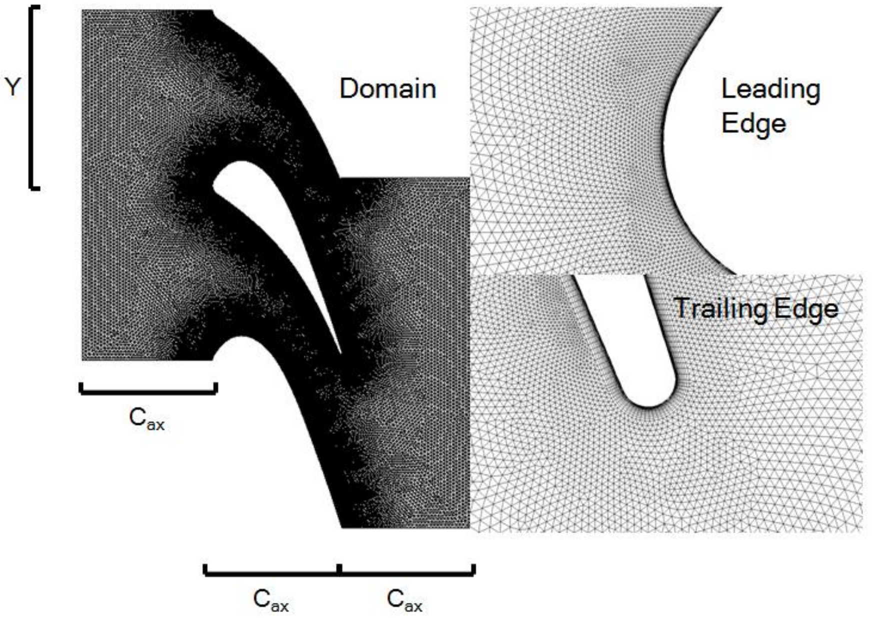

Figure A.7: B23 NGV airfoil grid and geometry information

Table A.7: Reference data for B23 NGV

Parameter	Value
C_{ax}	36.8 mm
Y	48.96 mm
P_0	853.6 kPa
T_0	432 K
P_2	488.4 kPa
Tu	4.5%
Λ	7.6 mm

Notes: The domain presented here is the two-passage domain used in the non-uniform inlet distortion study. Identical mesh strategies were employed for this domain and the single passage domain. Flow conditions reported in the above table are for the validation case study of the B23 NGV, derived from Nicholson (1981).

2D HPT First Stage

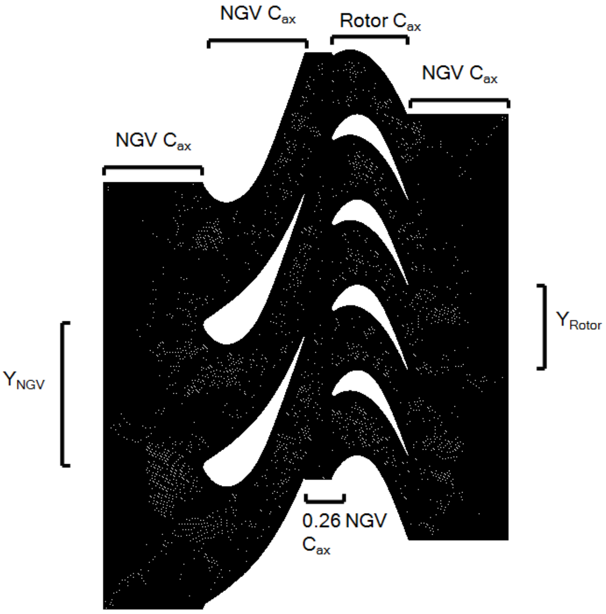

Figure A.8: 2D HPT first stage grid and geometry information

Table A.8: Reference data for 2D HPT first stage

Parameter	Value
NGV C_{ax}	31.98 mm
Rotor C_{ax}	24.21 mm
Y_{NGV}	44.51 mm
Y_{Rotor}	26.7 mm
P_0	804 kPa
T_0	432 K
P_3	282 kPa
U_{Rotor}	174 $\frac{m}{s}$
M_i	0.18
M_2	0.7
M_{2rotor}	0.32
M_{3rotor}	1.04

Notes: The domain presented here represents 2D constant streamtube profiles of the Oxford Rotor Facility blade geometries at mid-span. The starting point for the flow conditions in this domain is the experimental data from Sheard (1989).

3D B23 NGV

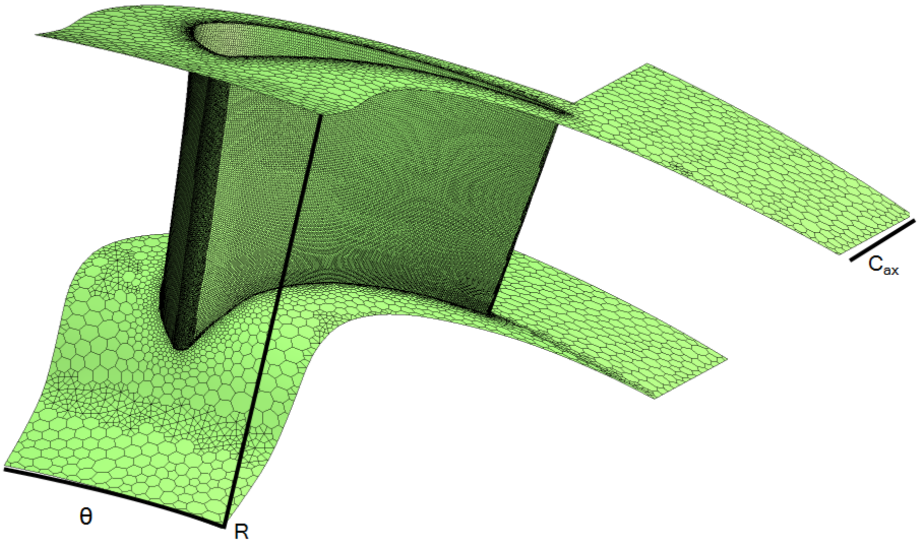

Figure A.9: 3D B23 NGV airfoil grid and geometry information

Table A.9: Reference data for 3D B23 NGV

Parameter	Value
C_{ax}	41.21
θ	10°
R	67.33 mm
P_0	804 kPa
T_0	432 K
P_2	450 kPa

Notes: The flow conditions reported above are the initial conditions for the validation of the 3D NGV surface pressure. The axial chord and inlet and exit conditions are based on mid-span experimental results from Sheard (1989).

Appendix B

Generation of Inlet Distortions

The bulk of this research introduced non-uniform inlet turbulence distortions to various computational domains to assess their effects on turbine blade heat transfer. The aim of this appendix is to detail the process for generating these inlet turbulence distortions.

Initially, these distortions were tested on 2D computational domains. The shape of the distortions was a simple sinusoidal profile according to the equation:

$$\Phi = Asin(Bx + C) + D \tag{B.1}$$

Where Φ can either be the inlet total temperature of the inlet turbulence intensity. The coefficient B is dictated by the pitch of the downstream NGV, C is determined by the desired clocking position of the inlet distortion, and the other coefficients depend on the variable modelled in the distortion. The procedure for generating the complete sequence of inlet conditions first requires converged velocity magnitude data from the inlet of the domain for the uniform inlet temperature and any cases with inlet temperature distortions. The inlet velocity data is then matched to either a uniform inlet turbulence intensity level of 10% or a given sinusoidal distribution. The four possible combinations are uniform inlet, turbulence distortion only, temperature distortion only, and combined temperature and turbulence distortion. The inlet turbulence is assumed to be isotropic, with a length scale of 7.6 mm. The equations derived for the tuned $k - \omega$ SST turbulence model in Chapter 6 are then applied to convert the velocity, Tu, and length scale values into profiles of turbulent kinetic energy k and specific dissipation rate ω at the inlet to the domain:

$$k = (V \cdot Tu)^2 \tag{B.2}$$

$$\begin{aligned} \omega &= \frac{\sqrt{k}}{AC_\mu^{0.25}l} \\ A &= .118 \end{aligned} \tag{B.3}$$

The final inlet turbulence intensity profiles were then double-checked against the uniform turbulence condition by a simple average of all the values of Tu. This verification was also performed for the inlet temperature distortion to ensure that the mean value matched the uniform inlet total temperature. In both cases the circumferentially averaged results perfectly matched the uniform flow conditions.

Producing the inlet distortions for the 3D NGV computational domain was a slightly more complex exercise. The topology of the inlet temperature distortion is roughly modelled on those used in Povey and Qureshi (2008). In order to be compared to the uniform flow conditions, the overall averaged total temperature at the inlet $\overline{T}_{0overall}$ must be equal to the uniform inlet total temperature. In order to accomplish this, the average of the radial variation in total temperature $\overline{T}_{0radial}$ was also set equal to the uniform inlet total temperature. These constraints were similarly applied to the inlet turbulence distortions to ensure that they matched the uniform inlet turbulence intensity level of 10%. The mathematical description of the distortion can be summarized in three functions: two sinusoids traveling in the radial and circumferential directions, and a Gaussian profile fitted to the amplitude of the circumferential flow variation for the purpose of minimizing the circumferential variation near the endwalls:

$$\begin{aligned} \Phi &= A_{overall}sin(B_{overall}\theta + C_{overall}) + \Phi_{radial} \cdot \Phi_u \\ A_{overall} &= A_{circumferential}[0.5(\frac{1}{\sqrt{2\pi\sigma^2}}e^{-\frac{(x-\mu)^2}{2\sigma^2}})] \\ \Phi_{radial} &= A_{radial}sin(B_{radial}r + C_{radial}) + 1 \end{aligned} \tag{B.4}$$

The coefficients B and C are constants associated with the radial and circumferential bounds of the inlet geometry, as well as adjustments for the position of the distortion peaks. The coefficient A is determined by the magnitude of the inlet distortion. The variables μ and σ are the mean value and the standard deviation of the damping function. These parameters are scaled to ensure that the peak value of the distortion occurs at 50% of the inlet boundary radius. The variable x is the radial coordinate r scaled by the radius of the inlet boundary R. In order to actually apply these equations to the domain, a very fine mesh quadrilateral mesh with $1.5 \cdot 10^5$ cells was generated to discretize the geometry of the inlet boundary and obtain the radial and angular coordinates. The above system of equations was then solved at each of the points for the inlet temperature distortion. The very high resolution of the initial grid ensured that the baseline model of the inlet distortion was very close to the analytical solution of the above equations based on the geometric constraints of the inlet planebefore interpolating the distortion onto the actual computational domain grid. Two series of checks were placed into effect to ensure that the area average of the inlet temperature distortion used in the study matched the uniform temperature conditions. The first check was performed on the high-resolution "ideal grid", and the second was an area average performed on the converged solution values extracted directly from FLUENT. The FLUENT area averaged values for the inlet temperature distortion differed by less than 1 K from the uniform inlet total temperature, indicating the method was successful. A similar procedure to the 2D domains then retrieved the cell-centered inlet velocity data from the converged solutions for uniform inlet total temperature and the two clocking positions of the inlet temperature distortion. This resulted once again in four possible combinations of uniform inlet, turbulence distortion only, temperature distortion only, and combined temperature and turbulence distortion. The only variation in the above equations was to expand the turbulent kinetic energy k to accommodate the 3D flowfield:

$$k = 1.5(V \cdot Tu)^2 \tag{B.5}$$

The overall average of the turbulence intensity was also checked against the uniform value of 10% from the FLUENT values, and the absolute variation in Tu was less than 0.1% off of the uniform flow. The final inlet distortions were previously shown in Chapter 8, and are presented once again for immediate reference.

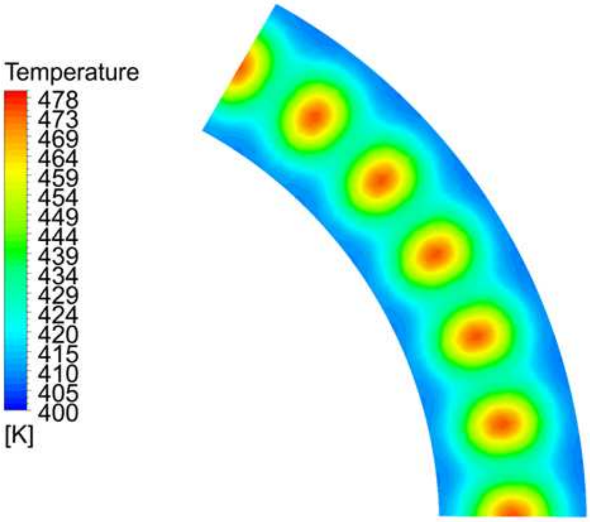

Figure B.1: Temperature contours at domain inlet illustrating hot streak clocked to middle of NGV passage

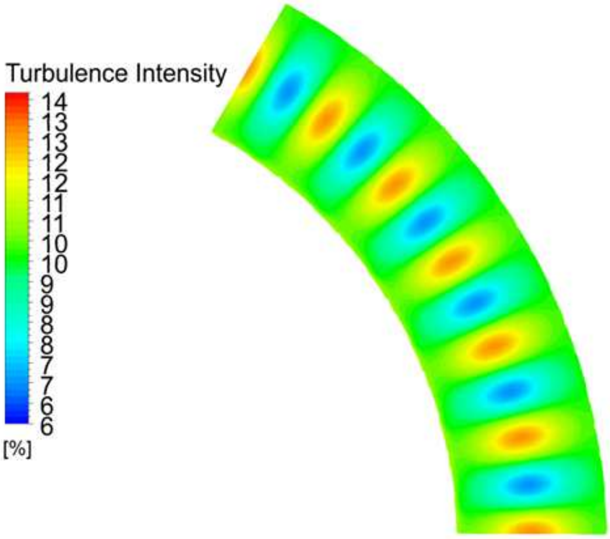

Figure B.2: Turbulence intensity contours at domain inlet illustrating turbulence distortion clocked to middle of NGV passage

References

Abhari, R., 1991, “An experimental study of the unsteady heat transfer process in a film cooled fully scaled transonic turbine stage,” Ph.D. thesis, Massachusetts Institute of Technology.

Allan, W., Ainsworth, R. and Thorpe, S., 2008, “Unsteady heat transfer measurements from transonic turbine blades at engine representative conditions in a transient facility,” *Journal of Engineering for Gas Turbines and Power*, vol. 130, no. 4 pp. 1–12.

Ames, F., 1997, “The influence of large-scale high-intensity turbulence on vane heat transfer,” *Journal of Turbomachinery*, vol. 119, no. 1 pp. 23–30.

Ames, F., 1998, “Aspects of vane film cooling with high turbulence: Part I-Heat transfer,” *Journal of Turbomachinery*, vol. 120, no. 4 pp. 768–776.

Ames, F., Argenziano, M. and Wang, C., 2004, “Measurement and prediction of heat transfer distributions on an aft-loaded vane subjected to the influence of catalytic and dry low NOx combustor turbulence,” *Journal of Turbomachinery*, vol. 126, no. 1 pp. 139–149.

Ames, F., Barbot, P. and Wang, C., 2003a, “Effects of aeroderivative combustor turbulence on endwall heat transfer distributions acquired in a linear vane cascade,” *Journal of Turbomachinery*, vol. 125, no. 2 pp. 210–220.

Ames, F. and Plesniak, M., 1997, “The influence of large-scale, high-intensity turbulence on vane aerodynamic losses, wake growth, and the exit turbulence parameters,” *Journal of Turbomachinery*, vol. 119, no. 2 pp. 182–192.

Ames, F., Wang, C. and Barbot, P., 2003b, “Measurement and prediction of the influence of catalytic and dry low NOx combuston turbulence on vane surface heat transfer,” *Journal of Turbomachinery*, vol. 125, no. 2 pp. 221–231.

Ames, F. E., 1994, “Experimental study of vane heat transfer and aerodynamics at elevated levels of turbulence,” *Tech. rep.*, National Aeronautics and Space Administration.

ANSYS, 2006, “Fluent user’s guide version 6.3,” *Lebanon, NH: Fluent Incorporated*, vol. 23 pp. 12–23.

Arts, T. and de Rouvroit, M., 1992, “Aero-thermal performance of a two-dimensional highly loaded transonic turbine nozzle guide vane. A test case for inviscid and viscous flow computations,” *Journal of Turbomachinery*, vol. 114, no. 1 pp. 147–154.

Ashworth, D. A., 1987, “Unsteady aerodynamics and heat transfer in a transonic turbine stage,” DPhil thesis, Oxford University.

Barringer, M., Richard, O., Walter, J., Stitzel, S. and Thole, K., 2002, “Flow field simulations of a gas turbine combustor,” *Journal of Turbomachinery*, vol. 124, no. 3 pp. 508–516.

Barringer, M., Thole, K. and Polanka, M., 2009a, “An experimental study of combustor exit profile shapes on endwall heat transfer in high pressure turbine vanes,” *Journal of Turbomachinery*, vol. 131, no. 2 pp. 1–10.

Barringer, M., Thole, K. and Polanka, M., 2009b, “Effects of combustor exit profiles on vane aerodynamic loading and heat transfer in a high pressure turbine,” *Journal of Turbomachinery*, vol. 131, no. 2 pp. 1–10.

Barringer, M., Thole, K., Polanka, M., Clark, J. and Koch, P., 2009c, “Migration of combustor exit profiles through high pressure turbine vanes,” *Journal of Turbomachinery*, vol. 131, no. 2 pp. 1–10.

Bons, J., MacArthur, C. and Rivir, R., 1996, “The effect of high free-stream turbulence on film cooling effectiveness,” *Journal of Turbomachinery*, vol. 118, no. 4 pp. 814–825.

Bunker, R., 2007, “Gas turbine heat transfer: Ten remaining hot gas path challenges,” *Journal of Turbomachinery*, vol. 129, no. 2 pp. 193–201.

Bureau of Transportation Statistics, 2010, “National transportation statistics,” *Tech. rep.*, U.S. Department of Transportation, `http://www.bts.gov/publications/national_transportation_statistics/pdf/entire.pdf`.

Cantwell, B. J., 2005, “Course material for AA283,” ”Website”, `http://www.stanford.edu/~cantwell/AA283_Course_Material/Jet_engine_images/`.

Chang, D. and Tavoularis, S., 2009, “Unsteady vortices and blade loading in a high-pressure turbine,” *Proceedings of the American Society of Engineers Turbo Expo*, vol. 7, pp. 1543–1552.

Choi, J., Teng, S., Han, J. and Ladeinde, F., 2004, “Effect of free-stream turbulence on turbine blade heat transfer and pressure coefficients in low Reynolds number flows,” *International Journal of Heat and Mass Transfer*, vol. 47, no. 14-16 pp. 3441–3452.

Cummings, R. M., Mortion, S. A., McDaniel, D. R., Forsythe, J. R. and Blake, D. C., 2004, “Course notes for AE 342,” Department of Aeronautics, United States Air Force Academy.

Davidson, P., 2004, *Turbulence: an introduction for scientists and engineers*, Oxford University Press.

De la Loma, A., Paniagua, G., Verrastro, D. and Adami, P., 2008, “Transonic turbine stage heat transfer investigation in presence of strong shocks,” *Journal of Turbomachinery*, vol. 130, no. 3 pp. 1–8.

Doorly, D. J., 1983, “A study of the effect of wake passing on turbine blades,” DPhil thesis, Oxford University.

Doorly, J. and Oldfield, M., 1987, “The theory of advanced multi-layer thin film heat transfer gauges,” *International Journal of Heat and Mass Transfer*, vol. 30, no. 6 pp. 1159–1168.

Dorney, D. and Sondak, D., 2000, “Effects of tip clearance on hot streak migration in a high-subsonic single-stage turbine,” *Journal of Turbomachinery*, vol. 122, no. 4 pp. 613–620.

Dullenkopf, K. and Mayle, R., 1994, “Effects of incident turbulence and moving wakes on laminar heat transfer in gas turbines,” *Journal of Turbomachinery*, vol. 116, no. 1 pp. 23–28.

Dunn, M., 2001, “Convective heat transfer and aerodynamics in axial flow turbines,” *Journal of Turbomachinery*, vol. 123, no. 4 pp. 637–686.

Economic Regulations Group, 2010, “UK airline statistics: 2009 - annual,” *Tech. rep.*, Civil Aviation Authority, `http://www.caa.co.uk/docs/80/airline_data/2009Annual/Table_0_1_4_Main_Outputs_of_UK_Airlines_1989_2009_Seat_Km_Avail_Used.pdf`.

Ellenberger, P., 2010, *Piping and pipeline calculations manual: Construction, design fabrication and examination*, Butterworth-Heinemann.

European Union, 2009, “Directive 2009/29/ec of the european parliament and of the council of 23 April 2009 amending directive 2003/87/EC so as to improve and extend the greenhouse gas emission allowance trading scheme of the community,” *Official Journal of the European Union* pp. 63–87.

Fitt, A., Forth, C., Robertson, B. and Jones, T., 1986, “Temperature ratio effects in compressible turbulent boundary layers,” *International Journal of Heat and Mass Transfer*, vol. 29, no. 1 pp. 159–164.

Garg, V., 1998, “Heat transfer on a film-cooled rotating blade using a two-equation turbulence model,” *International Journal of Rotating Machinery*, vol. 4, no. 3 pp. 201–216.

Giel, P., Boyle, R. and Bunker, R., 2004, “Measurements and predictions of heat transfer on rotor blades in a transonic turbine cascade,” *Journal of Turbomachinery*, vol. 126, no. 1 pp. 110–121.

Government Accountability Office, 2009, “Airline industry contraction due to volatile fuel prices and falling demand affects airports, passengers, and federal government revenues,” *Tech. rep.*, `http://www.gao.gov/new.items/d09393.pdf`.

Guibet, J. and Faure-Birchem, E., 1999, *Fuels and engines*, Editions Technip.

Haldeman, C., Dunn, M., Barter, J., Green, B. and Bergholz, R., 2005, “Aerodynamic and heat-flux measurements with predictions on a modern one and one-half state high pressure transonic turbine,” *Journal of Turbomachinery*, vol. 127, no. 3 pp. 522–531.

Han, J., Dutta, S. and Ekkad, S., 2000, *Gas turbine heat transfer and cooling technology*, Taylor & Francis Group.

He, L., Menshikova, V. and Haller, B., 2004, “Influence of hot streak circumferential length-scale in transonic turbine stage,” *Proceedings of the American Society of Mechanical Engineers Turbo Expo 2004*, vol. 5 B, pp. 1117–1126.

He, L., Menshikova, V. and Haller, B., 2007, “Effect of hot-streak counts on turbine blade heat load and forcing,” *Journal of Propulsion and Power*, vol. 23, no. 6 p. 1235.

He, L. and Oldfield, M., 2009, “Unsteady conjugate heat transfer modelling,” *Proceedings of the American Society of Mechanical Engineers Turbo Expo*, vol. 3, pp. 101–114.

Heitor, M. and Whitelaw, J., 1986, “Velocity, temperature, and species characteristics of the flow in a gas-turbine combustor,” *Combustion and Flame*, vol. 64, no. 1 pp. 1–32.

Holman, J., 1997, *Heat transfer*, 8 edn., McGraw-Hill.

Hori, M., Yata, J. and Minamiyama, T., 1997, “Effects of free stream turbulence on turbulent boundary layer on a flat plate with zero pressure gradient (P0art V: The calculation of heat transfer),” *Heat Transfer - Asian Research*, vol. 26, no. 2 pp. 97–106.

Hunt, J. C. R. and Savill, A. M., 2005, *Prediction of turbulent flows*, chap. Guidelines and criteria for the use of turbulence models in complex flows, Cambridge University Press, pp. 291–343.

Hurrion, J., 2002, “The effect of an inlet temperature profile on the heat transfer to gas turbine blades,” DPhil thesis, Oxford University.

Jenkins, S. and Bogard, D., 2005, “The effects of the vane and mainstream turbulence level on hot streak attenuation,” *Journal of Turbomachinery*, vol. 127, no. 1 pp. 215–221.

Jenkins, S. and Bogard, D., 2007, “Scaling of guide vane coolant profiles and the reduction of a simulated hot streak,” *Journal of Turbomachinery*, vol. 129, no. 3 pp. 619–627.

Jenkins, S., Varadarajan, K. and Bogard, D., 2004, “The effects of high mainstream turbulence and turbine vane film cooling on the dispersion of a simulated hot streak,” *Journal of Turbomachinery*, vol. 126, no. 1 pp. 203–211.

Johnson, A., Rigby, M., Oldfield, M., Ainsworth, R. and Oliver, M., 1989, “Surface heat transfer fluctuations on a turbine rotor blade due to upstream shock wave passing,” *Journal of Turbomachinery*, vol. 111, no. 2 pp. 105–115.

Johnson, A. B., 1988, “The aerodynamic effects of nozzle guide vane shock wave and wake passing on a transonic turbine rotor,” DPhil thesis, Oxford University.

Kearney, D., Kays, W. and Moffat, R., 1973, “Heat transfer to a strongly accelerated turbulent boundary layer: Some experimental results, including transpiration,” *International Journal of Heat and Mass Transfer*, vol. 16, no. 6 pp. 1289–1305.

Konig, S. and Stoffel, B., 2007, “On the applicability of a spoked-wheel wake generator for clocking investigations,” *Journal of Fluids Engineering*, vol. 129, no. 11 pp. 1468–1477.

Korakianitis, T., Papagiannidis, P. and Vlachopoulos, N., 2002, “Unsteady flow/quasi-steady heat transfer computations on a turbine rotor and comparison with experiments,” *Journal of Turbomachinery*, vol. 124, no. 1 pp. 152–159.

Kulisa, P. and Dano, C., 2006, “Assessment of linear and non-linear two-equation turbulence models for aerothermal turbomachinery flows,” *Journal of Thermal Science*, vol. 15, no. 1 pp. 14–26.

Laumert, B., Mårtensson, H. and Fransson, T., 2002, “Investigation of unsteady aerodynamic blade excitation mechanisms in a transonic turbine stagepart i: phenomenological identification and classification,” *Journal of Turbomachinery*, vol. 124, no. 3 pp. 410–418.

Lee, S., Jun, S., Park, B.-K. and Lee, J., 2004, “Effects of combustor-level high inlet turbulence on the endwall flow and heat/mass transfer of a high-turning turbine rotor cascade,” *KSME International Journal*, vol. 18, no. 8 pp. 1435–1450.

Levchenya, A. and Smirnov, E., 2010, “Numerical investigation of three-dimensional turbulent flow and endwall heat transfer in a large-scale cascade of turbine blades,” *High Temperature*, vol. 48, no. 1 pp. 57–67.

Liu, X. and Rodi, W., 1994, “Surface pressure and heat transfer measurements in a turbine cascade with unsteady oncoming wakes,” *Experiments in Fluids*, vol. 17, no. 3 pp. 171–178.

Liu, Y., 2007, “Aerodynamics and heat transfer predictions in a highly loaded turbine blade,” *International Journal of Heat and Fluid Flow*, vol. 28, no. 5 pp. 932–937.

Lowery, G. and Vachon, R., 1975, “The effect of turbulence on heat transfer from heated cylinders,” *International Journal of Heat and Mass Transfer*, vol. 18, no. 11 pp. 1229–1242.

Maaroofi, K., Nobari, M. and Shirani, E., 2007, “A numerical simulation of external heat transfer around turbine blades,” *Heat and Mass Transfer/Waerme- und Stoffuebertragung*, vol. 44, no. 1 pp. 61–70.

McDuonald, H. and Kreskovsky, J., 1974, “Effect of free stream turbulence on the turbulent boundary layer,” *International Journal of Heat and Mass Transfer*, vol. 17, no. 7 pp. 705–716.

Mehendale, A., Han, J., Ou, S. and Lee, C., 1994, “Unsteady wake over a linear turbine blade cascade with air and CO film injection: Part ii effect on film effectiveness and heat transfer distributions,” *Journal of Turbomachinery*, vol. 116, no. 4 pp. 730–737.

Menter, F., 1994, “Two-equation eddy-viscosity turbulence models for engineering applications,” *AIAA journal*, vol. 32, no. 8 pp. 1598–1605.

Monin, A. and Yaglom, A., 1971, *Statistical fluid mechanics*, Massachusetts Institute of Technology Press.

Morehouse, K. A. and Simoneau, R. J., 1986, “Effect of a rotor wake on the local heat transfer on the forward half of a circular cylinder,” *Heat Transfer, Proceedings of the International Heat Transfer Conference*, vol. 3, pp. 1249–1255.

Moss, R. and Oldfield, M., 1991, “Measurements of hot combustor turbulence spectra,” *American Society of Mechanical Engineers (Paper)*, pp. 1–8.

Moss, R. W., 1992, “The effects of turbulence length scale on heat transfer,” DPhil thesis, Oxford University.

Nasir, S., Carullo, J., Ng, W., Thole, K., Wu, H., Zhang, L. and Moon, H., 2009, “Effects of large scale high freestream turbulence and exit reynolds number on turbine vane heat transfer in a transonic cascade,” *Journal of Turbomachinery*, vol. 131, no. 2 pp. 1–11.

Nicholson, J. H., 1981, "Experimental and theoretical studies of the aerodynamic and thermal performance of modern gas turbine blades," DPhil thesis, Oxford University.

Nix, A. and Diller, T., 2009, "Experiments on the physical mechanism of heat transfer augmentation by freestream turbulence at a cylinder stagnation point," *Journal of Turbomachinery*, vol. 131, no. 2 pp. 1–7.

Papa, M., Goldstein, R. and Gori, F., 2007, "Numerical heat transfer predictions and mass/heat transfer measurements in a linear turbine cascade," *Applied thermal engineering*, vol. 27, no. 4 pp. 771–778.

Pope, S., 2000, *Turbulent flows*, Cambridge University Press.

Popp, O., 1998, "Steady and unsteady heat transfer in a film cooled transonic turbine cascade," Ph.D. thesis, Virginia Tech University.

Povey, T., Chana, K., Jones, T. and Hurrion, J., 2007, "The effect of hot-streaks on HP vane surface and endwall heat transfer: An experimental and numerical study," *Journal of Turbomachinery*, vol. 129, no. 1 pp. 32–43.

Povey, T. and Qureshi, I., 2008, "A hot-streak (combustor) simulator suited to aerodynamic performance measurements," *Proceedings of the Institution of Mechanical Engineers, Part G: Journal of Aerospace Engineering*, vol. 222, no. 6 pp. 705–720.

Prasad, D. and Hendricks, G., 2000, "A numerical study of secondary flow in axial turbines with application to radial transport of hot streaks," *Journal of Turbomachinery*, vol. 122, no. 4 pp. 667–673.

Priddy, W. and Bayley, F., 1985, "Effects of free stream turbulence on the distribution of heat transfer around turbine blade sections," *International Journal of Heat and Fluid Flow*, vol. 6, no. 3 pp. 181–192.

Qingjun, Z., Fei, T., Huishe, W., Xiaolu, Z. and Jianzhong, X., 2008, "Influence of hot streak temperature ratio on low pressure stage of a vaneless counter-rotating turbine," *Journal of Engineering for Gas Turbines and Power*, vol. 130, no. 3 pp. 1–10.

Radomsky, R. and Thole, K., 2000, "Flowfield measurements for a highly turbulent flow in a stator vane passage," *Journal of Turbomachinery*, vol. 122, no. 2 pp. 255–262.

Rahman, F., Visser, J. and Morris, R., 2005, “Capturing Sudden increase in heat transfer on the suction side of a turbine blade using a navier–stokes solver,” *Journal of Turbomachinery*, vol. 127, no. 3 pp. 552–556.

Rigby, M. J., 1990, “Effects of wake and shock passing on the heat transfer to a film cooled transonic turbine blade,” DPhil thesis, Oxford University.

Royal Commission on Environmental Pollution, 2002, “Short Report: The environmental effects of civil aircraft in flight,” `http://www.rcep.org.uk/reports/sr-2002-aircraft/documents/aviation-report.pdf`.

Schiestel, R., 2008, *Modeling and Simulation of Turbulent Flows*, International Society for Technology in Education.

Schobeiri, M., Ozturk, B., Kegalj, M. and Bensing, D., 2008, “On the physics of heat transfer and aerodynamic behavior of separated flow along a highly loaded low pressure turbine blade under periodic unsteady wake flow and varying of turbulence intensity,” *Journal of Heat Transfer*, vol. 130, no. 5 pp. 1–20.

Sheard, A. G., 1989, “Aerodynamic and mechanical performance of a high pressure turbine stage in a transient wind tunnel,” DPhil thesis, Oxford University.

Sokolov, K., Tumanovskiy, A., Gutnik, M., Sudarev, A., Zakharov, Y. and Winogradov, E., 1995, “Mathematical modeling of an annular gas turbine combustor,” *Journal of Engineering for Gas Turbines and Power*, vol. 117, no. 1 pp. 94–99.

Sugawara, S., Sato, T., Komatsu, H. and Osaka, H., 1988, “Effect of free stream turbulence on flat plate heat transfer,” *International Journal of Heat and Mass Transfer*, vol. 31, no. 1 pp. 5–12.

Talmor, E. and Weber, N., 1970, “Heat transfer from boundary layers undergoing an acceleration induced reverse transition,” *AIChE Journal*, vol. 16, no. 3 pp. 446–455.

Thibert, J., Grandjacques, M. and Ohman, L., 1979, “NACA 0012 airfoil,” *Experimental Data Base for Computer Program Assessment, AGARD-AR-138.*

Vakil, S. and Thole, K., 2005, “Flow and thermal field measurements in a combustor simulator relevant to a gas turbine aeroengine,” *Journal of Engineering for Gas Turbines and Power*, vol. 127, no. 2 pp. 257–267.

Van Fossen, G. and Bunker, R., 2001, “Augmentation of stagnation region heat transfer due to turbulence from a DLN can combustor,” *Journal of Turbomachinery*, vol. 123, no. 1 pp. 140–146.

Wu, X. and Durbin, P., 2000, “Numerical simulation of heat transfer in a transitional boundary layer with passing wakes,” *Journal of Heat Transfer*, vol. 122, no. 2 pp. 248–257.

Zhang, L. and Han, J., 1995, “Combined effect of free-stream turbulence and unsteady wake on heat transfer coefficients from a gas turbine blade,” *Journal of Heat Transfer*, vol. 117, no. 2 pp. 296–301.